INAUGURAL - DISSERTATION
zur
Erlangung der Doktorwürde
der
Naturwissenschaftlich-Mathematischen
Gesamtfakultät
der
Ruprecht-Karls-Universität
Heidelberg

Vorgelegt von
Master of Science (MSc) Geowissenschaften Manfred Vogt
aus Heidelberg

Tag der mündlichen Prüfung: 02.11.2018

Thema:

Acquisition of solar wind implanted neon by terrestrial precursor material resembled by iron meteorites and interplanetary dust: implications for the early evolution of the Earth´s mantle-atmosphere system

Gutachter: Prof. Dr. Mario Trieloff

Prof. Dr. Ulrich Ott

Abstract

Studying the origin and evolution of cosmo- and geochemical reservoirs particularly requires knowledge about the composition and occurrence of the inert noble gases (He, Ne, Ar, Kr, Xe). Earth's atmosphere is characterized by a "planetary" noble gas signature, i.e., depleted from solar element abundances more intensively in lighter than in heavier gases, whereas Earth's interior hosts light noble gases (He and Ne) with a distinct "solar" composition. In particular, Ne isotopic ratios of both the convecting and more primitive mantle, the latter sampled by oceanic island basalts (OIBs), resemble the solar wind (SW) implanted Ne-B component in meteorites with $^{20}Ne/^{22}Ne_{Ne\text{-}B}$ ~12.7. The atmosphere, instead, displays a lower $^{20}Ne/^{22}Ne$ ratio of 9.80.

The reservoir of the primitive noble gas signatures, traditionally assumed to be isolated in the deep mantle, is not precisely located and some models speculate about Earth's core as possible source. High resolution release experiments on interior samples of the iron meteorite Washington County (WC) were carried out in this study to identify volume correlated trapped noble gases and to investigate the possibility of noble gas partitioning into metal upon core segregation. Consisting of a mixture of predominantly cosmogenic and solar components, with only minor atmospheric additions, gases are released from schreibersite ($(Fe,Ni)_3P$) at ~1100 °C and kamacite-taenite (Fe,Ni) at ≳1400 °C. The solar signatures are distinct in Ne and He/Ne isotopic ratios with clear ^4He excess. Ar, Kr and Xe isotopic ratios are either dominated by spallation or are overprinted by air contamination. Measured ^{20}Ne concentrations of ~$4*10^{-8}$ cm^3STP/g imply that solar wind-implantation into terrestrial precursors and incorporation of <1% core material that resembled Washington County metal would have been sufficient to provide solar type Ne in the core that satisfies observed mantle fluxes. This would be consistent with the core as potential source region.

The actual acquisition of the light solar noble gases on Earth can be either explained by solar nebula gas dissolution into a magma ocean or accretion of solar wind irradiated material. The solar wind implantation model is assessed by applying constraints for the present terrestrial influx of particles ranging from 10^{-16}–10^{25} g, and the size-specific Ne inventory of extraterrestrial matter. Present-day Ne contributions to Earth's surface peak at interplanetary dust particle sizes of ~9 µm which contain a mean $^{20}Ne/^{22}Ne$ ratio of 12.61±0.41. This value represents Ne-B in unablated solar wind saturated particle surfaces and dominates the inventory of irradiated, though volatile-poor, matter that accreted to form Earth in the inner Solar system. This is opposed to volatile-rich objects from the outer Solar system containing planetary Ne-A with $^{20}Ne/^{22}Ne$ ~8.20. The data compilations allow determining the mass and size dependent upper atmosphere Ne flux and infer the contribution during early Earth formation of a) surface correlated Ne-B, dominated by ~75 µm particles with high surface/volume ratio and b) volume correlated Ne-A, dominated by larger bodies. The Ne-acquisition scenario considers delivery of solar wind implanted Ne-B shortly after dissipation of disk gas and Ne incorporation into Earth with $^{20}Ne/^{22}Ne$: 12.61±0.41 by dissolution into a magma ocean before the Moon-forming impact. The late veneer contribution of Ne-A to degassed mantle Ne-B establishes the atmospheric inventory with $^{20}Ne/^{22}Ne$: 9.80. The model calculations show that, because dominated by implanted components in cosmic dust, only a fraction of a few % of irradiated precursor material is sufficient to account for the solar Ne budget of Earth, thus, demonstrating the significance of dust accretion for the origin of volatiles.

Kurzfassung

Studien zu Ursprung und Entwicklung kosmo- und geochemischer Reservoire erfordern insbesondere Kenntnisse über Vorkommen und Zusammensetzung inerter Edelgase (He, Ne, Ar, Kr, Xe). Die Erdatmosphäre ist durch „planetare“ Edelgassignaturen mit starker Verarmung leichter gegenüber schweren Gasen relativ zu solaren Elementhäufigkeiten geprägt, während das Erdinnere He und Ne mit „solarer“ Signatur beinhaltet. Insbesondere die Zusammensetzung der Ne Isotope des konvektierenden und des primitiveren Mantels, letzterer durch Ozeaninselbasalte (OIBs) beprobt, entspricht der Sonnenwind-implantierten Ne-B Komponente in Meteoriten mit $^{20}Ne/^{22}Ne_{Ne\text{-}B}$ ~12.7. Die Atmosphäre hingegen zeigt einen niedrigeren $^{20}Ne/^{22}Ne$ Wert von 9.80.

Der im unteren, isolierten Mantel vermutete Ursprungsort der primordialen Edelgase ist bisher nicht eindeutig lokalisiert und Modelle spekulieren über den Erdkern als potentielle Quelle. Hochauflösende Entgasungsexperimente an Proben aus dem Inneren des Eisenmeteoriten Washington County wurden in dieser Studie durchgeführt, um volumenkorrelierte Edelgase nachzuweisen und die Möglichkeit zu prüfen, diese bei der Kernbildung ins Metall abzusondern. Eine Mischung aus vorrangig kosmogenen und solaren Gasen mit nur geringem atmosphärischem Beitrag wurde von Schreibersit ($(Fe,Ni)_3P$) bei ~1100 °C und Kamacit-Taenit (Fe,Ni) bei ≳1400 °C freigesetzt. Solare Signaturen sind durch Ne und He/Ne Isotope mit ^4He Überschuss messbar. Ar, Kr und Xe Isotope sind spallations-dominiert oder durch Luftverunreinigungen überprägt. Gemessene ^{20}Ne Mengen von ~$4*10^{-8}$ cm^3STP/g deuten an, dass Sonnenwind-Implantation in Vorläufermaterial der Erde und Eintrag von <1% Kernmaterial, das Washington County Metall ähnelte, ausreichend gewesen wäre, um genügend solares Ne im Erdkern aufzunehmen, so dass Mantelflüsse erklärt werden können. Dies wäre konsistent mit dem Erdkern als Quellregion.

Die Ansammlung der solaren Edelgase auf der Erde kann entweder durch Lösung des solaren Nebels in einen Magmaozean oder durch Akkretion bestrahlten Materials erklärt werden. Das Sonnenwind-Implantations-Modell wurde mit Parametern zum heutigen terrestrischen Eintrag von Partikelmassen zwischen 10^{-16}–10^{25} g und dem spezifischen Ne-Gehalt extraterrestrischer Körper überprüft. Der derzeitige maximale Ne-Eintrag auf die Erdoberfläche liegt bei Staub-Größen von ~9 µm mit einem mittleren $^{20}Ne/^{22}Ne$ von 12.61±0.41. Dieser Wert repräsentiert Ne-B in Sonnenwind-gesättigten Oberflächen und dominiert das Inventar von bestrahltem, aber volatilarmem, Material aus dem inneren Sonnensystem, das zur Erde akkretierte. Diesem Material stehen volatilreiche Objekte aus dem äußeren Sonnensystem mit planetarem Ne-A ($^{20}Ne/^{22}Ne$ ~8.20) gegenüber. Daten zum massen- und größenabhängigen Ne-Eintrag auf die obere Erdatmosphäre ermöglichen die Beitragsbestimmung für die frühe Erdbildung von a) oberflächenkorreliertem Ne-B, dominiert durch ~75 µm Partikel und b) volumenkorreliertem Ne-A, dominiert durch größere Körper. Das Ne-Akkretions-Szenario betrachtet den Eintrag von implantiertem Ne-B nach Auflösung des solaren Nebels und Aufnahme von Ne ins Erdinnere mit $^{20}Ne/^{22}Ne$: 12.61±0.41 durch Lösung in einen Magmaozean vor der Mondbildung. Durch späteren Ne-A Beitrag zu entgastem Mantel-Ne-B wird das atmosphärische $^{20}Ne/^{22}Ne$ mit 9.80 erzeugt. Das Modell zeigt, dass ein Anteil von nur einigen % bestrahlten Materials, durch implantierte Komponenten in kosmischem Staub dominiert, ausreicht, um das Budget der Erde an solarem Ne beizusteuern. Dies betont die Bedeutung von Staubakkretion für den Ursprung volatiler Elemente.

Table of contents

List of abbreviations

amu	atomic mass unit
ATM	atmosphere
at.%	atomic percent
AU	astronomical unit
BSE	back-scattered electron
CAI	Ca-Al-rich inclusion
CC	carbonaceous chondrite
cf.	confer
CI	CC of Ivuna-type
CM	CC of Mighei-type
CRE	cosmic ray exposure
CS	cosmic spherule
e.g.	exempli gratia (for example)
EMMAC	early-micrometeorite-accretion
EUV	extreme ultraviolet
eV	electron volt
FSW	fractionated solar wind
Ga	giga annus (billion years)
GCR	galactic cosmic rays
HSE	highly siderophile elements
IDP	interplanetary dust particle
i.e.	id est (that is)
keV	kilo electron volt
kV	kilovolt
kyr	kilo years (thousand years)
LDEF	Long Duration Exposure Facility
LHB	late heavy bombardment
Ma	mega annus (million years)
M_E	mass of Earth
mfl	mass fractionation line
MM	micrometeorite
MORB	mid ocean ridge bassalt
MPI	Max-Planck-Institute
OIB	ocean island basalt
ppm	parts per million
RDM	residual depleted mantle
ScMM	scoreaceous micrometeorite
SEM	scanning electron microscope
STP	standard temperature and pressure
SW	solar wind
UnMM	unmelted micrometeorite
vol%	volume percent
wt%	weight percent
µA	microampere
µm	micrometer

1 Outline

The research presented below refers to major aspects of noble gases (He, Ne, Ar, Kr and Xe) in cosmochemistry and geochemistry, their elemental and isotopic compositions as well as their abundance, distribution and evolution in different reservoirs. These reservoirs include Earth's interior and atmosphere, extraterrestrial matter like meteorites and asteroids and the solar wind (SW). The following chapters comprise two individual noble gas studies that intend to explore a possible interior reservoir of noble gases on Earth (Chapter 2) and to investigate the origin of terrestrial noble gases during Earth's formation as well as tracing the evolution of Earth's atmosphere (Chapter 3). Each chapter contains a detailed and comprehensive introduction.

Noble gases in geochemistry and cosmochemistry are important tracers to identify the sources and distribution of volatiles throughout the Solar System (Ozima and Podosek, 2002; Porcelli et al., 2002a; and references therein). Because of their scarcity and chemical inertness noble gases offer detailed insights in geochemical reservoir characteristics and terrestrial mantle geochemistry (Porcelli et al., 2002b; Porcelli and Ballentine, 2002). The study of these highly volatile elements furthermore implies unique constraints on the origin and evolution of terrestrial volatiles and the formation of Earth's atmosphere (Pepin and Porcelli, 2002; Moreira, 2013; and references therein).

For the purpose of the present investigations it is essential to distinguish trapped noble gases which are primordial components from in situ components that are secondary produced by nuclear interactions with cosmic radiation (cosmogenic noble gases) or radioactive decay (radiogenic noble gases). The trapped components are further subdivided into "solar" noble gases (derived, e.g., from SW-implantation) and "planetary" noble gases which are common to the atmospheres of the terrestrial planets (Earth, Mars and probably Venus) and to chondritic meteorites in which the planetary gases, however, represent again a complex mixture of various components, for example, presolar grains (Ott., 2014; and references therein). Overall, the planetary abundance pattern is universally characterized by a strong depletion of all noble gases compared to the solar abundances whereas the light noble gases (He, Ne) show a stronger depletion relative to the heavier ones (Ar, Kr, Xe).

While Earth's atmosphere contains planetary noble gases, Earth's interior incorporates distinct He and Ne signatures of solar origin. In particular the OIB (plume) source yields high contributions of light solar noble gases. This becomes explicitly clear from plume derived samples exhibiting high primordial $^{3}He/^{4}He$ ratios and a solar-like $^{20}Ne/^{22}Ne$ ratio that is indistinguishable from the SW-implanted Ne-B component in meteorites ($^{20}Ne/^{22}Ne_{Ne\text{-}B}$ ~12.5–12.7). Systematically lower $^{3}He/^{4}He$ ratios and slightly lower average maximum $^{20}Ne/^{22}Ne$ ratios in MORB derived samples can be explained by fractionation processes during degassing of the MORB mantle, crustal and atmospheric contamination in combination with convective stirring in the upper mantle and radiogenic ^{4}He additions. This requires at least two separate reservoirs in Earth's interior: a strongly degassed and well-homogenized reservoir in the upper mantle as source for MORBs and a pristine, isolated and gas rich reservoir deep in Earth's mantle that is sampled by plumes. Yet, this

primordial source region was never unambiguously located (Moreira, 2013; and references therein).

Mantle models for possible source regions of He with high $^3He/^4He$ ratios are discussed in length by Porcelli and Ballentine (2002) and are schematically shown in Figure 1.1. Degassing of the upper mantle which contributes to the atmospheric reservoir (ATM) occurs in all scenarios. In models involving layered convection, high $^3He/^4He$ ratios in OIBs are transferred by plumes from an isolated gas-rich reservoir comprising the lower mantle below 660 km. In the simplified limited interaction box model (1), two separate reservoirs without interactions, except for a minor flux to OIBs, exist in the lower mantle and upper mantle. In the steady-state box model (2), there is open interaction between the "closed" lower mantle, the upper mantle and the atmosphere. Inflows into the upper mantle from transferred lower mantle noble gases, subducted atmospheric (heavy) noble gases and production of radiogenic noble gases are equal (in steady-state) to outflows at mid-ocean ridges. Generally, however, models including layered convection are in conflict with geophysical evidence of plates subducted into the lower mantle. In models involving whole mantle convection across the 660 km boundary, high $^3He/^4He$ ratios in OIBs are transferred by plumes from a primitive gas-rich reservoir in isolated deep layers or preserved mantle heterogeneities ("blobs") (3). In a lower boundary layer above the core mantle boundary, high $^3He/^4He$ ratios are presumably sourced from a residual depleted mantle (RDM) (4) of subducted oceanic lithosphere (depleted in U and He) which presently yields OIB signatures but initially incorporated solar $^3He/^4He$ ratios. Altered oceanic crust (complementary to the oceanic lithosphere) in the underlying D" layer is strongly depleted in ^3He and likely contains radiogenic ^4He due to potential U enrichments. Complications for these models arise from the fact that subducted material may be too depleted to cause OIB signatures alone or how an additional fixed primitive reservoir with high $^3He/^4He$ ratios can remain convectively isolated over long time scales. In another model, high $^3He/^4He$ ratios in OIBs are transferred by plumes directly from Earth's core (5). This source remains possible but more speculative (Porcelli and Ballentine, 2002).

Chapter 2 ("Earth's core as source of light primordial noble gases") aims to investigate the potential of Earth's core to incorporate light solar noble gases (He and Ne, Fig. 1.1) and to act as potential source reservoir that might influence the terrestrial noble gas budget. Conclusions are drawn from the analysis of noble gases that are trapped within the metal of the iron meteorite Washington County that is, like Earth, a differentiated body and might represent a type of terrestrial building blocks.

The "planetary" composition of Earth's atmosphere and the occurrence of the "solar" composition (of light noble gases) in Earth's mantle directly lead to the discussion how these components were acquired on Earth. This implicitly involves the question of the origin and evolution of the atmosphere and volatiles on Earth in general. The planetary signature of the atmosphere points towards a secondary origin and results from a combination of degassing from the interior, delivery of chondritic material and elemental and isotopic fractionation. The solar signatures must have been acquired during an earlier stage of Earth's accretion. The origin of light noble gases (He, Ne, and Ar) on Earth was recently reviewed by Péron et al. (2018). Two outstanding models have been proposed for the origin of light solar noble gases within Earth: either dissolution of solar nebula gas into a magma ocean during early planet formation in a "gas-

rich" environment or SW-implantation into accreting materials after dissipation of the solar nebula in a "gas-poor" environment (e.g., Pepin, 1991). Both models are essentially based on the presence of solar-like Ne within Earth, however, the recognition of Ne as the SW-implanted Ne-B component requires valid scenarios and models of SW-irradiation during terrestrial accretion.

Chapter 3 ("Acquisition of solar Ne during terrestrial accretion") considers the origin of solar-like Ne within Earth if the SW-implantation model is valid. This model is reviewed to quantify its potential to account for the terrestrial Ne budget. It takes into account early accretionary fluxes of dust-sized particles with high surface to volume ratio as dominant carriers of surface implanted components supplying Ne-B. The evolution of the atmospheric composition is then established by mixing of a degassed solar component from the interior with a planetary component that is delivered by a chondritic veneer during a later stage of terrestrial accretion. Conclusions can be drawn for the acquisition of terrestrial volatiles and the importance of dust-sized matter during Earth's accretion.

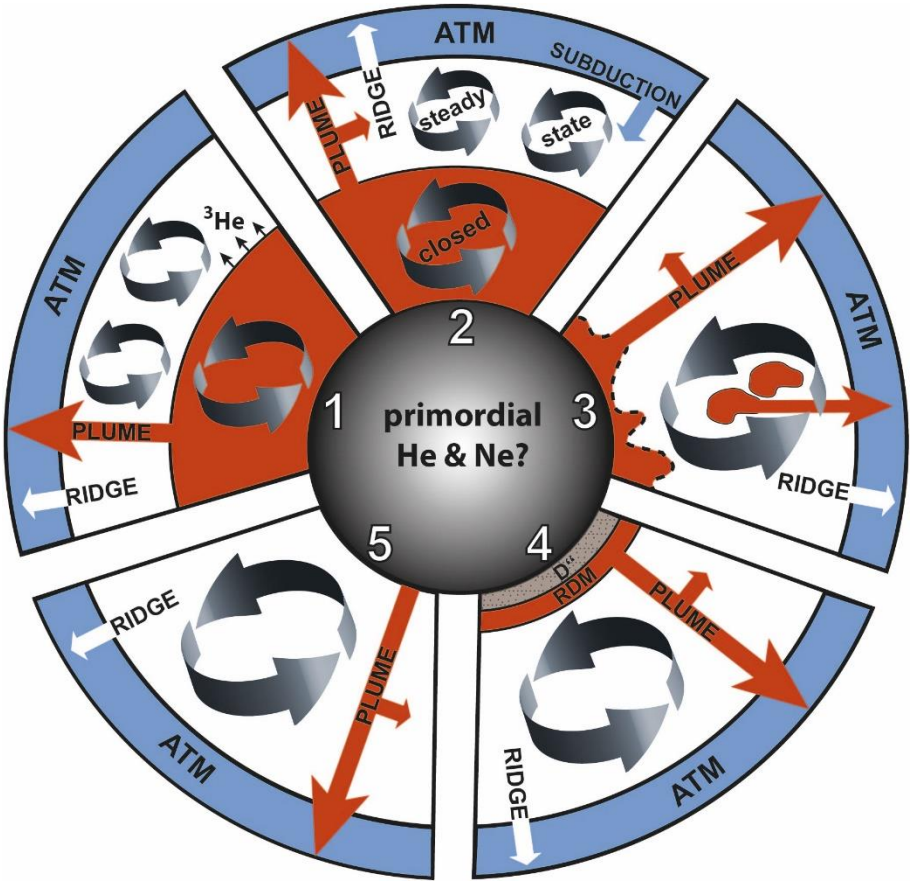

Fig. 1.1: Schematic mantel models showing possible reservoirs for He with high $^3He/^4He$ ratios (orange) and He fluxes as arrows. In models with layered convection, high $^3He/^4He$ ratios are sourced from the lower mantle below 660 km in the limited interaction box model (1) and the steady-state box model (2). In the limited interaction model, fluxes of ^3He from the lower mantle are required to compensate global He fluxes at mid-ocean ridges. In models with whole mantle convection, high $^3He/^4He$ ratios are sourced from deep isolated layers and preserved mantle heterogeneities (3), a residual depleted mantle (RDM) of subducted oceanic lithosphere above the core mantle boundary (4) or from the core (5) (see text for details). Chapter 2 investigates the core as possible reservoir for primordial He and Ne. ATM: Atmosphere, RDM: residual depleted mantle (redrawn and modified from Porcelli and Ballentine, 2002).

2 Earth's core as source of light primordial noble gases

2.1 Introduction

Noble gases are chemically inert tracers that comprise information on the origin and evolution of Earth's geochemical reservoirs (Porcelli and Ballentine, 2002). The interior of Earth hosts noble gases with a distinct solar-like component (e.g., Sarda et al., 1988; Honda et al., 1991; Pepin, 1998; Trieloff et al., 2000; Trieloff and Kunz, 2005; Marty, 2012; Halliday, 2013; Moreira, 2013). Especially the isotopic composition of neon observed in the mantle end-member ($^{20}Ne/^{22}Ne_{mantle}$: ≳12.5–~12.9) of mid ocean ridges (MORBs) and ocean island basalts (OIBs) points towards a solar origin for the mantle gases (Trieloff et al., 2000; Dixon et al., 2000; Yokochi and Marty, 2004; Ballentine et al., 2005; Mukhopadhyay, 2012; Moreira, 2013; Péron et al., 2017). This mantle value was identified by Trieloff et al. (2000, 2002) and Trieloff and Kunz (2005) to be indistinguishable from the Ne-B component ($^{20}Ne/^{22}Ne_{Ne\text{-}B}$: ~12.5–12.7, Black, 1972; Trieloff and Kunz, 2005; Moreira and Charnoz, 2016), which can be related to the solar wind (SW) composition ($^{20}Ne/^{22}Ne_{SW}$: 13.777±0.010; Heber et al., 2012 or respectively 14.001±0.042; Pepin et al., 2012) by isotopic fractionation during ion implantation. In order to establish the mantle composition, solar noble gases must have been incorporated into the deep mantle very early during Earth's history for which only few processes can provide an explanation (Harper and Jacobsen, 1996; Porcelli et al., 2001). Among the different mechanisms for the acquisition of the terrestrial noble gases (see Pepin and Porcelli, 2002), accretion of volatile-rich, dominantly small terrestrial precursor material, that contains high concentrations of implanted light solar noble gases derived from SW-irradiation, is a possible solution (Podosek et al., 2000; Trieloff et al., 2002; Moreira, 2013; Péron et al., 2017; Jaupart et al., 2017; Vogt et al., in prep.; see Chapter 3). An alternative model involves dissolution of solar gases into a magma ocean, which was generated through the blanketing effect of a gravitationally captured dense solar nebula (Mizuno et al., 1980; Sasaki and Nakazawa, 1990; Harper and Jacobsen, 1996; Sasaki, 1999; Woolum et al., 1999; Porcelli et al., 2001).

The flux from Earth's core itself could be an additional source for solar noble gases in the deep mantle (Porcelli and Halliday, 2001; Trieloff and Kunz, 2005). So far, the iron core has been recognized as a speculative but viable source region of isotopically distinctive helium to assess the nature of the high $^{3}He/^{4}He$ OIB source (Porcelli and Halliday, 2001; Porcelli and Ballentine, 2002). Assuming a diffusive flux of ^{3}He (and other noble gases) from the core into a thermal boundary layer at the bottom of the mantle, Moreira (2013) calculated that a thin boundary layer (~2 km in thickness) could be significantly enriched in helium and supply the signatures observed in OIBs. In this regard, primordial He isotopic ratios in hotspots may provide a tracer reflecting core-mantle interactions if plumes originate at the core-mantle boundary and if core material is transferred and/or entrained back into the mantle (Macpherson et al., 1998). Possible transport mechanisms across the core-mantle boundary have been discussed by Porcelli and Halliday (2001) and Porcelli and Ballentine (2002) and involve expulsion of noble gases from the outer core, diffusion processes, partitioning into overlying partial melts or bulk transfer of core material. Overall, partitioning of noble gases from the core into the mantle should be even more effective if

mantle noble gases were depleted by orders of magnitude during massive mantle degassing after core formation (Trieloff and Kunz, 2005).

The presence of high $^{3}He/^{4}He$ ratios within the core would have required trapping of sufficient primordial He during accretion unaccompanied by U and Th to prevent radiogenic production of ^{4}He (Porcelli and Ballentine, 2002). Furthermore, the incorporation into the core is not only dependent on the metal-silicate partitioning coefficients for the noble gases under core forming conditions but also on the initial noble gas concentrations and their availability (Porcelli and Ballentine, 2002; Trieloff and Kunz, 2005). These quantities moreover depend on whether the mantle was molten or solid during core segregation. Initial concentrations of $0.6–70*10^{11}$ atoms $^{3}He/g$ in the mantle may have been necessary to partition sufficient ^{3}He into the core if the present mantle fluxes of primordial He were assumed to be entirely maintained by this source (Porcelli and Halliday, 2001). On the other hand, partitioning of noble gases between metal- and silicate melt under pressures between 5 and 100 kbar may result in insufficient ^{3}He to be present in the core because measured noble gas partitioning coefficients are very low and decrease from $\sim4*10^{-2}$ to $\sim3*10^{-4}$ with increasing pressure (Matsuda et al., 1993). At very high core forming pressures (~50 GPa), however, silicate-metal partitioning coefficients are unknown for noble gases (Porcelli and Halliday, 2001; Moreira, 2013) and any change of physical properties of the (heavy) noble gases in the deep mantle might cause a different geochemical behavior; Xe for example forms high-density solids under these conditions (Jephcoat and Besedin, 1996; Jephcoat, 1998). Sequestering Xe into the metal phase could furthermore point towards an explanation for the 'missing Xe' paradox (Macpherson et al., 1998; Jephcoat, 1998) since Xe would then be sited within the core (Ozima and Podosek, 2002).

Although highly speculative, the scenario of incorporating primordial He into the core and transferring it from the core back into the mantle is also conceivable for Ne (Dixon et al., 2000; Trieloff and Kunz, 2005). The presence of Ne within the iron core would offer an alternative solution other than requiring a separate reservoir for solar-like Ne within Earth's mantle such as an isolated source region or subducted material (e.g., Porcelli and Halliday 2001; Trieloff and Kunz, 2005). In this regard, analyses of iron meteorites as a natural analogue of segregated core material offer a possibility to study the feasibility of sequestering noble gases into the metal phase. On the other hand, only the iron meteorite Washington County (Fig. 2.1) is known to contain volume correlated light solar noble gases that appear to be different from surface implanted components or solar gases sited within silicate inclusions (Murty and Ranjith Kumar, 2014). The concentration of this ^{3}He in Washington County is considered by Porcelli and Halliday (2001) as a possible indication for the incorporation of noble gases into the core. Similarly, Trieloff and Kunz (2005) consider the high concentration of ^{20}Ne in Washington County as sufficient to account for the required solar Ne concentration in the Earth's core if ~0.25% of Earth's precursor metal resembled this kind of iron meteorite.

After the first report of excess ^{4}He in Washington County unrelated to cosmic ray production (Schaeffer and Fisher, 1959), high excesses of non-cosmogenic light noble gases with a remarkably low $^{3}He/^{4}He$ ratio were verified by Signer and Nier (1962) and Hintenberger et al. (1967). These studies revealed also a striking excess of ^{20}Ne in these samples and the authors argued for the presence of trapped primordial gases. Signer and Nier (1962) observed the release of

(a factor of five) variable excesses incorporated into samples from adjacent areas even though yielding a constant $(^4He/^{20}Ne)_{excess}$ ratio of 420±40. Hintenberger et al. (1967) reported a similar excess $^4He/^{20}Ne$ ratio of 470 and postulated the pure metal phase as the only possible noble gas carrier. In shavings of unablated rear surface samples of Washington County Becker and Pepin (1982, 1984, 1987) found a ratio of trapped to spallation noble gases that was several times larger than in the previous studies and the inferred He, Ne, Ar elemental as well as the $^{20}Ne/^{22}Ne$ ratios turned out to be almost identical to those in the present-day solar wind. Murty and Ranjith Kumar (2014) performed a three-temperature stepwise pyrolysis analysis on surface and interior samples of Washington County and detected volume correlated trapped solar gases with a peak release temperature of 1700°C. Trapped elemental ratios were found to have fractionated solar values, with the Ne isotopic composition of interior samples indicative of the presence of SW-Ne within the metal.

Direct implantation of SW into metal grains prior to accretion was advocated as a possible explanation for the origin of the trapped solar composition gases (Becker and Pepin, 1982, 1984). Otherwise, these can only have been acquired by the iron meteorite during the formation of its parent body under very specific conditions involving a sudden melting event (Hintenberger et al., 1967; Becker and Pepin, 1984). On the other hand, similar to the case of the iron meteorite Kavarpura in which the trapped SW-component is attributed to inhomogeneously distributed inclusions rather than being hosted within the metal (Murty et al., 2008), the observed distribution of noble gases in Washington County might, in spite of the assertion of Hintenberger et al. (1967), as well point towards a heterogeneously distributed minor carrier phase (Murty and Ranjith Kumar, 2014).

In the following chapter the first high resolution temperature release study on interior samples of Washington County is presented that was performed to trace the trapped noble gas component. The presented results provide unique information relevant to the question which particular carrier phase hosts the analyzed noble gases. Whether or not SW-gases are present in the interior of Washington County has direct implications for the identification of a potential source region of solar noble gases within Earth's interior.

2.2 Experimental

2.2.1 Washington County iron meteorite

The iron meteorite Washington County was first described as moderately nickel-rich ataxite (Palache and Shannon, 1928) that contains ~9.9 wt% Ni (Cech, 1962; Wasson and Schaudy, 1971; Malvin et al., 1984) and appears distantly related to irons of group IIIB (Buchwald, 1975). The massive iron disk with dimensions of 15 and 20 cm and a thickness of 6 cm (Fig. 2.1) displays a slightly conical "front surface" which obtained its fusion crust and radial grooves called regmaglypts probably during atmospheric entry. The opposite surface is much smoother and more smoothly domed (Palache and Shannon, 1928; Buchwald, 1975). Metallographic investigations and thermal history interpretations suggest rapid cooling and solidification of the metal (Chech, 1962).

The present structure of Washington County may be interpreted as the result of metamorphism that involved severe shock, shear-deformation and annealing (Buchwald, 1975). A detailed structural and mineralogical description of Washington County can be found in Buchwald (1975).

A recent reinvestigation of the texture, phase composition and bulk composition by Ray and Ghosh (2014) reassigned Washington County to the structural group 'Reheated Medium Octahedrite', based on the formation of its thoroughly recrystallized texture (see section SEM analyses) and a bulk chemical composition of Co: 0.56 wt%, Cr: 0.01 wt%, Ga: 18 ppm, Ge: 33 ppm, Ir: 0.01 ppm and Cu: 220 ppm. According to these authors, Washington County is a member of the fractionated group IIIAB and, more specifically, IIIB despite strong effects of secondary reheating caused by high intensity of shock (>750 kbar).

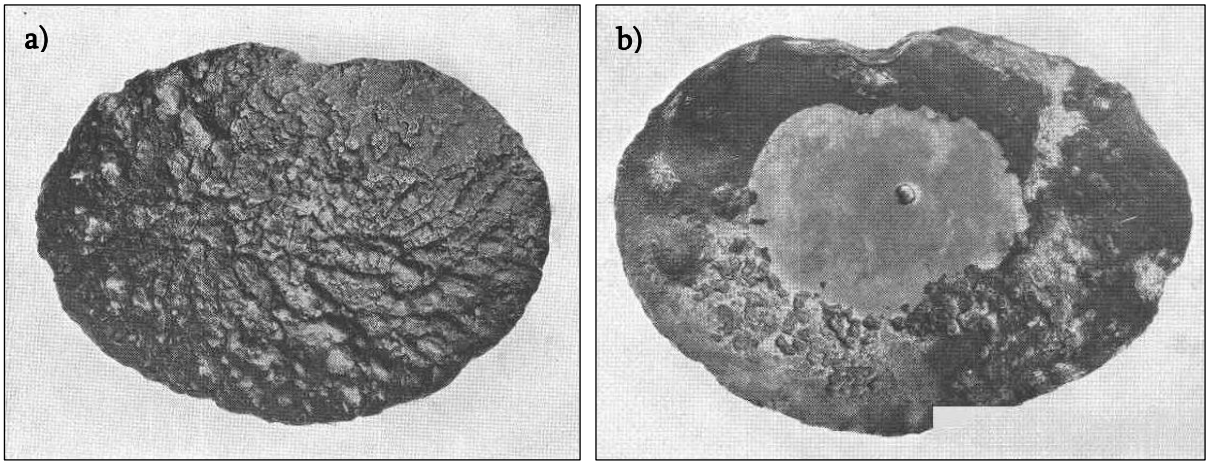

Fig. 2.1: Iron meteorite Washington County (Palache and Shannon, 1928). The major axes of the 6 cm thick metal disk are 15 and 20 cm. **a)** slightly conical "front surface" characterized by radial flutings. **b)** opposite smoothly domed surface. The 10x7 cm plane area in the center results from shaping in 1927 (Buchwald, 1975).

2.2.2 Sample preparation

A 3 cm long slab of Washington County (WC_3078A, 0.75 g, Fig. 2.2) was obtained from Dr. Jutta Zipfel from the collection at the Senckenberg Forschungsinstitut und Naturmuseum Frankfurt, Germany. One end exhibits the fusion crust of the former surface of the meteorite. The other end represents the interior of Washington County.

The slab surface was polished and cleaned at the Institut für Geowissenschaften in Heidelberg for reexamination of the previously reported (see Buchwald, 1975; Ray and Ghosh, 2014) primary mineral phases under the SEM. Of particular interest was the distribution of potential (minor) noble gas carrier phases.

After SEM analyses WC_3078A was cut with a 150 µm thick metal cutting saw blade in length to save one half of the slab for further investigations. The other half was cut in 15 aliquots (Fig. 2.2, WC_1 to WC_15 from surface to depth) of approximately equal size and weights of 7.3 to 21.1 mg to facilitate noble gas measurements of near-surface and interior samples.

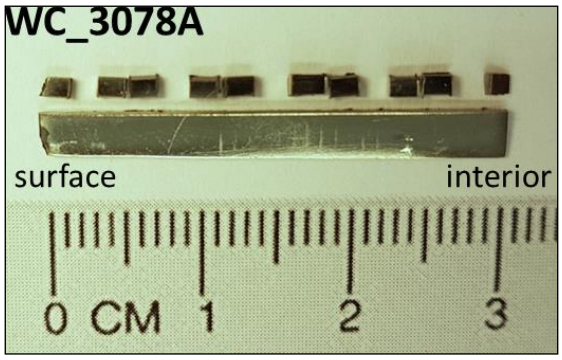

Fig. 2.2: Photograph of the Washington County sample slab (WC_3078A). Surface and interior orientation are indicated in reference to the former surface of the meteorite (fusion crust). The slab surface was polished to facilitate SEM-analyses. The cuttings that are aligned alongside and above the uncut polished slab-half (WC_1 to WC_15 from left to right) are aliquots that are intended for noble gas measurements of near-surface and interior samples. Missing in this photograph are WC_2, WC_5, WC_8, WC_11 and WC_14, which have been analyzed already and for which results are reported here. WC_8 was in preparation, but not measured.

2.2.3 SEM analyses

To document the texture and mineral distribution of WC_3078A the complete polished slab surface was investigated with 500-times magnifiction under the SEM (Fig. 2.3). The observed texture and phase composition corresponds to the description of Ray and Ghosh (2014) with respect to the complete destruction of all primary textures (thus formerly classified as chemically anomalous ataxite) and formation of a thoroughly recrystallized granulated kamacite matrix that contains common and evenly distributed taenite and schreibersite particles (Figs. 2.3, 2.4). Therefore, for this work, the chemical composition of the main minerals is adopted from Ray and Ghosh (2014): Washington County shows a recrystallized matrix (usually of 30 µm, but up to 70 µm in size) of granular kamacite ((Fe,Ni), Ni: 7.25±0.07 wt%) and evenly distributed particles (5–20 µm) of high-Ni taenite ((Fe,Ni), Ni: 32.30±1.12 wt%) as well as low-Ni taenite ((Fe,Ni), Ni: 22 wt%) and Ni-rich schreibersite $((Fe,Ni)_3P$, Ni: 46.60±0.08 wt%).

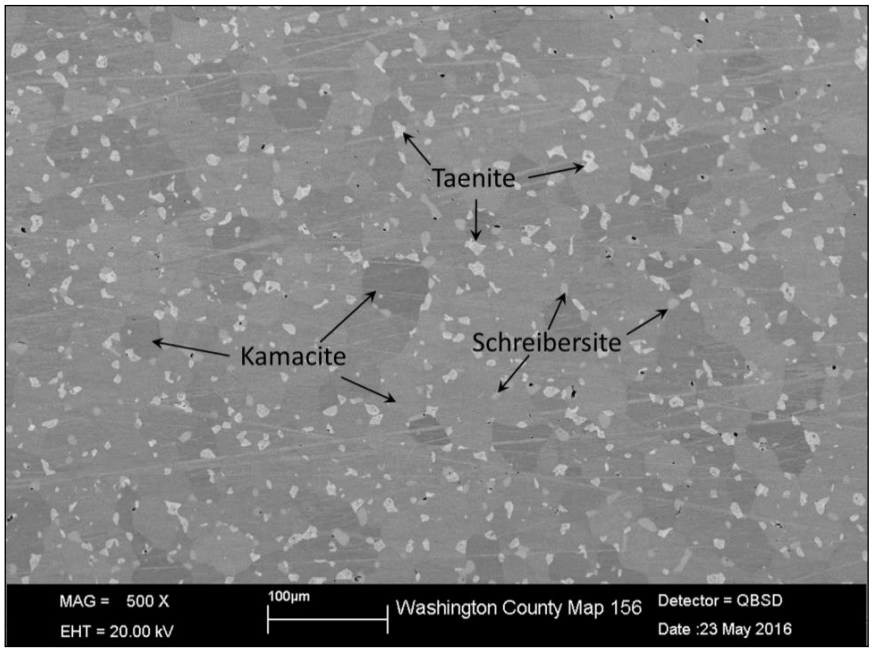

Fig. 2.3: SEM picture of the polished surface of WC_3078A. The granular kamacite matrix contains evenly distributed taenite and schreibersite particles.

Figure 2.4 shows the Fe, Ni and P element distributions of the investigated slab surface. The shown distribution of Fe corresponds essentially to the occurrence of kamacite with a phase abundance of about 90%. The Ni element distribution is equivalent to a phase abundance of ~7% taenite containing ~30 wt% Ni. The P element distribution marks the occurrence of schreibersite with a total phase abundance of ~3%.

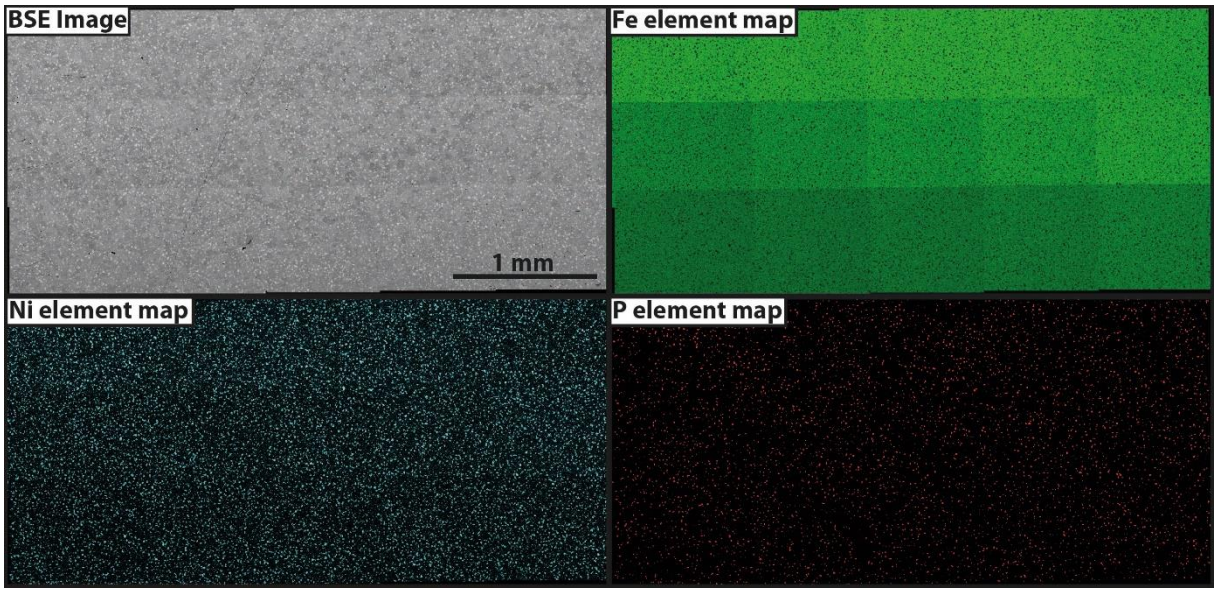

Fig. 2.4: BSE image of the WC_3078A slab surface and element distribution maps of Fe, Ni and P. The element distributions correspond to the occurrences of kamacite (Fe map), taenite (Ni map, ~30 wt% Ni) and schreibersite (P map).

The presence of a sporadically occurring dispersed angular to subangular high carbon phase reported by Ray and Ghosh (2014) could not be confirmed for the presently investigated slab. Instead, a previously unreported and hitherto unknown spinel phase was observed (Fig. 2.5). These angular to subangular spinels of 1–10 μm in size are distributed sporadically across the surface of WC_3078A. Here, their total abundance is estimated to ~0.01‰. Dependent on the chemical composition, these spinel phases are classified as manganese bearing chromites ($Fe^{2+}Cr_2O_4$) containing a few wt% Mn and up to ~0.1 wt% V, or as manganochromites ($(Mn,Fe^{2+})(Cr, V)_2O_4$). In the latter, Mn exceeds the Fe content reaching ~20 wt%, while the mean vanadium content reaches up to about ~0.4 wt%.

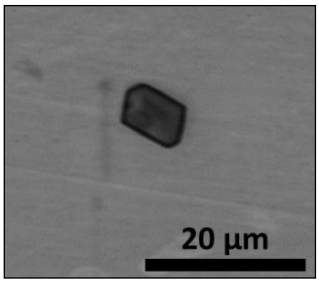

Fig. 2.5: Angular spinel phase.

2.2.4 Noble gas extraction and measurement

To investigate the depth dependent noble gas contents of Washington County and clarify the presence of SW-implanted noble gas isotopic compositions in interior samples, four aliquots (WC_2: 17.3 mg, WC_5: 18.3 mg, WC_11: 14.2 mg, WC_14: 20.9 mg, Fig. 2.2) comprising near-surface and interior parts of WC_3078A were selected and measured for noble gas composition (He, Ne, Ar and Xe, Tab. 2.1 and Tab. 2.3). Extraction and measurements were carried out at the Institut für Geowissenschaften, Universität Heidelberg, Germany. In order to constrain the noble gas release pattern a high-resolution stepwise heating schedule was applied (i.e., 25 steps, 600-1800 °C) for the first measured sample (WC_5, Fig. 2.6). The results were used to refine the measurement procedure for subsequently analyzed samples, in particular by reducing the number of performed gas release steps and by omitting Xe from the measurements.

All samples were weighed and wrapped in aluminum foil. The extraction and measurement procedures followed those described in Bartoschewitz et al. (2017), with some modifications. For gas extraction, a resistance heated furnace was used consisting of an outer Ta-tube containing an inner crucible consisting of molybdenum. Purification of the released gases was done by exposure to two cold Al-Zr-getters (WC_5) and two cold Ti-getters (WC_2, WC_5, WC_11, WC_14) during the furnace heating process. For samples WC_2, WC_11 and WC_14 only the Ti-getters were used. After heating, Ar and Xe were transferred to a charcoal finger cooled with liquid nitrogen. For WC_5 and WC_14 the remaining He and Ne were transferred to another, cryostatically cooled charcoal trap at ca. 20 K. Helium was then fully separated from neon at 48 K and subsequently measured. In case of WC_2 and WC_11 only Ne was transferred to the cryostatically cooled charcoal kept at ca. 48 K and the remaining He was directly measured. Neon release from the trap was achieved at 120 K and then measured. The heavy noble gas fraction was further cleaned by two hot Al-Zr-getters (ca. 400 °C, WC_5 only) and two hot Ti-getters (ca. 300 °C / 600 °C, all samples), respectively. Ar and Xe released from WC_5 were transferred to a cryostatically cooled stainless steel sponge adsorber and subsequent separation of Ar from Xe was achieved at 90 K. In this case, about 93% of the Ar fraction was present in the Ar analysis, and 100% of Xe in the Xe analysis. In case of WC_2, WC_11 and WC_14 Xe was not analysed and the full amount of Ar was available for analysis.

Measurements were performed with a VG 3600 noble gas mass spectrometer at 120 μA trap current, 5 kV acceleration voltage and a nominal ionization energy of 80 eV (He, Ne) and 60 eV (Ar, Xe) for WC_5. The nominal ionization energy was set to 80 eV (He, Ne, Ar) for WC_2, WC_11 and WC_14. All isotopes except ^{4}He and ^{40}Ar, which were measured on a Faraday cup, were detected by a channeltron in a single ion counting mode. During measurement of He and Ne the mass spectrometer volume was connected with charcoal cooled with liquid nitrogen to reduce mass interferences, in particular from ^{40}Ar. Potential interferences during Ne measurements were controlled by simultaneous measurement of masses 18 (H_2O), 40 (Ar), 44 (dominantly CO_2) and 42 (hydrocarbons). Interference corrections were applied accordingly. Sample analyses were corrected for instrumental mass fractionation based on frequent measurements of calibration gas bracketing the sample measurements, which also were used for calculating the absolute gas

amounts. The isotopic composition of all calibration gases is equivalent to air ratios except for He. For He, an artificial gas standard enriched in ^{3}He was used (^{4}He/^{3}He: 40183±87).

For data assessment, all temperature steps were corrected for blank contributions during measuring procedure from the furnace, as determined from a sequence of blank measurements for all gases and samples between 800 °C and 1800 °C (Tables A1 and Tab. A2). Blank uncertainties were conservatively set to ±10% for ^{4}He, ^{36}Ar and ^{129}Xe, ±5% for ^{20}Ne (1σ-errors) to take into account variations observed in the measured blanks. In general, isotopic compositions of the blanks were indistinguishable from air. This is also assumed for He although ^{3}He was always under detection limit. Thus, air composition (±20% for He, ±10% for Ar and Xe, ±5% for Ne, 1σ-errors) was used in blank corrections of sample analyses. Blank contributions were often substantial for ^{4}He, ^{20}Ne, ^{22}Ne, ^{36}Ar and ^{40}Ar (see Tab. A3), but generally low (at most few %) for the typical cosmogenic nuclides ^{3}He, ^{21}Ne and ^{38}Ar.

2.3 Results

2.3.1 Noble gas data

In Tables 2.1, 2.2 and 2.3, new bulk noble gas measurements of Washington County (WC_2, WC_5, WC_11, WC_14) performed at the Institut für Geowissenschaften, Universität Heidelberg, Germany are complemented by data obtained earlier at the Max-Planck-Institut für Chemie in Mainz, Germany using experimental procedures as described in Ott (1988) and Schelhaas et al. (1999) (WC_g: 22.40 mg bulk; WC_s: 21.87 mg bulk, WC_r: 8.54 mg residue). WC_g and WC_s are from different ends of a ~1 cm long piece, whileWC_r was a residue obtained by dissolution in sulfuric acid of 1.03 g of original material. The acid treatment left a 14.1 mg residue of almost pure schreibersite particles with sizes of 3–5 µm. The original Mainz-sample (0.5 cm x 0.5 cm x 1.5 cm) had been provided by O. Schaeffer and was subsequently obtained via H.Voshage and F. Begemann. Noble gas measurements on another part of this sample were previously reported by Hintenberger et al. (1967). The results of the combined analyses are compared in the following with the measurements previously reported by Schaeffer and Fisher (1959), Signer and Nier (1962), Merrihue (1964), Hintenberger et al. (1967) and Becker and Pepin (1984).

The noble gas release patterns related to the performed temperature steps for the samples analyzed by high-resolution temperature extraction (WC_2, WC_5, WC_11, WC_14) are shown in Figure 2.6 and APPENDIX A. Isotopic and elemental ratios of analyzed WC_samples are shown together with literature data in Figures 2.7 to 2.11. To better resolve the primary solar and cosmogenic noble gas components, totals given as total(1) (Tab. 2.1) were calculated as the sum of the intermediate temperature steps only. This is because gases released at low and high temperatures potentially include (a) gas component(s) with atmosphere-like composition indicative of terrestrial contamination. In particular, extraction steps at 600 °C and 700 °C (WC_5) have been omitted in all calculations because of contributions from melting and degassing of the aluminum foil used for wrapping the samples. Up to 850 °C, still the observed gas release is influenced by degassing of the aluminum foil as indicated by atmospheric-like ^{40}Ar/^{36}Ar ratios.

Tab. 2.1: Concentration and isotopic ratios of He, Ne and Ar of investigated Washington County samples

Sample (weight)	Temp. [°C]	^{4}He [10^{-8} cm³STP/g]	±	^{4}He/^{3}He	±	^{22}Ne [10^{-10} cm³STP/g]	±	^{20}Ne/^{22}Ne	±	^{21}Ne/^{22}Ne	±	^{4}He/^{20}Ne	±	^{20}Ne$_{excess}$ [10^{-10} cm³STP/g]	(^{4}He/^{20}Ne) (excess)	^{36}Ar [10^{-10} cm³STP/g]	±	^{38}Ar/^{36}Ar	±	^{40}Ar/^{36}Ar	±
WC_2[a]																					
(17.3 mg)	**800**	blank	-	-	-	blank	-	-	-	-	-	-	-	-	-	0.76	0.16	1.058	0.160	362.09	79.14
	1050	106.9	3.1	10.26	0.30	16.01	0.08	1.31	0.03	0.914	0.008	510.2	27.1	6.8	1161	33.01	0.85	1.550	0.011	2.21	0.29
	1140	353.1	8.6	10.48	0.26	59.38	0.17	1.48	0.01	0.900	0.007	401.4	16.5	36.3	727	144.00	3.41	1.533	0.007	1.43	0.08
	1350	636.2	15.1	10.99	0.27	110.78	0.26	1.55	0.01	0.893	0.006	370.2	14.7	76.1	635	267.97	6.27	1.527	0.006	0.60	0.05
	1380	232.4	5.9	11.55	0.30	43.48	0.20	1.57	0.01	0.886	0.008	340.5	14.6	30.7	584	101.84	2.48	1.521	0.009	-	-
	1390	26.1	1.7	12.06	0.81	4.78	0.06	1.22	0.09	0.918	0.014	446.8	54.8	1.6	1280	11.68	0.37	1.559	0.024	7.75	1.02
	1400	7.6	1.3	11.13	1.95	1.39	0.04	-	-	1.134	0.036	-	-	-	-	3.80	0.25	1.788	0.085	-	-
	1410	5.8	1.4	16.38	3.96	0.67	0.04	-	-	1.260	0.077	-	-	-	-	2.28	0.22	1.940	0.150	-	-
	1450	11.7	1.7	23.73	3.48	11.43	0.06	8.78	0.06	0.135	0.002	11.7	1.8	96.3	11	5.66	0.29	1.101	0.034	116.85	8.04
	1800	2.7	2.4	10.81	9.82	2.13	0.06	5.99	0.88	0.424	0.014	20.9	19.6	11.6	17	2.66	0.40	1.582	0.201	45.86	10.77
Total(1) (no high T)		**1368.0**	**18.7**	**10.92**	**0.16**	**236.49**	**0.39**	**1.50**	**0.01**	**0.898**	**0.004**	**381.7**	**8.9**	**151.5**	**684**	**564.58**	**7.62**	**1.533**	**0.004**	**0.94**	**0.04**
Total(2) (all T steps)		**1382.4**	**18.9**	**10.97**	**0.16**	**250.05**	**0.40**	**1.87**	**0.01**	**0.859**	**0.004**	**292.5**	**6.4**	**257.4**	**407**	**573.66**	**7.64**	**1.529**	**0.004**	**2.77**	**0.18**
WC_5[a]																					
(18.3 mg)	**600**	blank	-	-	-	blank	-	-	-	-	-	-	-	-	-	2.63	1.59	0.187	0.053	259.58	181.19
	700	blank	-	-	-	blank	-	-	-	-	-	-	-	-	-	12.38	4.02	0.198	0.030	299.76	110.96
	800	blank	-	-	-	blank	-	-	-	-	-	-	-	-	-	2.70	1.60	0.377	0.101	252.21	173.35
	850	4.7	1.3	5.35	1.54	0.08	0.04	-	-	-	-	-	-	-	-	2.04	1.45	0.520	0.188	233.58	196.99
	900	15.2	1.5	8.66	0.86	2.19	0.04	1.29	0.37	0.919	0.019	538.5	189.7	0.9	1186	5.80	2.37	0.768	0.141	160.77	80.96
	950	20.4	1.7	8.92	0.76	3.49	0.04	1.72	0.23	0.875	0.012	340.6	63.2	3.0	476	7.17	2.72	1.090	0.184	100.18	51.04
	1000	17.4	1.6	9.60	0.88	4.15	0.04	2.00	0.19	0.871	0.012	209.1	32.0	4.9	259	8.13	2.96	1.176	0.188	68.12	36.90
	1050	26.1	1.9	10.39	0.93	4.38	0.05	1.76	0.21	0.893	0.013	338.6	62.9	4.0	488	9.78	0.67	1.428	0.055	48.91	5.15
	1100	265.0	9.5	12.83	0.82	40.32	0.24	1.65	0.03	0.885	0.008	399.2	24.1	31.8	662	89.32	3.41	1.547	0.011	7.03	0.30
	1120	19.4	1.6	11.05	1.07	4.26	0.05	2.55	0.21	0.804	0.012	178.5	27.5	7.5	197	10.43	0.63	1.262	0.041	77.25	4.80
	1150	10.7	1.4	15.17	2.16	1.72	0.04	3.11	0.49	0.780	0.019	199.5	54.4	4.1	218	6.41	0.54	1.101	0.057	112.33	9.71
	1200	23.5	1.7	11.91	1.07	5.25	0.06	2.71	0.17	0.781	0.010	165.2	21.6	10.1	181	16.78	0.82	1.324	0.028	60.51	3.04
	1250	12.3	1.4	14.13	1.80	3.71	0.04	3.15	0.23	0.722	0.010	104.9	18.0	8.9	112	11.21	0.65	1.361	0.042	56.06	3.36
	1300	8.5	1.4	14.02	2.35	2.49	0.04	4.76	0.31	0.582	0.011	72.0	14.6	10.3	68	5.78	0.51	1.294	0.077	77.40	7.06
	1350	9.0	1.5	13.40	2.29	2.77	0.04	5.07	0.28	0.536	0.010	64.2	12.7	12.3	59	5.46	0.54	1.217	0.076	74.98	7.73
	1400	111.2	4.6	10.33	0.68	18.03	0.11	2.00	0.05	0.847	0.008	308.9	23.0	21.0	395	44.03	2.03	1.528	0.014	15.90	0.74
	1425	830.6	30.5	9.91	0.62	120.69	0.58	1.65	0.01	0.878	0.007	416.5	23.2	95.9	635	285.69*	12.07*	1.583	0.008	1.21	0.06
	1450	9.9	1.8	12.63	2.34	2.30	0.05	3.14	0.42	0.728	0.016	137.6	37.4	5.5	143	5.42	0.55	1.231	0.082	49.86	6.15
	1475	7.4	1.6	13.70	3.00	1.76	0.04	3.57	0.55	0.676	0.018	117.6	37.8	5.0	119	3.88	0.52	1.284	0.123	82.06	13.06
	1500	4.8	1.6	9.63	3.29	1.43	0.04	2.04	0.80	0.860	0.025	162.6	98.9	1.7	199	4.10	0.53	1.420	0.132	42.08	6.64
	1525	5.4	1.5	15.39	4.32	1.03	0.03	2.82	1.07	0.791	0.026	188.0	112.6	2.1	215	4.02	0.53	1.443	0.139	37.34	6.31
	1550	1.5	1.4	5711	5356	0.16	0.03	6.47	6.16	0.154	0.036	151.4	266.4	0.9	165	2.60	0.50	0.466	0.051	266.35	52.08
	1650	3.4	1.6	17546	9323	0.30	0.04	10.49	6.23	0.089	0.017	108.4	89.9	3.1	111	0.73	0.54	0.886	0.512	164.20	128.15
	1750	2.8	1.8	20098	13998	3.47	0.07	10.03	0.92	0.032	0.002	8.0	5.4	33.8	8	3.18	0.74	0.239	0.038	163.97	39.69
	1800	6.2	2.1	44897	25991	8.13	0.09	9.87	0.51	0.030	0.001	7.7	2.7	78.0	8	2.25	0.82	0.196	0.060	326.39	120.72
Total(1) (no high T)		**1396.8**	**32.8**	**10.55**	**0.42**	**219.95**	**0.66**	**1.88**	**0.02**	**0.859**	**0.004**	**337.4**	**11.7**	**229.0**	**457**	**523.40**	**13.69**	**1.507**	**0.007**	**17.76**	**1.40**
Total(2) (all T steps)		**1415.4**	**33.1**	**10.62**	**0.42**	**232.09**	**0.67**	**2.30**	**0.03**	**0.818**	**0.004**	**264.6**	**9.3**	**344.7**	**308**	**536.90**	**13.92**	**1.478**	**0.008**	**23.32**	**1.94**

Tab. 2.1: continued

Sample (weight)	Temp. [°C]	^{4}He [10^{-8} cm³STP/g]	±	^{4}He/^{3}He	±	^{22}Ne [10^{-10} cm³STP/g]	±	^{20}Ne/^{22}Ne	±	^{21}Ne/^{22}Ne	±	^{4}He/^{20}Ne	±	^{20}Ne$_{excess}$ [10^{-10} cm³STP/g]	(^{4}He/^{20}Ne) (excess)	^{36}Ar [10^{-10} cm³STP/g]	±	^{38}Ar/^{36}Ar	±	^{40}Ar/^{36}Ar	±
WC_11[a]																					
(14.2 mg)	**1050**	151.6	4.2	8.17	0.23	27.60	0.15	1.16	0.02	0.926	0.011	473.8	18.9	7.4	1392	57.98	0.58	1.531	0.019	3.53	0.10
	1100	267.7	3.9	8.54	0.13	53.23	0.27	1.27	0.01	0.921	0.011	397.2	10.7	20.3	910	137.34	0.89	1.570	0.018	0.86	0.01
	1150	59.2	2.0	8.39	0.29	11.91	0.11	1.00	0.04	0.950	0.014	495.7	31.4	1.2	3400	27.34	0.36	1.502	0.021	-	-
	1250	69.9	1.9	8.68	0.24	17.04	0.11	1.15	0.03	0.937	0.012	355.3	16.4	4.5	1089	46.68	0.48	1.528	0.019	1.19	0.10
	1300	12.2	2.0	7.91	1.29	4.18	0.06	0.67	0.11	0.972	0.018	436.6	106.6	-	-	11.14	0.24	1.645	0.034	-	-
	1320	3.3	1.6	7.49	3.62	1.00	0.05	-	-	1.139	0.065	-	-	-	-	2.74	0.22	1.917	0.138	-	-
	1340	4.2	1.7	10.64	4.45	0.57	0.04	-	-	1.312	0.097	-	-	-	-	1.93	0.22	1.964	0.198	-	-
	1360	4.0	1.7	13.67	5.70	0.49	0.04	-	-	1.214	0.108	-	-	-	-	1.28	0.21	2.434	0.372	-	-
	1380	6.2	1.9	9.99	2.99	1.13	0.04	-	-	1.065	0.038	-	-	-	-	2.65	0.25	1.939	0.151	-	-
	1390	9.8	1.5	11.56	1.76	1.86	0.05	2.44	0.21	0.838	0.024	215.1	41.0	3.1	247	4.33	0.24	1.645	0.077	9.66	2.80
	1400	23.0	1.9	9.11	0.75	4.57	0.05	0.98	0.10	0.937	0.015	514.0	73.5	0.4	4649	11.16	0.23	1.699	0.035	-	-
	1410	37.8	1.9	9.02	0.46	7.47	0.07	1.19	0.06	0.929	0.013	425.5	34.7	2.2	1199	19.07	0.32	1.654	0.027	-	-
	1420	60.6	2.3	9.16	0.36	11.98	0.10	1.26	0.04	0.920	0.013	400.7	23.1	4.5	951	29.55	0.47	1.612	0.025	-	-
	1430	81.8	2.0	8.51	0.22	17.19	0.12	1.26	0.03	0.919	0.012	377.5	16.0	6.4	876	42.48	0.51	1.549	0.021	-	-
	1440	351.2	8.8	7.93	0.20	79.16	0.34	1.25	0.01	0.914	0.011	356.1	11.8	28.5	822	193.42	1.44	1.599	0.019	0.72	0.02
	1450	21.9	2.3	9.64	1.04	3.92	0.06	1.04	0.12	0.952	0.020	535.2	91.5	0.6	2824	9.83	0.20	1.607	0.031	-	-
	1800	14.2	2.7	6.91	1.31	6.08	0.05	3.30	0.07	0.690	0.010	70.7	13.6	15.5	56	14.11	0.20	1.365	0.021	38.43	0.57
Total(1) (no high T)		**1164.4**	**12.6**	**8.40**	**0.09**	**243.28**	**0.53**	**1.20**	**0.01**	**0.926**	**0.005**	**393.7**	**6.2**	**74.8**	**1067**	**598.93**	**2.14**	**1.584**	**0.008**	**0.93**	**0.02**
Total(2) (all T steps)		**1178.6**	**12.9**	**8.38**	**0.09**	**249.36**	**0.53**	**1.25**	**0.01**	**0.920**	**0.005**	**373.0**	**5.8**	**90.3**	**893**	**613.04**	**2.15**	**1.579**	**0.008**	**1.80**	**0.03**
WC_14[a]																					
(20.9 mg)	**800**	blank	-	-	-	blank	-	-	-	-	-	-	-	-	-	1.16	0.20	1.070	0.113	431.94	80.93
	1050	24.9	1.6	3.43	0.22	14.16	0.09	0.94	0.05	0.936	0.010	187.2	21.8	0.4	1294	32.91	1.02	1.570	0.035	3.35	0.16
	1140	94.8	2.5	4.48	0.12	24.39	0.14	1.02	0.03	0.923	0.010	379.6	30.6	3.0	1303	89.18	2.68	1.572	0.034	2.80	0.10
	1350	107.7	2.6	4.36	0.11	41.79	0.22	1.16	0.02	0.921	0.009	221.7	15.2	11.3	374	103.87	3.13	1.556	0.034	1.79	0.07
	1480	316.9	6.4	4.63	0.10	216.86	1.04	1.71	0.01	0.862	0.008	85.5	5.0	185.7	73	554.85	16.48	1.546	0.033	2.62	0.08
	1600	2.8	1.2	55.81	23.58	4.32	0.06	9.45	0.19	0.066	0.001	6.9	2.9	39.5	7	1.49	0.20	0.750	0.073	258.20	35.96
	1800	blank	-	-	-	blank	-	-	-	-	-	-	-	-	-	0.24	0.31	1.967	2.339	449.55	623.43
Total(1) (no high T)		**544.3**	**7.5**	**4.48**	**0.06**	**297.21**	**1.08**	**1.54**	**0.01**	**0.879**	**0.006**	**118.9**	**5.6**	**200.4**	**111**	**780.82**	**17.01**	**1.551**	**0.025**	**2.56**	**0.06**
Total(2) (all T steps)		**547.1**	**7.6**	**4.50**	**0.06**	**301.53**	**1.08**	**1.65**	**0.01**	**0.867**	**0.006**	**109.7**	**4.8**	**239.9**	**93**	**783.71**	**17.02**	**1.549**	**0.024**	**3.82**	**0.26**
WC_g[b]																					
(22.4 mg)	**1800**	1032.1	38.7	6.54	0.06	247.54	9.34	1.31	0.02	0.910	0.007	317.6	17.3	106.8	576	700.0	28.1	1.396	0.012	34.10	0.40
	2000	22.3	0.7	6.93	0.08	5.83	0.23	0.95	0.42	0.920	0.016	401.2	179.1	0.3	5100	17.0	0.7	1.395	0.050	37.73	7.71
	Total	**1054.3**	**38.7**	**6.55**	**0.05**	**253.34**	**9.34**	**1.30**	**0.02**	**0.910**	**0.007**	**319.0**	**11.7**	**107.0**	**587**	**717.0**	**28.2**	**1.396**	**0.011**	**34.19**	**0.43**
WC_s[b]																					
(21.87 mg)	**800**	16.0	0.5	17.45	0.23	2.56	0.12	1.49	0.99	0.840	0.025	418.9	279.4	1.6	852	10.6	0.6	1.286	0.077	71.95	13.00
	1800	2107.4	78.6	16.14	0.17	253.08	9.51	2.35	0.02	0.831	0.007	353.9	19.0	391.0	451	626.0	19.7	1.492	0.012	7.00	0.29
	2000	9.6	2.5	17.30	0.16	10.73	0.42	2.31	0.23	0.826	0.014	38.8	10.9	16.1	51	30.0	1.1	1.401	0.031	24.70	4.44
	Total	**2214.0**	**78.6**	**16.15**	**0.16**	**266.36**	**9.52**	**2.34**	**0.02**	**0.831**	**0.007**	**341.8**	**12.1**	**408.7**	**454**	**666.6**	**19.7**	**1.485**	**0.012**	**8.83**	**0.40**
WC_r[b]																					
(8.54 mg)	**800**	18.9	0.8	7.59	0.25	5.32	0.54	1.54	0.35	1.035	0.104	230.4	58.2	3.6	342	90.0	7.0	0.459	0.015	239.02	5.76
	1800	2372.0	84.1	8.26	0.10	453.56	12.96	1.39	0.01	0.915	0.009	376.9	17.6	231.8	696	1356.8	91.7	1.548	0.019	2.28	0.55
	2000	5.5	0.6	6.61	0.68	0.77	0.33	-	-	1.438	0.696	-	-	-	-	-	-	-	-	-	-
	Total	**2390.5**	**84.1**	**8.25**	**0.10**	**459.65**	**12.98**	**1.38**	**0.02**	**0.917**	**0.009**	**375.1**	**13.2**	**232.0**	**700**	**1446.8**	**92.0**	**1.480**	**0.019**	**17.00**	**1.55**

Blank entries: indistinguishable from blank. All uncertainties 1σ. [a]Measurements performed at the Institut für Geowissenschaften, Heidelberg. [b]Measurements performed at MPI für Chemie, Mainz. *volume partitioning before measuring: ~8% of the released Ar was analyzed. Underlined values are not used for calculation of total(1) because of atmospheric contributions, including potential release of air from secondary iron oxides at high temperature. Double underlined values are not used for calculation of both total(1) and total(2) because of release of air contamination from aluminum foil at 600 and 700 °C

Above 1525 °C the released gas amounts include contributions from degassing of Fe(III)- and Fe(II,III) oxides (melting points: 1565 °C and 1597 °C, respectively (Lide, (2009)) that possibly formed along cracks during atmospheric entry or during terrestrial weathering.

Gas amounts that are missing in total(1) values can be seen as the difference to the total(2) values, which include all temperature steps with the exception of the 600 °C and 700 °C steps in case of WC_5. For ^{3}He and ^{4}He, this amonts to <2% and to <3% for the mostly cosmogenic isotopes ^{21}Ne, ^{36}Ar and ^{38}Ar. Missing amounts of ^{22}Ne are at maximum in the order of 5%, but for the major trapped/atmospheric isotopes (^{20}Ne, ^{40}Ar) the difference is larger. Data points for total(2) values are also shown for comparison in Figures 2.7 to 2.11 (parts a).

2.3.2 Degassing pattern

The degassing pattern for He, Ne and Ar of the first investigated sample WC_5 (Fig. 2.6) was used as reference for subsequent measurements (Figs. A1–A3). Figure 2.6 shows the fractional gas release F against the release temperature, where F is defined as :

$$F = \frac{C_i(fraction)}{C_i(total) * \Delta T}$$

Here, Ci(fraction) is the concentration of an isotope i for a particular release step, Ci(total) is the total and ΔT the width of the temperature step.

Two major degassing peaks are apparent in the high resolution stepwise degassing, at 1100 °C and 1425 °C. These are consistent in temperature and relative peak heights, with ~20% being released in the low temperature peak, for all isotopes, except for ^{40}Ar (Tab. 2.1). The peak release temperatures correlate with the melting points of schreibersite at 1048 °C (La Cruz et al., 2016) and kamacite-taenite (Fe-Ni alloy) at >1422 °C (Swartzendruber et al., 1991), respectively. It should be noted, however, that Swartzendruber et al. (1991) found the most probable minimum liquidus temperature in the Fe-Ni system at 1440 °C and 66 at.% Ni. According to the compilation by these authors, a liquidus in the range 1496–1515 °C and a solidus of 1479–1504 °C should apply for Washington County with a bulk concentration of 9.9 wt% Ni.

The two major degassing peaks that reflect the mineralogical composition of Washington County are observed also for WC_2, WC_11, and WC_14. The down-shift of the kamacite-taenite peak to 1380 °C for WC_2 (schreibersite peak at 1140 °C, Fig. A1) may be caused either by analytical problems with the temperature control or different degassing behavior of the near-surface sample that was prone to chemical reactions during atmospheric entry or terrestrial weathering. For WC_11, the kamacite-taenite degassing peak occurs at a higher temperature of 1440 °C (schreibersite peak at 1100 °C, Fig. A2). This may either also reflect analytical problems or may be caused by a variation in Ni content of the predominantly occurring Fe-Ni phase. A third possibility would be trapping of noble gases in a recrystallized structure that formed during the small temperature steps of 10 °C preceding the peak release temperature (see Tab. 2.1). Because of the lower temperature resolution, the peaks for WC_14 (1140 °C and 1480°C, Fig. A3) do not provide further information.

Additional to the major degassing peaks observed, a peak release of ^{20}Ne, ^{22}Ne and ^{40}Ar occurs for WC_2 at 1450 °C indicative of an atmospheric contribution (Tab. 2.1, Fig. A1). This points towards the presence of a secondary phase that formed along cracks in the near-surface sample. If an uncertainty in temperature control is consider, degassing of iron oxides with melting points above 1525 °C may be responsible. If chemical reactions at the near-surface of Washington County were involved, atmospheric noble gases could have been trapped in a recrystallized Fe-Ni phase. Indeed, temperature steps for all samples above 1525 °C are most likely influenced by contributions of noble gases from iron oxides yielding atmospheric-like compositions.

Figure 2.6 moreover shows $^{4}He/^{3}He$ ratios (see Tab. 2.1) in the temperature range around the gas release peaks. It is obvious that the helium isotopic composition of each sample is essentially constant regardless from which phase, schreibersite or kamacite-taenite, the gas is released. In this regard, the $^{4}He/^{3}He$ ratios seem largely unaffected by cosmogenic production of helium caused by spallation reactions involving phosphorus in schreibersite. Consistently, the almost pure schreibersite sample (WC_r) is not characterized by a comparatively higher value. Consequently, all ^{4}He excesses over the GCR end-member that are measured for WC_2, WC_5, WC_11 and WC_14 have to be ascribed to a trapped rather than to a cosmogenic component.

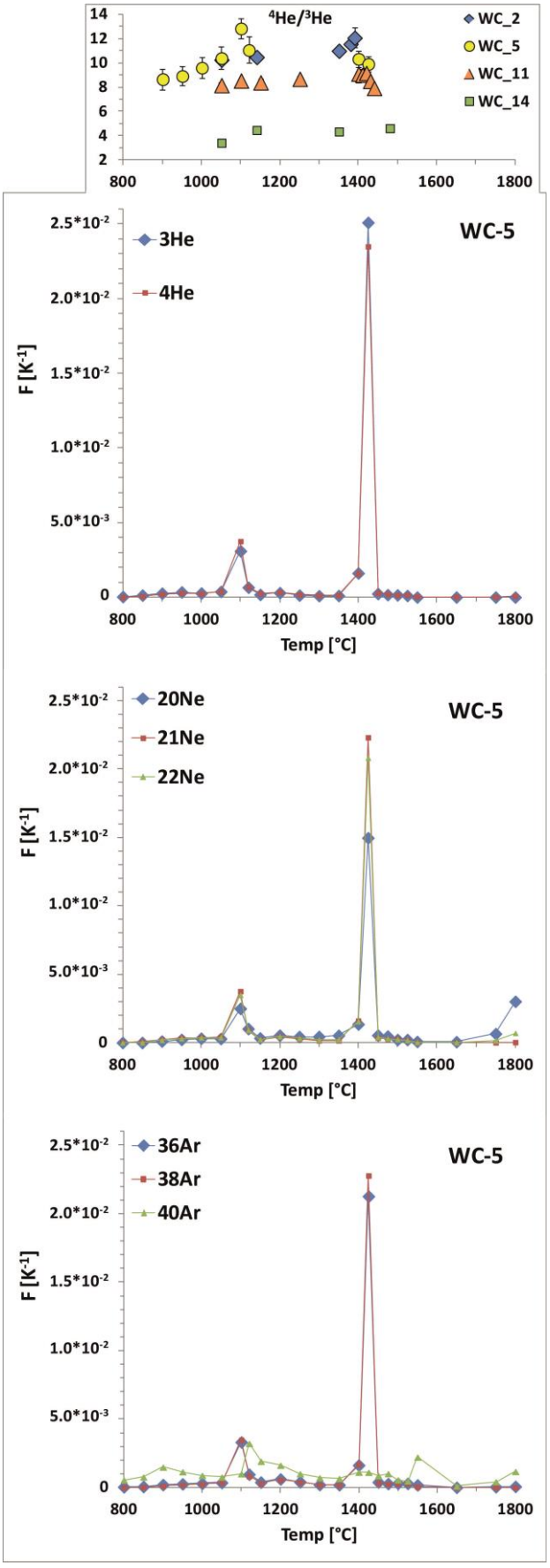

Fig. 2.6: Fractional degassing pattern of WC_5 for He, Ne and Ar in 1/K. Measured $^{4}He/^{3}He$ ratios for degassing steps associated with the peak release temperatures are shown at the top of the diagrams (see text for details).

2.3.3 Helium

The total concentrations of ^{4}He measured for WC_samples in cm^3STP/g (Tab. 2.1) range from $544*10^{-8}$ (WC_14, total(1)) to $2391*10^{-8}$ (WC_r) and are consistent with concentrations reported by Signer and Nier (1962) of $(870–2570)*10^{-8}$ cm^3STP/g. Higher ^{4}He concentrations of $(2700–3100)*10^{-8}$ cm^3STP/g, $3307*10^{-8}$ cm^3STP/g, $8110*10^{-8}$ cm^3STP/g and $8980*10^{-8}$ cm^3STP/g were reported by Schaeffer and Fisher (1959), Hintenberger et al. (1967), Merrihue (1964) and Becker and Pepin (1984), respectively. Helium isotopic ratios are diagnostic only in combination with Ne isotopes (see below).

2.3.4 Neon

The total concentrations of ^{22}Ne measured for WC_samples in cm^3STP/g (Tab. 2.1) range from $220*10^{-10}$ (WC_5, total(1)) to $460*10^{-10}$ (WC_r) and are consistent with data given by Schaeffer and Fisher (1959) of $(220–260)*10^{-10}$ cm^3STP/g, Signer and Nier (1962) of $(225–387)*10^{-10}$ cm^3STP/g, Merrihue (1964) of $387*10^{-10}$ cm^3STP/g, Hintenberger et al. (1967) of $250*10^{-10}$ cm^3STP/g and Becker and Pepin (1984) of $290*10^{-10}$ cm^3STP/g. Figure 2.7 shows the $^{20}Ne/^{22}Ne$ ratio against the $^{21}Ne/^{22}Ne$ ratio of all measured Washington County samples for totals (Fig. 2.7a) and for single temperature steps (Fig. 2.7b) compared to data from the literature. The isotopic compositions of four possible end-members are also indicated: SW is from Heber et al. (2012), Ne-B from Trieloff and Kunz (2005) and Air from Eberhardt et al. (1965). The range of the galactic cosmic radiation (GCR) end-member (shown as a bar) was determined in a twofold way: First, the cosmogenic production rate (Leya and Masarik, 2009) for a chemical composition of 90.1 wt% Fe, 9.9 wt% Ni and a pre-atmospheric meteoroid radius of 10 cm (cf. Murty and Ranjith Kumar, 2014 and section 'Cosmic-ray exposure ages') was used to calculate a $^{20}Ne/^{22}Ne$ range of 0.90–0.92 and a $^{21}Ne/^{22}Ne$ ratio of 0.950. Second, the minimum GCR $^{21}Ne/^{22}Ne$ end-member ratio of 0.934 was compiled from data presented in Schultz and Franke (2004) for iron meteorites that contain a maximum $^{20}Ne/^{22}Ne$ ratio of 0.90. Mixing lines to SW-, Ne-B- and Air composition are drawn from the most cosmogenic isotopic ratios measured for Washington County, which is in the 1050 °C release step of WC_14 (Fig. 2.7a inset).

It is clear from Figure 2.7a that all Ne data for Washington County, except for WC_14, trend along a mixing line from cosmogenic towards SW composition or Ne-B. Even the integration of high temperature release steps (Fig. 2.7a inset) does not change this observation, except for WC_5. Furthermore, single temperature steps (Fig 2.7b) for all measured samples, except for WC_14, are within 1σ errors (2σ only for the 1200 °C temperature step of WC_5) consistent with the presence of a SW- or Ne-B component. Data for WC_14, on the other hand, suggest mixing between GCR and Air, however, are still consistent with mixing of GCR and Ne-B within 1σ (2σ for the 1480 °C temperature step). In general, the temperature steps for WC_11 and WC_14 show the most cosmogenic compositions. With increasing release temperature, isotopic ratios of WC_2 trend towards solar composition; for WC_14 towards air composition. No general trend is obvious for the release steps of WC_5 and WC_11. For WC_2, the peak release step for high temperatures (kamacite-taenite peak: 1380 °C) contains a slightly higher solar wind

contribution compared to the low temperature peak (schreibersite peak: 1140 °C). Both release peaks of WC_5 and WC_11 (1100 °C, 1425 °C and 1100 °C, 1440 °C, respectively) have almost identical isotopic ratios (within 1σ), however they are more solar-like for WC_5 and more GCR-like for WC_11. For WC_14, the high temperature peak (1480 °C) contains a more air-like composition compared to the more GCR-like composition of the low temperature peak (1140 °C). Because of comparably large errors, literature data (Schaeffer and Fisher, 1959; Signer and Nier, 1962; Hintenberger et al., 1967) preclude clear evidence for the presence of a solar-like Ne component and the data from Merrihue (1964) cannot be ascertained since they are given without errors. The highest $^{20}Ne/^{22}Ne$ and lowest $^{21}Ne/^{22}Ne$ ratios, including small errors, are reported by Becker and Pepin (1984) and denote the most remarkable trend towards SW composition. Concerning these data, though, concentrations of cosmogenic ^{21}Ne are only about half of what has been found in the recent and other studies (Signer and Nier, 1962; Hintenberger et al., 1967; Murty and Ranjith Kumar, 2014), which may point towards incomplete gas release. Extraction of noble gases by Becker and Pepin (1984) was by combustion at 1180 °C only, and a repeat step at the same temperature relased more than 30% of the gas in the first step (step 1: $1.14*10^{-8}$ cm^3STP/g, step 2: $0.37*10^{-8}$ cm^3STP/g). Incomplete noble gas extraction notably could also lead to the observed Ne isotopic ratios if the cosmogenic Ne is suppressed relative to SW-Ne.

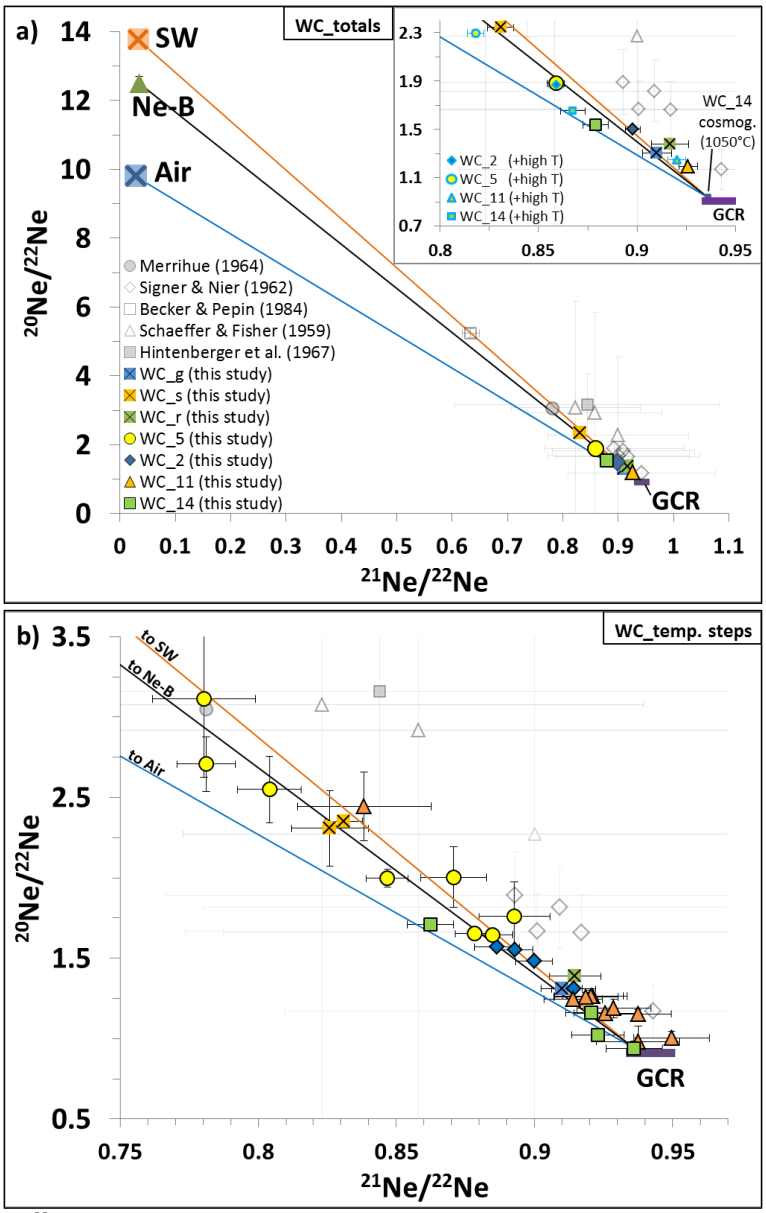

Fig. 2.7: $^{20}Ne/^{22}Ne$–$^{21}Ne/^{22}Ne$ diagram showing literature and measured data for Washington County: **a)** WC_totals, **b)** WC_temperature steps (see Tab. 2.1). For new measurements (WC_2, WC_5, WC_11, WC_14, WC_g, WC_s, WC_r) only data with errors (1σ) ≤15% for $^{20}Ne/^{22}Ne$ and <5% for $^{21}Ne/^{22}Ne$ are shown. The inset of Fig. 2.7a shows total(2) values including high temperature steps (>1525 °C) that are probably influenced by an air component. These data points plot close to air composition and outside the range shown in Fig. 2.7b. For reference, mixing lines are shown from the GCR endmember composition towards the compositions of SW, Ne-B and Air (see text for details).

2.3.5 He-Ne systematics

Figure 2.8 shows the $^{4}He/^{21}Ne$ ratio against the $^{4}He/^{3}He$ ratio of all measured Washington County samples for calculated totals (Fig. 2.8a) and individual temperature steps (Fig. 2.8b) compared to data from the literature. The isotopic compositions of three possible end-members are also indicated: Both, SW ($^{4}He/^{21}Ne$: ~2.7*10^{5}, $^{4}He/^{3}He$: ~2150, after Heber et al. (2012)) and Air ($^{4}He/^{21}Ne$: ~107.8, $^{4}He/^{3}He$: ~7*10^{5}, after Ozima and Podosek (2002)) are off scale. The GCR end-member that is shown for Washington County ($^{4}He/^{21}Ne$: ~150–204, $^{4}He/^{3}He$: ~2.35–2.95) was determined taking into account the chemical composition of 90.1 wt% Fe and 9.9 wt% Ni and by assuming a pre-atmospheric meteoroid radius of 10 cm (cf. Murty and Ranjith Kumar, 2014 and

section 'Cosmic-ray exposure ages'). The cosmogenic production rates for iron meteorites (Ammon et al., 2009) were used to calculate the respective ratios. They fall into the same range as the ratios obtained by applying the cosmogenic production rates for stony meteorites using the same chemical composition (Leya and Masarik, 2009). Typical values for cosmogenic isotopes in iron meteorites are: $^{4}He/^{21}Ne$ = 200–440 and $^{4}He/^{3}He$ = 3.2–4.4 (Wieler, 2002a).

Measured $^{4}He/^{21}Ne$ ratios for WC_samples range from ~170 (WC_14, 1480 °C) to ~1000 (WC_s, 1800 °C) and measured $^{4}He/^{3}He$ ratios from 3.4 (WC_14, 1050 °C) to 17.4 (WC_s, 800 °C) (Fig. 2.8). It is important to note that all available data for Washington County show excesses of ^{4}He with respect to the GCR end-member and all data, with few exceptions, trend towards solar wind composition or comprise a mixture of GCR, SW and possibly very minor contributions of terrestrial air. Even the most cosmogenic values observed in WC_14 exhibit an excess of ^{4}He, although in two temperature steps (1050 °C and 1480 °C) this could be due to an atmospheric component (inset of Fig. 2.8a and Fig. 2.8b). With increasing release temperature, isotopic ratios of WC_2 and WC_s trend towards air composition. The high temperature step of WC_s (2000 °C) likewise suggests a two component mixture between GCR and Air. No general trend is obvious for the release steps of WC_5 and WC_11. For WC_2 and WC_14, peak release steps for high temperatures (kamacite-taenite peak: 1380 °C and 1480 °C, respectively) contain a more air-like composition compared to the low temperature peaks (schreibersite peak: both 1140 °C). For WC_5, the high temperature peak (1425 °C) is shifted towards the mixing line between GCR and SW compared to the low temperature peak (1100 °C). For WC_11, the low temperature peak (1100 °C) contains a more solar-like composition compared to the more GCR-like composition of the high temperature peak (1440 °C). Increasing $^{4}He/^{3}He$ ratios are observed for WC_g, WC_r, WC_11, WC_5, WC_2 and WC_s. These ^{4}He excesses are in the range of earlier measurements (Schaeffer and Fisher, 1959; Signer and Nier, 1962). Data from Hintenberger et al. (1967) and Merrihue (1964) are consistent with a trend towards SW composition. Ratios from Merrihue (1964), however, are given without errors. The highest $^{4}He/^{3}He$ and $^{4}He/^{21}Ne$ values, implying the greatest ^{4}He excesses, have been reported by Becker and Pepin (1984).

In the $^{4}He/^{21}Ne$–$^{4}He/^{3}He$ diagram, their data point plots above the GCR-SW mixing line which is also the case for data reported by Schaeffer and Fisher (1959) and Merrihue (1964). This could simply be explained by incomplete sample degassing as discussed above (section on neon). The data for the recently investigated samples (WC_2, WC_5, WC_11, WC_14, WC_g, WC_s, WC_r) fall right on the GCR-SW mixing line or plot, possibly because of atmospheric contributions, slightly below.

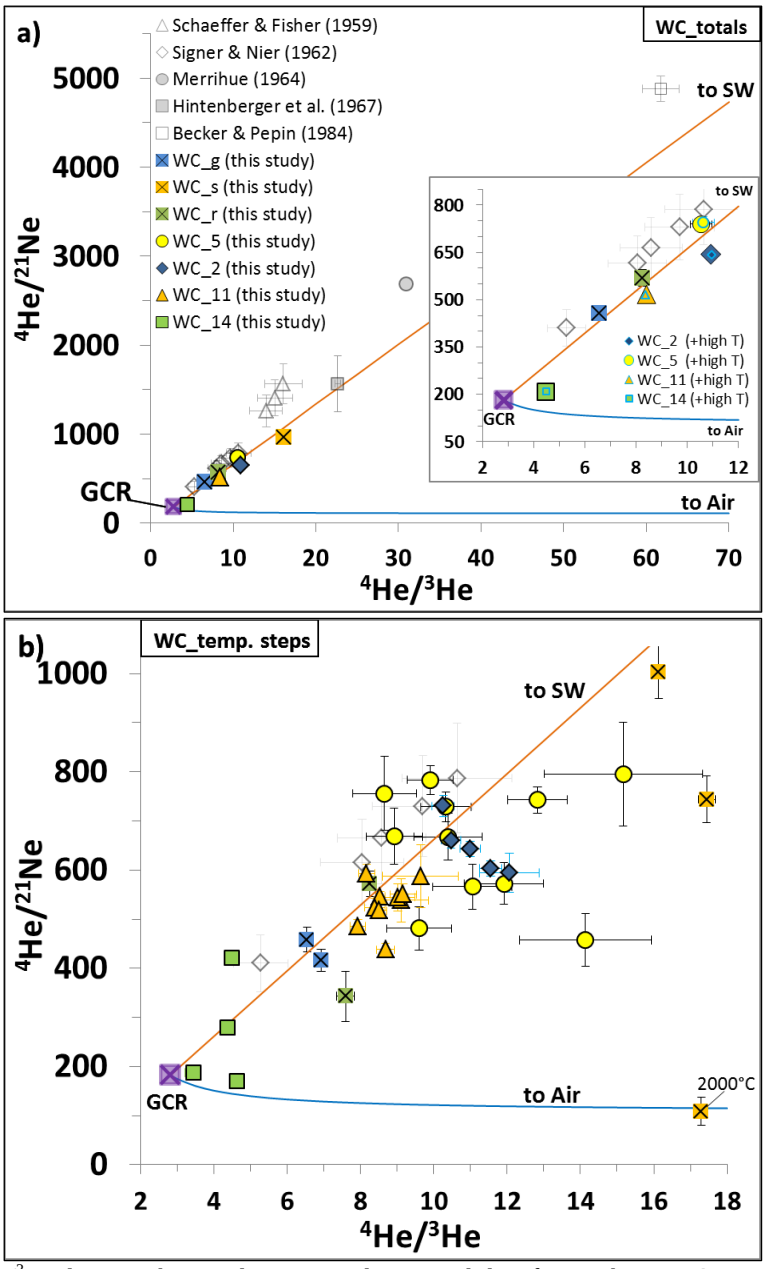

Fig. 2.8: $^{4}He/^{21}Ne$–$^{4}He/^{3}He$ diagram showing literature and measured data for Washington County: **a)** WC_totals and **b)** WC_temperature steps (see Tab. 2.1). For the new measurements reported here (WC_2, WC_5, WC_11, WC_14, WC_g, WC_s, WC_r) only data with errors (1σ) <15% for $^{4}He/^{21}Ne$ and $^{4}He/^{3}He$, respectively, are shown. Note that the error for WC_s (2000 °C) is 26% for $^{4}He/^{21}Ne$. The inset of Fig. 2.8a shows total(2) values including high temperature steps (>1525 °C) that appear to be influenced by an air component. These data points have uncertainties greater than the error cut or plot outside the range shown in Fig. 2.8b. For reference the GCR end-member composition is shown as well as mixing lines towards the compositions of SW, and Air (both off-scale; see text for details).

Figure 2.9 shows the $^{4}He/^{21}Ne$ ratio against the $^{22}Ne/^{21}Ne$ ratio of all measured Washington County samples for totals in Fig. 2.9a and for single temperature steps in Fig. 2.9b, compared to data from the literature. The isotopic compositions of possible end-members are also indicated, where both, SW ($^{4}He/^{21}Ne$: ~$2.7*10^{5}$, $^{22}Ne/^{21}Ne$: ~30.4, after Heber et al. (2012)) and Air ($^{4}He/^{21}Ne$: ~107.8, $^{22}Ne/^{21}Ne$: ~34.5, after Ozima and Podosek (2002)) are off scale. The range of the GCR end-member ($^{4}He/^{21}Ne$: ~150–204, $^{22}Ne/^{21}Ne$: 1.050) was determined using the cosmogenic production rate (Ammon et al., 2009) for an iron meteorite with a chemical composition of 90.1 wt% Fe, 9.9 wt% Ni and a pre-atmospheric meteoroid radius of 10 cm (cf. Murty and Ranjith

Kumar, 2014 and section 'Cosmic-ray exposure ages'). The maximum GCR $^{22}Ne/^{21}Ne$ end-member ratio of 1.075 was taken from the data compiled in Schultz and Franke (2004) for iron meteorites with a $^{20}Ne/^{22}Ne$ ratio of <0.9.

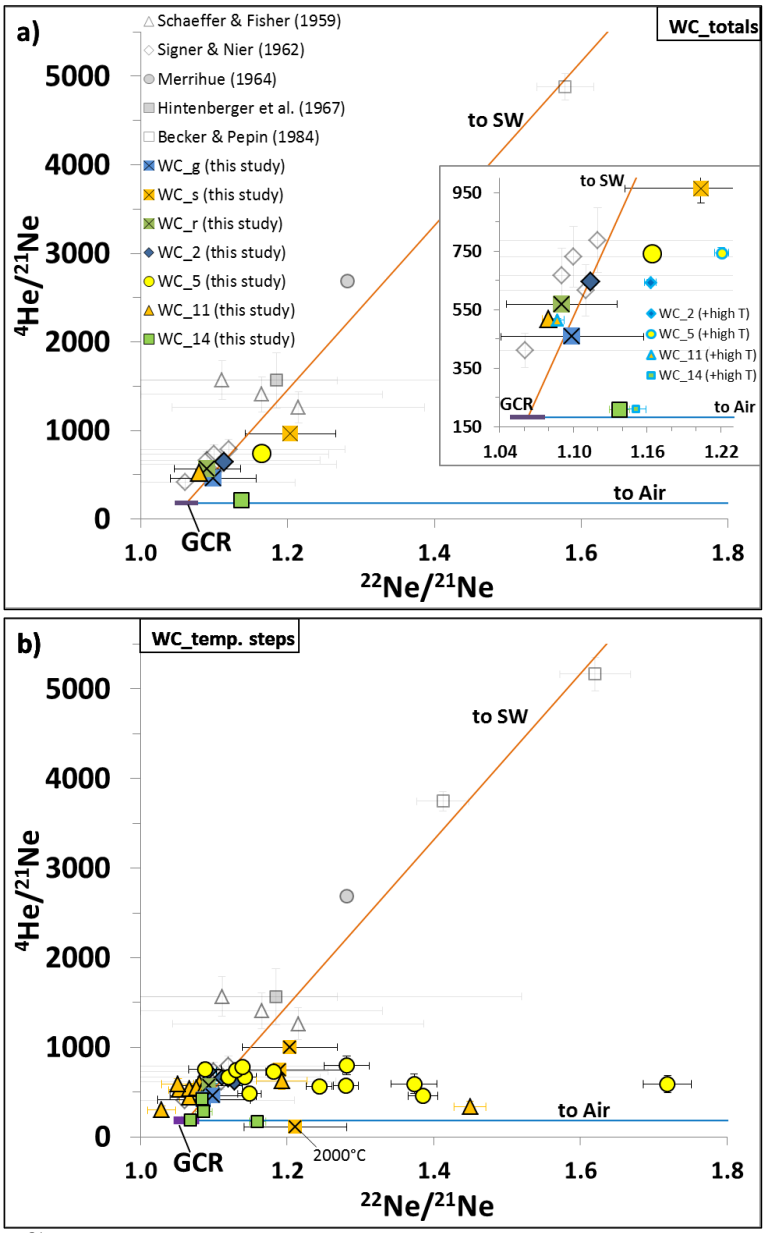

Fig. 2.9: $^{4}He/^{21}Ne$–$^{22}Ne/^{21}Ne$ diagram showing literature and new data for Washington County: **a)** WC_totals and **b)** WC_temperature steps (see Tab. 2.1). For new measurements (WC_2, WC_5, WC_11, WC_14, WC_g, WC_s, WC_r) only data with errors (1σ) <20% for $^{4}He/^{21}Ne$ and <10% for $^{22}Ne/^{21}Ne$ are shown. Note that the error for $^{4}He/^{21}Ne$ in WC_s (2000 °C) is 26%. The inset of Fig. 2.9a shows total(2) values including high temperature steps (>1525 °C) that are probably influenced by an air component. These data points have uncertainties greater than the error cut or plot outside the range shown in Fig. 2.9b. For reference the GCR end-member composition is shown as well as mixing lines towards the compositions of SW, and Air (both off-scale; see text for details).

Overall, the trends in Figure 2.9 are the same as in Figure 2.8, where $^{4}He/^{3}He$ ratios were plotted rather than $^{22}Ne/^{21}Ne$. Increasing $^{4}He/^{21}Ne$ ratios are observed in the order WC_g, WC_11, WC_r, WC_2, WC_5, WC_s and are consistent, except for WC_14, with mixing of GCR, SW and Air (Fig. 2.9a). Only WC_14 (total) suggests mixing of GCR and Air only. A more noticeable shift towards air composition results when the high temperature steps are included (total(2) values).

This trend towards more air-like compositions becomes even more evident from single temperature steps, in particular for the WC_5 steps following the peak release and for the high temperature steps of WC_14 (1480 °C), WC_11 (1800 °C) and WC_s (2000 °C) (Fig. 2.9b). The trend towards solar wind falls within the range of earlier measurements (Signer and Nier, 1962). More significant SW contributions were found by Schaeffer and Fisher (1959), Hintenberger et al. (1967), Merrihue (1964) and Becker and Pepin (1984).

Figure 2.10 shows the $^{4}He/^{20}Ne$ ratio against $^{21}Ne/^{22}Ne$ for all measured Washington County samples for totals (Fig. 2.10a) and single temperature steps (Fig. 2.10b) compared to data from the literature. The isotopic compositions of three possible end-members are also indicated: SW is from Heber et al. (2012), Air from Ozima and Podosek (2002). Since Ammon et al. (2009) do not give cosmogenic production rates for ^{20}Ne, the cosmogenic production rates for ordinary chondrites (Leya and Masarik, 2009) with a chemical composition of 90.1 wt% Fe, 9.9 wt% Ni and a pre-atmospheric meteoroid radius of 10 cm (cf. Murty and Ranjith Kumar, 2014 and section 'Cosmic-ray exposure ages') were used to determine the Washington County GCR end-member: $^{4}He/^{20}Ne$ with a range of ~180–209 and a $^{21}Ne/^{22}Ne$ ratio of 0.95. The minimum GCR $^{21}Ne/^{22}Ne$ end-member ratio of ~0.93 was compiled from data presented in Schultz and Franke (2004) for iron meteorites that contain a maximum $^{20}Ne/^{22}Ne$ ratio of 0.9. WC_14 (1050 °C) is identical to the GCR end-member.

It is obvious from Figure 2.10a that, except for WC_14, all Washington County samples have $^{4}He/^{20}Ne$ ratios above ~200, which indicates the presence of a SW component. WC_14 ($^{4}He/^{20}Ne$ ~110–120, total) falls on the trend from GCR to Air instead. A trend towards air composition is also evident for the totals(2), where the high temperature steps are included. The influence of Air is even more evident for single temperature steps (Fig. 2.10b). A trend towards the Air end-member is obvious in particular for the WC_5 temperature steps following the peak releases and for the high temperature steps of WC_2 (1450 °C and 1800 °C), WC_11 (1800 °C), WC_14 (1480 °C and 1600 °C) and WC_s (2000 °C). The shift towards lower $^{21}Ne/^{22}Ne$ ratios for these steps is caused by progressively higher ^{22}Ne contribution from Air. Contribution from air is also evident in ^{20}Ne through progressively lower $^{4}He/^{20}Ne$ ratios. Peak release steps for all samples due to schreibersite (WC_2: 1140 °C, WC_5: 1100 °C, WC_11: 1100 °C, WC_14: 1140 °C) and kamacite-taenite (WC_2: 1380 °C, WC_5: 1425 °C, WC_11: 1440 °C) show $^{4}He/^{20}Ne$ ratios between ~340 (WC_2) and ~420 (WC_5) indicating a trend towards SW in reference to the GCR end-member. Only the high temperature peak of WC_14 (1480 °C) with a $^{4}He/^{20}Ne$ ratio of ~85 indicates mixing between GCR and Air. Except for WC_14, (Fig. 2.10a), $^{4}He/^{20}Ne$ ratios for totals(1), are within the range of 331±47–371±52 reported by Signer and Nier (1962). Ratios from Schaeffer and Fisher (1959) of 338-620 and from Hintenberger et al. (1967) of 419 have large errors and the ratio from Merrihue (1964) of 687 is given without errors. The most remarkable trend towards SW composition including small errors with a $^{4}He/^{20}Ne$ ratio of 590±18 is reported by Becker and Pepin (1984).

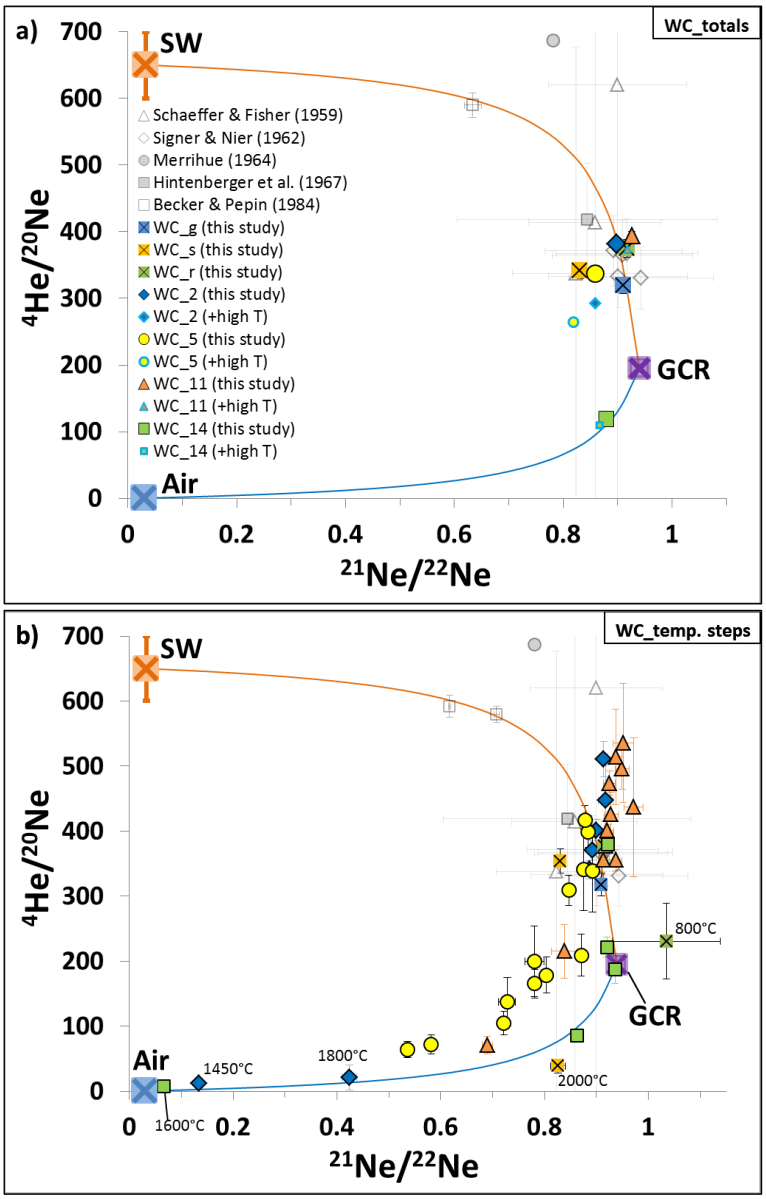

Fig. 2.10: $^{4}He/^{20}Ne$–$^{21}Ne/^{22}Ne$ diagram showing literature and measured data for Washington County: **a)** WC_totals and **b)** WC_temperature steps (see Tab. 2.1). For new measurements (WC_2, WC_5, WC_11, WC_14, WC_g, WC_s, WC_r) only data with errors (1σ) <30% for $^{4}He/^{20}Ne$ and <5% for $^{21}Ne/^{22}Ne$ are shown. Note that errors of WC_2 (1800 °C) and WC_14 (1600 °C) are 94% and 43% for $^{4}He/^{20}Ne$, respectively. The error for WC_r (800 °C) is 10% for $^{21}Ne/^{22}Ne$. Fig. 2.10a also shows total(2) values including high temperature steps (>1525 °C) that appear to be influenced by an air component. End-member compositions of GCR, SW and Air are shown as well as mixing lines towards the GCR between these components (see text for details).

In terms of the $^{4}He/^{20}Ne$ ratios, more diagnostic indication for the presence of an actual solar wind component is provided by ratios of excess gas compared to the cosmogenic values. A constant $(^{4}He/^{20}Ne)_{excess}$ ratio of 420±40, for example, was reported by Signer and Nier (1962) between adjacent samples, pointing towards solar values (see discussion for further considerations). Comparable $(^{4}He/^{20}Ne)_{excess}$ ratios for all WC_samples (Tab. 2.1) can be calculated with:

$$\frac{^4He_{exess(i)}}{^{20}Ne_{excess(i)}} = \frac{\left(\frac{\frac{^3He}{^4He}_{meas(i)} - \frac{^3He}{^4He}_{GCR}}{\frac{^3He}{^4He}_{SW} - \frac{^3He}{^4He}_{GCR}}\right) * {}^4He_{meas(i)}}{\left(\frac{\frac{^{22}Ne}{^{20}Ne}_{meas(i)} - \frac{^{22}Ne}{^{20}Ne}_{GCR}}{\frac{^{22}Ne}{^{20}Ne}_{SW} - \frac{^{22}Ne}{^{20}Ne}_{GCR}}\right) * {}^{20}Ne_{meas(i)}}$$

where $^4He_{meas(i)}$, $^{20}Ne_{meas(i)}$, $\frac{^3He}{^4He}_{meas(i)}$, $\frac{^{22}Ne}{^{20}Ne}_{meas(i)}$ are measured concentrations of ^{4}He, ^{20}Ne and measured isotopic ratios of $\frac{^3He}{^4He}$ and $\frac{^{22}Ne}{^{20}Ne}$ for a temperature step i or a particular total value, respectively, $\frac{^3He}{^4He}_{GCR}$ and $\frac{^{22}Ne}{^{20}Ne}_{GCR}$ the isotopic ratios of the cosmogenic end-member (i.e., $\frac{1}{2.65}$ and $\frac{1}{0.91}$, respectively) and $\frac{^3He}{^4He}_{sw}$ and $\frac{^{22}Ne}{^{20}Ne}_{SW}$ the isotopic ratios of the solar wind end-member (i.e. $\frac{1}{2150}$ and $\frac{1}{13.777}$, respectively).

Table 2.1 lists also the calculated concentrations of $^{20}Ne_{excess}$ and the $(^4He/^{20}Ne)_{excess}$ ratios. Total $^4He_{excess}$ concentrations show variations of a factor of up to ~3.5 between adcajent samples (WC_11 and WC_14), but differ by a factor of more than 8 between WC_14 and WC_s. Total $^{20}Ne_{excess}$ concentrations vary with a factor of up to ~2.5 between adcajent samples (WC_11 and WC_14) but are different within a factor of ~5.5 between WC_11 and WC_s. All total(1) $(^4He/^{20}Ne)_{excess}$ values have higher excess ratios compared to total(2) values because likely atmospheric contributions during high temperature release steps are not included in the former. $(^4He/^{20}Ne)_{excess}$ ratios based in total(1) generally range between ~450 (WC_5, WC_s), consistent with Signer and Nier (1962), and ~700 (WC_r). The highest total $(^4He/^{20}Ne)_{excess}$ ratio of 1067 is calculated for WC_11. The lowest excess ratios of ~110 observed for WC_14 is in accordance with the dominant air-like composition of the high temperature release peak for this sample (1480 °C: $(^4He/^{20}Ne)_{excess}$ = 73). As for the others, both, low and high temperature peaks (WC_2: 1140 and 1380 °C, WC_5: 1100 and 1425 °C, WC_11: 1100 and 1440 °C, WC_14: 1140 °C), have $(^4He/^{20}Ne)_{excess}$ ratios between 584 and 1303 whereas the low temperature peaks (schreibersite) always show higher ratios.

2.3.6 Argon

The total concentrations of ^{36}Ar measured for WC_samples in cm³STP/g (Tab. 2.1) range from $523*10^{-10}$ (WC_5, total(1)) to $1447*10^{-10}$ (WC_r) and are consistent with data given by Schaeffer and Fisher (1959) of $(510–560)*10^{-10}$ cm³STP/g, Signer and Nier (1962) of $(672–1048)*10^{-10}$ cm³STP/g, Merrihue (1964) of $1350*10^{-10}$ cm³STP/g and Becker and Pepin (1984) of of $559*10^{-10}$ cm³STP/g.

Figure 2.11 shows the $^{40}Ar/^{36}Ar$ ratio against the $^{38}Ar/^{36}Ar$ ratio of all measured Washington County samples for totals (Fig. 2.11a) and for individual temperature steps (Fig. 2.11b) compared to the literature data. The isotopic compositions of four possible end-members are also indicated: solar is from Heber et al. (2012), planetary (Q) from Busemann et al. (2000) and Air from Ozima

and Podosek (2002). The GCR end-member ratio ($^{40}Ar/^{36}Ar = 0$, $^{38}Ar/^{36}Ar = 1.57$) was inferred from data listed in Schultz and Franke (2004) for iron meteorites that have a $^{40}Ar/^{36}Ar$ ratio of <2.

All available Washington County data cluster within errors around the GCR $^{38}Ar/^{36}Ar$ end-member (Fig. 2.11b inset) or comprise a mixture of the GCR component and variable quantities of Air as indicated by high $^{40}Ar/^{36}Ar$ ratios. Relative to the most cosmogenic total(1) values of WC_2 and WC_11, an increase in the Air contribution is indicated by progressively higher $^{40}Ar/^{36}Ar$ ratios in the order WC_14, WC_s, WC_r, WC_5 and WC_g (Fig. 2.11a). The value of WC_2 agrees with data from Becker and Pepin (1984) and suggests mixing of GCR and a trapped component that is predominantly solar or planetary with possibly some small air contribution. The shift towards air composition becomes more evident when the high temperature steps are added, i.e., in the total(2) values. The highest Air contribution is seen in temperature steps of WC_r (800 °C), WC_2 (1450 °C), WC_5 (1150 °C and other steps following the peak release temperatures), WC_s (800 °C), WC_11 (1800 °C) and WC_g (1800 °C and 2000 °C) (Fig. 2.11b). The three temperature steps that are least influenced by Air ($^{40}Ar/^{36}Ar$ <1.5) (WC_2, 1140 °C and 1350 °C; WC_11, 1250 °C) indicate the presence of a distinct solar or planetary component (Fig. 2.11b inset). This is also true for WC_11 (1050 °C), WC_s (1800 °C) and WC_s (total) although air must also contribute as shown by the enhanced $^{40}Ar/^{36}Ar$ ratio. Data from Merrihue (1964) likewise show a shift towards solar or planetary. No general trend is evident for peak release temperatures (schreibersite and kamacite-taenite peak). The high temperature peaks for WC_5 and WC_11 (1425 °C and 1440 °C, respectively) have higher (within 2σ) $^{38}Ar/^{36}Ar$ ratios than the nominal GCR, reflecting uncertainties in the end-member composition. Data from Signer and Nier (1962) reveal maximum $^{40}Ar/^{36}Ar$ values of ~5, but $^{38}Ar/^{36}Ar$ uncertainties are larger.

It should be noted that the high abundance of cosmogenic Ar in Washington County makes a reliable detection of SW-Ar difficult. For one, production of cosmogenic ^{36}Ar on iron is much more efficient than that ^{20}Ne: For the chemical composition of Washington County a cosmogenic $^{36}Ar/^{22}Ne$ ratio of ~3 is predicted by Ammon et al. (2008, 2009) and, with cosmogenic $^{20}Ne/^{22}Ne$ ratio of ~0.91, the $^{36}Ar/^{20}Ne$ ratio is >3 as well. On the other hand, ^{36}Ar is much scarcer in the solar wind compared to ^{20}Ne ($^{36}Ar/^{20}Ne_{SW}$: ~0.024, Heber et al., (2012)). A ^{20}Ne excess of $\sim 36*10^{-10}$ cm^3STP/g (exemplified case for WC_2, 1140 °C, Tab.2.1) implies a ^{36}Ar excess of $0.9*10^{-10}$ cm^3STP/g which is only ~0.6% of the measured ^{36}Ar. Therefore, the detection of solar Ar is only possible if measured ratios are very precise and the GCR end-member composition would be precisely known. This is not the case because of uncertainties in the cosmogenic $^{38}Ar/^{36}Ar$ production ratio (Ammon et al., 2009).

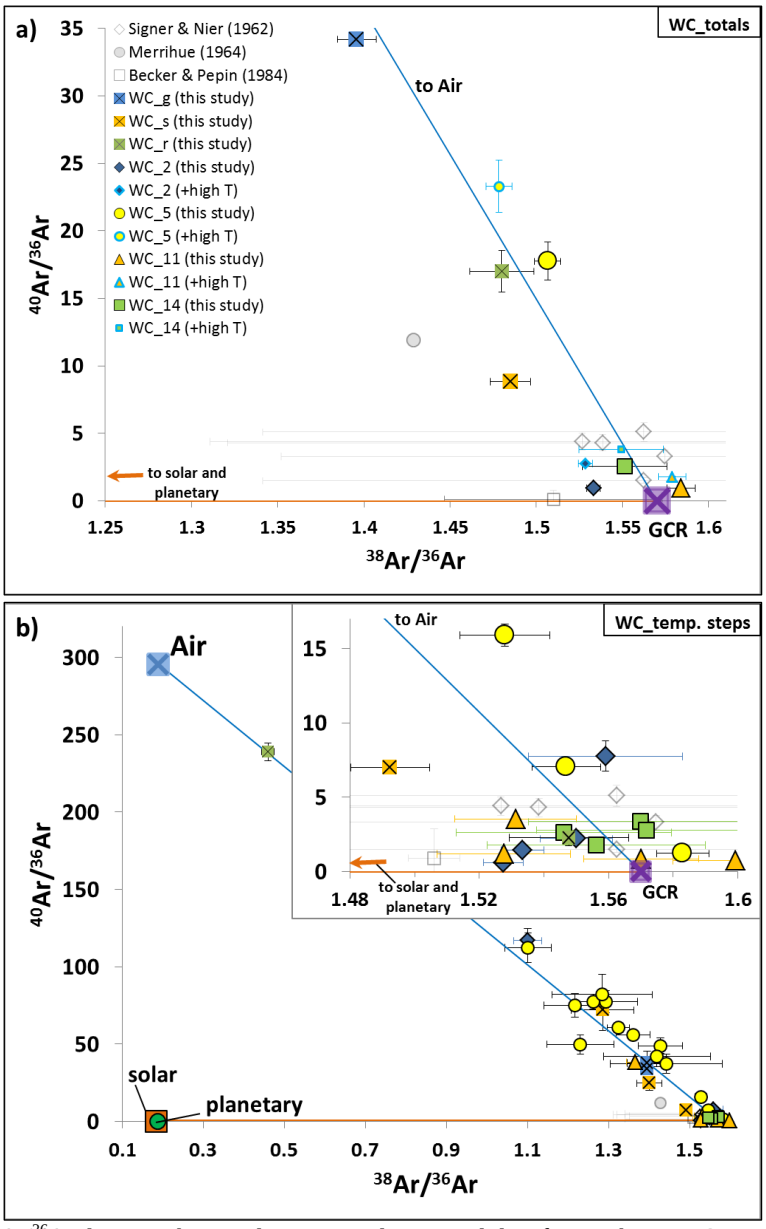

Fig. 2.11: $^{40}Ar/^{36}Ar$–$^{38}Ar/^{36}Ar$ diagram showing literature and measured data for Washington County: **a)** WC_totals and **b)** WC_temperature steps (see Tab. 2.1). For the new measurements (WC_2, WC_5, WC_11, WC_14, WC_g, WC_s, WC_r) only data with errors (1σ) <25% for $^{40}Ar/^{36}Ar$ and <10% for $^{38}Ar/^{36}Ar$ are shown. Fig. 2.11a also shows total(2) values including high temperature steps (>1525 °C) that are likely compromised by an air component. End-member compositions of SW (solar), planetary (Q), Air and mixing lines between these and the GCR end-member composition are indicated (see text for details).

2.3.7 Krypton

Krypton was measured for WC_g, WC_s and WC_r (Tab. 2.2). To date, no previous krypton measurements exist for Washington County. The total measured ^{84}Kr concentrations (1σ errors) of $(200.52\pm3.65)*10^{-12}$ cm^3STP/g, $(45.90\pm1.50)*10^{-12}$ cm^3STP/g and $(607.13\pm29.38)*10^{-12}$ for WC_g, WC_s and WC_r, respectively, compare to $(4.98–126)*10^{-12}$ cm^3STP/g ^{84}Kr in other iron meteorites (Munk, 1967a, b; Hennecke and Manuel, 1977). These authors speculate about a cosmogenic origin of the observed krypton isotopes. In particular the iron meteorites Carbo and Costilla Peak show $^{83}Kr/^{84}Kr$ ratio of 0.389±0.007 and 0.381±0.005, respectively, indicating cosmogenic

contributions (Fig. 2.12). The present results allow identifying a cosmogenic excess from the $^{83}Kr/^{84}Kr$ ratios of 0.2601±0.0091 and 0.2638±0.0130 in the 1800 °C steps for WC_s and WC_r, respectively (Tab. 2.2, Fig. 2.12). The krypton isotopic ratios for WC_g show more air-like values.

Tab. 2.2: Kr concentrations, isotopic ratios of WC_g, WC_s, WC_r and reservoir composition of SW, planetary (Q) and Air

Sample (weight)	Temp. [°C]	^{84}Kr [10^{-12} cm³STP/g]	±	$^{78}Kr/^{84}Kr$	±	$^{80}Kr/^{84}Kr$	±	$^{82}Kr/^{84}Kr$	±	$^{83}Kr/^{84}Kr$	±	$^{86}Kr/^{84}Kr$	±
WC_g[1)]													
(22.4 mg)	**1800**	195.64	3.51	-	-	0.0442	0.0011	0.2133	0.0040	0.2095	0.0020	0.3090	0.0037
	2000	4.88	0.97	-	-	0.0313	0.0318	0.2276	0.0296	0.2453	0.0307	0.3199	0.0498
	Total	**200.52**	**3.65**	-	-	**0.0439**	**0.0014**	**0.2137**	**0.0040**	**0.2104**	**0.0021**	**0.3092**	**0.0038**
WC_s[1)]													
(21.87 mg)	**800**	6.03	0.80	-	-	0.0089	0.0323	0.1894	0.0323	0.2129	0.0280	0.2127	0.0959
	1800	33.10	0.96	-	-	0.0750	0.0061	0.2593	0.0079	0.2601	0.0091	0.2975	0.0178
	2000	6.76	0.83	-	-	0.0299	0.0285	0.2296	0.0331	0.2345	0.0258	0.2465	0.0843
	Total	**45.90**	**1.50**	-	-	**0.0597**	**0.0075**	**0.2457**	**0.0087**	**0.2501**	**0.0085**	**0.2788**	**0.0219**
WC_r[1)]													
(8.54 mg)	**800**	576.83	28.18	0.0067	0.0011	0.0370	0.0015	0.1989	0.0056	0.1987	0.0032	0.2944	0.0050
	1800	93.30	8.31	0.0200	0.0069	0.0692	0.0075	0.2573	0.0223	0.2638	0.0130	0.2994	0.0276
	2000	1.00	6.00	-	-	-	-	-	-	-	-	-	-
	Total	**670.13**	**29.38**	**0.0085**	**0.0013**	**0.0415**	**0.0017**	**0.2070**	**0.0057**	**0.2078**	**0.0033**	**0.2951**	**0.0058**
Reservoir													
SW[a)]				0.00642	0.00005	0.0412	0.0002	0.2054	0.0002	0.2034	0.0002	0.3012	0.0004
planetary (Q)[b)]				0.00603	0.00003	0.03937	0.00007	0.2018	0.0002	0.2018	0.0002	0.3095	0.0005
Air[c)]				0.006087	0.000020	0.039599	0.000020	0.20217	0.00004	0.20136	0.00021	0.30524	0.00025

All data are corected for blank. All uncertainties 1σ. [1)]Measurements performed at MPI für Chemie, Mainz. [a)]from Meshik et al. (2014), [b)]from Busemann et al. (2000), [c)]from Basford et al. (1973)

Figure 2.12 shows the $^{82}Kr/^{84}Kr$–$^{83}Kr/^{84}Kr$ isotopic ratios of WC_g, WC_s and WC_r in reference to the krypton ratios measured in the iron meteorite Carbo (Munk, 1967a) and Costilla Peak (Munk, 1967b). Mixing lines are drawn from the SW end-member to the spallation composition calculated by Munk (1967a) for iron meteorites ($^{82}Kr/^{84}Kr$ = 6.41 $^{83}Kr/^{84}Kr$ = 7.58) and to the spallation krypton composition of achondrites ($^{82}Kr/^{84}Kr$ = 1.7857, $^{83}Kr/^{84}Kr$ = 2.3810) obtained from measurements of eucrites (Stannern and Pasamonte, Hohenberg et al. (1967)). The cosmogenic $^{83}Kr/^{84}Kr$ ratios for WC_s (1800 °C) and WC_r (1800 °C) plot above the achondritic mixing line (although errors are large) and fall together with the value of Carbo and Costilla Peak on the "iron meteorite" mixing line that points towards a possible cosmogenic krypton end-member. Different cosmogenic ratios compared to achondrites may be caused by high abundances of platinum group elements like Ru in iron meteorites as discussed by Munk (1967a). Either or not this is true for Washington County, the data for WC_g, WC_s and WC_r are consistent within errors with cosmogenic production rates in iron meteorites and achondrites.

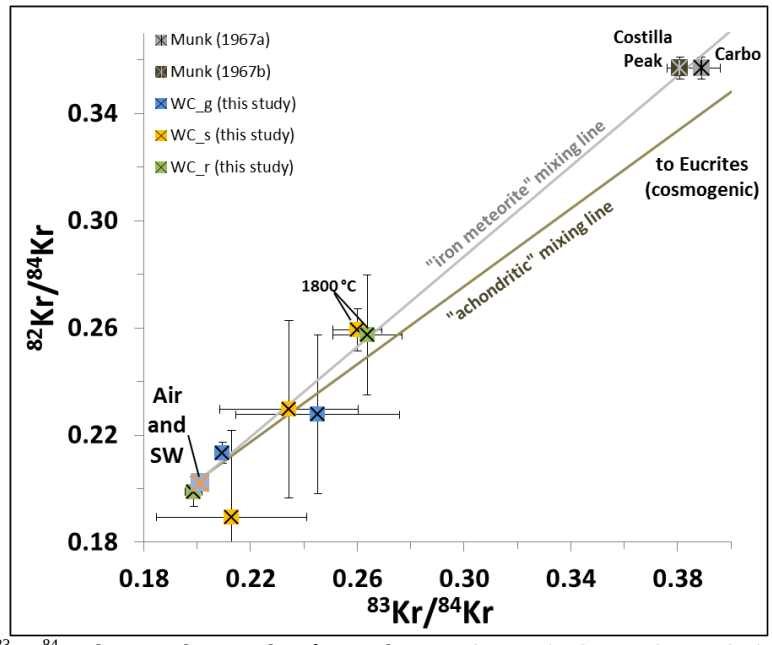

Fig. 2.12: $^{82}Kr/^{84}Kr$ – $^{83}Kr/^{84}Kr$ diagram showing data for Washington County (WC_g, WC_s, WC_r) and the iron meteorites Carbo (Munk, 1967a) and Costilla Peak (Munk, 1967b). Errors are 1σ. The "achondritic" mixing line is drawn from the SW (and Air) end-member to the spallation krypton composition in eucrites (Hohenberg et al., 1967). The "iron meteorite" mixing line is drawn from the SW (and Air) end-member to the cosmogenic iron meteorite end-member calculated by Munk (1967a). The 1800 °C steps of WC_s and WC_r are in agreement with the "iron meteorite" mixing line although they are also consistent within errors with the "achondritic" mixing line.

2.3.8 Xenon

Xenon was measured for WC_5, WC_g, WC_s and WC_r (Tab. 2.3). Previous xenon analyses for Washington County were only mentioned in an abstract in which Reynolds et al. (1962) noted that no excess ^{129}Xe was found. The recent investigation reconfirms the lack of ^{129}Xe excesses. Total $^{129}Xe/^{132}Xe$ ratios (1σ errors) measured for WC_g, WC_s and WC_r are 0.999±0.019, 1.045±0.099 and 0.964±0.033, respectively. ^{132}Xe concentrations are $(25.60\pm1.08)*10^{-12}$ cm^3STP/g, $(6.72\pm2.00)*10^{-12}$ cm^3STP/g and $(116.59\pm7.67)*10^{-12}$ for WC_g, WC_s and WC_r, respectively. This compares to $(0.57–50)*10^{-12}$ cm^3STP/g ^{132}Xe in other iron meteorites (Munk, 1967a, b; Hennecke and Manuel, 1977). One of them, Carbo, moreover shows an excess of ^{129}Xe, with $^{129}Xe/^{132}Xe$ of 1.295±0.019 (Munk, 1967a).

The results for WC_5 have large errors because of very low gas amounts below detection limit or slightly above blank (Tab A2). Totals listed in Table 2.3 have been obtained by summing the intermediate temperature steps only (see section 'Noble gas data' and Tab. 2.1). No attempt was made to include low and high temperature release steps into to calculation of the totals. Within 2σ errors the isotopic compositions of temperature steps and total values of WC_5 are indistinguishable from SW-, planetary- and Air composition. Due to less extraction steps, measurements for WC_g, WC_s and WC_r result in more reliable data. In general, however, isotopic ratios are either indistinguishable from air or are too imprecise when gas concentrations are low (Tab. 2.3). Respectively, no further discussion of the Xe composition of Washington County is possible without higher precision data.

Tab. 2.3: Xe concentrations and isotopic ratios of WC_5, WC_g, WC_s, WC_r and reservoir composition of SW, planetary (Q) and Air

Sample (weight)	Temp. [°C]	^{129}Xe [10^{-12} cm³STP/g]	±	^{132}Xe [10^{-12} cm³STP/g]	±	^{124}Xe/^{132}Xe	±	^{126}Xe/^{132}Xe	±	^{128}Xe/^{132}Xe	±	^{129}Xe/^{132}Xe	±	^{130}Xe/^{132}Xe	±	^{131}Xe/^{132}Xe	±	^{134}Xe/^{132}Xe	±	^{136}Xe/^{132}Xe	±
WC_5[1)]																					
(18.3 mg)	**600**	1.15	0.78	2.80	2.22	0.0055	0.0160	-	-	0.0220	0.0702	0.4120	0.4277	0.091	0.110	1.6373	1.8932	0.330	0.390	0.1552	0.1861
	700	3.21	0.97	4.64	1.63	0.0142	0.0131	0.0053	0.0065	0.0439	0.0407	0.6912	0.3204	0.111	0.059	1.1126	0.5506	0.288	0.147	0.2574	0.1339
	800	1.23	0.73	3.68	2.60	0.0368	0.0406	0.0036	0.0086	0.0513	0.0629	0.3353	0.3085	0.051	0.054	1.7965	1.8464	0.259	0.256	0.1501	0.1550
	850	0.74	0.92	1.50	2.15	-	-	0.0374	0.0912	0.6069	1.3179	0.4965	0.9394	0.254	0.530	5.7958	12.5123	0.075	0.275	0.2060	0.4275
	900	blank	-	0.94	2.88	0.0553	0.2208	0.1098	0.4325	0.4512	1.7810	-	-	0.060	0.326	5.0844	20.0128	-	-	0.1502	0.7697
	950	1.23	0.79	2.58	1.93	0.0369	0.0476	-	-	0.2776	0.3104	0.4753	0.4686	0.080	0.089	2.1227	2.3281	0.173	0.194	0.1732	0.1933
	1000	0.03	0.75	1.23	40.87	-	-	0.0002	0.0371	0.2490	11.7361	0.0255	1.0406	-	-	5.3162	250.8251	-	-	-	-
	1050	blank	-	3.98	13.30	0.0526	0.2482	0.0109	0.0516	0.1834	0.8549	-	-	0.007	0.089	5.0114	23.1986	0.003	0.155	0.0152	0.1801
	1100	0.13	0.94	1.57	15.25	0.0512	0.7161	0.1690	2.3653	0.2521	3.5077	0.0827	0.9989	0.001	0.102	3.8721	53.9558	0.075	0.972	0.1502	2.0155
	1120	3.03	1.23	4.75	2.11	0.0151	0.0121	0.0255	0.0192	0.0871	0.0577	0.6382	0.3834	0.088	0.058	1.5376	0.9789	0.323	0.204	0.2601	0.1667
	1150	1.50	1.04	1.70	1.33	0.1538	0.1875	0.1736	0.2084	0.0966	0.1177	0.8831	0.9266	0.277	0.310	1.8032	2.0247	0.266	0.328	0.4426	0.4917
	1200	0.05	0.87	0.92	23.82	-	-	0.1419	5.2465	-	-	0.0500	1.5960	-	-	3.1537	116.2698	0.296	10.777	0.1363	4.8990
	1250	blank	-	blank	-	-	-	-	-	-	-	-	-	-	-	-	-	-	-	-	-
	1300	3.64	1.23	5.08	1.86	0.0157	0.0117	0.0581	0.0412	0.0411	0.0260	0.7166	0.3563	0.148	0.078	1.1246	0.5871	0.250	0.136	0.2971	0.1574
	1350	2.55	1.16	4.09	2.10	0.0204	0.0178	0.0180	0.0176	0.0528	0.0511	0.6224	0.4274	0.061	0.055	1.4073	1.0260	0.247	0.180	0.1972	0.1482
	1400	0.06	0.91	1.46	32.92	0.0569	1.8363	0.0578	1.8655	-	-	0.0384	1.0709	0.052	1.649	3.2727	105.3740	-	-	0.0404	1.2213
	1425	blank	-	blank	-	-	-	-	-	-	-	-	-	-	-	-	-	-	-	-	-
	1450	0.39	1.00	1.45	4.59	0.1114	0.5288	0.0143	0.1034	0.2187	1.0144	0.2678	1.0896	-	-	2.1256	9.8219	0.277	1.214	0.0331	0.2399
	1475	blank	-	blank	-	-	-	-	-	-	-	-	-	-	-	-	-	-	-	-	-
	1500	0.90	1.00	1.12	1.46	-	-	0.1588	0.3207	-	-	0.7999	1.3711	0.052	0.145	2.8978	5.4787	0.207	0.426	0.0847	0.2990
	1525	0.58	0.95	2.58	5.27	0.0434	0.1313	0.0296	0.0983	0.0855	0.2516	0.2234	0.5853	0.095	0.270	1.6129	4.7648	0.262	0.743	0.1229	0.3411
	1550	2.25	0.93	3.59	1.64	0.0191	0.0176	0.0127	0.0127	0.1276	0.0885	0.6263	0.3859	0.102	0.072	1.8882	1.2523	0.334	0.224	0.3150	0.2057
	1650	blank	-	1.03	2.36	-	-	0.1814	0.5117	-	-	-	-	-	-	2.2510	6.6153	-	-	-	-
	1750	0.31	0.82	0.84	2.59	-	-	0.3855	1.8271	0.1356	0.6226	0.3746	1.5122	-	-	-	-	0.370	1.613	0.1391	0.6060
	1800	2.58	1.01	4.24	1.83	0.0051	0.0039	-	-	0.0793	0.0522	0.6093	0.3557	0.097	0.062	1.4361	0.8886	0.269	0.166	0.2362	0.1466
	Total	**14.06**	**3.46**	**33.45**	**61.71**	**0.0513**	**0.1176**	**0.0747**	**0.2003**	**0.1338**	**0.4209**	**0.4205**	**0.7826**	**0.077**	**0.152**	**2.6109**	**9.4643**	**0.192**	**0.418**	**0.1743**	**0.3466**
WC_g[2)]																					
(22.4 mg)	**1800**	25.56	1.19	25.60	1.08	0.0041	0.0009	0.0038	0.0021	0.0810	0.0105	0.9986	0.0193	0.159	0.006	0.7886	0.0146	0.390	0.009	0.3278	0.0095
	2000	-	-	0.66	0.91	-	-	-	-	-	-	-	-	-	-	-	-	-	-	-	-
	Total	**25.56**	**1.19**	**25.60**	**1.08**	**0.0041**	**0.0009**	**0.0038**	**0.0021**	**0.0810**	**0.0105**	**0.9986**	**0.0193**	**0.159**	**0.006**	**0.7886**	**0.0146**	**0.390**	**0.009**	**0.3278**	**0.0095**
WC_s[2)]																					
(21.87 mg)	**800**	0.86	1.60	0.65	1.15	-	-	-	-	-	-	1.3353	0.7063	0.218	0.141	0.8154	0.3228	0.449	0.193	0.1870	0.3350
	1800	2.60	1.30	2.39	1.16	-	-	-	-	-	-	1.0877	0.1299	0.145	0.040	0.6196	0.1664	0.330	0.082	0.3086	0.0478
	2000	3.56	1.14	3.68	1.16	-	-	-	-	-	-	0.9664	0.0630	0.152	0.026	0.6449	0.1152	0.311	0.055	0.2904	0.0326
	Total	**7.02**	**2.20**	**6.72**	**2.00**	**-**	**-**	**-**	**-**	**-**	**-**	**1.0450**	**0.0992**	**0.156**	**0.027**	**0.6523**	**0.0960**	**0.331**	**0.049**	**0.2868**	**0.0440**
WC_r[2)]																					
(8.54 mg)	**800**	96.58	6.60	98.52	5.98	0.0025	0.0010	0.0029	0.0042	0.0572	0.0131	0.9803	0.0308	0.149	0.006	0.7976	0.0220	0.431	0.070	0.3277	0.0093
	1800	15.78	4.84	18.06	4.80	0.0106	0.0041	0.0140	0.0201	0.0160	0.0731	0.8735	0.1335	0.149	0.025	0.6901	0.0608	0.683	0.341	0.3132	0.0337
	2000	-	-	-	-	-	-	-	-	-	-	-	-	-	-	-	-	-	-	-	-
	Total	**112.36**	**8.35**	**116.59**	**7.67**	**0.0037**	**0.0011**	**0.0046**	**0.0047**	**0.0509**	**0.0158**	**0.9637**	**0.0333**	**0.149**	**0.006**	**0.7809**	**0.0208**	**0.470**	**0.079**	**0.3254**	**0.0094**
Reservoir																					
SW[a)]						0.00489	0.00006	0.00420	0.00007	0.0842	0.0002	1.0405	0.0010	0.1648	0.0003	0.8256	0.0012	0.3698	0.0006	0.3003	0.0005
planetary (Q)[b)]						0.00455	0.00002	0.004057	0.000018	0.0822	0.0002	1.042	0.002	0.1619	0.0003	0.8185	0.0009	0.3780	0.0011	0.3164	0.0008
Air[c)]						0.00354	0.00001	0.00330	0.00002	0.07136	0.00009	0.9832	0.0012	0.15136	0.00012	0.7890	0.0011	0.3879	0.0006	0.3294	0.0004

All data are corrected for blank, blank: indistinguishable from blank. All uncertainties are 1σ. Underlined values are not used for calculation of totals because of atmospheric interactions as seen for He, Ne and Ar (see Tab. 1) and potential formation of secondary iron oxides. [1)]Measurements performed at the Institut für Geowissenschaften, Heidelberg. [2)]Measurements performed at MPI für Chemie, Mainz. [a)]from Meshik et al. (2014, 2015),[b)]from Busemann et al. (2000), [c)]from Basford et al. (1973)

2.4 Cosmic-ray exposure ages

Helium, neon and argon isotopic abundances in meteorites (see Schultz and Franke, 2004) are usually strongly influenced by spallation reactions due to exposure to high energetic cosmic radiation, i.e., galactic cosmic rays, during travel through space (e.g., Wieler, 2002a; Eugster, 2003; Eugster et al., 2006). When production rates are known (Leya and Masarik, 2009; Ammon et al., 2009), especially the record in the commonly rare isotopes ^{3}He, ^{21}Ne and ^{38}Ar allows determination of cosmic-ray exposure (CRE). Shielding effects cause different production rates related to the sample depth within the meteorite and its size. Isotopic ratios particularly of $(^{22}Ne/^{21}Ne)_c$, $(^{3}He/^{21}Ne)_c$ and $(^{38}Ar/^{21}Ne)_c$ can therefore be used as depth indicator (Wieler, 2002a; Eugster, 2003; Eugster et al., 2006; Ammon et al., 2009). Cosmogenic production rates and isotopic compositions naturally also vary as a function of sample chemistry. They also depend on the primary GCR energy spectrum because, for example, production on Fe of ^{21}Ne is dominantly by high energy particles whereas ^{4}He from Fe is mostly produced from lower energies in the range of a few 100 MeV (Ammon et al., 2009). Due to their physical strength against collisional fragmentation in space, iron meteorites generally are exposed to cosmic radiation over hundreds of millions of years. Stony meteorites have shorter cosmic-ray exposure ages of only millions to tens of millions of years (Wieler, 2002a; Eugster, 2003; Eugster et al., 2006; Ammon et al., 2009).

Voshage (1967) determined for Washington County a long exposure age of 575±80 Ma but noted relatively large uncertainties because of unknown radiation hardness. Murty and Ranjith Kumar (2014) used $(^{38}Ar/^{21}Ne)_c$ ratios of Washington County to estimate a sample depth of nearly 6 cm below the surface of a pre-atmospheric meteoroid of 12±2 cm radius. Applying the models from Ammon et al. (2008, 2009) to deduce production rates for $^{21}Ne_c$ and $^{38}Ar_c$, they calculated an average cosmic-ray exposure age of 276±41 Ma. Some inconsistency has to be noted, however, in the work by Murty and Ranjith Kumar (2014) in that the measured $(^{3}He/^{21}Ne)_c$ ratios indicate a shallower sample depth than $(^{38}Ar/^{21}Ne)_c$ and, hence, different production rates. A possible reason for the inconsistency is helium loss from the analyzed samples.

All concentrations and ratios of cosmogenic nuclides for the recent Washington County measurements in Table 2.4 were calculated using an iterative procedure. The determined $(^{3}He/^{21}Ne)_c$ and $(^{38}Ar/^{21}Ne)_c$ ratios give a more consistent picture when compared to cosmogenic model production ratios from Ammon et al. (2009) indicating a shallow sample depth in the uppermost ~2 cm of an iron meteoroid of less than 15 cm pre-atmospheric radius (Fig. 2.13a). $(^{22}Ne/^{21}Ne)_c$ model ratios (Fig. 2.13b) show less variations for shallow sample depths and are therefore less indicative. The high $(^{22}Ne/^{21}Ne)_c$ ratios for WC_samples compared to the model ratios are probably caused by cosmogenic reactions on phosphorus and sulfur in Washington County (cf. Murty and Ranjith Kumar, 2014).

After correcting the measured noble gas abundances for solar (^{3}He, ^{21}Ne) and atmospheric (^{38}Ar) contributions, cosmic-ray exposure ages were calculated for the near-surface and interior samples (WC_2, WC_5, WC_11, WC_14). For this, production rates based on the systematics from Ammon et al. (2009) and using a chemical composition of 90.1 wt% Fe and 9.9 wt% Ni for a pre-

atmospheric iron meteoroid of 10 cm radius were determined. Production rates for a sample depth of 0–1 cm (WC_2 and WC_5) and 2–3 cm (WC_11 and WC_14) were used. The results shown in Table 2.4 are overall consistent for each sample. The younger $^{3}He_c$ age of WC_14 compared to the $^{21}Ne_c$ and $^{38}Ar_c$ ages may be caused by He loss from the sample. An obvious trend goes from generally younger exposure ages for near-surface samples of 107±15–114±16 Ma (WC_2) and 101±14–113±16 Ma (WC_5) to generally older ages for the interior samples of 126±18–136±19 Ma (WC_11) and 110±16–167±24 Ma (WC_14). The average exposure age for Washington County using abundances of $^{3}He_c$, $^{21}Ne_c$ and $^{38}Ar_c$ is 123±5 Ma, 150 Ma younger than determined by Murty and Ranjith Kumar (2014) and significantly shorter than the age reported by Voshage (1967).

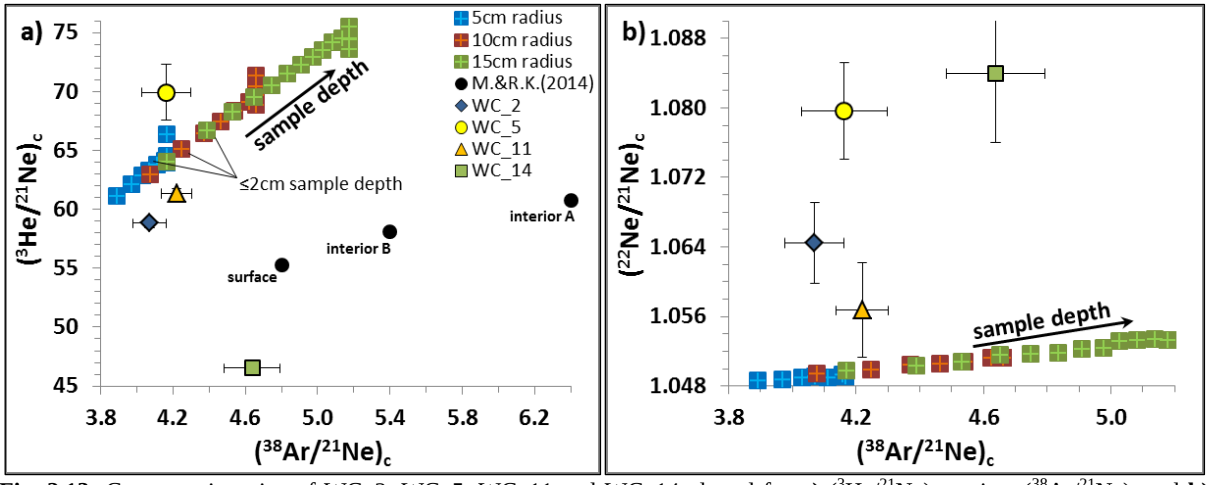

Fig. 2.13: Cosmogenic ratios of WC_2, WC_5, WC_11 and WC_14 plotted for **a)** $(^{3}He/^{21}Ne)_c$ against $(^{38}Ar/^{21}Ne)_c$ and **b)** $(^{22}Ne/^{21}Ne)_c$ against $(^{38}Ar/^{21}Ne)_c$. Cosmogenic model production ratios for iron meteoroids with 5, 10 and 15 cm pre-atmospheric radius containing 90.1 wt% Fe and 9.9 wt% Ni are also shown and are based on Ammon et al. (2009). The model ratios imply increasing ratios with increasing sample depth. Model $(^{3}He/^{21}Ne)_c$ and $(^{38}Ar/^{21}Ne)_c$ ratios for a sample depth of 2 cm in meteoroids are labeled for reference. $(^{3}He/^{21}Ne)_c$ and $(^{38}Ar/^{21}Ne)_c$ ratios for WC_samples (Tab. 2.4) best fit a sample depth of ≤2 cm in an pre-atmospheric meteoroid of ≤15 cm radius. Data given by Murty and Ranjith Kumar (2014) for their Washington County surface and interior samples (A and B, Fig. 2.13a) seem not to be in accordance with model ratios. $(^{22}Ne/^{21}Ne)_c$ model ratios (Fig. 2.13b) show less variations with sample depth. For WC_samples $(^{22}Ne/^{21}Ne)_c$ ratios are higher than the model ratios but have large uncertainties.

Tab. 2.4: Cosmogenic gas amounts (cm^3STP/g) and ratios for investigated WC_samples calculated from total(1) values. Cosmic-ray exposure ages are calculated from production rates ($[10^{-8}]cm^3STP/g/Ma$) of $^{3}He_c$, $^{21}Ne_c$ and $^{38}Ar_c$ in an 10 cm iron meteoroid (Ammon et al., 2009) for a sample depth of 0–1 cm (WC_2, WC_5) and 2–3 cm (WC_11, WC_14).

	WC_2	WC_5	WC_11	WC_14
$(^{3}He/^{21}Ne)_c$	58.8±0.4	69.9±2.4	61.4±0.4	46.5±0.4
$(^{38}Ar/^{21}Ne)_c$	4.07±0.09	4.16±0.14	4.22±0.08	4.64±0.15
$(^{22}Ne/^{21}Ne)_c$	1.064±0.005	1.080±0.006	1.057±0.005	1.084±0.008
$^{21}Ne_c$ $[10^{-8}]$	2.12±0.01	1.88±0.01	2.25±0.01	2.61±0.02
prod.$^{3}He_c$	1.1698	1.1698	1.1002	1.1002
T_3 [a)] [Ma]	**107±15**	**113±16**	**126±18**	**110±16**
prod.$^{21}Ne_c$	0.0186	0.0186	0.0166	0.0166
T_{21} [a)] [Ma]	**114±16**	**101±14**	**136±19**	**158±22**
prod.$^{38}Ar_c$	0.0758	0.0758	0.0724	0.0724
T_{38} [a)] [Ma]	**114±16**	**103±15**	**131±19**	**167±24**

[a)]Assumed errors of gas measurements and production rates are 10%, respectively. All uncertainties are 1σ

2.5 Discussion

Because of typically long exposure ages compared to stony meteorites (Voshage, 1967; Wieler, 2002a; Eugster, 2003; Eugster et al., 2006; Ammon et al., 2009) most iron meteorites are dominated by a noble gas component for He, Ne and Ar that is produced by interactions with cosmic radiation and often contains pure cosmogenic He (Wieler, 2002a; Schultz and Franke, 2004). In addition, there may be an atmospheric component that was incorporated by contamination during passage through Earth's atmosphere (e.g., Wieler, 2002a; Osawa; 2012). In the recent noble gas study of Washington County, clear ^{4}He excesses are found (Fig. 2.8) as well as helium to neon isotopic ratios clearly distinct from the GCR and Air end-member composition (Figs. 2.9 and 2.10). From ^{4}He/^{3}He ratios that show no large difference between the major degassing peaks (Fig. 2.6) it can be excluded that the ^{4}He excess is from spallation reactions on phosphorus in schreibersite compared to spallation in kamacite and taenite. Therefore, in combination with ^{20}Ne excesses and diagnostic Ne isotopic ratios (Fig. 2.7) a SW component for the light noble gases in Washington County that is (also) present in its interior can safely be identified. Ar isotopes (Fig. 2.11) may also indicate the presence of a component that differs in composition from GCR and Air. The Ar data are, however, less indicative and it is not possible to unambiguously assign this to solar wind, because mixing with planetary composition would result in essentially the same isotopic trends.

The present study confirms earlier reports of excess primordial light noble gases detected in Washington County (Schaeffer and Fisher, 1959; Signer and Nier, 1962; Hintenberger et al., 1967; Becker and Pepin, 1984, 1987; Murty and Ranjith Kumar, 2014) and furthermore underlines the SW characteristics of the trapped gases. The most remarkable noble gas trend towards present-day SW was found by Becker and Pepin (1982, 1984). However, it was later questioned whether this represents trapped noble gases from the interior of Washington County with unfractionated solar elemental (He, Ne and Ar) and Ne isotopic ratios. Becker and Pepin (1987) instead concluded that the observed solar signatures might rather reflect more recent implantation of solar wind into their analyzed rear surface sample. It is known that implanted components in small particles like IDPs and micrometeorites (MMs) can survive atmospheric entry heating (Schwarz et al., 2005; Osawa, 2012). It is however unclear how surface correlated components of larger bodies should survive ablation processes other than in an almost unaffected rear surface. The presence of trapped noble gases in Washington County with fractionated solar elemental and SW-Ne isotopic ratios was furthermore reported in an abstract by Murty and Ranjith Kumar (2014). Based on their results for surface and interior samples the authors suggest that these are volume correlated rather than surface implanted. However, no complete dataset is reported in this abstract and depending on the cosmogenic end-member isotopic ratio (unspecified in their Ne 3-isotope plot) the data could either indicate mixing between GCR and SW or GCR and Air. In contrast, the recent study provides an unambiguous report for the presence of trapped SW noble gases in the interior of Washington County.

The degassing patterns of WC_2, WC_5, WC_11 and WC_14 (Fig. 2.6, Figs. A1–A3) furthermore confirm that trapped noble gases are hosted within Washington County as reflected

by peak degassing from the main mineralogical constituents: schreibersite and kamacite-taenite. This slightly contrasts with the study of Hintenberger et al. (1967) who claimed that the pure metal phase was the only carrier of primordial noble gases and inclusions of silicates and schreibersite were excluded. That trapped gases are present in schreibersite is even more clearly demonstrated by the results for WC_r, a sample of almost pure schreibersite, which also shows the trend towards SW composition indicating the presence of primordial gases. On the other hand, it is not straightforward to explain why – based on the relative height of the two release peaks – schreibersite with a total abundance of ~3% (Fig. 2.4) releases about 20% of the total noble gas amount (except ^{40}Ar) from WC_5 (Tab. 2.1, Fig. 2.6) and even up to ~40% from WC_11 (Tab. 2.1, Fig. A2). A possible explanation would be extraction of additional noble gases during melting of schreibersite particles caused by eutectic melting of metal in adjacent areas.

In general, all samples contain significant amounts of cosmogenic He, Ne and Ar, and temperature steps of WC_14 contain the most cosmogenic compositions for He and Ne (Figs. 2.7 to Fig. 2.10). The strongest indication for the presence of SW among the samples is seen in WC_s, WC_5 and WC_2 (Figs. 2.7 to 2.9). While galactic cosmic radiation has a mean penetration depth of about 50 cm (Wieler, 2002a), the presence of light noble gases implanted by the solar wind is restricted to depths of less than 1 μm of the meteorite surface (Grimberg et al., 2006; Heber et al., 2009). Solar wind implanted into the surface of meteorites is moreover strongly affected by ablation losses during atmospheric entry (e.g., Bhandari et al., 1980; Farley et al. 1997; Wieler, 2002b; Toppani et al., 2003; Osawa, 2012; Füri et al., 2013). It is obvious from the results, however, that solar gases, even if once surface implanted, must have reached the interior of Washington County because not only the near-surface samples in depths of >2 mm (WC_2, WC_5) but also samples in depths of >2 cm (WC_11, WC_14) contain solar wind gases. As mentioned earlier, gases with atmospheric composition may have been released from a chemically distinct Fe-Ni phase or iron oxides that formed during atmospheric entry or terrestrial weathering (see section 'Noble gas data' and 'Degassing pattern'). Indeed, most high temperature release steps contain a significant atmospheric component that causes a shift towards air (Figs. 2.7 to 11). In consequence, both, total(1) and (2) values of WC_14 are dominated by the air contribution released in the high temperature peak (1480 °C). For the same reason, Ne isotopic ratios of WC_14 are the only data in the Ne three isotope plot (Fig. 2.7) that are located on the mixing line between GCR and Air, whereas all other data are consistent with mixing of GCR and SW or Ne-B.

Variations of trapped noble gas concentrations in Washington County were noted earlier for samples in adjacent areas (Signer and Nier, 1962) and were found on a sub-mm scale by Becker and Pepin (1984) which was inferred by these authors from relative amounts of trapped and spallation gases that differ between the two combustion steps for the same sample. Variations of the trapped noble gas contents on a small scale are also observed in the present study (Tab. 2.1) between WC_2 and WC_5 but are more remarkable between innermost samples (WC_11 and WC_14). They are, however, not as substantial as reported by Signer and Nier (1962) who found excess noble gas variations of a factor of 5 in adjacent samples. In the present study, differences in $^{4}He_{excess}$ with a factor of ~5 (Tab. 2.1) are observed between more distant samples (WC_2 and WC_14, WC_5 and WC_14) but reach up to a factor of more than 8 between WC_s and WC_14. $^{20}Ne_{excess}$ variations with a factor of ~3 exist between distant samples (WC_5 and WC_11) and

reach up to a factor of ~5.5 between WC_s and WC_11. In contrast to the constant $(^4He/^{20}Ne)_{excess}$ ratio of 420±40 reported by Signer and Nier (1962) that was considered to rule out a predominantly radiogenic origin for the ^4He excesses, a wider range of excess ratios can now be seen among samples of Washington County. A similar $^4He/^{20}Ne$ excess ratio as in Signer and Nier (1962) of 470 was reported by Hintenberger et al. (1967). Murty and Ranjith Kumar (2014) measured lower $^4He/^{20}Ne$ ratios between 150 and 320 for the trapped component that was identified as solar gas whereas an excess $^4He/^{20}Ne$ ratio of 640, derived from the data given by Becker and Pepin (1984), is identical to unfractionated solar wind ($^4He/^{20}Ne_{SW}$ = 650±50; Wieler, 2002b). Compared to these, equally high total(1) $(^4He/^{20}Ne)_{excess}$ ratios are observed for some of the new samples (e.g., WC_2: ~680, Tab. 2.1) but generally vary between ~450 and ~700. All total(2) values that probably include atmospheric contributions in the high temperature steps show consistently lower $(^4He/^{20}Ne)_{excess}$ ratios. The highest total(1) excess ratios of ~1070 is that for WC_11. Even the WC_11 total(2) value of ~890 is higher than any previously reported ratios. The lowest total(1) $(^4He/^{20}Ne)_{excess}$ ratio among the samples of ~110 is that found for WC_14 and is caused by air contribution in the high temperature peak (1480 °C). It is worth noting that in all other cases the gas released in the high temperature peak (kamacite-taenite peaks of WC_2, WC_5 and WC_11) have "moderate" $(^4He/^{20}Ne)_{excess}$ ratios ranging between ~580 and ~820 whereas higher excess ratios ranging from ~660 to ~1300 are observed in the respective low temperature peaks (schreibersite peaks of WC_2, WC_5, WC_11 and WC_14). Likewise, the pure schreibersite sample WC_r reveals the second highest bulk $(^4He/^{20}Ne)_{excess}$ ratio of 700. Overall, excess $^4He/^{20}Ne$ ratios measured in Washington County are not unlike those for metal separates from ordinary chondrites, which contain a surface-sited solar wind component with $^4He/^{20}Ne$ ratios of 647±62 (Murer et al., 1997) and possibly up to 800 (Becker and Pepin, 1991).

In essence, the results show that SW noble gases in the interior of Washington County must have been acquired during the formation of its parent body (Murty and Ranjith Kumar, 2014) under very special conditions that may have involved a sudden melting event of chondritic material or of a solar wind irradiated regolith that was loaded with primordial gases (Hintenberger et al., 1967; Becker and Pepin, 1984). Possible origins of unfractionated solar gases in Washington County were further discussed by Becker and Pepin (1984). Most likely explanations would be occlusion of nebular gas in voids during accretion or direct implantation of solar wind into metal grains prior to accretion. If SW-implantation happened before accretion, this process was certainly not unique for a single iron meteorite (Becker and Pepin, 1984) and a similar process could have led to the presence of volume correlated solar noble gases not only in Washington County but also in the interior of Earth (Murty and Ranjith Kumar, 2014). So far, only one other iron meteorite, Kavarpura, has been found to show solar noble gases that are heterogeneously distributed in interior samples, but in this case, they have been inferred to be present in minor inclusions rather than in the metal phase (Murty et al., 2008). An investigation of the inhomogeneously distributed spinel phase now detected for Washington County may provide an insight to the question if tiny silicate inclusions in iron meteorites are possible carriers of SW-implanted noble gases (instead of or in addition to the metal phase).

The implications of the presence of light solar noble gases in the interior of Washington County and possibly one other iron meteorite (Kavarpura) are of high relevance for Earth and the

iron core as a potential reservoir for noble gases. This is because the flux of light noble gases from the core is an alternative source of solar He and Ne within Earth that traditionally is believed to be located in a primitive deep mantle reservoir sampled by plumes (see Moreira, 2013 and references therein). It would furthermore remove the requirement for a separate noble gas reservoir in the mantle (Porcelli and Ballentine, 2002). Under certain conditions of diffusivity, a flux of ^{3}He and other noble gases from the core could significantly enrich a thermal boundary layer at the bottom of the mantle that samples the primitive noble gas signatures observed in OIBs (Moreira, 2013). Up to now, however, the idea of the core as a source of primordial He and Ne is regarded as highly speculative (Macpherson et al., 1998; Dixon et al., 2000). Despite this, the core as possible source of He and the required constraints for its incorporation were discussed in length by Porcelli and Halliday (2001) and Porcelli and Ballentine (2002). In detail, partitioning of helium into the core depends on prevailing conditions during its formation, in particular on initial gas concentrations and partition coefficients $D(He)_{Fe/LSi}$ of noble gases between liquid metal and liquid silicate. These are, however, generally very low and actually decrease from $\sim 4*10^{-2}$ to $\sim 3*10^{-4}$ with increasing pressures of 5–100 kbar (Matsuda et al., 1993). More favorable coefficients $D(He)_{Fe/SSi}$ of $1*10^{-2}$ at high pressures (~100 kbar) result from partitioning of noble gases (i.e., He) between solid silicates and liquid metal (Porcelli and Halliday, 2001). This value is expected to furthermore increase up to ~5 with lower pressures (5 kbar) when calculated with $D(He)_{Fe/SSi} = D(He)_{Fe/LSi}/D(He)_{SSi/LSi}$ and using a coefficient $D(He)_{SSi/LSi}$ for partitioning He between solid silicate and liquid silicate of $8*10^{-3}$ (Marty and Lussiez, 1993). Therefore, considering accretion of terrestrial building blocks that are sufficiently small to form in a low-pressure scenario, partitioning of light solar noble gases into liquid metal is feasible when SW-implanted He and/or Ne is present either in irradiated silicates or metal. Direct incorporation of SW-implanted light noble gases in irradiated metal grains into the core is not dependent on the pressure regime but would require accretion without gas losses or interactions with silicates, a process that seems not readily feasible.

Incorporation of noble gases into metal in low pressure scenarios were assessed in detail by Trieloff and Kunz (2005). Feasible concentrations of noble gases in metal in low pressure regimes were thereby derived from studies of iron meteorites as natural analogues. By referring to ^{20}Ne concentrations of up to 10^{-7} cm^3STP/g reported for Washington County by Becker and Pepin (1984), Trieloff and Kunz (2005) estimated that only ~0.25% of Earth's precursor metal, if resembling Washington County, is sufficient to cause concentrations of solar Ne in the core that satisfy observed OIB and MORB fluxes as calculated from global ^{3}He fluxes of 4 $atoms/cm^2/s$ over 4.6 Ga (Craig et al., 1975; Ozima and Podosek, 2002) and estimated mantle elemental ratios of $^{3}He/^{22}Ne$ ~3 (Trieloff et al., 2002). With the newly determined mean ^{20}Ne concentration in bulk WC_samples of $\sim 4*10^{-8}$ cm^3STP/g, the required amount of gas-rich precursor metal would increase to ~0.63%. In any case, metal could have carried sufficient light solar noble gases into the interior of Earth (Becker and Pepin, 1984) even if the solar wind irradiated only fractions of its protolith material and implanted solar gases into surfaces prior to accretion.

2.6 Conclusions

High resolution temperature release sequences on near-surface and interior samples of the Washington County iron meteorite were performed for the first time, proving the existence of volume correlated trapped primordial noble gases in this iron meteorite. Two prominent degassing peaks were observed that are assigned to schreibersite at lower extraction temperatures (~1100 °C) and kamacite-taenite at higer extraction temperatures (≳1400 °C). Analysis of an etch residue (WC_r) consisting of essentially pure schreibersite particles is further proof to the assignment of the low temperate release peak to this mineral. These sample release patterns thus reflect degassing of noble gas host phases which are the main mineralogical constituents of Washington County and confirm that noble gases are trapped in the interior of this iron meteorite.

The analyzed samples show (mostly) minor variations in noble gas concentrations but always contain ^{4}He excesses compared to GCR and Air. The He-Ne elemental and particularly Ne isotopic compositions allow conclusive identification of a distinct SW or Ne-B component present in all samples of Washington County. High temperature release steps of most samples also contain a significant air contribution most likely released from secondary alteration poducts. The argon isotopic ratios cannot be unambigiously interpreted as showing a solar wind contribution. The isotopic composition of krypton and xenon isotopes generally have uncertainties too large to draw further conclusions although cosmogenic contributions are seen in some of the Kr data.

The acquisition of the solar gases found in the interior of Washington County most probably happened in a low-pressure regime that favored noble gas partitioning from silicates into metal during metal-silicate separation. Even though occlusion of nebular gas cannot be excluded, the original derivation of solar noble gases is suitably explained by SW-implantation into surfaces of protolith material prior to accretion; a process which is conceivable for all other Solar System bodies including Earth. If less than 1% of Earth's precursor metal gained solar noble gases in abundance similar to that found for Washington County, the core would have incorporated sufficient solar Ne concentrations to satisfy observed MORB and OIB fluxes. With evidence for light solar noble gases in interior samples of Washington County, Earth's core gains more relevance as a potential source reservoir for He and Ne than previously supposed.

In addition, sporadically distributed silicate inclusions of up to 10 μm in diameter have been seen in Washington County for the first time and are identified as chromites and manganochromites. Their estimated abundance of 0.01‰ makes a significant contribution to the noble gas budget unlikely. Nevertheless, it remains to be shown in future studies if these minor spinel phases are possible carriers of solar noble gases in Washington County and other iron meteorites.

3 Acquisition of solar Ne during terrestrial accretion

3.1 Introduction

The atmosphere is regarded as the major terrestrial noble gas reservoir (Ozima and Podosek, 2002) and is assumed to have inherited its present-day noble gases from different sources involving mantle degassing, meteoritic additions and fractionation processes during Earth's history (Pepin, 1991; 2006; Zahnle, 1998; Ozima and Podosek, 2002; Marty, 2012; Halliday, 2013). Excesses of radiogenic ^{40}Ar and ^{129}Xe in the mantle when compared to the atmosphere hint to intense or even "catastrophic" degassing during the first 100–200 Ma after planet formation started in the Solar System (Staudacher and Allègre, 1982; Ozima and Podosek, 2002; Marty and Dauphas, 2002). The continuing decay of the radionuclides ^{40}K (decay to ^{40}Ar; $t_{1/2}$: 1.25 Ga) and ^{129}I (decay to ^{129}Xe; $t_{1/2}$: 15.7 Ma) in the solid Earth coupled with early degassing of their daughter isotopes then resulted in further enhancement of ^{40}Ar/^{36}Ar and ^{129}Xe/^{130}Xe ratios in the mantle. Outgassing is a still ongoing process and takes place at mid oceanic ridges, oceanic islands and other volcanoes, yet contributing only negligible amounts to the atmospheric noble gas reservoir, since at least the upper mantle reservoir is thought to have already been degassed between 85% and up to >99% (Staudacher and Allègre, 1982; Allègre et al., 1987; Ozima and Podosek, 2002).

Compared to the solar abundances the noble gases in the terrestrial atmosphere are depleted by several orders of magnitude, with the lightest noble gases (He, Ne) showing the strongest depletion (Fig. 3.1). The enrichment of heavy noble gases (Ar, Kr, Xe) on the terrestrial planets and in meteorites relative to the lighter ones and "solar" composition is termed "planetary" noble gas pattern (Signer and Suess, 1963; Pepin and Signer, 1965). For Earth and Mars, sharing similar abundance patterns for noble gases and Xe isotopes (Owen, 2008), the low Xe/Kr ratio compared to meteoritic gases has been identified as the yet unresolved "missing-Xe" paradox (Ozima and Podosek, 2002 and references therein).

The overall fractionated pattern of the terrestrial noble gases compared to the sun (Fig. 3.1) gave rise to several models for the origin and evolution of the atmosphere, either assuming that terrestrial accretion took place in the presence of a solar nebula or without ambient gas. Standard models were constructed implying hydrodynamic escape of a gravitationally captured primordial atmosphere with solar nebula composition and subsequent planetary degassing (Pepin and Porcelli, 2002; Pepin, 2006) or include volatile delivery by chondritic material with a planetary component (Marty and Dauphas, 2002; Marty, 2012).

While the noble gases in the terrestrial atmosphere must contain a component derived from mantle degassing, they must have been further modified. For example, ^{20}Ne/^{22}Ne ratios of mantle rocks (see for example Honda et al., 1991; Moreira et al., 1998; Trieloff et al., 2000; Ballentine et al., 2005; Moreira, 2013) indicate a "solar" composition (^{20}Ne/^{22}Ne ~12.7), indistinguishable from the SW-implanted Ne-B component in meteorites. This led Trieloff et al. (2000), Trieloff et al. (2002) and Trieloff and Kunz (2005) to suggest Ne-B as a "solar" mantle end-member that is sampled by all mantle derived MORB and OIB suites (Fig. 3.2). On the other hand, the atmosphere displays a clear "planetary" signature (^{20}Ne/^{22}Ne = 9.80±0.08; Eberhardt et al., 1965). This requires the addition of a "planetary" component, so that the compositions of Earth's atmosphere and

interior can be readily explained by simple mixing of various chondritic and solar components (Marty, 2012; Halliday, 2013).

The occurrence of supposably solar wind implanted gases in the interior of a large planet like the Earth requires irradiation and implantation at the stage of small bodies or particles, which have a high surface to volume ratio. Indeed, He and Ne isotopes in micrometeorites (MMs) and interplanetary dust particles (IDPs) are dominated by SW-implantation (Wieler, 2002b; Osawa, 2012). Moreover, even today's flux of extraterrestrial material to Earth is dominated by small MM-sized particles in the range of ~200 μm (Love and Brownlee, 1993; Cremonese et al., 2012). Hence, the Ne-B component in irradiated dust can be considered as a possibly significant source for the origin of the terrestrial noble gases. In this context it is important to note that MMs of a few 100 μm in size experience severe atmospheric entry heating and deliver much of their volatile inventory directly to the atmosphere, while smaller, tens of μm-sized IDPs are hardly degassed and generally richer in volatile elements (e.g., Engrand et al., 2005; Kehm et al., 2002; Osawa et al., 2010; Osawa, 2012, Stuart et al., 1999; Flynn et al., 2003; Marty et al., 2005). In addition, benefiting from their large surface/volume ratio, IDPs often carry high concentrations of surface correlated SW-noble gases (Nier and Schlutter, 1990, 1992, 1993; Pepin et al., 2000, 2001; Osawa, 2012) as was also suggested by the modeling work of Farley et al. (1997) for implanted solar wind He. Hence, they can deliver volatile elements to Earth's surface largely unaffected by atmospheric entry heating (Marty et al., 2005; Schwarz et al., 2005).

At the time before the formation of planetary embryos, when micron-sized dust with large surface/volume ratio was common in the young Solar System (Moreira and Charnoz, 2016), implanted SW-gases would have certainly governed the signatures of small volatile-rich material during accretion. The basic assumption of a major contribution of volatiles by MMs and IDPs as important carriers of these elements was noted earlier by Marty et al. (2005). The importance of large interplanetary dust particles (MMs) for the origin of volatiles on Earth and the formation of the atmosphere and oceans just after the last major impact that eroded any nascent gas phase was furthermore assessed by Maurette et al. (2000) and Maurette (2006). Their “early-micrometeorite-accretion” scenario (EMMAC) describes the origin of Ne, organics, CO_2, N_2 and H_2O with the early accretion of micrometeorites.

In the following model calculations, the feasibility of the implantation mechanism will be explored to provide solar-type noble gases to the Earth, in particular neon. The model calculations take into consideration a number of well constrained and accepted framework parameters for Earth’s evolution and are based on recent measurements of the Ne inventory of particles and their fluxes to Earth. Also taken into account is the existence of isotopic and elemental fractionation, i.e., more or less subtle differences between solar gas, solar wind and implanted solar wind (Wieler, 2002b; Heber et al., 2012). For the model, concentrations of solar neon in MMs and IDPs are assessed by compiling data available in the literature. To obtain data for other mass ranges the size dependent concentration of solar wind implanted neon for smaller particles is calculated and literature data are used for larger bodies. By combining different particle flux models, an annual particle flux model is then constructed for solid matter incident on Earth, ranging from 10^{-16}g–10^{25}g comprising β-meteorites, IDPs, micrometeorites, and larger particles and bodies. The size and mass dependent Ne concentrations as well as the annual mass flux allow for calculation of the

respective Ne flux to Earth. These fluxes are used as basic input parameters to model terrestrial Ne accretion. In the model, early delivery of solar wind type neon, degassing into a dense steam atmosphere, dissolution into an early magma ocean, protoatmosphere loss during the Moon-forming impact, and late addition of a planetary neon component will be considered.

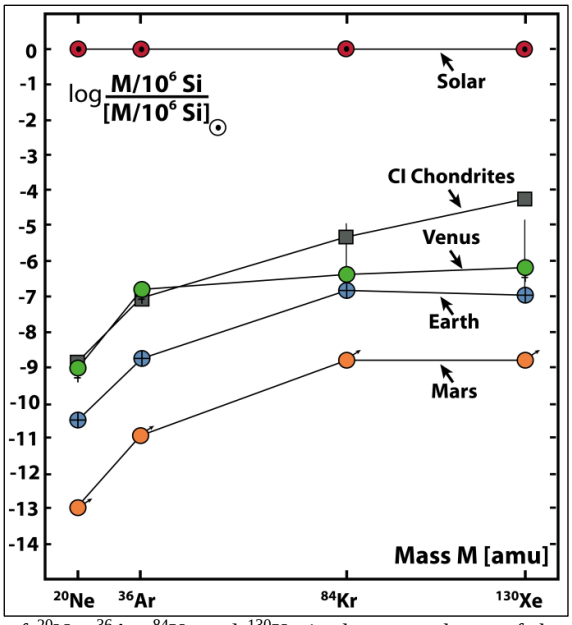

Fig. 3.1: Noble gas abundances of ^{20}Ne, ^{36}Ar, ^{84}Kr and ^{130}Xe in the atmospheres of the terrestrial planets (Venus, Earth, Mars) and in CI chondrites in comparison to the solar values. Units are atoms per 10^6 Si atoms (redrawn from Baecker, 2014; modified after Pepin (2006) and references therein).

3.2 Ne inventory of the Earth

The ^{20}Ne/^{22}Ne isotopic composition of Earth's atmosphere (ATM: 9.80±0.08, Eberhardt et al., 1965) is distinct from the mantle values (MORB and OIB: estimated as between 12.49±0.06 and 13.0±0.2, all given errors are 1σ, otherwise indicated, Trieloff et al., 2000; Yokochi and Marty, 2004). This allows for comparison with specific components found as the solar wind (SW: 13.777±0.010, Heber et al., 2012 or accordingly 14.001±0.042, Pepin et al., 2012), as fractionated solar wind (FSW: 11.2±0.2, Wieler, 2002b), Ne-B (~12.5–12.7, Black, 1972; Trieloff and Kunz, 2005; Moreira and Charnoz, 2016), in phase Q (10.4±0.3, Busemann et al., 2000) and with "planetary" Ne-A (8.2±0.4, Black and Pepin, 1969; Black, 1972). The latter is a common composition often present in primitive meteorites that do not contain solar wind-derived noble gases and constitutes a mixture of essentially Ne-HL, Ne-Q and Ne-E (Ott, 2014) (Fig. 3.2). The Ne isotopic composition therefore is essential to trace the origin of noble gases in the Earth's mantle and the mechanism of their incorporation.

As ^{20}Ne and ^{22}Ne in Earth´s mantle are considered as primordial and non-radiogenic, showing only insignificant nucleogenic contributions (Mukhopadhyay, 2012; Moreira, 2013), the ^{20}Ne/^{22}Ne ratio of MORB and OIB sources has not evolved over time and is thought to reflect a pristine mantle component with a solar-like end-member. This solar mantle signature was either acquired by dissolution of nebular gas into a magma ocean (Mizuno et al., 1980; Sasaki and

Nakazawa, 1990; Harper and Jacobsen, 1996; Porcelli et al., 2001; Marty 2012) with a $^{20}Ne/^{22}Ne$ ratio of 13.36±0.09 (Heber et al., 2012) or was derived from SW-irradiated planetary precursors containing the meteoritic Ne-B component (Trieloff et al., 2000, 2002; Trieloff, 2002, 2007; Ballentine et al., 2005; Jaupart et al., 2017; Péron et al., 2017, 2018) having $^{20}Ne/^{22}Ne_{Ne\text{-}B}$ = 12.7±0.1 (Moreira and Charnoz, 2016). Earth's atmosphere, on the other hand, displays a "planetary"-like pattern (Fig. 3.2a). Overall, the difference in Ne isotopic ratios observed between Earth's mantle and the atmosphere can be readily explained by mixing the various chondritic and solar components in different proportions (Marty, 2012; Halliday, 2013). In contrast to ^{20}Ne and ^{22}Ne, ^{21}Ne is produced in the mantle in significant amounts through the nuclear reactions $^{18}O(\alpha,n)^{21}Ne$ and $^{24}Mg(n,\alpha)^{21}Ne$ (Yatsevich and Honda, 1997; Leya and Wieler, 1999; Moreira, 2013). The (relative) ^{21}Ne excess in the MORB source is significantly higher than in the OIB mantle since the upper mantle is assumed to be more extensively degassed from the primordial components. Among OIBs, originating from the lower mantle, the Galápagos (Fernandina) samples are derived from the most primitive (non-nucleogenic) source region compared to Iceland and Hawaii (Loihi) (Fig. 3.2a).

A major issue in determining the pristine $^{20}Ne/^{22}Ne$ ratio of Earth's mantle is contamination with an atmospheric component (e.g., Moreira, 2013; Colin et al., 2015) and, furthermore, the upper MORB mantle might, to some extent, be sensitive to noble gas recycling via subduction (e.g., Kendrick et al., 2011; Jackson et al., 2013). This process, however, is thought to be insignificant in case of Ne (e.g., Staudacher and Allègre, 1988; Holland and Ballentine, 2006; Schwarz et al., 2005). MORB derived samples show maximum $^{20}Ne/^{22}Ne$ values of 12.76±0.18 (2πD43 "popping rock", Moreira et al., 1998), but otherwise show values between air and 12.5 (Moreira et al., 1998; Raquin and Moreira, 2009; Moreira, 2013). Values of the lower mantle reservoirs that likely represent direct measurements of the pristine component derive from samples of Loihi dunites, Icelandic volcanic glasses and the most primitive Galápagos volcanic glasses and exhibit maximum $^{20}Ne/^{22}Ne$ ratios of between 12.57±0.06 to 13.10±0.35 (Valbracht et al., 1997; Trieloff et al., 2000), 12.73±0.04 to 12.88±0.06 (Trieloff et al., 2000; Mukhopadhyay, 2012; Colin et al., 2015) and 12.43±0.07 to 12.91±0.07 (Raquin and Moreira, 2009; Kurz et al., 2009; Péron et al., 2016), respectively. Vesicles of submarine glass samples from one Galápagos volcano furthermore indicate a lower mantle source isotopic ratio between 12.65±0.04 (Péron et al., 2017) and 12.87±0.20 (Péron et al., 2016). Values up to 13.0 were found for samples from the Kola Peninsula by Yokochi and Marty (2004), but with large errors of ±0.4 (2σ). Overall, therefore, a value between ≳12.5 and ~12.9 is considered to be a reasonable range for the $^{20}Ne/^{22}Ne$ ratio of the solar-like mantle end-member sampled by all MORB and OIB suites. A value of 12.7±0.2 appears a good compromise for the pristine mantle.

Measured mantle $^{20}Ne/^{22}Ne$ ratios unaffected by atmospheric contamination are thus close to the Ne-B ratio. Furthermore, the Ne-B ratio was found by Trieloff et al. (2000) to be indistinguishable from Earth's mantle end-member and was therefore suggested by Trieloff et al. (2000, 2002) and Trieloff and Kunz (2005) to represent the pristine mantle component. Ne-B itself was identified as its own "component" (i.e., characteristic composition) reflecting the implantation of SW ions in irradiated surfaces (Trieloff et al., 2002; Moreira, 2013) coupled with "space-erosion" (sputtering) effects (Raquin and Moreira, 2009; Moreira and Charnoz, 2016). The solar wind has a

$^{20}Ne/^{22}Ne$ ratio of ~13.8, but ^{22}Ne has a higher energy than ^{20}Ne and is more deeply implanted. Hence, deeper surface layers are enriched in ^{22}Ne resulting in the FSW composition of $^{20}Ne/^{22}Ne$ of ~11.2 (Wieler, 2002b). To explain the origin and composition of Ne-B, a steady state implantation and sputtering model was developed by Raquin and Moreira (2009) and was extended by Moreira (2013) and Moreira and Charnoz (2016). In this model the attained value depends basically on the grain size and irradiation time at a given distance from the sun. It is the result of deeper implantation of the heavier isotope in combination with sputtering and removal of the superficial particle layer that is enriched in the lighter isotope. This leads to a residue that becomes continually enriched in the heavy isotope until a steady state ratio is achieved. Depending on the solar wind $^{20}Ne/^{22}Ne$ ratio used in this model, either 13.777±0.010 (Heber et al., 2012) or 14.001±0.042 (Pepin et al., 2012), the steady state value for Ne-B is 12.53 or 12.73, respectively. If the steady state value is not reached because the irradiation time is too short, the resulting $^{20}Ne/^{22}Ne$ ratio is higher than the steady state ratio (e.g., ~12.9) (Moreira and Charnoz, 2016). Within uncertainties, the Ne-B value of 12.7±0.1 favored by Moreira and Charnoz (2016) is compatible with the old value for Ne-B given by Black (1972) of 12.52±0.18.

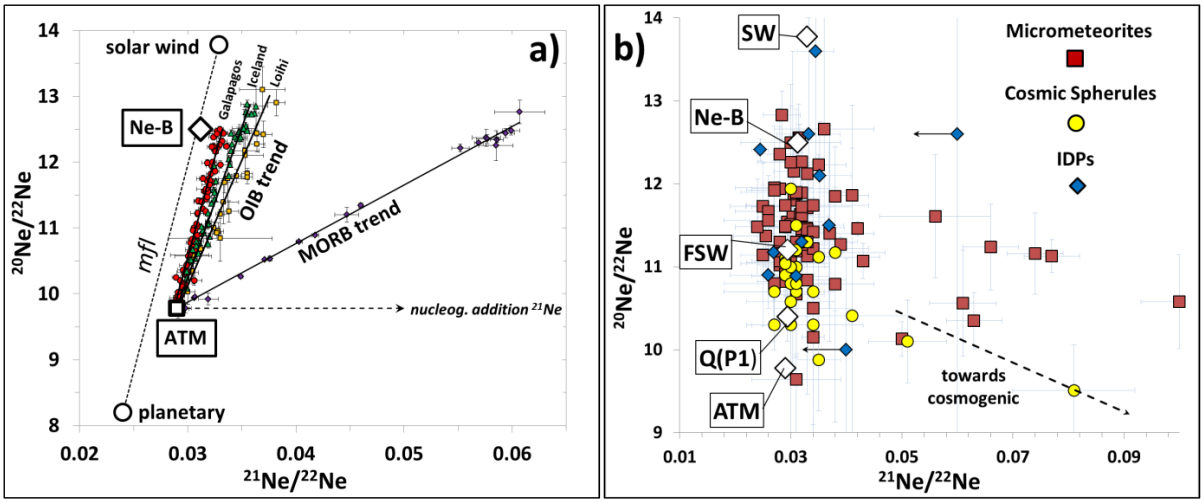

Fig. 3.2: a) Neon three-isotope-plot showing the solar wind composition (Heber et al., 2012), Ne-B (modified by Trieloff and Kunz, 2005 after the original Ne-B $^{21}Ne/^{22}Ne$ value of 0.0335 given by Black, 1972) and planetary Ne-A on a mass fractionation line (mfl). Mass dependent isotopic fractionation from solar Ne was likely responsible for the origin of Ne-B. The atmospheric value (ATM, Eberhardt et al., 1965) is shifted to higher $^{21}Ne/^{22}Ne$ values because of nucleogenic ^{21}Ne additions. The OIB source for Galápagos (Fernandina) samples (Kurz et al., 2009; Raquin and Moreira, 2009) contains the most unradiogenic Ne isotopic ratios compared to the Icelandic samples (Trieloff et al., 2000; Mukhopadhyay, 2012; Colin et al., 2015) and Loihi samples (Valbracht et al., 1997). The most radiogenic samples are derived from the MORB (2∏D43 "popping rock") source (Moreira et al., 1998; Raquin and Moreira, 2009). Both, OIB and MORB trend, suggest a solar-like $^{20}Ne/^{22}Ne$ mantle end member while the MORB source displays higher $^{21}Ne/^{22}Ne$ values compared to the OIB source because of nucleogenic ^{21}Ne additions combined with a higher degree of degassing of the MORB mantle. **b)** Neon three-isotope-plot showing Ne data (errors <30% for $^{21}Ne/^{22}Ne$ except two upper limits) for IDPs (data from Nier and Schlutter, 1990; Pepin et al., 2000), micrometeorites (MMs) and cosmic spherules (CSs) (data from Osawa et al., 2000, 2003a, 2003b, 2010; Osawa and Nagao, 2002a, 2002b; Marty et al., 2005; Bajo et al., 2011; Baecker, 2014; Okazaki et al., 2015) as well as the composition for SW (Heber et al., 2012), Ne-B (Trieloff and Kunz, 2005), fractionated solar wind (FSW, Wieler, 2002b), phase Q (Busemann et al., 2000) and the atmospheric value (ATM, Eberhardt et al., 1965). Within uncertainties (1σ) most MMs, CSs and IDPs cluster around FSW and plot between Ne-B and the atmospheric composition which is probably due to variable degrees of air contamination during atmospheric entry. The atmospheric component is prevailing in the completely melted cosmic spherules as consequence of severe heating during atmospheric entry. Some data points plot towards higher $^{21}Ne/^{22}Ne$ ratios which is because of exposure to cosmic rays ($^{20}Ne/^{22}Ne$ <1; $^{21}Ne/^{22}Ne$ ≈0.5–1).

The nature of Ne-B as the dominant type of surface correlated implanted Ne in extraterrestrial solid matter moreover indicates that solar-like mantle Ne could have been supplied

by SW-irradiated materials during early accretionary stages before the formation of Earth was terminated (Podosek et al., 2000; Trieloff et al., 2000, 2002). As soon as the solar nebula was dissipated after about ~6 Ma (Haisch et al., 2001) or some tens of millions of years (Pfalzner et al., 2014), the solar wind was able to irradiate the surfaces of solids (Trieloff et al., 2002; Trieloff, 2007). During terrestrial accretion the implanted Ne-B may then have been delivered to Earth, mainly by small particles and grains with large surface/volume ratio since the protoplanetary disk was dust-rich (Moreira and Charnoz, 2016).

3.3 Flux of mass and Ne to Earth

In a model for terrestrial Ne accretion it is necessary to estimate the total amount of Ne that has been delivered to Earth. As a first step, the total amount of carrier material that *presently* impacts the upper atmosphere (e.g., solid matter of all masses and sizes incident on Earth) has therefore to be evaluated. Considering an annual particle flux to Earth over a range of 10^{-16}–10^{25} g in combination with the respective Ne concentrations of each carrier type, the annual amount of Ne that is delivered to Earth can be calculated. These Ne carriers are divided from small to large into six groups: β-meteorites (10^{-16}–10^{-10} g), IDPs (10^{-10}–10^{-7} g), MMs (10^{-7}–10^{-3} g), large particles (10^{-3}–10^{2} g), large bodies (10^{2}–10^{15} g) and very large bodies (>10^{15} g) (see section 3.3.3), each one distinct in its Ne isotopic composition as well as in its Ne concentration (see APPENDIX B, Tab. B1). To assess the amount of Ne delivered by all types of carriers *early* in Earth's history, this flux is scaled back in time for early mass fluxes during terrestrial accretion in order to deduce the *early* Ne delivery to Earth. It is hereby tacitly assumed that the size distribution, i.e., the relative contributions from larger bodies and small particles are similar, because small particles are the collisional outcome of the large body population. It is also assumed that the dynamics delivering small particles to Earth (e.g., Poynting-Robertson effect) and large bodies to Earth crossing orbits (gravitational perturbations by giant planets) were similar throughout Solar System history.

3.3.1 Ne-inventory of particle types

Cosmic dust consisting of MMs in the size range of 50–500 μm currently dominates the extraterrestrial mass flux to Earth with a major peak at ~200 μm (Love and Brownlee, 1993; Engrand et al., 2005; Marty et al., 2005; Cremonese et al., 2012). In addition, most small particles preserve SW-implanted He, Ne, and Ar (Osawa, 2012). A compilation of available Ne measurements of both particle types (MMs and IDPs) will therefore yield a reasonable estimate of the present Ne flux to Earth. The Ne concentrations of even smaller sized particles (β-meteorites) can be readily deduced by simple geometric downscaling of the size-correlated particle surface assuming a SW-saturated outermost layer given by the Ne concentration of the smallest measured IDPs (see section 3.3.2). Bulk Ne measurements of carbonaceous chondrites and their primordial components (Mazor et al., 1970) serve as the basis to estimate the inventory of large-sized Ne carriers (large particles, large bodies and very large bodies).

3.3.2 $^{20}Ne/^{22}Ne$ ratio and ^{20}Ne concentration of particle types

Only materials with large surface/volume ratio are able to incorporate large concentrations of SW-implanted Ne-B and are thus efficient to distribute the Ne-B component (Moreira, 2013; Moreira and Charnoz, 2016). Implanted solar wind comprises the major fraction of helium and neon in IDPs and MMs (Pepin et al., 2001; Wieler, 2002b) and in particular Ne in IDPs is dominated by surface correlated SW-implanted Ne (Kehm et al., 1998). In recognition of their significance available data for the $^{20}Ne/^{22}Ne$ ratios and ^{20}Ne concentrations were therefore compileded (Fig. 3.3) for IDPs (Nier and Schlutter, 1990; Pepin et al., 2000; Kehm et al., 2006) and MMs (Osawa et al., 2000, 2003a, 2003b, 2010; Osawa and Nagao, 2002a, 2002b; Bajo et al., 2011; Baecker, 2014; Okazaki et al., 2015). Additional data for the ^{20}Ne concentrations only of IDPs were published by Pepin et al. (2001) and Kehm et al. (2002).

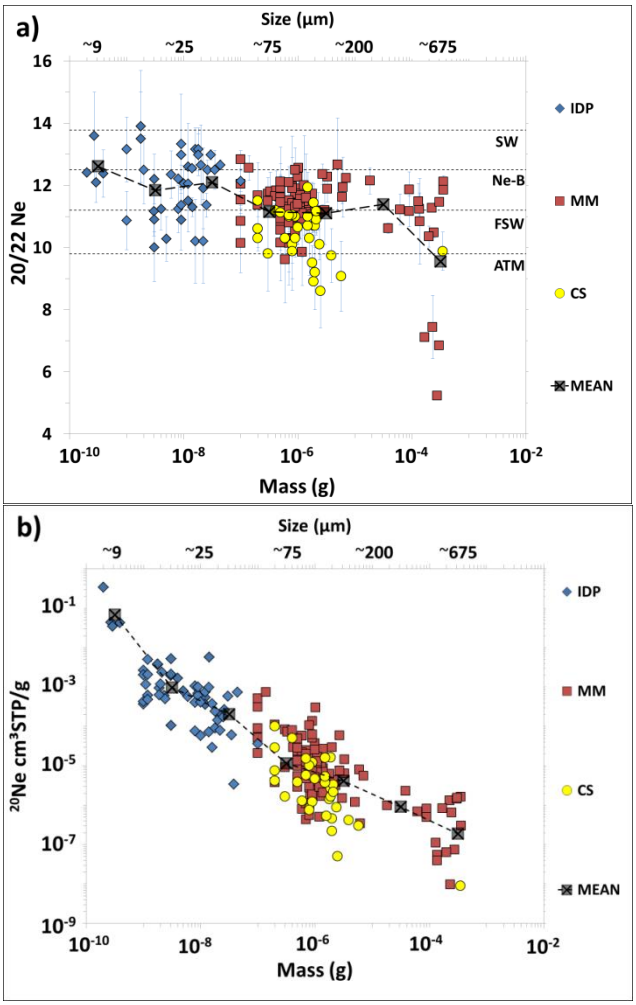

Fig. 3.3: Ne isotopic data for measurements of IDPs, MMs and CSs. The mass range from $1*10^{-10}$ g–$1*10^{-3}$ g is divided into decadal mass bins (gray squares) which allow calculating the mean geometric value for all data within each bin. Only values with uncertainties <15% for the $^{20}Ne/^{22}Ne$ ratio are shown. **a)** $^{20}Ne/^{22}Ne$ ratios of particles are plotted against their mass in g and size in µm. Data for IDPs are from Nier and Schlutter (1990), Pepin et al. (2000) and Kehm et al. (2006). Data for MMs and CSs are from Osawa et al. (2000, 2003a, 2003b, 2010), Osawa and Nagao (2002a, 2002b), Bajo et al. (2011), Baecker (2014) and Okazaki et al. (2015). For comparison, $^{20}Ne/^{22}Ne$ of SW (13.777, Heber et al., 2012), Ne-B (12.5, Trieloff and Kunz, 2005) and FSW (11.2, Wieler, 2002b) are shown. **b)** ^{20}Ne concentrations of particles are plotted against the mass in g and size in µm. Data for IDPs are from Nier and Schlutter (1990), Pepin et al. (2000, 2001) and Kehm et al. (2002). Data for MMs and CSs are from Osawa et al. (2000, 2003a, 2003b, 2010), Osawa and Nagao (2002a, 2002b), Bajo et al. (2011), Baecker (2014) and Okazaki et al. (2015). Both plots display progressively lower $^{20}Ne/^{22}Ne$ ratios and ^{20}Ne concentrations with progressively larger particle masses and sizes.

In Figure 3.3, available data for the $^{20}Ne/^{22}Ne$ ratio (Fig. 3.3a) and ^{20}Ne concentration (Fig. 3.3b) in IDPs, MMs and cosmic spherules (CSs: MMs that completely melted due to atmospheric entry heating) are plotted against the particle mass. The particle masses are divided into decadal mass bins ranging from 10^{-10} g to 10^{-9} g at the low end up to 10^{-4} g to 10^{-3} g at the upper end. IDPs occupy the range 10^{-10} g to 10^{-7} g, whereas MMs and CSs plot in the range 10^{-7} g to 10^{-3} g. For each mass bin the geometric mean $^{20}Ne/^{22}Ne$ ratio and the geometric mean ^{20}Ne concentration was calculated. As noted by Osawa et al. (2003b) and Osawa et al. (2010), the noble gas concentrations in cosmic dust are not distributed normally, but log-normally, so the geometric mean is more appropriate than the arithmetic mean. Only data for complete particles were used. Values from individual fragments of initially larger particles were omitted to avoid misinterpretation. However, if all fragments of an initially larger particle were measured, e.g., by Baecker (2014), the Ne isotopic composition and the Ne amount were calculated by adding the fragments according to their mass. Furthermore, data below detection limits were also excluded from the compilation, so the mean ^{20}Ne concentrations should be considered as upper limits.

It is obvious from Figure 3.3 that, with progressively lower particle masses, IDPs and MMs display progressively higher $^{20}Ne/^{22}Ne$ ratios and ^{20}Ne concentrations, with a maximum mean $^{20}Ne/^{22}Ne$ ratio of 12.61±0.41 and a highest mean ^{20}Ne concentration of $6.92*10^{-2}$ cm^3STP/g in the smallest IDPs. Even though compiled from a limited number of data, these highest values are regarded as representative for the maximum Ne inventory in small particles that are unaffected by atmospheric entry heating (Nier and Schlutter, 1990, 1992; Love and Brownlee, 1991). The smaller $^{20}Ne/^{22}Ne$ values in larger particles may be caused by heating and/or ablation of the outer particle layer during atmospheric entry in combination with evaporative loss of surface sited solar wind noble gases. Such losses would preferably affect the shallowly implanted solar wind neon (with higher $^{20}Ne/^{22}Ne$ ratio), so that the more deeply implanted FSW neon with $^{20}Ne/^{22}Ne$ of about 11.2 would become dominant. $^{20}Ne/^{22}Ne$ ratios lower than 11.2 may be caused by the admixture of a volume correlated component, e.g., Ne-A, that will gain in importance relative to the implanted Ne-B component as the surface to volume ratio decreases with increasing particle size. However, a more likely explanation for most of the data is probably uptake of atmospheric neon, as, in particular completely melted cosmic spherules – which should have also lost the Ne-A component and are frequently associated with atmospheric argon - display roughly atmospheric neon compositions (Fig. 3.3a).

Most $^{20}Ne/^{22}Ne$ data for IDPs and MMs plot, within errors (1σ), between SW and FSW and the mean values for MMs in the mass bins between 10^{-7} and 10^{-4} g of 11.14; 11.10 and 11.39, respectively, are all very close to FSW ($^{20}Ne/^{22}Ne_{FSW}$: 11.2). The mean values for the IDPs in the bins between 10^{-9} and 10^{-7}g are 11.84 and 12.10, respectively, and plot above FSW, while the mean for the bin with the lightest IDPs (10^{-10}–10^{-9} g) has the highest mean $^{20}Ne/^{22}Ne$ ratio of 12.61±0.41, which is compatible with Ne-B. The bin containing the heaviest MMs (10^{-4}–10^{-3} g) contains the MMs with the lowest $^{20}Ne/^{22}Ne$ ratios and has a mean $^{20}Ne/^{22}Ne$ value of 9.55. Probably due to air contamination and isotopic fractionation during atmospheric entry virtually all CSs plot below FSW, exhibiting substantially lower $^{20}Ne/^{22}Ne$ ratios compared to unmelted MMs.

For the ^{20}Ne concentration the mean values for the mass bins show a progressive increase from the heaviest MM-particles containing the lowest concentrations ($1.89*10^{-7}$ cm^3STP/g for the

mass bin 10^{-4} to 10^{-3} g) towards the lightest IDP-particles (mean $6.92*10^{-2}$ cm³STP/g for the mass bin 10^{-10} to 10^{-9} g) (Fig. 3.3b). The concentration in the smallest particles with a mean diameter of ~9 µm is almost an order of magnitude higher than the concentration of $3.25*10^{-3}$ cm³STP/g in similar bulk grain size fractions of 15 µm in lunar fines (Eberhardt et al., 1970). In fact, this grain size fraction in lunar fines is associated with the same $^{20}Ne/^{22}Ne$ ratio of 12.61±0.2 as found in the compiled smallest IDP data. The maximum ^{20}Ne concentration measured in the smallest lunar samples with 1.4 µm is determined as $1.24*10^{-2}$ cm³STP/g with an isotopic ratio of $^{20}Ne/^{22}Ne$=12.83±0.15 which is in good agreement with the maximum IDP values. The ^{20}Ne concentration of larger SW irradiated lunar ilmenites amounts to ~10^{-3} cm³STP/g for ~50 µm grain sizes and to ~$5*10^{-4}$ cm³STP/g for >100 µm grain sizes (Eberhardt et al., 1970; Benkert et al., 1993). These values are more than an order of magnitude higher than the compiled data for particles of similar size, but it has to be kept in mind that the measured MMs and IDPs have experienced atmospheric ablation losses and consequently contain lower amounts of SW-implanted noble gases. Therefore, the highest measured ^{20}Ne concentration in IDPs is considered as a good compromise to represent saturation of SW-implanted Ne after sputtering (cf. Moreira and Charnoz, 2016) in the outermost particle layer. The typical penetration depth of SW-He with an average solar wind ion speed of 400 km/s (equivalent to an energy of about 1 keV/nucleon) is 40 nm (Heber et al., 2009; Okazaki et al., 2015). The maximum depth of about 500 nm can be reached by ^{132}Xe ions that are implanted with 1200 km/s (a velocity that is, however, rarely observed for the solar wind, Heber et al., 2009). According to Grimberg et al. (2006) SW noble gas ions with 300–800 km/s are implanted into the surface of dust grains up to a depth of ~200 nm. For the average penetration depth of SW-Ne coupled with sputtering a value of ~50 nm is assumed for the model calculations, which is also what was used by Maurette (2006) for the implantation depth of SW-Ne with an energy of typically ~1 keV/amu.

To determine the ^{20}Ne concentration in spherically shaped smaller particles (e.g., β-meteorites with an assumed density of 1.5 g/cm³, cf. Pepin et al. 2000, 2001; Kehm et al., 2002), it is assumed that the particles have a SW-Ne saturated spherical outer particle shell of 50 nm thickness with the same $^{20}Ne/^{22}Ne$ ratio of 12.61±0.41 as the smallest measured IDPs. With a mean concentration in the lightest IDP particles of $6.92*10^{-2}$ cm³STP/g, the ^{20}Ne concentration in this shell is 1.73 cm³STP/g (APPENDIX B1) if it is assumed that the entire implanted Ne inventory resides therein and represents pure implanted SW. Such a concentration might seem astonishing but no analog exists for the concentration of pure implanted solar wind Ne in nm-scale volumes. With the geometric downscaling of the ^{20}Ne concentration (Tab. B2) for a particle with a weight of 10^{-16} g to 10^{-15} g (~74 nm in diameter) such a shell comprises the whole particle, therefore the lightest mass bin that are going to be included in the model described below is in this range. Here, it should be noted that a 74 nm particle might generally not comprise the solar wind saturated 50 nm shell of a previously irradiated particle because the implantation/sputtering model (Moreira and Charnoz, 2016) implies 150–250 nm sputtering before the steady state Ne-B value is obtained.

A model particle in the 10^{-16} to 10^{-15} g bin would have the highest possible ^{20}Ne concentration of 1.73 cm³STP/g. The smallest IDPs and β-meteorites may carry almost exclusively the Ne-B component with $^{20}Ne/^{22}Ne$=12.61±0.41, which is nominally higher but consistent within errors to the canonical Ne-B value of 12.52±0.18 from Black (1972). In the model, the $^{20}Ne/^{22}Ne$

ratio of 12.61±0.41 is the value of SW irradiated cosmic dust that transfers the implanted Ne-B component into Earth's interior. The ^{20}Ne concentration of large particles, large bodies and very large bodies is assumed to depend on the carrier type. It should be noted, however, that $^{20}Ne/^{22}Ne$ ratios of individual meteorite measurements indicate that meteoritic neon is a mixture of planetary Ne-A and solar wind implanted Ne-B, the latter probably acquired during regolith irradiation before meteorites were separated from their parent body. In this way the meteorite population may oversample surface sited regolith breccias, while large asteroids are likely to preserve a purer Ne-A component. Hence, for large impacting bodies from the asteroid belt or beyond, at first order approximation it is assumed that these bodies all contain the "planetary" Ne-A component of primitive meteorites with a $^{20}Ne/^{22}Ne$ ratio of 8.2 (Black and Pepin, 1969; Black, 1972), but in the model calculations a wider range is permitted (see section 3.4.4). Taking Ne-A and Ne-B as endmembers, the primordial Ne budget of gas rich carbonaceous chondrites given by Mazor et al. (1970) allows for estimation of the respective portion of both components that is present in large-sized matter. Mean values of bulk measurements indicate that a primordial $^{20}Ne/^{22}Ne$ ratio of 8.90 is associated with CI chondrites, in which therefore 22.5% of ^{20}Ne belongs to the Ne-B endmember ($^{20}Ne/^{22}Ne$=12.61) and 77.5% to the Ne-A endmember ($^{20}Ne/^{22}Ne$=8.2). This results in a mean ^{20}Ne concentration of $2.57*10^{-7}$ cm³STP/g for the pure primordial Ne-A component in CI chondrites which is used as value for the planetary Ne-A component in the model calculations below. It should be noted that the mean primordial $^{20}Ne/^{22}Ne$ ratio of 10.76 associated with CM chondrites implies a lower mean ^{20}Ne concentration of $2.23*10^{-7}$ cm³STP/g for the pure Ne-A in CI-CM chondrites. This, however, would not significantly change the calculated model results.

3.3.3 Particle flux to Earth

As mentioned above, MMs are dominating the present mass flux to Earth. The most cited value of 40,000±20,000 tons/year incident on Earth has been determined for particles in the mass range of 10^{-9}–10^{-4} g and shows a peak at a size of 220 µm (~10^{-5} g). This has been derived from the examination of hypervelocity impact craters on the Long Duration Exposure Facility (LDEF) which measured the extraterrestrial particle flux in low Earth orbit (Love and Brownlee, 1993). Compared to this, a more recent re-calibration of the LDEF data (Cremonese et al., 2012) yields a lower mass accretion rate of 7400 tons/year, if the source of the dust is asteroidal and 4200 tons/year if cometary (Fig. 3.4a).

Estimates by other methods for the terrestrial accretion rate also vary significantly depending on the sampling area and study method. Accretion rates evaluated from Antarctic MMs range from 2700±1400 tons/year about 500–900 years ago (Taylor et al., 1998, 2007) up to between 11000±6600 and 16,000±9100 tons/year 27–33 kyr ago (Yada et al., 2004). A MM flux reaching Earth's surface of ~20,000 tons/year has been reported by Engrand and Maurette (1998) based on direct particle counts in the Greenland and Antarctic ice sheets and fluxes of 30,000±15,000 tons/year to the sea floor were estimated in a study of deep-sea sediments and marine osmium by Peucker-Ehrenbrink and Ravizza (2000). Comprehensive overviews of various flux estimates are provided by Peucker-Ehrenbrink (1996) and Karner et al. (2003).

Constraints on present fluxes of extraterrestrial matter to Earth can be used to construct an annual mass flux model (Fig. 3.5). As this model shall be used to scale present fluxes to early accretionary times, it has to include the complete range of masses that contribute, contributed and potentially contributed to the material influx during Earth's history. For example, objects with sizes of the largest known asteroid Ceres could have potentially contributed during early Earth's history. Compared to the LDEF-based studies, the flux models provided by Grün et al. (1985) and Anders (1989) include data for lower and higher masses down to 10^{-18} g and up to 10^{18} g, respectively (Fig. 3.4a, b). In the flux model masses from 10^{-18}–10^{-16} g are neglected because the contribution in this range is considered to be insignificant.

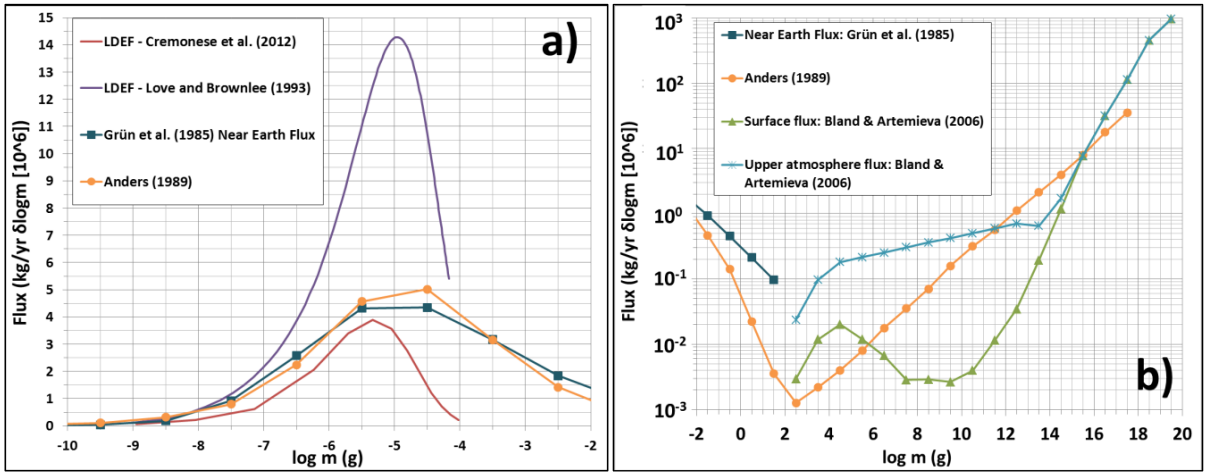

Fig. 3.4: a) Annual mass flux to Earth in kg/year δ(log m) versus mass in logarithmic units. Only the lower mass range from 10^{-10} to 10^{-2} g is shown. The different flux models are from Love and Brownlee (1993) (violet), Cremonese et al. (2012) (red), both, based on LDEF-data, from Grün et al. (1985) (green) based on space observation, and from Anders (1989) (yellow) based on meteor and crater observations. A factor of 2 was superimposed onto the interplanetary flux model from Grün et al. (1985) to correct for gravitational focusing by the Earth. **b)** Annual mass flux to Earth in kg/year δ(log m) versus mass in logarithmic units. The higher mass range from 10^{-2} to 10^{20} g is shown. The different flux models are from Grün et al. (1985) (green) and Anders (1989) (yellow) as in Figure 3.4a, and from Bland and Artemieva (2006). As for the latter, relying on a compilation of flux rates at the upper atmosphere and on a model for the impact rate at the surface, data for the impactor flux on the upper atmosphere (blue) as well as on Earth's surface (light green) are provided.

For particles in the mass range from 10^{-16} to 10^{-3} g, the interplanetary dust flux model from Grün et al. (1985) is a good compromise between the different LDEF based estimates and consistent with the Anders (1989) model (Fig. 3.4a). Gravitational focusing by the Earth was included by scaling the given flux values with a factor of two. As pointed out by Mann et al. (2011), the validity of this interplanetary dust flux model at 1 AU is confirmed by more recent Ulysses- and Stereo-Spacecraft as well as ISS impact crater measurements. The absolute flux magnitude that peaks around 10^6 kg/year for small mass intervals is consistent with data from Hughes (1978) and Lal and Jull (2002). For the mass range from 10^{-3} to 10^2 g the global mass influx data from Anders (1989) were used which are based on meteor observations and impact crater statistics (Fig. 3.4a, b). Bland and Artemieva (2006) provide information for flux estimates to the atmosphere and to Earth's surface for masses from 10^2 to 10^{20} g (Fig. 3.4b). Based on a comparison of their flux data for impactors in the range of 10^{15} to 10^{20} g with the asteroid main belt distribution of the same sizes (Bottke et al., 2005) the mass fluxes for the 10^{20} to 10^{25} g bins were extrapolated (Fig. 3.5). According to this model, the total average mass flux to Earth amounts to

about $2.7*10^{10}$ kg/year delivered by all particle types to Earth's upper atmosphere. This is of the order of $4.5*10^{-15}$ of the total mass of the Earth of $5.97*10^{24}$ kg (Tab. B1).

Other assessments of the total combined annual mass flux in the range of 10^{-18}–10^{18} g are provided by Ceplecha et al. (1998) and Drolshagen et al. (2017). By also using the interplanetary flux model of Grün et al. (1985), the former study obtains an annual flux model comparable in size distribution and flux magnitude to the compiled model. The latter, however, results in an almost one order lower flux to Earth because the differential fluxes were calculated with the choice of 0.001 decades which numerically lowered the magnitude for each mass bin.

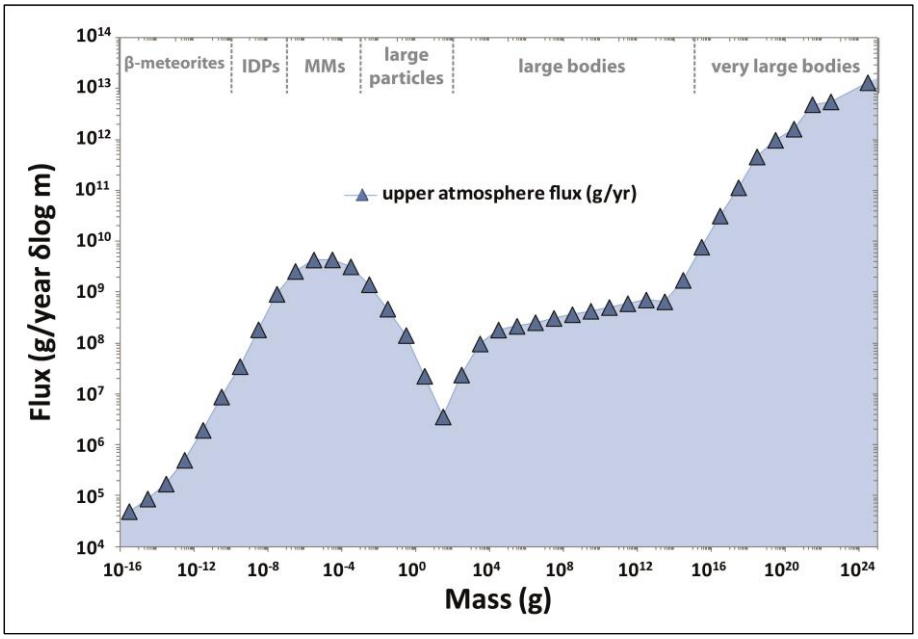

Fig. 3.5: Annual particle flux to Earth's upper atmosphere g/year vs. mass. The mass of the different particle types ranges from 10^{-16}–10^{25}g (β-meteorites, IDP, MM, large particles, large bodies, very large bodies) and is divided in decadal mass bins.

3.3.4 Ne flux to Earth

Based on the compilation of Ne-data (section 3.3.2) in combination with the extraterrestrial material flux to Earth (section 3.3.3), the size and mass dependent Ne flux to Earth is calculated. For this purpose, the subdivision in decadal mass bins is essential to assign a particular particle mass range to its corresponding Ne inventory. The results shown in Figures 3.6 and 3.7 serve then as input parameters for the calculation of terrestrial Ne acquisition during accretionary processes. Assuming a steam-atmosphere induced magma ocean on early Earth, all incoming material, regardless of size, will release neon to the dense hot atmosphere, and incorporation into the solid Earth is only possible via dissolution into the magma ocean. Therefore, only the upper atmosphere fluxes, i.e., before atmospheric entry losses, need to be considered (section 3.5) and the actual flux at the surface as shown in Figure 3.6 does not affect the model including a magma ocean. A scenario without a magma ocean, and instead direct incorporation of irradiated material into the growing planet, depends on details of atmospheric ablation processes and evaporation during atmospheric entry and will be discussed in section 3.6.

3.3.5 Mass and size dependent Ne flux to Earth

To compute a neon influx model from annual mass-flux data the compilation of ^{20}Ne concentrations of different particle types is used. Multiplying the annual particle flux in g/year of each decadal mass bin with the respective (average) ^{20}Ne concentration in cm³STP/g yields the annual ^{20}Ne flux in cm³STP/year to Earth (Figs. 3.6, 3.7). The compiled MM and IDP data (Fig. 3.3) thereby represent the flux to Earth's surface. The flux of Ne to the upper atmosphere for all particles, on the other hand, is inferred from the amount of surface-correlated Ne-B found within the smallest IDPs in the compilation, i.e., such that escaped severe losses during atmospheric entry heating (see below and APPENDIX B2, Tab. B3, Tab. B4). The Ne flux to the surface from MMs and IDPs (Fig. 3.6), in contrast, is influenced by atmospheric entry degassing: the smaller particles deliver their complete neon to Earth´s surface, while larger particles are more strongly decelerated and heated, resulting in substantial gas loss to the atmosphere. The ^{20}Ne influx to the upper atmosphere (i.e., before any losses; Fig. 3.6) peaks at the 10^{-7} to 10^{-6} g MM bin (mean diameter ~75 µm) which amounts to $2.14*10^{7}$ cm³STP/year ^{20}Ne. This flux follows the same trend as the mass influx (Fig. 3.5), but is shifted to lower particle sizes because of their higher surface to volume ratio and accordingly higher Ne-B contents. For the contribution from small particles to the surface, on the other hand, there is a maximum contribution from the 10^{-10} to 10^{-9} g IDP bin (mean diameter ~9 µm) which amounts to $2.39*10^{6}$ cm³STP ^{20}Ne (Fig. 3.6). This size is in very good agreement with the diameter value ~7 µm for particles that, according to Farley et al. (1997), carry most of the surface-correlated (hence, SW-implanted) He.

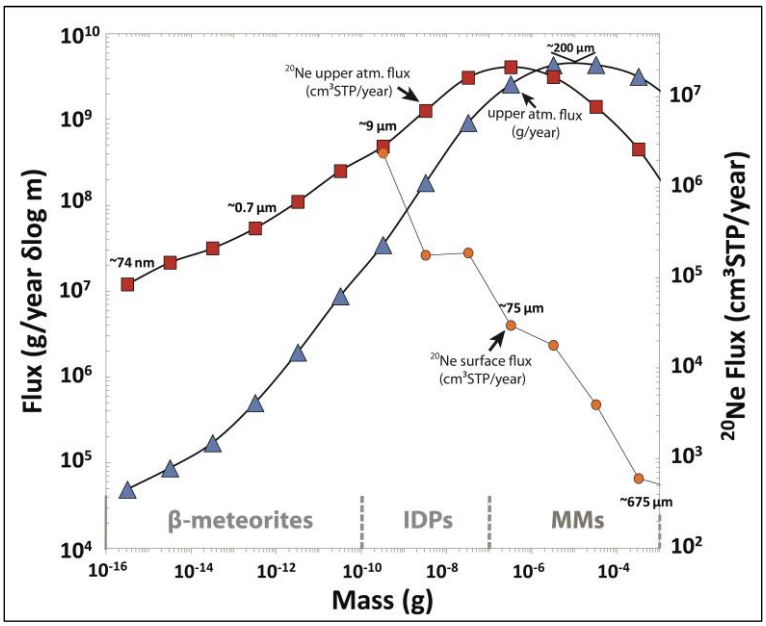

Fig. 3.6: Detail of the particle mass flux from Figure 3.5 for β-meteorites, IDPs and MMs divided in decadal mass bins (blue triangles). The annual ^{20}Ne flux to Earth in cm³STP/year is shown for the same mass intervals (red squares). The maximum ^{20}Ne flux for measured particles to Earth's surface (orange circles) is contributed by IDPs in the mass range 10^{-10} g to 10^{-9} g (mean diameter ~9 µm). Note that approximate sizes of MMs and IDPs are mean values derived from the compilation; sizes of β-meteorites are calculated assuming a spherical particle shape. The mass flux for MMs peaks at ~200 µm whereas the ^{20}Ne flux to the upper atmosphere peaks at ~75 µm and is calculated from the mean ^{20}Ne concentration of the smallest measured IDPs. The graph for the particle flux in g/year (blue triangles and grey circles) corresponds to the ordinate on the left side of the diagram and the graph for the Ne flux in cm³STP/year (orange circles and red squares) corresponds to the ordinate on the right side of the diagram.

Figure 3.7 shows the total annual influx of ^{20}Ne (i.e., incident on Earth's upper atmosphere) including all mass ranges (Tab. B4). For these, the isotopically different components planetary Ne-A – which is volume correlated – and solar wind implanted Ne-B, which is surface correlated have to be distinguished. Small particles are dominated by surface correlated solar wind (Ne-B), whereas Ne-A is dominant in large bodies. While the main material accreting to early Earth from the inner Solar System likely contains only Ne-B, Ne-A is likely only present in volatile-rich bodies from the outer Solar System beyond the snow line. For example, carbonaceous chondrites carry both components, i.e., their neon flux can be computed by adding the respective Ne-A and Ne-B curves. Here, the subdivision in decadal mass bins furthermore allows distinguishing between time dependent Ne fluxes delivered by variable Ne carriers during different periods of terrestrial accretion. If the main accretion happened either from the outer or the inner Solar System then the fluxes of Ne to Earth would be dominated by either the Ne-A or the Ne-B component.

The flux of Ne-A to the upper atmosphere (Fig. 3.7) would have only be dominant as part of a late veneer of volatile-rich carriers coming from the outer asteroid belt (Morbidelli et al., 2012 and discussion therein). The mass and size dependent Ne-A flux in the model is computed with the mean primordial CI ^{20}Ne concentration of $2.57*10^{-7}$ cm^3STP/g (see section 3.3.2, Tab. B4).

On the other hand, during the early stages of terrestrial accretion, most of the accreting material was not delivered from the outer asteroid belt or beyond, but from the inner Solar System (Hansen, 2009; Raymond et al., 2009; Walsh et al., 2011; Morbidelli et al., 2012). Based on the implantation/sputtering model for the young Solar System (Moreira and Charnoz, 2016) it is possible to achieve a steady state Ne-B value of 12.53–12.73 within several thousands of years. This corresponds to an irradiation age that, according to their model, is easily reached by 100 μm particles at distances of 0.8–1.2 AU from the sun.

Hence, in applying the model, assumptions have to be made on the mass distribution and neon content of the relevant materials. Concerning mass distribution, it is assumed that inner Solar System objects were in a similar collisional equilibrium producing similar size distributions of large and small bodies and debris dust as today. Concerning neon content, it is reasonable to assume that these bodies were heavily depleted in volatiles and essentially devoid of any planetary Ne-A, and that solar wind implantation into the outermost particle layer was the only source of neon, i.e., Ne-B with the compiled IDP $^{20}Ne/^{22}Ne$ ratio of = 12.61±0.41.

In the case of accretion from the inner Solar System the flux of Ne-B to the upper atmosphere (Fig. 3.7, Tab. B4) is the dominant source for Ne delivered to Earth. To determine the respective Ne concentration of each mass interval for the "inner Solar System bodies" the assumption of simple geometric upscaling is used (as for the geometric downscaling for β-meteorites; section 3.3.2) with a 50 nm thick SW-Ne saturated particle surface layer and a ^{20}Ne concentration of 1.73 cm^3STP/g (APPENDIX B2, Tab. B3) that is based on the observed mean ^{20}Ne concentration ($6.92*10^{-2}$ cm^3STP/g) of the smallest IDPs. For the "inner Solar System bodies" that were available during terrestrial accretion, the density is assumed to be 2.5 g/cm^3 (after Grotheer and Livi, 2014). The calculated concentration represents the inventory of particles before any losses due to atmospheric entry heating, i.e., the maximum amount of SW-implanted Ne. This determines the flux of Ne-B to the upper atmosphere shown in Figures 3.6 and 3.7.

The thus derived total annual amount of ^{20}Ne arriving at the Earth's upper atmosphere today (Fig 3.7) is about 6.88*10^{6}cm^{3}STP for carbonaceous chondrite-like carriers which contain the Ne-A component and 7.82*10^{7} cm^{3}STP for "inner Solar System bodies" which carry Ne-B. These are only very tiny fractions of 10^{-13} and 10^{-12} of the present-day atmospheric ^{20}Ne inventory of 6.52*10^{19} cm^{3}STP (Zhang, 2014). Even the largest hypothetical carbonaceous chondrite-like body of about 1000 km diameter included in the annual mass flux model would deliver only 3.38*10^{6} cm^{3}STP ^{20}Ne (Ne-A) to the upper atmosphere, which is similar to the amount of ^{20}Ne (2.39*10^{6} cm^{3}STP per year, Ne-B) that is delivered by small IDPs which reach the surface. Of the Ne-A incident on Earth's atmosphere via carbonaceous chondrite-like material, more than 99.9% is contributed by "large matter" (large particles, large bodies and very large bodies) whereas only <0.1% is contributed by "small matter" (MMs, IDPs and β-meteorites). Concerning Ne-B, <1% of the ^{20}Ne is contributed by "large matter" whereas >99% is contributed by "small matter".

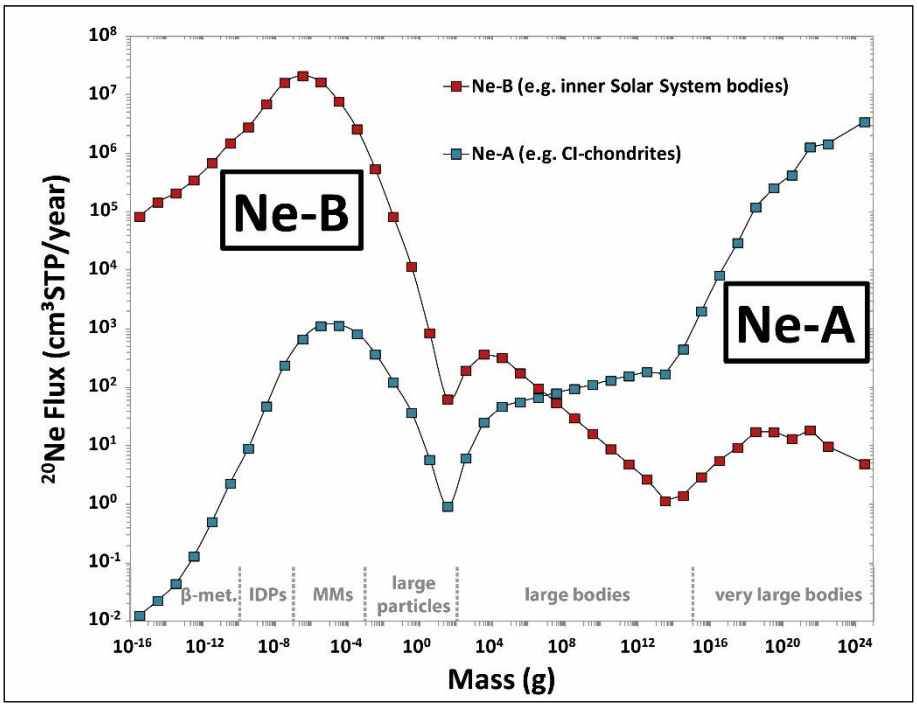

Fig. 3.7: Annual ^{20}Ne flux to Earth's upper atmosphere in cm^{3}STP/year against the mass of different particle types divided in decadal mass bins. The present ^{20}Ne flux contributed by carbonaceous chondrite-like carriers containing the Ne-A component (turquoise squares) is compared to the annual ^{20}Ne flux modelled for "inner Solar System bodies" (red squares). The "inner Solar System bodies" are devoid of any Ne component other than the SW-Ne-saturated surface layer (see text for details), thus, only contributing the Ne-B component.

3.3.6 Scaling present fluxes to early Earth

The compiled annual particle flux model is regard to be a direct consequence of the process that constantly produces micrometeorites and smaller particles through collisional processes (Cordier and Folco, 2014). Therefore, it is assumed that early mass fluxes during terrestrial accretion are characterized by a similar size / mass distribution and that the flux at a given time is given by the current flux multiplied by a factor determined by the time of contribution.

The earliest episode of terrestrial accretion that occurred within the solar nebula may have been characterized by mass fluxes in the range 10^{6} to 10^{8} times the present flux (see Hartmann,

1999; Ryder, 2002; Koeberl, 2004, 2006; Maurette, 2006). Flux models for subsequent periods are controversially debated based on the lunar cratering record, e.g., low bombardment prior to 4.0 Ga culminating into a unique spike at 4.0 to 3.9 Ga, or intense cratering prior to 4.0 Ga that declined constantly into the present day mass flux. Alternatively, data from the late lunar impact record can be interpreted as multiple episodic bombardments or asteroid showers before 3.8 Ga (Mojzsis et al., 1999; Arrhenius and Lepland, 2000).

Estimates for the mass flux differ significantly between decreasing flux models and models including a terminal lunar cataclysm (e.g., Ryder, 2002). In their noncataclysm model, Chyba and Hand (2006) estimate mass fluxes of $1*10^{12}$ kg/year at 4.0 Ga, which is equivalent to 180 times their calculated current average flux, and $5*10^{11}$ kg/year at 3.9 Ga that is 94 times the flux they calculate for today. On the other hand, the leading hypothesis of a post-accretion rapid decrease of the impactor flux predicts that after the last giant impact there was a persistent flux only about 2 times higher than today (Claeys and Morbidelli, 2011), until during terminal cataclysm fluxes increased by several orders of magnitude. Significant mass fluxes during a late heavy bombardment (LHB) of ~$5*10^{21}$ to 10^{23} g have been calculated for the inner Solar System (Ryder, 2001, 2002; Levison et al., 2001). Based on lunar cratering data from Ryder et al. (2000), a terminal LHB can be linked to fluxes at least ~1000 times the present flux between 3.90 Ga to 3.85 Ga and still a few hundred times enhanced fluxes from 3.85 Ga to 3.80 Ga (Koeberl, 2004, 2006). In contrast, following the lunar cratering record of Hartmann (1999), the EMMAC scenario (Maurette et al., 2000; Maurette, 2006) considers two distinct time windows: a first one, termed sterilization episode, lasting ~100 Ma at the end of the formation time interval of the Earth at 4.45 Ga characterized by a MM influx ~$2*10^6$ times the present flux, and a second one, termed early life episode, exhibiting a ~500 times greater MM flux from 4.2 to 3.9 Ga ago.

In view of the wide range of estimates given above for the model initial mass fluxes at the start of accretion are considered to be enhanced up to 10^8 times the present flux. These mass fluxes were followed by decreasing rates until during late veneer acquisition mass fluxes increased by several orders of magnitude. In the model calculations below the compiled current average annual particle flux of $2.7*10^{10}$ kg/year (section 3.3.3) are continued being used to scale for early fluxes during Earth's accretion according to an enhanced average mass flux discussed in detail in section 3.4.

3.4 Framework of Ne accretion

The model for the terrestrial Ne acquisition during planetary accretion is based on the flux model described above. The advantage of the mass dependent Ne flux (section 3.3.5) is that it simultaneously considers, both, the interdependent amount of accreted mass and the amount of accreted Ne. Adequately adjusted to a framework for the terrestrial accretion and scaled for early mass fluxes these input data are used to perform model calculations trying to fit the current terrestrial atmospheric and mantle neon inventories and their isotopic compositions (Tab. 3.1).

Values that are to be reconciled with the model for the atmosphere are 9.80 for the $^{20}Ne/^{22}Ne$ ratio (Eberhardt et al., 1965) and $6.52*10^{19}$ cm^3 for the ^{20}Ne inventory (Zhang, 2014). As

discussed in section 3.2, the pristine mantle $^{20}Ne/^{22}Ne$ ratio is assumed to have a value of 12.7±0.2, which resembles the implanted Ne-B value of 12.7±0.1 (Moreira and Charnoz, 2016). The mantle ^{20}Ne inventory amounts to $(6.55±3.62)*10^{18}$ cm³ (Marty, 2012) if the (whole) mantle is only moderately degassed (plume-type). Assuming a strongly degassed mantle (MORB is more intensively degassed) and a ratio MORB mantle/plume mantle = 80/20, only a fifth of this amount has to be considered, i.e. $1.31*10^{18}$ cm³. Following Staudacher and Allègre, (1988) and Holland and Ballentine (2006), substantial subduction of Ne is unlikely and negligible for the calculations. In the model it is further assumed that the Earth's mass at the time of the impact of a ~Mars-size (~0.1–0.2 Earth masses (M_E)) body about 100 Ma after Solar System origin (Wade and Wood, 2016) did not exceed ~95% of its final mass. A fraction of $(4.86±1.63)*10^{-3}$ M_E that is thought to have accumulated on Earth after the last giant impact by a late chondritic veneer (Jacobson et al., 2014; Morbidelli and Wood, 2015) is considered as another reference point for the model.

For the framework of the terrestrial Ne accretion model (Fig. 3.8) an early pre-lunar impact era ("phase I") of terrestrial accretion in a shielded disk environment is considered that prevented irradiation of dust in the mid-plane and subsequent completion of accretion in a cleared disk. Concerning accretion within the gas shielded disk, there may have been some implantation of SW in off-disk regions, but this is considered to be insignificant for the calculations. The formation of a steam atmosphere in combination with degassing of accreted material induces the dissolution of solar gases into a magma ocean. The assumed chronology of Ne accretion during "phase I" is as follows:

1) Up to ca. 10 Ma: Shielded accretion within the solar nebula. High mass fluxes between $8*10^6$–$5*10^7$ times the present flux resulted in accretion of ~18 to 94% Earth's present mass. Earth's building blocks were largely devoid of SW implanted Ne-B and contained negligible amounts only of planetary Ne-A.
2) Several Ma to tens of Ma: Accretion within a cleared disk and mass fluxes between $3*10^5$–$2.5*10^7$ times the present flux until a mass of ~95% M_E has been reached. Earth´s accreting material mainly consisted of SW-irradiated dust and inner Solar System bodies. Depending on the volatile (water) content of incoming planetesimals, an insulating steam atmosphere and a magma ocean formed and most of the accreting material was degassed into the protoatmosphere. The accreted Ne dissolved into the magma ocean. The mass influx decreased until the giant Moon-forming impact.

The subsequent post-lunar impact era ("phase II") occured after atmospheric loss caused by the Moon-forming impact (close to 100% loss in the simplified model) at around 4.45 Ga, whereupon mantle degassing and the contribution of a late chondritic veneer completed the atmospheric inventory. The assumed chronology of Ne accretion during "phase II" is as follows:

3) Intensive mantle degassing due to high convection rates, and possibly due to a brief time interval of a post-lunar impact magma ocean. Significantly lower mass accretion, possibly episodic bombardments terminating in the Lunar Heavy Bombardment 4.0-3.8 Ga ago. A significant portion of accreted material was volatile-rich and dominated by Ne-A.

4) 3.8 Ga of approximately present-day mass flux. The accreted material corresponds to the present-day mixture of Solar System materials, derived from small body populations in the asteroid belt and Kuiper belt.

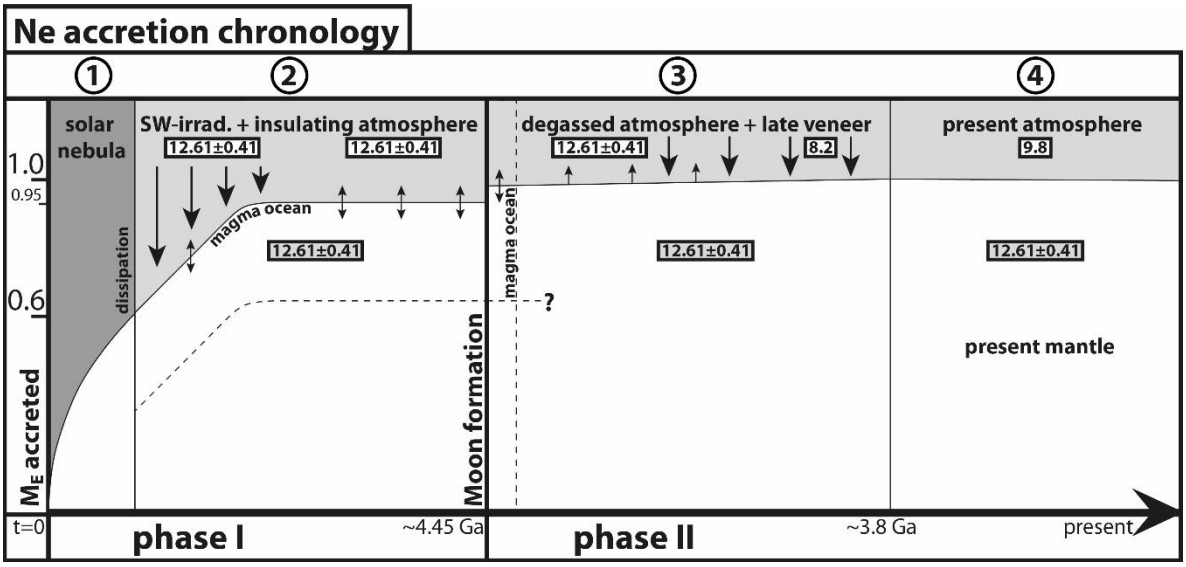

Fig. 3.8: Chronology of terrestrial Ne accretion. The fraction of accreted Earth (M_E) is indicated by a steep solid line in sections 1 and 2 and by horizontal solid lines in sections 2 to 4 that separate the solid Earth from the overlying atmosphere. The $^{20}Ne/^{22}Ne$ isotopic composition prevailing within the mantle and atmosphere throughout the respective period of accretion is indicated by the inset boxes. Note that the widths of the sections and thickness of atmosphere are not to scale. **(1)** In the early "phase I" planetary formation starts within a solar nebula disk shielded from irradiation by the Sun, and Earth accretes to more than ~0.5 M_E in less than 10 Ma. **(2)** After dissipation of the solar nebula accretion continues until ~95% of Earth is completed. The accreted "inner Solar System bodies" contain the Ne-B component ($^{20}Ne/^{22}Ne$ = 12.61±0.41) implanted by SW-irradiation. Prior to the giant Moon-forming impact the Ne-B component dissolves into a magma ocean that is generated through thermal insulation by an atmosphere that formed from impact degassing of accreted planetesimals. **(3)** "Phase II" starts after the Moon-forming impact at ~4.45 Ga that erodes the pre-existing atmosphere. The impact-induced energy creates a magma ocean from which the previously dissolved Ne-B degasses. The Ne-B component mixes with a planetary Ne component (with a composition like Ne-A: $^{20}Ne/^{22}Ne$ = 8.2) delivered by a late chondritic veneer of CI type carriers until 3.8 Ga. **(4)** The generated atmospheric Ne inventory is not significantly altered by the material accreted after the late veneer which fixes the present $^{20}Ne/^{22}Ne$ value of 9.8.

3.4.1 Earliest terrestrial accretion and protoplanetary disk lifetime

Various numerical planetary accretion models suggest timescales of ~30–100 Ma for the formation of the terrestrial planets (e.g., Morbidelli et al., 2012 and references therein). The model-ages highly depend on the mechanisms of accretion and core formation. Kleine et al. (2002) used Hf-W chronometry to date core formation on Earth and Mars to 33±2 Ma and 13±2 Ma, respectively, after the beginning of the Solar System. Identical $^{182}W/^{184}W$ ratios of terrestrial and lunar rocks, however, indicate that the giant Moon-forming impact and, thus, the final stages of terrestrial core formation extended to more than ~50 Ma after CAIs, i.e., after ^{182}Hf became extinct (Kleine et al., 2009).

Prior to the Moon-forming event, during a probably heterogeneous accretion that included differentiated larger bodies and potentially differentiated smaller bodies, metal-silicate equilibration at high pressures was essential for core formation (Rubie et al., 2011; Wade and Wood, 2016). Well-developed multistage core formation models consider partial or complete equilibration of the metal from an impactor with a fraction of a silicate magma ocean at every step of accretion, followed by partitioning into the proto-core of the accreting Earth during each core

growth event (Rubie et al., 2011, 2015). Considering an equilibrium accretion model and taking into account a giant impact about 100 Ma after the start of accretion, high-pressure partitioning data have been used to construct a corresponding accretion scenario (Halliday and Wood, 2009). This scenario implies rapid early accretion and core formation suggesting that the main terrestrial formation phase lasted less than 10 Ma, with little further growth and a substantial accretion hiatus before the last giant impact that formed the Moon.

As an alternative to formation within the solar nebula, accretion of (volatile-rich) material could have likewise happened *after* the dissipation of disk gas (Trieloff, et al., 2002; Trieloff, 2002, 2007). This scenario is primarily constrained by the timing of disk dispersal. A lifetime of ~6 Ma is predicted by Haisch et al. (2001), which is much shorter than terrestrial planet formation. Thus, the final stages of accretion can reasonably be assumed to have taken place in a cleared disk environment. In support of this and as a consequence of photoevaporation, the evolution of protoplanetary disks surrounding T Tauri stars suggests complete dispersal on timescales of 10^5 years, after a disk lifetime of just a few million years (Alexander et al., 2006). Note, however, that from observational data there are hints that disk lifetimes of up to tens of millions of years are also possible (Pfalzner et al., 2014).

For the Ne accretion model accretion within a solar nebula environment is considered that is shielded from solar wind by nebula gas, followed by a subsequent period of accretion in a cleared disk in which SW-implantation distributes the Ne-B component ($^{20}Ne/^{22}Ne$ = 12.61±0.41, Tab. 3.1) to the surface of "inner Solar System bodies". This period is constrained in such a way that accretion under, both, shielded and cleared conditions together account for no more than ~0.95 M_E.

3.4.2 Steam atmosphere and magma ocean

The existence of early magma oceans during terrestrial planet formation is a consequence of the high energy of accretion that is delivered by giant impacts, early radiogenic heating and the insulating effect of a massive early atmosphere (Elkins-Tanton, 2012; Tucker and Mukhopadhyay, 2014; de Vries et al., 2016). A sufficiently dense atmosphere consisting of water vapor and CO_2 favoring melting of the surface through thermal blanketing and the development of a magma ocean can be generated by degassing of accreted volatile-bearing planetesimals (Matsui and Abe, 1986; Zahnle et al., 1988; Abe, 1993; Elkins-Tanton, 2008). An impact-generated steam atmosphere forms if the terrestrial building blocks contain a few % of chondritic planetesimals with H_2O and CO_2 (Schaefer and Fegley, 2010). Fegley et al. (2016) moreover postulate the formation of a massive (~1100 bar) steam atmosphere on the early Earth composed of ~75% water steam and 25% CO_2.

The generation of giant impact induced magma oceans during terrestrial accretion is also consistent with noble gas data. Based on $^3He/^{22}Ne$ isotopic ratios of Earth's mantle reservoirs, Tucker and Mukhopadhyay (2014) modelled multiple episodes of magma ocean-degassing in combination with atmospheric blow-off by giant impacts. As the last generation of a magma ocean is associated with the Moon-forming giant impact, solubility-controlled ingassing of noble gases

from an insulating atmosphere should therefore be possible throughout the early history of terrestrial accretion.

In the Ne accretion model including a magma ocean a given amount of ^{20}Ne (see section 3.5.2) has to be dissolved into a magma ocean of variable depths. This amount is prescribed by the amount of ^{20}Ne (Ne-B component) that is degassing from the mantle after the giant Moon-forming impact (see section 3.4.3) to mix with the amount of ^{20}Ne (Ne-A component) that is delivered during a late veneer (see section 3.4.4). In this way, the present atmospheric and mantle ^{20}Ne inventories are generated. The dissolution of ^{20}Ne can be either modelled using variable solubility coefficients or variable partial pressures of ^{20}Ne in the atmosphere, where the latter is a function of the amount of accreted SW-implanted ^{20}Ne.

Here, the dissolution of Ne that degassed from accreted material into a magma ocean is modelled by assuming a fixed neon solubility of $2.5*10^{-4}$ cm³STP/g/bar in tholeiitic melt (Jambon et al., 1986; Paonita, 2005) and a variable partial pressure of ^{20}Ne. To obtain the required weight of the melt the volume of a magma ocean with variable depths is fitted that formed on a growing Earth assuming a density of 2.8 g/cm³ for basaltic melts. The partial pressure of the dissolving Ne is calculated by dividing the total amount of ^{20}Ne that is accreted with the particle flux model by the total inventory of today's (i.e., comprising all the constituents of) dry air of $3.961*10^{24}$ cm³STP (Ozima and Podosek, 2002), which is presently considered as the best estimate for the atmospheric volume.

3.4.3 Moon-forming impact and mantle degassing

It is generally assumed that the Moon originated from the collision of the proto-Earth with a Mars-sized planetary embryo during the last stage of terrestrial formation (e.g., contributions in Canup and Righter, 2000; Canup and Asphaug, 2001; Canup, 2004). This event is also thought to represent the last major step in the accretion of Earth (Canup, 2008) and to be synonymous with the time of the last giant impact at approximately 4.45 Ga (Koeberl, 2006). Based on geochemical properties it is expected that the Earth-Moon system was generated by the impact of a reduced body of ~0.1–0.2 M_E on an oxidized proto-Earth that had grown to between 50 and 95% of its final mass (Wade and Wood, 2016). It should be noted, however, that in contrast to multistage core formation scenarios heterogeneous accretion models successfully apply an oxidized impactor (Rubie et al., 2011). Simulations imply that after the Moon-forming impact the Earth was >95% accreted (Canup, 2004).

The consequences expected from this event include almost complete loss of a primary atmosphere and the generation of a (renewed) magma ocean (references in Canup and Righter, 2000; Koeberl, 2006). A natural secondary consequence of a magma ocean is the equilibration with the atmosphere through solubility-controlled outgassing of previously dissolved noble gases (e.g., the Ne-B component) and the associated atmospheric growth (Elkins-Tanton, 2008; Tucker and Mukhopadhyay, 2014). Partial or complete loss of the atmosphere is also implied by the presence of primordial ^{3}He/^{22}Ne ratios in the present-day mantle. Multiple episodes (at least two) of giant impact induced atmospheric blow-off and subsequent re-equilibration of a captured solar nebula (^{3}He/^{22}Ne ~1.5) with the mantle by magma ocean outgassing are required to generate a primitive

$^{3}He/^{22}Ne$ ratio of ~2.3–3 in a primitive mantle reservoir (fractionated during nebular ingassing) and a fractionated (by outgassing) $^{3}He/^{22}Ne$ ratio of ≥10 in the depleted shallower mantle (Tucker and Mukhopadhyay, 2014). According to Zahnle et al. (2007), however, the Moon-forming impact may, but also may not, have expelled a substantial fraction of Earth's pre-existing atmosphere and a giant impact that induced atmospheric blow-off by shock waves would have led to atmospheric loss from the impactor of 30% and only 10% from the proto-Earth (Genda and Abe, 2003). A significant fraction of a primary atmosphere might therefore as well have been retained. In the case of a protoplanet covered with a water ocean, atmospheric blow-off, however, becomes more effective (Genda and Abe, 2005).

For the sake of simplicity, in a first step, a case is considered where the Moon-forming impact expelled the entire formerly accreted atmospheric Ne. In a next step the cases of incomplete atmospheric erosion are investigated, with up to 8% retained Ne. The giant impact generated a magma ocean which subsequently degassed from the mantle the previously dissolved Ne and caused its accumulation within the atmosphere. In the model including a magma ocean, 8% retained Ne is the maximum fraction that is allowed to be present in the atmosphere before mantle degassing after the Moon-forming impact adds to the atmospheric reservoir to generate today's Ne budget. Note though that even without a magma ocean, intense degassing would have occurred due to high convection rates. Very active global mantle geodynamics during the Hadean implies that the volatile flux from the mantle was at least one order of magnitude higher than today (Yokochi and Marty, 2005).

3.4.4 Post-moon-forming accretion and late veneer

According to the "Nice" model, migration of Jupiter and Saturn involving a 1:2 resonance crossing caused a sudden massive impactor flux consisting of a mixture of comets and asteroids into the inner Solar System ~700 Ma after the planets formed (Gomes et al., 2005). Tera et al. (1974), Wetherill (1975) and Koeberl (2004, 2006) used the term "Late Heavy Bombardment" to denote the intense and cataclysmic spike in bombardment in the inner Solar System around 3.85 Ga derived from lunar chronology. Based on the arguments of Ryder et al. (2000) for the ages of the large impact basins on the Moon, a ~60 Ma period of considerable bombardment should have occurred on the Moon between 3.90 and ~3.84 Ga.

Furthermore, to account for the abundance of highly siderophile elements (HSE) in the primitive upper mantle, geochemists advocate a late veneer of chondritic material by which an amount of <1% M_E was added by to the Earth after core formation had ceased (Chou, 1978; Morbidelli and Wood, 2015). The Earth/Moon HSE abundance ratio is suitably explained as long as Earth's veneer was contributed from large bodies including impactors with diameters of ≳500 to 1000 km (Raymond et al., 2013). According to Halliday (2013), however, a late veneer of chondrites and/or comets does not explain the high H/C and C/N of the silicate Earth. Relying on oxygen isotopes rather than on HSE abundances, Albarède (2009) and Albarède et al. (2013) suggest that a late veneer of ~4% CI chondritic material played an important role in the acquisition of volatiles by the Earth, with direct implications for the terrestrial noble gas budget.

A late contribution of material after Earth's main accretion period without an effective process to introduce the incident material into the mantle (e.g., dissolution into a magma ocean) would have supplied all volatiles contained in this matter directly to the atmospheric reservoir, if the impactors were large and impacted with high velocity. Hence, the isotopic Ne composition delivered by a late veneer will have diluted the Ne component outgassed after the Moon-forming impact and will have added to the existing atmospheric Ne inventory. Similar to the sudden massive delivery of large impactors in case of the LHB (Gomes et al., 2005; Raymond et al., 2013), the late chondritic veneer in the model is dominated by large bodies (large particles, large bodies and very large bodies). For these, a somewhat variable Ne isotopic composition of carbonaceous chondrite type carriers is used ($^{20}Ne/^{22}Ne$: 5.2 to 9.2, Tab. 3.1; $2.57*10^{-7}$ cm^3STP/g of ^{20}Ne). It is emphasized, though, that a preferable $^{20}Ne/^{22}Ne$ ratio is 8.2 (Ne-A) and a ratio of 5.2 is highly unlikely and rather hypothetical as only one (bulk meteorite) measurement on Alais (Zähringer, 1968) implies a non-cosmogenic $^{20}Ne/^{22}Ne$ ratio of ~5.9. No other primordial (i.e., non-cosmogenic) bulk Ne composition with a value that low is known for carbonaceous chondrites (Mazor et al., 1970). It is also important to note that the model does not require a specific timing for such late accreted neon other than it must have been delivered after the Moon-forming impact. However, delivery between 4.4 and 3.8 Ga ago is considered as most likely.

Tab. 3.1: Current terrestrial atmospheric and mantle Ne inventories and isotopic compositions that are aimed to be reproduced with the model by using the Ne composition found in the Ne-A and Ne-B components.

Atmosphere	
$^{20}Ne/^{22}Ne$	9.80 **(a)**
^{20}Ne [cm^3]	$6.52*10^{19}$ **(b)**
moderately degassed mantle	
$^{20}Ne/^{22}Ne$	≳12.5–~12.9 **(c)**
^{20}Ne [cm^3]	$6.55*10^{18}$ **(d)**
strongly degassed mantle	
$^{20}Ne/^{22}Ne$	≳12.5–~12.9 **(c)**
^{20}Ne [cm^3]	$1.31*10^{18}$ **(e)**
"planetary" Ne (Ne-A) (model fluxes)	
$^{20}Ne/^{22}Ne$	5.2–9.2
^{20}Ne [cm^3]	variable
"solar" Ne (Ne-B) (model fluxes)	
$^{20}Ne/^{22}Ne$	12.61±0.41
^{20}Ne [cm^3]	variable

a) Eberhardt et al. (1965), **b)** Zhang (2014),
c) see Moreira (2013), **d)** Marty (2012)
e) modified after Marty (2012)

3.5 Ne-accretion model including a magma ocean

The presented model calculations are based on the most recent observations of current particle fluxes to Earth and measured Ne inventories of cosmic dust particles (MMs and IDPs) to

constrain the current terrestrial Ne acquisition. It is therefore essential to combine this quantitative mass dependent Ne flux to Earth (section 3.3.5) with a framework for terrestrial accretion (section 3.4). Because the amount of accreted Ne depends on the amount and type of accreted mass it is possible to double-check the results. The fundamental observations that are aimed to be reproduced in the Ne accretion model are the current terrestrial atmospheric and mantle Ne inventories and their isotopic compositions. Fit parameters that are to some extent free, but also interdependent, are the Ne isotopic composition of the late veneer, the degree of degassing of the mantle, the depth of the pre-lunar impact magma ocean and the fraction of solar wind irradiated material that accreted to Earth. Plausible parameter combinations are used to explain the terrestrial Ne signatures, in particular with respect to the isotopically solar-like Ne of Earth's mantle and the "planetary" composition of the atmosphere.

The approach can be briefly outlined as follows: As today´s mantle and atmospheric neon inventories are well constrained, the atmospheric contributions derived from a late veneer and by mantle degassing are simply constrained by the late veneer´s isotopic composition. The degree of mantle degassing then also determines the pre-lunar impact mantle neon content, which in turn is a function of solubility-controlled neon dissolution into a magma ocean of a certain depth, as well as the neon content of the protoatmosphere. The latter in turn is determined by the fraction of solar wind irradiated material accreting to Earth (Tab. B5, Tab.B6, Tab. B7). The Ne-B component with an isotopic ratio of $^{20}Ne/^{22}Ne=12.61\pm0.41$ (section 3.3.2) implanted into the accreting particles is incorporated into Earth's interior by dissolution of neon into the magma ocean from the impact degassed insulating atmosphere. After the enclosure of Ne-B and solidification of the magma ocean the isotopic composition within Earth remains unaffected by later additions to the atmosphere and is sampled as the pristine Ne mantle end-member observed today.

3.5.1 Degree of mantle degassing and Ne from the late veneer

The present day´s atmospheric neon inventory of $6.52*10^{19}$ cm³ ^{20}Ne (Zhang, 2014) and its isotopic composition ($^{20}Ne/^{22}Ne=9.80$) strongly constrain the contributions from Earth´s mantle (Ne-B value in the model with $^{20}Ne/^{22}Ne=12.61$) and the late veneer. For example, a late veneer with $^{20}Ne/^{22}Ne=8.20$ (Ne-A) implies that 53% of the atmospheric ^{20}Ne are from the late veneer, 47% from mantle ^{20}Ne. In turn, if 47% of the atmospheric ^{20}Ne are degassed from the mantle (i.e., $3.04*10^{19}$ cm³) then the degree of degassing is simply determined by the remaining mantle inventory of $6.55*10^{18}$ cm³ ^{20}Ne (case of moderately degassed plume-type mantle), resulting in 82% degassing. A more strongly degassed MORB-type mantle containing only $1.31*10^{18}$ cm³ ^{20}Ne would result in a degassing degree of 96%. These cases are shown in Figure 3.9a.

Also shown in Fig. 3.9a is the degree of degassing when different $^{20}Ne/^{22}Ne$ isotopic ratios are assumed for the late veneer neon. For example, if the isotopic composition was the same as in today´s atmosphere ($^{20}Ne/^{22}Ne=9.8$), no mantle contribution would be needed, i.e. the required mantle degassing degree would be zero. It should be noted, however, that the actual degree of mantle degassing can be inferred from other nuclide systems like $^{40}Ar/^{36}Ar$ or $^{129}Xe/^{130}Xe$, which makes such an extreme "zero scenario" unlikely. The highest degree of mantle degassing for a moderately or a strongly degassed mantle is ~89% and ~98%, respectively, if the late veneer

contributes a $^{20}Ne/^{22}Ne$ ratio as low as 5.2, which is, however, as well unlikely, as such a component is not found to be typical for meteorites.

Figure 3.9b shows, as a function of the isotopic composition of the late veneer neon, the contribution of the late veneer to the atmospheric ^{20}Ne inventory as well as the mass contribution, assuming typical carbonaceous chondrite-like concentrations. The most likely case of Ne-A composition ($^{20}Ne/^{22}Ne$ ratio of 8.2) implies that a contribution of 2.26% M_E from the late veneer would contribute 53% of the atmospheric ^{20}Ne. The case of the low $^{20}Ne/^{22}Ne$ ratio of 5.2 would imply a mass contribution of only 0.85% M_E and the contribution of approximately 20% to the atmospheric ^{20}Ne (Tab. B5). Finally, the degree of mantle degassing determines the pre-lunar impact mantle inventory, a point which is dealt with in the following section 3.5.2.

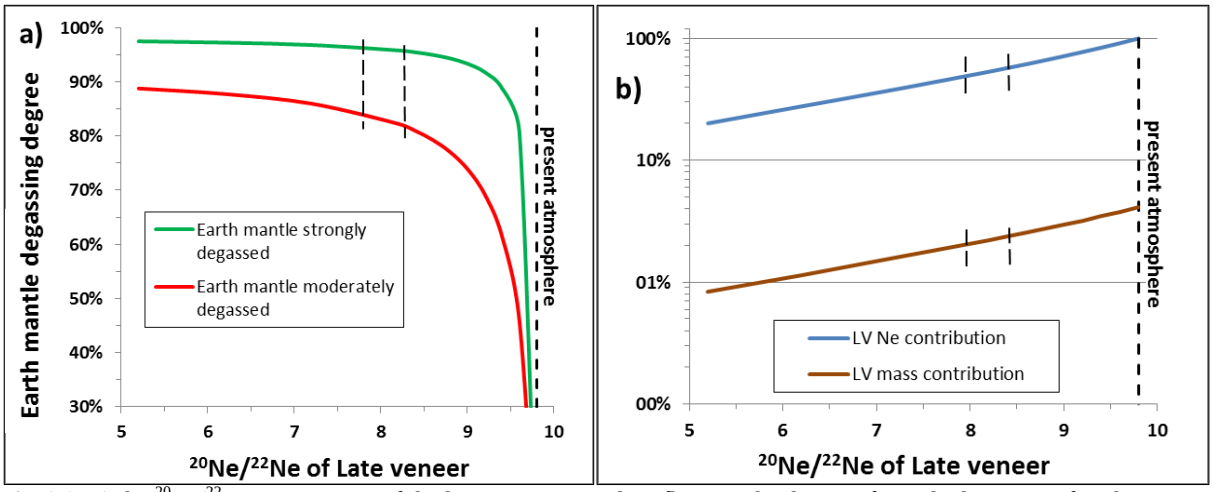

Fig. 3.9: a) the $^{20}Ne/^{22}Ne$ composition of the late veneer strongly influences the degree of mantle degassing after the Moon-forming impact. The two curves pertain to different assumptions about the current ^{20}Ne inventory of the mantle: a strongly degassed mantle (green) or a more moderately degassed mantle (red). The dashed lines indicates a planetary $^{20}Ne/^{22}Ne$ composition of ~8.2 (Ne-A), with an inferred mantle degassing of around 82–96%. No mantle degassing is required if the late veneer delivers the atmospheric $^{20}Ne/^{22}Ne$ ratio of 9.8. The maximum degree of 89–98% mantle degassing is necessary if the late veneer delivers the lowest $^{20}Ne/^{22}Ne$ ratio considered of 5.2. **b)** the mass contribution of the late veneer is compared to the resulting ^{20}Ne contribution: ~2.26% M_E delivers ~53% of the atmospheric ^{20}Ne (dashed lines, for $^{20}Ne/^{22}Ne$ = 8.2), ~4.24% M_E delivers ~100% of the atmospheric ^{20}Ne ($^{20}Ne/^{22}Ne$ = 9.8), and ~0.85% M_E delivers ~20% of the atmospheric ^{20}Ne ($^{20}Ne/^{22}Ne$ = 5.2).

3.5.2 Fraction of SW-irradiated material and depth of magma ocean

A certain amount of solar wind implanted ^{20}Ne had to be dissolved into the magma ocean before the Moon-forming impact in order to account for the present mantle and atmospheric neon compositions and concentrations that are a result of degassing from the mantle after the giant impact event and the addition of the late veneer. On the other hand, this amount of dissolved ^{20}Ne (in the magma ocean) can be inferred by the present atmospheric and mantle ^{20}Ne inventories. The pre-lunar impact mantle inventory of solar wind-implanted Ne during the early "phase I" is determined by i) the fraction of irradiated material that accreted to Earth and degassed into the hot steam-protoatmosphere and by ii) dissolution into the magma ocean.

In the model for a moderately degassed mantle, total amounts of ~$2.1*10^{19}$ cm^3, ~$3.7*10^{19}$ cm^3 and ~$5.9*10^{19}$ cm^3 ^{20}Ne had to be present in the mantle, if Ne-A in the late veneer had $^{20}Ne/^{22}Ne$ ratios of 9.2, 8.2 and 5.2, respectively. For a strongly degassed mantle, total amounts of

~1.6*10^{19} cm^3, ~3.2*10^{19} cm^3 and ~5.3*10^{19} cm^3 ^{20}Ne had to be present for late veneer Ne-A having ^{20}Ne/^{22}Ne ratios of 9.2, 8.2 and 5.2, respectively (Tab. B6). These absolute values refer to any possible depth of a magma ocean and, assuming a fixed solubility of neon in the melt, are a function of the ^{20}Ne partial pressure in the atmosphere. This partial pressure in turn reflects different amounts of accreted ^{20}Ne.

While solubilities are experimentally well constrained for Henry's law conditions, a major unknown is the volume or the depth of the magma ocean. Figure 3.10 shows the fraction of dissolved Ne (relative to the total amount of solar wind implanted Ne) contributed by "inner Solar System bodies" that were irradiated *after* dissipation of the solar nebula. It becomes clear that less than 12% of the total accreted Ne is dissolved by solubility-controlled ingassing into a magma ocean, if the magma ocean has a depth of less than 2500 km. A shallower magma ocean requires a higher neon partial pressure in order to achieve the required mantle neon concentrations, i.e. it demands a higher fraction of irradiated accreting material and a higher concentration of dissolved ^{20}Ne (Tab. B6).

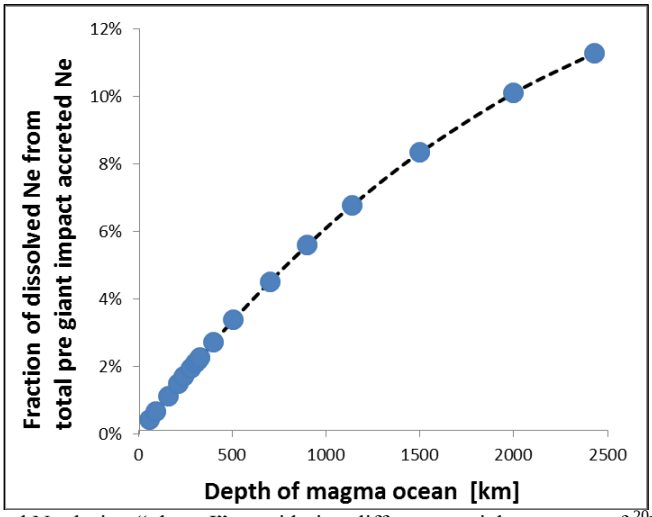

Fig. 3.10: Fraction of dissolved Ne during "phase I" considering different partial pressures of ^{20}Ne as a function of the depth of the early magma ocean. The fraction of dissolved Ne (from the Ne that accreted with the "inner Solar System bodies" after the dissipation of the solar nebula) correlates with the depth of the early magma ocean. The shown maximum value of slightly less than 12% of dissolved ^{20}Ne corresponds to a ≲2% fraction of SW-irradiated material (Figs. 3.11, 3.12) that dissolves into a magma ocean of ~2500 km depth. A fraction of 1% irradiated material already requires an unrealistic magma ocean depth of >10000 km (see text).

Amongst the terrestrial building blocks, dust-sized particles (MMs, IDPs and β-meteorites) with high surface/volume ratios must have been the dominant carriers of the surface-sited solar gases during early accretion. If a steam atmosphere and a magma ocean were present, virtually all neon partitioned into the protoatmosphere (>88%; Fig. 3.10) and incorporation into the proto-mantle was only possible via dissolution into the magma ocean. The Moon-forming giant impact at around 4.45 Ga ago eroded the pre-existing atmosphere, so that the subsequent atmosphere formed by mantle degassing and from the late veneer.

Figure 3.11 shows the fraction of SW-irradiated terrestrial precursor material that is required to establish Earth's mantle Ne inventory in combination with a certain depth of the early magma ocean if the Moon-forming impact expelled 100% of the atmospheric Ne. This relationship is again a function of the Ne isotopic composition of the late veneer, for which ^{20}Ne/^{22}Ne ratios

between 5.2 and 9.2 are considered. It becomes evident that small fractions of irradiated material are already sufficient to explain the terrestrial Ne inventory, even when assuming a relatively shallow magma ocean. In the case the mantle is moderately degassed (Fig. 3.11a) somewhat higher fractions of SW-irradiated material and greater magma ocean depths are required compared to a more strongly degassed mantle (Fig. 3.11b).

The preferred $^{20}Ne/^{22}Ne$ ratio of 8.2 (planetary Ne-A) for the Ne that is delivered by the late veneer requires a mantle degassing of 82% in the case of a moderately degassed mantle and 96% in the case of a strongly degassed mantle. This constrains the fraction of SW-irradiated material for a moderately degassed mantle to 10% for a magma ocean depth of ~320 km and a minimum of SW-irradiated material of 2% for a depth of ~2430 km. For a strongly degassed mantle the limit of 10% applies to a magma ocean depth of ~280 km and a 2% minimum applies to a magma ocean depth of ~1870 km. A fraction of 1% irradiated material only requires unrealistic magma ocean depths of 10590 km and 9880 km, respectively. For each of these and the following cases fractions of SW-irradiated material of ~50% and more are possible but would require unrealistically shallow magma oceans of just several ten km depth (Tab. B7).

For a late veneer contribution with a $^{20}Ne/^{22}Ne$ ratio of 5.2 (9.2), degassing degrees of 89% (69%) and 97% (91%) are required for a moderately degassed mantle and a strongly degassed mantle, respectively. In these cases, a fraction of SW-irradiated material of 10% limits the magma ocean depths to ~520 km (~180 km) and ~470 km (~140 km). For a ratio of 5.2 a minimum fraction of 3% of irradiated material corresponds to ~2640 km depth for a moderately degassed mantle and ~2210 km depth for a strongly degassed mantle, while a fraction of 2% requires unrealistic magma ocean depths of 9480 km and 8870 km. For a ratio of 9.2 a minimum fraction of 2% irradiated material corresponds to ~1080 km for a moderately degassed mantle, while a fraction of 1% requires an unrealistic magma ocean depth of 3300 km. A minimum fraction of 1% corresponds to a magma ocean depth of ~1880 km for a strongly degassed mantle, while fractions <1% imply unrealistic magma ocean depths (Tab. B7).

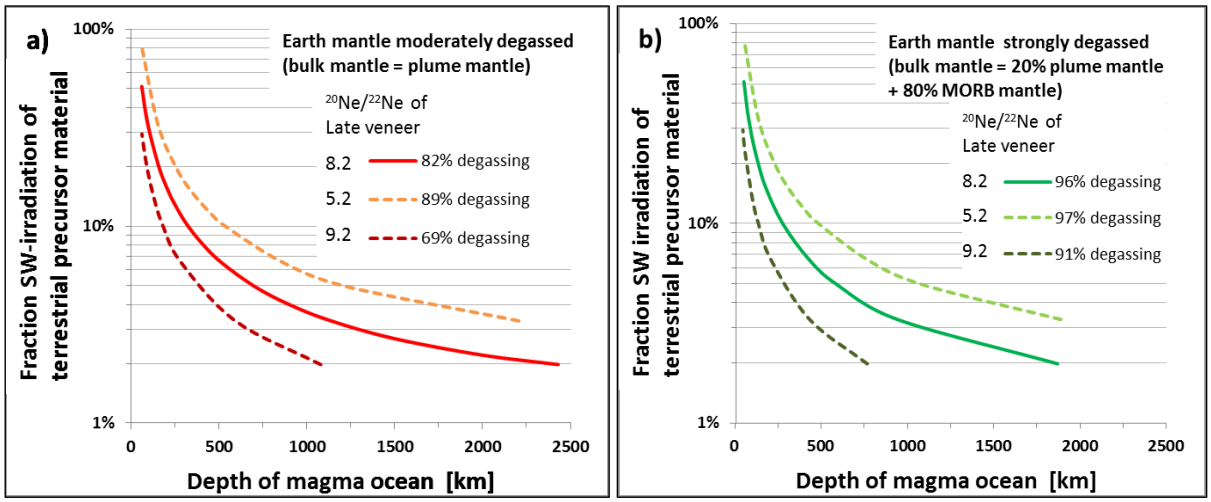

Fig. 3.11: Fraction of SW-irradiated material that is accreted during early "phase I" compared to the depth of the early magma ocean in which the Ne-B component is dissolved. The terrestrial inventory of SW-implanted Ne (Ne-B) is limited by the depth of the magma ocean. The amount of required SW-irradiated material depends on the $^{20}Ne/^{22}Ne$ composition of the late chondritic veneer (5.2–9.2) and also depends on the assumedt degree of mantle degassing. **a)** shows the case for a moderately degassed mantle (69–89% degassing) and **b)** for a strongly degassed mantle (92–98% degassing).

3.5.3 Atmospheric erosion by the Moon-forming impact

Figure 3.12 shows an enlarged view of the lower (up to 12%) range for the fraction of SW-irradiated material required to establish Earth's Ne inventory as a function of the depth of the early magma ocean (see Fig. 3.11), for a late veneer $^{20}Ne/^{22}Ne$ composition of 8.2. In addition to the case of 100% protoatmosphere loss by the giant Moon-forming impact assumed in section 3.5.2, incomplete atmospheric erosion is also considered allowing retention of up to 8% of the Ne in the protoatmosphere. As this Ne becomes part of the secondary atmosphere and adds to the solar neon degassed from the mantle, it is clear that lower fractions of previously irradiated material are needed in this case. For a moderately degassed mantle (Fig. 3.12a) a maximum of ≤1.5% SW-irradiated material applies to a fraction of ≳4% retained Ne and magma ocean depths of ~2500 km. For a strongly degassed mantle (Fig. 3.12b) a maximum of ≤1.5% SW-irradiated material corresponds to a fraction of ≳2% retained Ne and a magma ocean depth of ~2500 km (Tab. B8). The higher the fraction of retained protoatmospheric neon, the less contribution by mantle degassing is required, i.e., for about 8% protoatmosphere Ne retention, the depth of the magma ocean hardly plays a role.

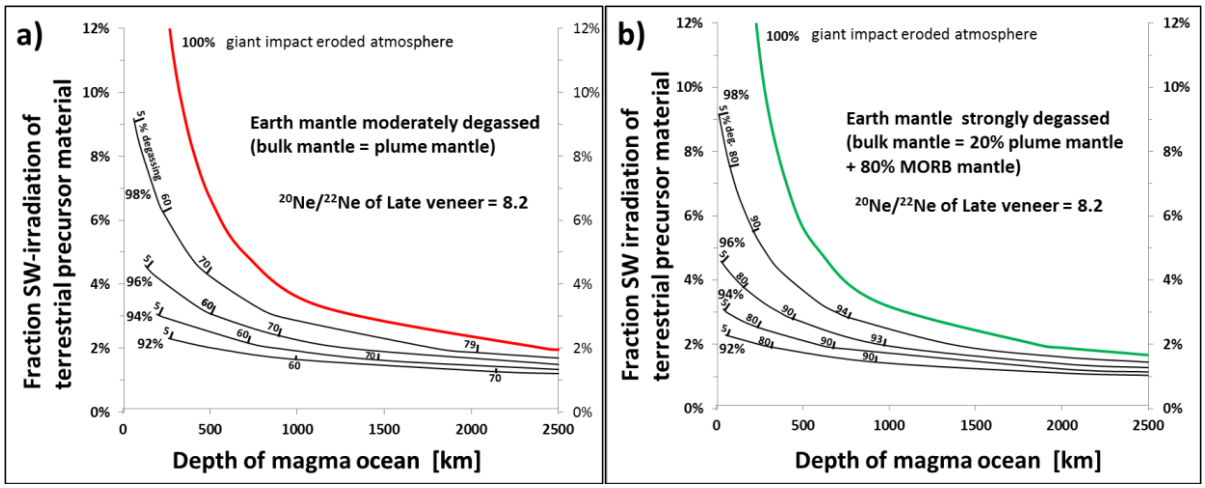

Fig. 3.12: Fraction of SW-irradiated material that is accreted during early "phase I" compared to the depth of the early magma ocean in which the Ne-B component is dissolved. Only the contribution of a late veneer with a $^{20}Ne/^{22}Ne$ composition of 8.2 is modelled for incomplete atmospheric erosion of 98%, 96%, 94% and 92% after the Moon-forming impact for **a)** a moderately degassed mantle and **b)** a strongly degassed mantle. These fractions (black solid lines) are compared to 100% atmospheric erosion (colored solid line) as shown in Figure 3.11. Smaller fractions of SW-irradiated material down to ~1% are needed if the amount of Ne increases from 2%, 4%, 6% up to 8%. The respective amounts of retained Ne require different degrees of mantle degassing (marks on black solid lines) to account for the present-day Ne compositions.

3.5.4 Contributions of outer Solar System bodies

In the model including a magma ocean, all material accreting before the Moon-forming impact is from the inner Solar System and is considered as volatile-poor, containing implanted Ne-B only. Due to the heat of the magma ocean and the steam atmosphere, noble gases from accreting bodies are released into the protoatmosphere and subsequently dissolved into the magma ocean, thereby incorporating solar wind neon into Earth´s mantle. This ignores the possibility that a certain portion of Ne-A may have been brought in by outer Solar System bodies during the first 100 Ma of accretion, causing a shift in the isotope ratios of Ne ratio that becomes dissolved into

Earth's interior towards a more planetary composition. As Ne-B in the model has a $^{20}Ne/^{22}Ne$ ratio of 12.61 (disregarding errors) and a value as low as ~12.5 has been observed for the lower limit values of the Loihi and Galápagos mantle reservoir (see discussion in section 3.2) the admixture of a planetary Ne-A component with a $^{20}Ne/^{22}Ne$ ratio of 8.2 may have been responsible for decreasing the isotopic ratio. For the total delivered ^{20}Ne before the giant impact, a flux from Ne-A (Fig. 3.7) of 20% would be allowed in addition to the flux from Ne-B, if the dissolved $^{20}Ne/^{22}Ne$ ratio in Earth´s mantle has to retain a value of ~12.5. This case, however, applies only to the most intense decrease of the isotopic ratio because it is recognized that most measured pristine mantle values clearly exceed a $^{20}Ne/^{22}Ne$ ratio of ~12.5. Consequently, only lower fractions of Ne-A fluxes might be allowed.

A <20% contribution of outer Solar System bodies to the accreting Earth is therefore fully consistent with current terrestrial accretion scenarios.

3.6 Neon-accretion model without a magma ocean

An alternative mechanism to explain the solar noble gas signatures in Earth's interior is direct incorporation of solid and undegassed SW-irradiated materials during accretion. This scenario implies retention of most of the accumulated gases in the growing planet without being lost by degassing into the protoatmosphere. This model requires that the terrestrial building blocks accreted without the formation of a magma ocean (see section 3.5).

If a magma ocean did not exist, then small accreting particles will directly contribute their solar neon to the solid inner Earth, while larger particles and bodies will release part or virtually all neon by ablation or impact degassing into the atmosphere (Fig. 3.13). When constructing a neon influx model for this scenario, it is important to distinguish between neon delivered to the atmosphere and Ne delivered to the solid Earth. Hence, (partial) degassing of small particles upon atmospheric entry and complete degassing by ablation of meteoritic material during atmospheric passage and/or impact explosion of large crater forming bodies have to be included.

3.6.1 Ablation losses upon atmospheric entry

Depending on mass, size, density, velocity and entry angle micrometeorites suffer variable degrees of heating during their passage through Earth's atmosphere (Flynn, 1989; Toppani et al., 2001; Füri et al., 2013) resulting in different types of MMs such as fine-grained, slightly vesicular unmelted micrometeorites (UnMM), partially melted, highly vesicular scoriaceous micrometeorites (ScMM) and completely melted CSs (Toppani et al., 2001; Füri et al., 2013). Incoming ~50 μm particles with 15-20 km/s entry velocity experience peak temperatures above melting point (1350 °C) for about 2 seconds at altitudes between 85 and 90 km. Grains with a velocity of 20 km/s that were initially larger than 20 μm inescapably undergo melting (Love and Brownlee, 1991; Okazaki et al., 2015) and thermodynamic modeling by Genge (2017) suggests that particles larger than 150 μm with an entry velocity of 12 km/s and an entry angle greater than 10° will completely melt. Completely melted cosmic spherules dominate the MM influx in the >50 μm

fraction and occur in sizes between 50–2280 μm (Taylor et al., 2012; Cordier and Folco, 2014). Effects of progressive heating and evaporation were identified by Taylor et al. (2000) in a classification sequence amongst stony spherules. A comprehensive review of the petrology, geochemistry as well as the classification of micrometeorites into UnMMs, ScMMs, CS, their types and subtypes is provided by Kurat et al. (1994) and Genge et al. (2008).

Atmospheric entry heating moreover causes extensive degassing of noble gases and other volatiles in the upper atmosphere and ScMMs and CSs are expected to retain only diminutive fractions of their initial inventory (Toppani et al., 2003; Füri et al., 2013). In spite of the fact that Osawa et al. (2010) found that about 90% of the Ne and Ar and 95% of the He had been released from MMs that transformed into CSs through severe heating, about 40% of the spherules still show preserved extraterrestrial noble gases features, albeit concentrations are very low (Osawa, 2012). Supporting this, it is obvious from Figures 3.2b and 3.3a,b that cosmic spherules show stronger $^{20}Ne/^{22}Ne$ isotopic fractionation and lower ^{20}Ne concentrations compared to unmelted micrometeorites.

Roughly 60-90% of MM material is lost during atmospheric entry through melting and evaporation according to Cordier and Folco (2014), however most authors favor losses of 90% or more (Love and Brownlee, 1991; Taylor et al., 1998; Briani et al., 2013). According to Mann et al. (2011), objects with a diameter above 200 μm evaporate almost completely at altitudes between 80 and 100 km. Grains with sizes below 50 μm, on the other hand, are able to radiate energy so rapidly that they experience only very little heating during atmospheric descent (Nier and Schlutter, 1990, 1992; Flynn et al., 2003; Osawa, 2012). IDPs with sizes ≤50 μm and velocities <20 km/s can survive atmospheric entry without significant melting (Kehm et al., 2002) and those with 12 km/s do not melt at all (Love and Brownlee, 1991). For surface correlated components like SW-implanted noble gases, analyses of He in seafloor sediments suggest that most of the relevant surface area that contains implanted SW is carried by particles of ~7 μm diameter, for which the temperature during transit through the atmosphere must have remained below the release temperature for He (~600°C) (Farley et al., 1997). Similar to micrometeorites, larger particles suffer considerable ablation during atmospheric entry (Hughes, 1994). A cumulative size frequency distribution compiled for impactors on the upper atmosphere as well as on Earth's surface (Bland and Artemieva, 2006) indicates that atmospheric ablation and evaporation leads to mass losses of >30 to >99% for projectiles between 10^2–10^{20} g depending on the respective mass interval, impact angle, pre-atmospheric velocity as well as on projectile properties. At still larger masses and sufficient impact speeds (>5 km/s; Zahnle et al. 2010), increasing destruction in the atmosphere or on impact (Baldwin and Sheaffer, 1971; Anders, 1989) will cause almost complete ablation or evaporation into the atmosphere.

Figure 3.13 shows the presently delivered average annual mass flux incident on Earth's upper atmosphere and reaching Earth's surface intact or undegassed taking into account vaporization and ablation during atmospheric entry and/or on impact. In this model, the smallest particles (β-meteorites and IDPs) are considered to escape atmospheric entry heating providing intact mass transfer to Earth's surface. Suffering from severe entry heating, micrometeorites lose on average 60 to 90% of their mass to the atmosphere. In the annual mass flux model (Fig. 3.13, Tab. B1), both, the cases for the upper and lower limit vaporization are considered. Since the

transition from MMs to the "large particle" group is considered as being transitional and because cosmic spherules that are classified as micrometeorites are found within this size range (Taylor et al., 2012; Cordier and Folco, 2014), the "large particle" group is tentatively assumed to suffer the same amount of loss (60 to 90%). In the range of the "large bodies" and "very large bodies" a threshold is set at 10^{11} to 10^{12} g: Large bodies below this threshold experience 88 to 99% ablation and evaporation processes (Bland and Artemieva, 2006). Bodies that border on the threshold are modelled to suffer >99% impact erosion. Above 10^{12} g, large bodies and very large bodies are entirely evaporated upon impact (Fig. 3.13).

From the total average mass flux of $2.7*10^{10}$ kg/year (section 3.3.3) that is incident on Earth >99.9% is evaporated during atmospheric entry and/or on impact and is contributed by the largest size regimes (large particles, large bodies and very large bodies) whereas <0.1% is impacting on the surface and contributed by the smallest size regimes (MMs, IDPs and β-meteorites). According to the current particle flux estimate, up to $2.9–7.8*10^{6}$ kg/year reach Earth's surface. IDPs and β-meteorites survive atmospheric entry without being evaporated. From the mass portion that is ablated or evaporated during atmospheric entry and/or on impact, more than 99.9% stems from particle types larger than MMs of which 99.97% is contributed by very large bodies. From the mass portion that survives atmospheric entry and impacting the surface, ~90% is derived by small material (Fig. 3.13, Tab. B1).

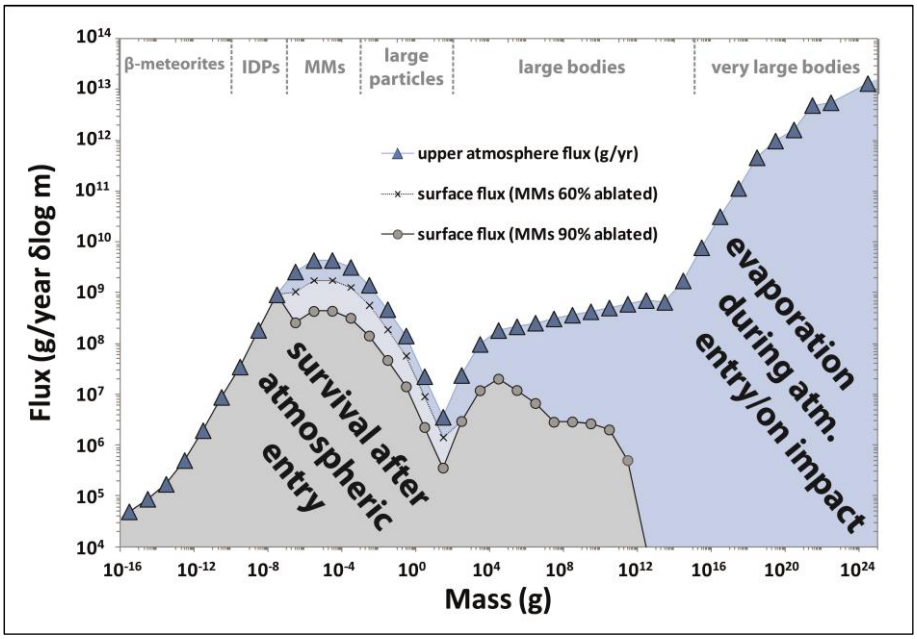

Fig. 3.13: Annual particle flux to Earth's upper atmosphere and surface in g/year vs. mass. The mass of the different particle types ranges from 10^{-16}–10^{25}g (β-meteorites, IDP, MM, large particles, large bodies, very large bodies) and is divided in decadal mass bins. The mass that reaches Earth's surface intact, thereby surviving atmospheric entry without ablation or evaporation is shown in grey, while the mass that is ablated or evaporated during atmospheric entry and/or on impact is shown in blue. For MMs the lighter color indicates the mass that would be lost assuming 90% vaporization instead of 60% (see text for details).

3.6.2 Mass and size dependent Ne flux to Earth's surface

As discussed earlier, the influx of ^{20}Ne to Earth (Tab. B4) is calculated by multiplying the concentration of ^{20}Ne with the mass flux of the respective particle type (Tab. B1). Compared to the

upper atmosphere fluxes (see also Fig. 3.6 and Fig. 3.7) the fluxes to the surface of MMs, IDPs is influenced by atmospheric entry degassing (Fig. 3.14 and Fig. 3.15). Figure 3.14 shows that the smallest IDPs contributes the maximum amount of 2.39*10^6 cm³STP ^{20}Ne to Earth´s surface and β-meteorites deliver their complete neon inventory. As mentioned in section 3.3.4 the IDP size (mean diameter ~9 µm) that annually contributes the maximum amount of ^{20}Ne to the surface is in very good agreement with the value of ~7 µm found by Farley et al. (1997) for particles that carry most surface implanted SW-He to the surface.

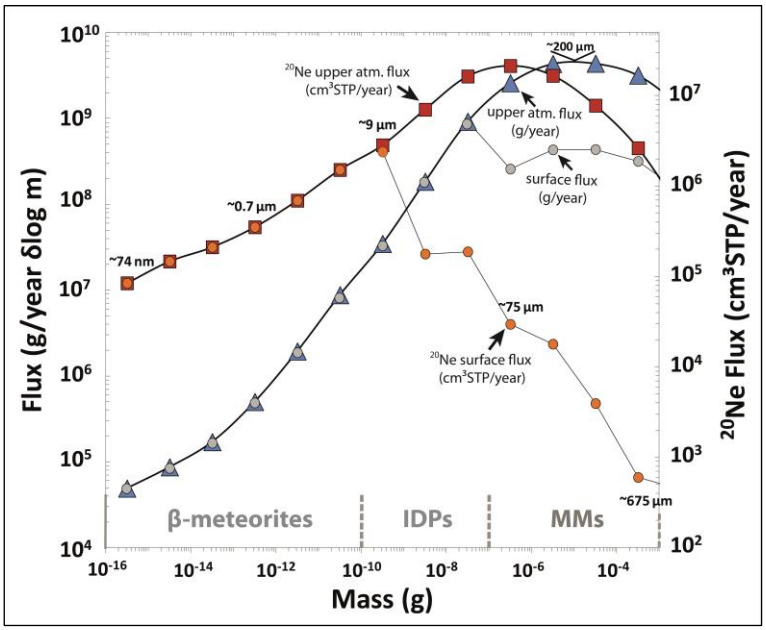

Fig. 3.14: Detail of the particle mass flux from Figure 3.13 for β-meteorites, IDPs and MMs divided in decadal mass bins (blue triangles) and 90% mass loss for MMs (grey circles). The annual 20Ne flux to Earth in cm³STP/year is shown for the same mass intervals (red squares). The maximum ^{20}Ne flux for measured particles to Earth's surface (orange circles) is contributed by IDPs in the mass range 10^{-10} g to 10^{-9} g (mean diameter ~9 µm). Note that approximate sizes of MMs and IDPs are mean values derived from the compilation, sizes of β-meteorites are calculated assuming a spherical particle shape. The mass flux for MMs peaks at ~200 µm whereas the ^{20}Ne flux to the upper atmosphere peaks at ~75 µm and is calculated from the mean ^{20}Ne concentration of the smallest measured IDPs. The graph for the particle flux in g/year (blue triangles and grey circles) corresponds to the ordinate on the left side of the diagram and the graph for the Ne flux in cm³STP/year (orange circles and red squares) corresponds to the ordinate on the right side of the diagram.

Figure 3.15 shows the combined flux of ^{20}Ne for the Ne-A and Ne-B component to the upper atmosphere (see also Fig. 3.7) and the flux of both components to Earth's surface after losses upon atmospheric entry. Compared to the cumulative upper atmosphere Ne flux, approximately 7% of ^{20}Ne reach the Earth's surface surviving atmospheric losses and/or impact evaporation. Only small particles up to MM-sizes that escape severe heating and ablation during the atmospheric entry contribute to the surface flux of the implanted Ne-B component. Larger particles and bodies lose their total surface correlated Ne budget during ablation or on impact, contributing only the Ne-A component to the surface. An exception to that would be meteoritic material that represents reworked irradiated regolith, but for simplicity such material will be neglected in first order considerations. The amount of 5.81*10^6 cm³STP ^{20}Ne that is annually delivered by the Ne-B surface flux with small particles compares to 5.43*10^2 cm³STP/year for the Ne-A surface flux from larger particles and bodies and amounts to 99.99% of the total flux of ^{20}Ne to the surface (Tab. B4).

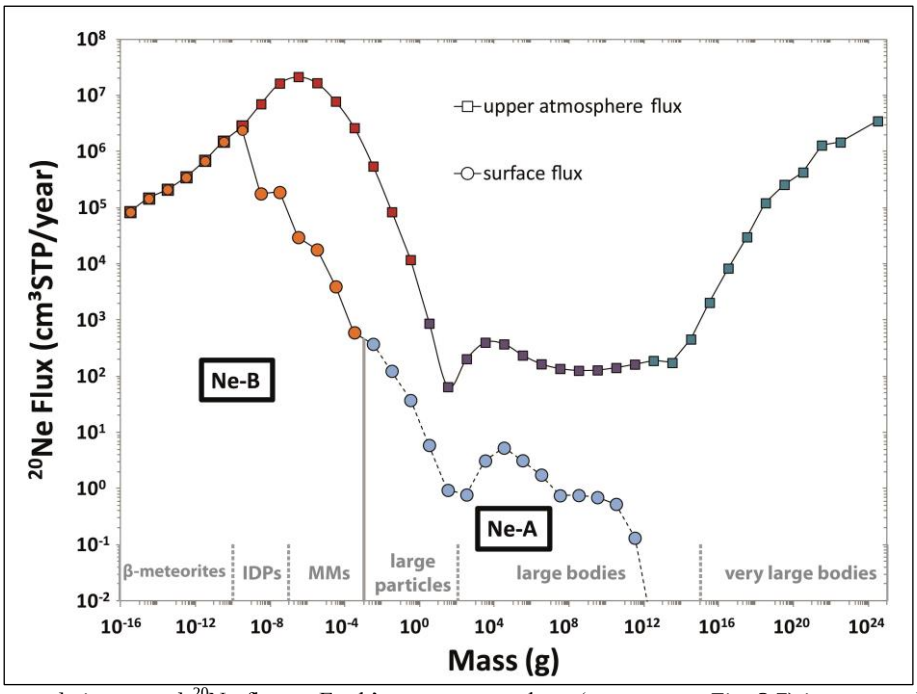

Fig. 3.15: The cumulative annual ^{20}Ne flux to Earth's upper atmosphere (squares, see Fig. 3.7) is compared to the surface flux of ^{20}Ne (circles) which is derived from the accreted mass that survives atmospheric ablation and/or impact (see Fig. 3.13). The cumulative upper atmosphere flux consists of fluxes that are dominated by Ne-B carriers (red squares) and Ne-A carriers (turquois squares) or consists of a mixture of Ne-B and Ne-A carriers (purple squares). The flux of Ne-B to the surface is only contributed by small particles up to MM-sizes whereas larger particles and large bodies deliver the Ne-A component to the surface after loss of the surface sited Ne-B during atmospheric entry ablation. In the diagram, carriers of Ne-B to the surface (β-meteorites, IDP, MM, orange circles) are separated by a straight line from carriers of Ne-A to the surface (large particles, large bodies, blue circes).

3.6.3 Fraction of SW-irradiated material and Ne from the late veneer

In an accretion scenario without a magma ocean the Ne-B inventory of Earth's mantle is no longer a function of the depth of an early magma ocean. It only depends on the amount of SW-irradiated material that was available for direct incorporation into Earth's interior, i.e. particles that reach the surface without severe gas losses during entry through a protoatmosphere or losses caused by impact. It is assumed here that this amount is given by the Ne-B surface flux shown in Figure 3.15 which is derived from the data compilation for IDPs and MMs (section 3.3.4). According to this flux, a ^{20}Ne/^{22}Ne ratio of 12.55 reaches the surface (Tab. B4) that determines the Ne-B like value of the mantle. An additional $8*10^2$ times higher contribution of neon (Ne-A surface flux) from the outer Solar System (Fig. 3.15, Tab. B4) would be necessary to decrease the ^{20}Ne/^{22}Ne ratio below 12.50.

It is furthermore assumed that the ablation processes during entry through a protoatmosphere affected the particles in a similar manner as today´s flux. Assuming a lower entry velocity for inner Solar System particles, these particles would retain a more pristine ^{20}Ne/^{22}Ne ratio, i.e., up to 12.61 and deliver a higher Ne-B value to the surface. The surface flux is used to calculate the Ne inventory of the mantle without consideration of an early magma ocean in "phase I" (Fig. 3.8). All the other flux parameters in "phase I" or "phase II" remain unchanged according to the framework of terrestrial Ne accretion (see section 3.4).

Figure 3.16 shows the fraction of SW-irradiated material from the terrestrial precursor material that is required to establish the terrestrial Ne inventories in dependency of the $^{20}Ne/^{22}Ne$ composition of the late veneer in the case of a moderately and a strongly degassed mantle. It is obvious that, if the late veneer contributes the Ne composition of the present atmosphere ($^{20}Ne/^{22}Ne$ = 9.80) the fraction of SW-irradiated terrestrial precursors is zero. The modeling of 100% atmospheric erosion by the giant Moon-forming impact and a late veneer with a low isotopic ratio of $^{20}Ne/^{22}Ne$ = 5.20 results in fractions of irradiated material of 4.8% and 4.4% for a moderately and strongly degassed mantle, respectively. Lower fractions of irradiated material are needed for higher values for the Ne isotopic ratio delivered by the late veneer. For the preferred planetary ratio ($^{20}Ne/^{22}Ne$ = 8.2) the fractions of irradiated material are 3.0% and 2.6% for a moderately and strongly degassed mantle, respectively.

In case of incomplete atmospheric erosion by the Moon-forming impact, increasing amounts of retained atmospheric Ne lead to decreasing fractions of SW-irradiated materials. Moreover, increasing $^{20}Ne/^{22}Ne$ ratios for the late veneer demand lower degrees of mantle degassing after the giant Moon-forming impact. In case of a moderately degassed mantle, a maximum of 17% retained Ne (83% atmospheric erosion) is still consistent with the delivery of the complete range of possible $^{20}Ne/^{22}Ne$ ratios for the late veneer. Higher values, e.g., 30% retained atmospheric Ne (70% atmospheric erosion) exclude the contribution of a late veneer with $^{20}Ne/^{22}Ne$ >8.6, because the delivered amount of Ne would keep the retained Ne above today's atmospheric inventory even if assuming no degassing after the giant impact. In case of a strongly degassed mantle a portion of 30% retained atmospheric Ne allows the contribution of the complete range of Ne isotopic ratios that have been considered for the late veneer but constrains the fraction of irradiated material to <1% (Tab. B9).

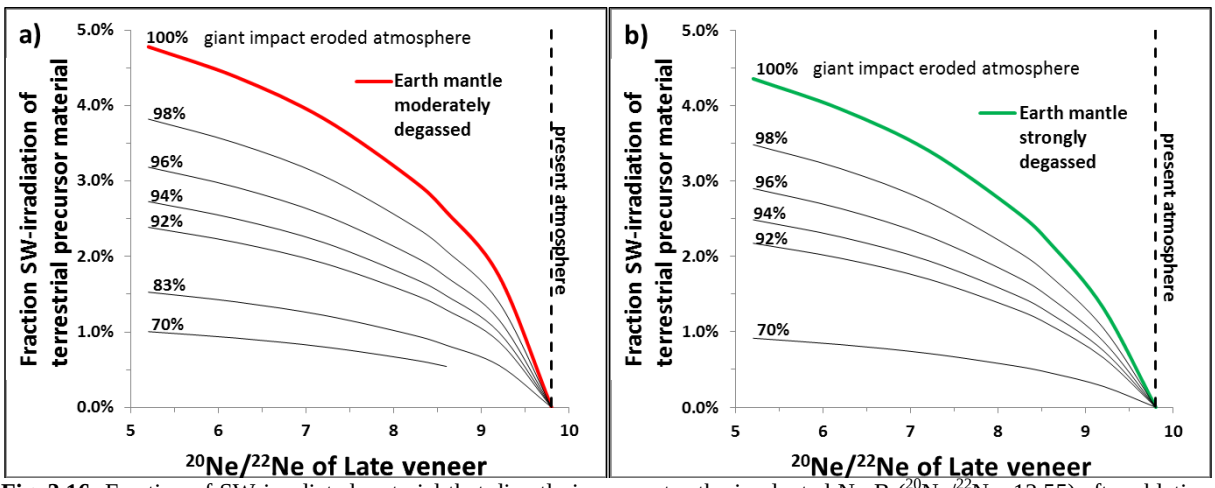

Fig. 3.16: Fraction of SW-irradiated material that directly incorporates the implanted Ne-B ($^{20}Ne/^{22}Ne$=12.55) after ablation during atmospheric entry into Earth's interior during early "phase I" in the absence of a magma ocean as a function of the $^{20}Ne/^{22}Ne$ ratio assumed for the late veneer that is delivered during "phase II". Cases assuming 100% atmospheric erosion by the Moon-forming impact are shown a) for a moderately degassed mantle (red curve) and b) for a strongly degassed mantle (green curve). Both imply decreasing fractions of SW-irradiated precursor material from a maximum fraction of 4.8% and 4.4%, respectively, with increasing values for $^{20}Ne/^{22}Ne$ of the late veneer. Decreasing degrees of mantle degassing apply to an increasing isotopic ratio of the late veneer and are shown in Figure 3.9a for the colored curves. Increasing retention of atmospheric Ne after the giant impact further decreases the fraction of SW-irradiated material as well as the required degree of mantle degassing (see text for details).

3.7 Discussion

No simple model exists so far that describes Earth's accretion history and volatile acquisition, while claiming that all important aspects and parameters have been taken into account. In the previous section, each of the parameters that influence the developed Ne accretion scenario was therefore briefly discussed: the Ne inventory of accreting matter of all sizes, current and past mass fluxes to Earth as well as time dependent fluxes of the Ne-A and Ne-B component, accretion within a gas-shielded disk and after nebular dissipation, dissolution of Ne into the magma ocean, the Moon-forming impact and its consequences and post-lunar delivery of Ne by late accretion. The discussion below focuses on the two competing models for the origin of solar-type neon within Earth (solar wind implantation and solar nebula gas dissolution) and the relation to the presented model. A comprehensive discussion on different models for the origin of light noble gases (He, Ne, and Ar) on Earth is also given in a recent review article by Péron et al. (2018).

The existence of solar-like Ne in Earth's mantle constrains the mechanisms of how Ne and other rare gases were initially incorporated and trapped within the Earth during accretion and how a protoatmosphere was lost afterwards (Porcelli et al., 2001). If Earth accreted within the solar nebula, high concentrations of the light noble gases could have been dissolved from the captured dense solar atmosphere into a magma ocean and could have been transported into the inner Earth through convection (Mizuno et al., 1980; Sasaki and Nakazawa, 1990; Harper and Jacobsen, 1996; Porcelli et al., 2001). The early captured atmosphere would have been subsequently fractionated during hydrodynamic escape triggered by giant impacts and/or intense ultraviolet radiation (EUV) from the young sun (Hunten et al., 1987; Pepin, 1991, 1997, 2006). However, the residual atmospheric composition after hydrodynamic escape (of hydrogen and helium) from a solar-composition gas is different for several components such as CO_2 (63.2 vol%), Ne (21.8 vol%) and N_2 (9.7 vol%) from what we observe today (Lewis et al., 2013; Fegley, 2016 pers. comm.).

In addition, there would presumably have been further modifications due to (non-fractionating) gas losses from the atmosphere and from the interior due to impact erosion (Chyba, 1990; Ahrens, 1993) and the catastrophic Moon-forming event (Benz and Cameron, 1990). Losses from the interior must have also occurred during extensive mantle degassing, most likely linked to the solidification of a magma ocean (Elkins-Tanton, 2008). Overall, these loss processes require a high primordial abundance of noble gases, such as gravitational capture of nebular gas. According to Jaupart et al. (2017), however, dissolution of a captured solar atmosphere seems not to be an appropriate mechanism to account for the neon budget within Earth because this process would only account for less than 2.5% of their best estimate for the Ne concentration of the primitive mantle if the solar nebula completely disappeared before growth of planetary embryos to ~0.2 M_E.

The gravitational capture model indeed requires the growth of protoplanets to at least Mercury to Mars size before nebular dissipation (Porcelli and Pepin, 2011). The results of several numerical models, however, predict timescales of ~30–100 Ma for the formation of the terrestrial planets (Morbidelli et al., 2012 and references therein). Along these lines, Kleine et al. (2002, 2009) used Hf-W chronometry to date core formation on Earth with the conclusion that it was completed not earlier than ~30 Ma after CAI formation and on Mars to have occurred during the

first ~20 Ma of the Solar System, thus supporting a protracted accretion. In contrast, a protoplanetary disk lifetime of ~6 Ma is predicted by Haisch et al. (2001). If so, it would have been dispersed well before completion of terrestrial planet formation, although observational data hint that in some cases disk lifetimes may be as long as tens of millions of years (Pfalzner et al., 2014).

In contrast, the model for incorporating noble gases into the Earth together with the process of solar wind implantation into accreting matter could have taken place after dissipation of disk gas. This enables irradiation of solid surfaces with solar wind and favors the SW-implantation model for the origin of light noble gases on Earth (Podosek et al., 2000; Trieloff et al., 2000, 2002; Trieloff, 2002, 2007; Ballentine et al., 2005; Moreira and Charnoz, 2016; Jaupart et al., 2017; Péron et al., 2017, 2018). The scenario is primarily based on the recognition that neon in Earth´s mantle appears to be isotopically fractionated Ne-B, a typical component resulting from solar wind implantation. In a still dust-rich accretionary environment, early fluxes should have been dominated by SW-implanted light noble gases that contributed large amounts of the Ne-B component after the solar nebula was cleared; therefore, the timing of disk dispersal is crucial in this case.

Before disk gas dissipation SW-implantation is already possible in less opaque off-disk regions (Sasaki, 1991). In regions up to 1.5 AU from the Sun implantation could occur on the surface of the disk and in some parts of the optically thick mid-plane (Moreira and Charnoz, 2016). Vertical movements would then disperse the irradiated particles. A certain amount of irradiated dust grains before the dissipation of the solar nebula would, however, not compromise the described model. Rather it would just serve to decreased the amount of irradiated dust particles required in the presented model.

Irrespective of incorporation of the solar wind irradiated particles before or after disk gas dispersal, the accreted Ne-B component should resemble the Ne inventory of currently found SW-irradiated particles that remained largely unaffected by atmospheric entry heating. Following Nier and Schlutter (1990, 1992) and Love and Brownlee (1991) this is probably the case for the smallest IDPs (10^{-10} to 10^{-9} g) that are available for measurement in the laboratory. This is furthermore justified by the observation of overall increasing ^{20}Ne concentrations and $^{20}Ne/^{22}Ne$ ratios, with decreasing particle size, exhibiting a maximum mean concentration of $6.92*10^{-2}$ cm^3STP/g and a maximum mean isotopic ratio of 12.61±0.41 (Fig. 3.3) for this range. Once dissolved from the protoatmosphere and incorporated within Earth, the Ne-B component stays unaltered after solidification of the magma ocean. A late accreted Ne component of planetary Ne-A is unable to modify the Ne composition within Earth's interior since substantia subduction of Ne is regarded unlikely (Staudacher and Allègre, 1988; Holland and Ballentine, 2006). In this way, the $^{20}Ne/^{22}Ne$ ratio of 12.61±0.41 that is here compiled from the smallest IDPs directly mirrors the incorporated Ne-B component that is sampled as the pristine mantle end-member for Ne.

In consequence, the incorporation of solar-like neon by dissolution of SW-implanted Ne in cosmic dust particles must have happened during the existence of a magma ocean and therefore almost exclusively before the Moon-forming impact or shortly after. Constraining the acquisition of Ne to the magma ocean stage would also apply to scenarios that involve dissolution of a captured solar nebula. Of course, both types of acquisition described in the two models may have contributed to Earth's Ne budget, to different extents at different periods during Earth's accretion.

Despite questioning the solar gas dissolution origin for neon and advocating the solar wind implantation in solid grains, Péron et al. (2016) discussed the possibility of mixing both models. According to their estimate, ~30% of terrestrial lower mantle neon could derive from dissolution of solar nebula gas during formation of the Earth.

Here, to the qualitative discussion of the solar wind irradiation model (Péron et al., 2018), quantitative constraints from particle fluxes and size dependent Ne concentrations are added. The present study shows that the SW-implantation model alone may well be even quantitatively able to explain Earth's neon inventories and that this process may have a greater importance for the acquisition of volatiles on Earth than previously acknowledged.

3.8 Conclusions

The Ne accretion model proposes the origin of the solar noble gas signatures of Earth's interior by the accretion of solar wind-irradiated material during an early episode of terrestrial formation, shortly after the dissipation of the solar nebula. A significant contribution of dust-sized particles with high surface/volume ratios during the early acquisition of terrestrial volatiles is required to explain Earth's mantle signatures. Starting from actually observed cosmic dust properties like particle fluxes to Earth and Ne inventories, the model provides evidence for the feasibility of the SW-implantation model to explain the origin of solar Ne within Earth.

Within the model, solubility-controlled ingassing of the accreted Ne into a magma ocean that underlies an insulating steam atmosphere or direct incorporation of SW-irradiated particles determine the amount of Ne-B in the mantle. Ne-B degassed after the giant Moon-forming impact, and possibly a small fraction of the protoatmosphere survived the giant impact. These mix with the contribution of a late veneer with a "planetary Ne" component, which completes the atmospheric Ne inventory and generates the atmospheric $^{20}Ne/^{22}Ne$ ratio of 9.80.

Detailed results of the study are as follows:

1) High Ne-B concentrations of accreting material correlate with low particle masses (small (small sizes, thus, high surface/volume ratio). The maximum present-day Ne-flux to Earth's surface is contributed by IDPs with sizes that peak at ~9 µm (10^{-10}–10^{-9} g). The maximum Ne-flux to the upper atmosphere is contributed by MMs with sizes of ~75 µm (10^{-7}–10^{-6} g). The mean $^{20}Ne/^{22}Ne$ ratio of 12.61±0.41 of the smallest measured IDPs represents the SW-Ne-saturated outermost particle layer and is incorporated in all particles before atmospheric entry losses. This ratio determines the Ne inventory of volatile-poor "inner Solar System bodies" that accreted to form Earth.
2) The isotopic composition of Ne added by the late veneer has a strong influence on the inferred degree of mantle degassing after the Moon-forming impact. A late veneer of ~2.26% M_E with the favored planetary $^{20}Ne/^{22}Ne$ ratio of 8.2 contributes ~53% of the atmospheric ^{20}Ne and requires a degree of mantle degassing between ~82 and 96%.
3) *In the case of accretion with an early magma ocean:* A fraction of less than 12% of the pre-giant impact accreted Ne is dissolved into an early magma ocean with a maximum depth of less than 2500 km. The dissolved Ne component has a $^{20}Ne/^{22}Ne$ ratio of 12.61±0.41 and is

consistent with all literature data given for the pristine lower mantle source. Low fractions of irradiated material are sufficient to explain the terrestrial Ne inventory, even assuming a relatively shallow magma ocean. A magma ocean of a few hundred km depth constrains the fraction of SW-irradiated material to less than 10%, whereas a depth of more than 1000 km is consistent with fractions of less than ~5%. In any case, a minimum of ≳1% SW-irradiated material is needed to explain the terrestrial Ne inventories.

The Ne inventory and isotopic ratios of Earth's atmosphere and mantle can be reconciled only if the amount of pre-existing atmospheric Ne that is retained after the Moon-forming impact is small (≲8%, if any at all).

4) *In the case without an early magma ocean:* Low fractions of SW-irradiated material that are directly incorporated in Earth's interior are sufficient to explain the terrestrial Ne inventories. The accretion of SW-irradiated particles including atmospheric ablation effects generates a $^{20}Ne/^{22}Ne$ ratio of 12.55 in Earth's mantle. This value is identical to the mantle endmember of 12.49±0.06 identified by Trieloff et al. (2000). If the late veneer delivered a low $^{20}Ne/^{22}Ne$ ratio of 5.2, a maximum of ~4.8% irradiated material is required. For the preferred late veneer Ne ratio of 8.2 the required fraction of irradiated material decreases to ~3%. If more than 30% of Ne were retained after the giant Moon-forming impact, the required fraction of SW-irradiated material decreases to less than 1%.
5) The model does not put constraints on the particular point in time for terrestrial Ne accretion, neither for Ne accretion prior to the giant Moon-forming impact in a protoplanetary disk that was cleared from gas, nor for the contribution of planetary Ne by the late veneer. This problem needs to be addressed by studies involving noble gas tracers such as the time sensitive $^{129}I/^{129}Xe$ system.

All in all, it is concluded that the acquisition of sufficient Ne-B and its incorporation into Earth´s mantle is not a major problem, as the accreted material most likely contained a dust population of which only a small fraction needs to be irradiated by the solar wind after solar nebula dissipation. The quantitative results underline the importance of the solar wind implantation model to explain the origin of light solar noble gases within Earth and may point towards a possible explanation for the acquisition of other volatiles on Earth.

Ne-A contributions before the Moon-forming impact were likely small, and would hardly change the isotopically solar neon composition of a protoatmosphere that dissolved into the magma ocean or influence directly accreting solid materials in scenarios without a magma ocean. Establishing the isotopic signature of atmospheric neon requires addition of a Ne-A type component, likely by post lunar impact accretion of a late veneer.

4 Summary and prospects

The research presented here offers new insights into the field of noble gas geo- and cosmochemistry and implies constraints for Earth's core as potential source reservoir for light primordial noble gases (Chapter 2) and for the origin and early acquisition of volatiles, in particular Ne, on Earth (Chapter 3). Detailed conclusions of the individual noble gas studies are to be taken from the respective chapters. Remaining problems and open questions that arise from both studies offer chances for further investigations and are pointed out below.

The model involving Earth's core as possible reservoir of primordial noble gases and source of solar-like Ne in Earth's mantle, formerly recognized as rather speculative, gains more importance as it is shown in Chapter 2 that metal in the iron meteorite Washington County is unambiguously identified as carrier of trapped light solar noble gases. If the origin of light solar noble gases in Washington County through SW-irradiation is valid, then the SW-implantation model further imposes that irradiation of <1% of terrestrial precursor material which gained noble gases in abundances similar to Washington County and which formed terrestrial precursor metal is sufficient to account for Ne concentrations in Earth's core that satisfy observed mantle fluxes.

The model must now be reinforced by confirming the presence of light solar noble gases within the metal or minor inclusions in other iron meteorites, such as Kavarpura (Murty et al., 2008). First, this can be achieved by a thorough data compilation of iron meteorites that possibly contain solar noble gases starting with irons of the groups IIIAB and IIIB which are related to Washington County and possibly share a common evolutionary background. Second, the selected candidates have to be analyzed for noble gases. The reinvestigation of Kavarpura and the newly discovered spinel phases in Washington County may furthermore reveal minor silicate inclusions as possible noble gas carriers in iron meteorites.

In contrast to considerations that SW-irradiation in a "gas-poor" environment after solar nebula dissipation might not lead to implantation of solar Ne abundances that are sufficient to explain the terrestrial Ne inventory, the SW-implantation model is found in Chapter 3 to be able to account quantitatively for the terrestrial mantle Ne budget if only a fraction of a few % of the total terrestrial precursor material was irradiated and was loaded with the surface implanted Ne-B component. The accreted Ne-B signature must have been overwhelmingly contributed by dust-sized particles with high surface to volume ratio containing high amounts of surface implanted components. Delivery must have happened before the Moon-forming impact during early terrestrial accretion when incorporation of Ne-B into the interior of Earth was possible through dissolution into a magma ocean, or direct incorporation during dry accretion, while completion of the atmospheric reservoir was achieved during a late chondritic veneer contributing a planetary Ne-A component that admixed to a degassed solar Ne-B component from the interior of Earth.

Refining of the presented model calculations is further possible if additional Ne data would be available to reinforce the basic input data. As the model is essentially based on the maximum average Ne concentration (^{20}Ne: $6.92*10^{-2}$ cm³STP/g) and ^{20}Ne/^{22}Ne isotopic ratio (12.61±0.41) of a limited number of small IDPs, additional measurements of similarly small or even smaller particles would yield important information. A major issue will remain in determining the exact

distribution of the implanted Ne-B component in the surface of irradiated particles and the thickness of the SW-saturated outermost particle shell. Here, the model results will be certainly influenced if the assumed equal surface distribution and the Ne implantation depth of 50 nm that is assumed to represents the thickness of the particle shell are modified. The application of a more sophisticated model of early dust fluxes during accretion would furthermore sustain the validity of the model. As the only time constraint for the incorporation of Ne-B into Earth' interior is the pre-lunar period, the implementation of radiogenic noble gas isotopes (^{40}Ar and ^{129}Xe) into the model could set further limits for the timing of accretion. This, however, requires a thorough data compilation (similar to Ne) for ^{40}Ar and ^{129}Xe data of cosmic dust and demands more measurements, especially for Xe isotopes, of IDPs and MMs. Because the existing models for the origin of light solar noble gases within Earth (SW-implantation model or solar nebula dissolution model) are partly built on top of the maximum measured ^{20}Ne/^{22}Ne values of the solar-like mantle end-member a re-examination and re-assessment of the Ne composition would validate the relevance of either model.

Collectively, the noble gas studies carried out above suggest that only a small fraction of SW-irradiated material is needed to generate the Ne inventories observed on Earth. The significance of surface implanted SW in cosmic dust for the acquisition of Ne on Earth highlights the importance of a dust-sized component during planetary accretion. A SW-irradiated dust component might have also been an important carrier of other volatile elements during accretion. It was shown by Bradley et al. (2014) that water (H_2O, liquid or vapor) is detectable in vesicles within space-weathered surfaces of IDPs that are produced by irradiation with the solar wind. If water in surfaces of dust particles is a common byproduct of SW-irradiation, high early accretionary dust fluxes might also imply an important delivery of water to Earth. Péron et al. (2017) furthermore advocated SW-irradiation and implantation of ions with a solar nebula δD value of -870‰ to infer a possible explanation of the low δD value of -218‰ measured for the lower mantle (Hallis et al., 2015). Hence, this could point towards a source for water on Earth. Another important property of IDPs is their ability to escape atmospheric entry heating and their potential to carry intact organic compounds to Earth's surface. According to Anders (1989), IDPs in the mass range between 10^{-12}–10^{-6} g currently deliver 320 tons/year intact organics to Earth. Early IDP fluxes, 4.4 Ga ago, may have delivered intact exogenous organics of as much as 10^6 tons/year which might represent an inventory for the origin of life on Earth (Chyba and Sagan, 1992). During the period preceding the origin of life, IDPs and MMs may have not only been the main source for organic carbon on Earth but also for nitrogen as both elements seem to occur in association (Matrajt et al., 2003).

A combined study of the elemental and isotopic noble gas inventory of IDPs that integrates the investigation of other volatile components (H, C, N) seems therefore to be highly promising to provide relevant results for tracing the origin and evolution of volatiles on Earth and to decipher sources for the ingredients of the origin of life on Earth. If acquisition of considerable amounts of highly volatile elements during accretion of SW-irradiated cosmic dust and/or volatile-rich IDPs is a suitable explanation for Earth's volatile budget this certainly implies constraints for the source of volatiles on other terrestrial planets. These questions, however, have to be resolved in future studies.

5 Reference list

Abe, Y. (1993) Physical state of the very early Earth. *Lithos* **30**, 223–235.

Ahrens, T.J. (1993) Impact Erosion of Terrestrial Planetary Atmospheres. *Annual Review of Earth and Planetary Sciences* **21**, 525–555.

Albarède, F. (2009) Volatile accretion history of the terrestrial planets and dynamic implications. *Nature* **461**, 1227–1233.

Albarède, F., Ballhaus, C., Blichert-Toft, J., Lee, C.T., Marty, B., Moynier, F. and Yin, Q.Z. (2013) Asteroidal impacts and the origin of terrestrial and lunar volatiles. *Icarus* **222**, 44–52.

Alexander, R.D., Clarke, C.J. and Pringle, J.E. (2006) Photoevaporation of protoplanetary discs – II. Evolutionary models and observable properties. *Monthly Notices of the Royal Astronomical Society* **369**, 229–239.

Allègre, C.J., Staudacher, T. and Sarda, P. (1987) Rare gas systematics: formation of the atmosphere, evolution and structure of the Earth's mantle. *Earth and Planetary Science Letters* **81**, 127–150.

Ammon, K., Masarik, J. and Leya, I. (2008) Noble gases in Grant and Carbo and the influence of S- and P-rich mineral inclusions on the ^{41}K-^{40}K dating system. *Meteoritics & Planetary Science* **43**, 685–699.

Ammon, K., Masarik, J. and Leya, I. (2009) New model calculations for the production rates of cosmogenic nuclides in iron meteorites. *Meteoritics & Planetary Science* **44**, 485–503.

Anders, E. (1989) Pre-biotic organic matter from comets and asteroids. *Nature* **342**, 255–257.

Arrhenius, G. and Lepland, A. (2000) Accretion of Moon and Earth and the emergence of life. *Chemical Geology* **169**, 69–82.

Baecker, B. (2014) Primordial and other Noble Gases in Micrometeorites (Diss.). Heidelberg, p. 326.

Bajo, K.-I., Akaida, T., Ohashi, N., Noguchi, T., Nakamura, T., Nakamura, Y., Sumino, H. and Nagao, K. (2011) Single grain noble gas analysis of Antarctic micrometeorites by stepwise heating method with a newly constructed miniature furnace. *Earth, Planets and Space* **63**, 1097–1111.

Baldwin, B. and Sheaffer, Y. (1971) Ablation and breakup of large meteoroids during atmospheric entry. *Journal of Geophysical Research* **76**, 4653–4668.

Ballentine, C.J., Marty, B., Sherwood Lollar, B. and Cassidy, M. (2005) Neon isotopes constrain convection and volatile origin in the Earth's mantle. *Nature* **433**, 33–38.

Bartoschewitz, R., Appel, P., Barrat, J.-A., Bischoff, A., Caffee, M.W., Franchi, I.A., Gabelica, Z., Greenwood, R.C., Harir, M., Harries, D., Hochleitner, R., Hopp, J., Laubenstein, M., Mader, B., Marques, R., Morlok, A., Nolze, G., Prudêncio, M.I., Rochette, P., Ruf, A., Schmitt-Kopplin, P., Seemann, E., Szurgot, M., Tagle, R., Wach, R.A., Welten, K.C., Weyrauch, M. and Wimmer, K. (2017) The Braunschweig meteorite – a recent L6 chondrite fall in Germany. *Chemie der Erde* **77**, 207-224.

Basford, J.R., Dragon, J.C., Pepin, R.O., Coscio, M.R., Jr. and Murthy, V.R. (1973) Krypton and xenon in lunar fines, *4th Lunar and Planetary Science Conference Proceedings*, 1915–1955.

Becker, L. and Pepin, R.O. (1982) Solar wind noble gases in the Washington County iron meteorite. *Meteoritics* **17**, 182–183.

Becker, R.H. and Pepin, R.O. (1984) Solar composition noble gases in the Washington County iron meteorite. *Earth and Planetary Science Letters* **70**, 1–10.

Becker, R.H. and Pepin, R.O. (1987) Solar composition noble gases in the Washington County iron meteorite: a correction. *Earth and Planetary Science Letters* **84**, 356.

Becker, R.H. and Pepin, R.O. (1991) Composition of solar wind noble gases released by surface oxidation of a metal separate from the Weston meteorite. *Earth and Planetary Science Letters* **103**, 55–68.

Benkert, J.-P., Baur, H., Signer, P. and Wieler, R. (1993) He, Ne, and Ar from the solar wind and solar energetic particles in lunar ilmenites and pyroxenes. *Journal of Geophysical Research: Planets* **98**, 13147–13162.

Benz, W. and Cameron, A.G.W. (1990) Terrestrial effect of the Giant Impact, in: Newsom, H.E., Jones, J.H. (Eds.), *Origin of the Earth*. Oxford University Press, Oxford, pp. 61–67.

Bhandari, N., Lal, D., Rajan, R.S., Arnold, J.R., Marti, K. and Moore, C.B. (1980) Atmospheric ablation in meteorites: A study based on cosmic ray tracks and neon isotopes. *Nuclear Tracks* **4**, 213–262.

Black, D.C. (1972) On the origins of trapped helium, neon and argon isotopic variations in meteorites—I. Gas-rich meteorites, lunar soil and breccia. *Geochimica et Cosmochimica Acta* **36**, 347–375.

Black, D.C. and Pepin, R.O. (1969) Trapped neon in meteorites — II. *Earth and Planetary Science Letters* **6**, 395–405.

Bland, P.A. and Artemieva, N.A. (2006) The rate of small impacts on Earth. *Meteoritics & Planetary Science* **41**, 607–631.

Bottke Jr, W.F., Durda, D.D., Nesvorný, D., Jedicke, R., Morbidelli, A., Vokrouhlický, D. and Levison, H. (2005) The fossilized size distribution of the main asteroid belt. *Icarus* **175**, 111–140.

Bradley, J.P., Ishii, H.A., Gillis-Davis, J.J., Ciston, J., Nielsen, M.H., Bechtel, H.A. and Martin, M.C. (2014) Detection of solar wind-produced water in irradiated rims on silicate minerals. *Proceedings of the National Academy of Sciences of the United States of America* **111**, 1732–1735.

Briani, G., Pace, E., Shore, S.N., Pupillo, G., Passaro, A. and Aiello, S. (2013) Simulations of micrometeoroid interactions with the Earth atmosphere. *Astronomy & Astrophysics* **552**, A53.

Buchwald, V.F. (1975) *Handbook of Iron Meteorites: Their History, Distribution, Composition and Structure*. University of California Press.

Busemann, H., Baur, H. and Wieler, R. (2000) Primordial noble gases in "phase Q" in carbonaceous and ordinary chondrites studied by closed-system stepped etching. *Meteoritics & Planetary Science* **35**, 949–973.

Canup, R.M. (2004) Simulations of a late lunar-forming impact. *Icarus* **168**, 433–456.

Canup, R.M. (2008) Accretion of the Earth. *Philosophical Transactions of the Royal Society A: Mathematical, Physical and Engineering Sciences* **366**, 4061–4075.

Canup, R.M. and Asphaug, E. (2001) Origin of the Moon in a giant impact near the end of the Earth's formation. *Nature* **412**, 708–712.

Canup, R.M. and Righter, K. (eds.) (2000) *Origin of the Earth and Moon*. University of Arizona Press, Tuscon. 555pp.

Cech, R.E. (1962) Metallography of the Washington County Meteorite. *Geochimica et Cosmochimica Acta* **26**, 993–998.

Ceplecha, Z., Borovička, J., Elford, W.G., ReVelle, D.O., Hawkes, R.L., Porubčan, V. and Šimek, M. (1998) Meteor Phenomena and Bodies. *Space Science Reviews* **84**, 327–471.

Chou, C.-L. (1978) Fractionation of siderophile elements in the earth's upper mantle, *9th Lunar and Planetary Science Conference Proceedings*, pp. 219–230.

Chyba, C.F. (1990) Impact delivery and erosion of planetary oceans in the early inner Solar System. *Nature* **343**, 129–133.

Chyba, C.F. and Hand, K.P. (2006) Comets and Prebiotic Organic molecules on Early Earth, in: Thomas, P., Hicks, R., Chyba, C., McKay, C. (Eds.), *Comets and the Origin and Evolution of Life*. Springer Berlin Heidelberg, pp. 169–206.

Chyba, C.F. and Sagan, C. (1992) Endogenous production, exogenous delivery and impact-shock synthesis of organic molecules: an inventory for the origins of life. *Nature* **355**, 125–132.

Claeys, P. and Morbidelli, A. (2011) Late Heavy Bombardment, in: Gargaud, M., Amils, R., Quintanilla, J.C., Cleaves, H.J., Irvine, W.M., Pinti, D.L., Viso, M. (Eds.), *Encyclopedia of Astrobiology*. Springer Berlin Heidelberg, Berlin, Heidelberg, pp. 909–912.

Colin, A., Moreira, M., Gautheron, C. and Burnard, P. (2015) Constraints on the noble gas composition of the deep mantle by bubble-by-bubble analysis of a volcanic glass sample from Iceland. *Chemical Geology* **417**, 173–183.

Cordier, C. and Folco, L. (2014) Oxygen isotopes in cosmic spherules and the composition of the near Earth interplanetary dust complex. *Geochimica et Cosmochimica Acta* **146**, 18–26.

Craig, H., Clarke, W.B. and Beg, M.A. (1975) Excess ^{3}He in deep water on the East Pacific Rise. *Earth and Planetary Science Letters* **26**, 125–132.

Cremonese, G., Borin, P., Martellato, E., Marzari, F. and Bruno, M. (2012) New Calibration of the Micrometeoroid Flux on Earth. *The Astrophysical Journal Letters* **749**, L40.

de Vries, J., Nimmo, F., Melosh, H.J., Jacobson, S.A., Morbidelli, A. and Rubie, D.C. (2016) Impact-induced melting during accretion of the Earth. *Progress in Earth and Planetary Science* **3**, 10.1186/s40645-40016-40083-40648.

Dixon, E.T., Honda, M., McDougall, I., Campbell, I.H. and Sigurdsson, I. (2000) Preservation of near-solar neon isotopic ratios in Icelandic basalts. *Earth and Planetary Science Letters* **180**, 309–324.

Drolshagen, G., Koschny, D., Drolshagen, S., Kretschmer, J. and Poppe, B. (2017) Mass accumulation of earth from interplanetary dust, meteoroids, asteroids and comets. *Planetary and Space Science* **143**, 21–27.

Eberhardt, P., Eugster, O. and Marti, K. (1965) A Redetermination of the Isotopic Composition of Atmospheric Neon. *Z. Naturforsch A* **20**(4), 623–624.

Eberhardt, P., Geiss, J., Graf, H., Grögler, N., Krähenbühl, U., Schwaller, H., Schwarzmüller, J. and Stettler, A. (1970) Trapped solar wind noble gases, exposure age and K/Ar-age in Apollo 11 lunar fine material. *Proceedings of the Apollo 11 Lunar Science Conference*, 1037–1070.

Elkins-Tanton, L.T. (2008) Linked magma ocean solidification and atmospheric growth for Earth and Mars. *Earth and Planetary Science Letters* **271**, 181–191.

Elkins-Tanton, L.T. (2012) Magma Oceans in the Inner Solar System. *Annual Review of Earth and Planetary Sciences* **40**, 113–139.

Engrand, C. and Maurette, M. (1998) Carbonaceous micrometeorites from Antarctica. *Meteoritics & Planetary Science* **33**, 565–580.

Engrand, C., McKeegan, K.D., Leshin, L.A., Herzog, G.F., Schnabel, C., Nyquist, L.E. and Brownlee, D.E. (2005) Isotopic compositions of oxygen, iron, chromium, and nickel in cosmic spherules: Toward a better comprehension of atmospheric entry heating effects. *Geochimica et Cosmochimica Acta* **69**, 5365–5385.

Eugster, O. (2003) Cosmic-ray Exposure Ages of Meteorites and Lunar Rocks and Their Significance. *Chemie der Erde - Geochemistry* **63**, 3–30.

Eugster, O., Herzog, G.F., Marti, K. and Caffee, M.W. (2006) Irradiation Records, Cosmic-Ray Exposure Ages, and Transfer Times of Meteorites, in: Lauretta, D.S., McSween, H.Y. (Eds.), *Meteorites and the Early Solar System II*. University of Arizona Press, Tucson, pp. 829–851.

Farley, K.A., Love, S.G. and Patterson, D.B. (1997) Atmospheric entry heating and helium retentivity of interplanetary dust particles. *Geochimica et Cosmochimica Acta* **61**, 2309–2316.

Fegley, B.J., Jacobson, N.S., Williams, K.B., Plane, J.M.C., Schaefer, L. and Lodders, K. (2016) Solubility of Rock in Steam Atmospheres of Planets. *The Astrophysical Journal* **824**, 103.

Flynn, G.J. (1989) Atmospheric entry heating: A criterion to distinguish between asteroidal and cometary sources of interplanetary dust. *Icarus* **77**, 287–310.

Flynn, G.J., Keller, L.P., Feser, M., Wirick, S. and Jacobsen, C. (2003) The origin of organic matter in the solar system: evidence from the interplanetary dust particles. *Geochimica et Cosmochimica Acta* **67**, 4791–4806.

Füri, E., Aléon-Toppani, A., Marty, B., Libourel, G. and Zimmermann, L. (2013) Effects of atmospheric entry heating on the noble gas and nitrogen content of micrometeorites. *Earth and Planetary Science Letters* **377–378**, 1–12.

Genda, H. and Abe, Y. (2003) Survival of a proto-atmosphere through the stage of giant impacts: the mechanical aspects. *Icarus* **164**, 149–162.

Genda, H. and Abe, Y. (2005) Enhanced atmospheric loss on protoplanets at the giant impact phase in the presence of oceans. *Nature* **433**, 842–844.

Genge, M.J. (2017) The entry heating and abundances of basaltic micrometeorites. *Meteoritics & Planetary Science* **52**, 1000–1013.

Genge, M.J., Engrand, C., Gounelle, M. and Taylor, S. (2008) The classification of micrometeorites. *Meteoritics & Planetary Science* **43**, 497–515.

Gomes, R., Levison, H.F., Tsiganis, K. and Morbidelli, A. (2005) Origin of the cataclysmic Late Heavy Bombardment period of the terrestrial planets. *Nature* **435**, 466–469.

Grimberg, A., Baur, H., Bochsler, P., Bühler, F., Burnett, D.S., Hays, C.C., Heber, V.S., Jurewicz, A.J.G. and Wieler, R. (2006) Solar Wind Neon from Genesis: Implications for the Lunar Noble Gas Record. *Science* **314**, 1133–1135.

Grotheer, E.B. and Livi, S.A. (2014) Small meteoroids' major contribution to Mercury's exosphere. *Icarus* **227**, 1–7.

Grün, E., Zook, H.A., Fechtig, H. and Giese, R.H. (1985) Collisional balance of the meteoritic complex. *Icarus* **62**, 244–272.

Haisch, K.E.J., Lada, E.A. and Lada, C.J. (2001) Disk Frequencies and Lifetimes in Young Clusters. *The Astrophysical Journal Letters* **553**, L153–L156.

Halliday, A.N. (2013) The origins of volatiles in the terrestrial planets. *Geochimica et Cosmochimica Acta* **105**, 146–171.

Halliday, A.N. and Wood, B.J. (2009) How Did Earth Accrete? *Science* **325**, 44–45.

Hallis, L.J., Huss, G.R., Nagashima, K., Taylor, G.J., Halldórsson, S.A., Hilton, D.R., Mottl, M.J. and Meech, K.J. (2015) Evidence for primordial water in Earth's deep mantle. *Science* **350**, 795–797.

Hansen, B.M.S. (2009) Formation of the Terrestrial Planets from a Narrow Annulus. *The Astrophysical Journal* **703**, 1131–1140.

Harper, C.L. and Jacobsen, S.B. (1996) Noble Gases and Earth's Accretion. *Science* **273**, 1814–1818.

Hartmann, L. (1999) *Moons and Planets, 4th Edition*. Wadsworth, Belmont 456pp.

Hartmann, W.K., Ryder, G., Dones, L. and Grinspoon, D. (2000) The Time-Dependent Intense Bombardment of the Primordial Earth/Moon System, in: Canup, R.M., Righter, K. (Eds.), *Origin of the Earth and Moon*. University of Arizona Press, Tuscon, Arizona, pp. 493–512.

Heber, V.S., Wieler, R., Baur, H., Olinger, C., Friedmann, T.A. and Burnett, D.S. (2009) Noble gas composition of the solar wind as collected by the Genesis mission. *Geochimica et Cosmochimica Acta* **73**, 7414–7432.

Heber, V.S., Baur, H., Bochsler, P., McKeegan, K.D., Neugebauer, M., Reisenfeld, D.B., Wieler, R. and Wiens, R.C. (2012) Isotopic Mass Fractionation of Solar Wind: Evidence from Fast and Slow Solar Wind Collected by the Genesis mission. *The Astrophysical Journal* **759**, 121

Hennecke, E.W. and Manuel, O.K. (1977) Argon, krypton and xenon in iron meteorites. *Earth and Planetary Science Letters* **36**, 29–43.

Hintenberger, H., Schultz, L., Wänke, H. and Weber, H. (1967) Helium- und Neonisotope in Eisenmeteoriten und der Tritiumverlust in Hexaedriten. *Zeitschrift für Naturforschung A* **22**, 780–787.

Hohenberg, C.M., Munk, M.N. and Reynolds, J.H. (1967) Spallation and fissiogenic xenon and krypton from stepwise heating of the Pasamonte achondrite; The case for extinct plutonium 244 in meteorites; Relative ages of chondrites and achondrites. *Journal of Geophysical Research* **72**, 3139–3177.

Holland, G. and Ballentine, C.J. (2006) Seawater subduction controls the heavy noble gas composition of the mantle. *Nature* **441**, 186–191.

Honda, M., McDougall, I., Patterson, D.B., Doulgeris, A. and Clague, D.A. (1991) Possible solar noble gas in Hawaiian basalts. *Nature* **349**, 149–151.

Hughes, D.W. (1978) Meteors, in: McDonnell, J.A.M. (Ed.), *Cosmic dust*. John Wiley, Chichester, England, pp. 123–185.

Hughes, D.W. (1994) Comets and asteroids. *Contemporary Physics* **35**, 75–93.

Hunten, D.M., Pepin, R.O. and Walker, J.C.G. (1987) Mass fractionation in hydrodynamic escape. *Icarus* **69**, 532–549.

Jackson, C.R.M., Parman, S.W., Kelley, S.P. and Cooper, R.F. (2013) Noble gas transport into the mantle facilitated by high solubility in amphibole. *Nature Geoscience* **6**, 562–565.

Jacobson, S.A., Morbidelli, A., Raymond, S.N., O'Brien, D.P., Walsh, K.J. and Rubie, D.C. (2014) Highly siderophile elements in Earth/'s mantle as a clock for the Moon-forming impact. *Nature* **508**, 84–87.

Jambon, A., Weber, H. and Braun, O. (1986) Solubility of He, Ne, Ar, Kr and Xe in a basalt melt in the range 1250–1600°C. Geochemical implications. *Geochimica et Cosmochimica Acta* **50**, 401–408.

Jaupart, E., Charnoz, S. and Moreira, M. (2017) Primordial atmosphere incorporation in planetary embryos and the origin of Neon in terrestrial planets. *Icarus* **293**, 199–205.

Jephcoat, A.P. (1998) Rare-gas solids in the Earth's deep interior. *Nature* **393**, 355–358.

Jephcoat, A.P. and Besedin, S.P. (1996) Temperature Measurement and Melting Determination in the Laser-Heated Diamond-Anvil Cell. *Philosophical Transactions of the Royal Society of London. Series A: Mathematical, Physical and Engineering Sciences* **354**, 1333–1360.

Karner, D.B., Levine, J., Muller, R.A., Asaro, F., Ram, M. and Stolz, M.R. (2003) Extraterrestrial accretion from the GISP2 ice core. *Geochimica et Cosmochimica Acta* **67**, 751–763.

Kehm, K., Flynn, G.J., Sutton, S.R. and Hohenberg, C.M. (1998) Combined noble gas and trace element measurements in single IDPs from the L2036 collector. *Lunar and Planetary Science Conference* **29**, abstract#1970.

Kehm, K., Flynn, G.J., Sutton, S.R. and Hohenberg, C.M. (2002) Combined noble gas and trace element measurements on individual stratospheric dust particels. *Meteoritics & Planetary Science* **37**, 1323–1335.

Kehm, K., Flynn, G.J. and Hohenberg, C.M. (2006) Noble gas space exposure ages of individual interplanetary dust particles. *Meteoritics & Planetary Science* **41**, 1199–1217.

Kendrick, M.A., Scambelluri, M., Honda, M. and Phillips, D. (2011) High abundances of noble gas and chlorine delivered to the mantle by serpentinite subduction. *Nature Geoscience* **4**, 807–812.

Kleine, T., Munker, C., Mezger, K. and Palme, H. (2002) Rapid accretion and early core formation on asteroids and the terrestrial planets from Hf-W chronometry. *Nature* **418**, 952–955.

Kleine, T., Touboul, M., Bourdon, B., Nimmo, F., Mezger, K., Palme, H., Jacobsen, S.B., Yin, Q.-Z. and Halliday, A.N. (2009) Hf–W chronology of the accretion and early evolution of asteroids and terrestrial planets. *Geochimica et Cosmochimica Acta* **73**, 5150–5188.

Koeberl, C. (2004) The late heavy bombardmentin the inner solar system: Is there any connectionto kuiper belt objects?, in: Davies, J.K., Barrera, L.H. (Eds.), *The first decadal review of the Edgeworth-Kuiper Belt*. Kluwer Academic Publishers, Dordrecht, pp. 79–87.

Koeberl, C. (2006) The record of impact processes on the early Earth: A review of the first 2.5 billion years. *Geological Society of America Special Papers* **405**, 1–22.

Kurat, G., Koeberl, C., Presper, T., Brandstätter, F. and Maurette, M. (1994) Petrology and geochemistry of Antarctic micrometeorites. *Geochimica et Cosmochimica Acta* **58**, 3879–3904.

Kurz, M.D., Curtice, J., Fornari, D., Geist, D. and Moreira, M. (2009) Primitive neon from the center of the Galápagos hotspot. *Earth and Planetary Science Letters* **286**, 23–34.

La Cruz, N.L., Qasim, D., Abbott-Lyon, H., Pirim, C., McKee, A.D., Orlando, T., Gull, M., Lindsay, D. and Pasek, M.A. (2016) The evolution of the surface of the mineral schreibersite in prebiotic chemistry. *Physical Chemistry Chemical Physics* **18**, 20160–20167.

Lal, D. and Jull, A.J.T. (2002) Atmospheric Cosmic Dust Fluxes in the Size Range 10^{-4} to 10 Centimeters. *The Astrophysical Journal* **576**, 1090–1097.

Levison, H.F., Dones, L., Chapman, C.R., Stern, S.A., Duncan, M.J. and Zahnle, K. (2001) Could the Lunar "Late Heavy Bombardment" Have Been Triggered by the Formation of Uranus and Neptune? *Icarus* **151**, 286–306.

Lewis, J.S., Prinn, R.G. and Donn, W.L. (2013) *Planets and Their Atmospheres: Origins and Evolution*. Elsevier Science. 470pp.

Leya, I. and Masarik, J. (2009) Cosmogenic nuclides in stony meteorites revisited. *Meteoritics & Planetary Science* **44**, 1061–1086.

Leya, I. and Wieler, R. (1999) Nucleogenic production of Ne isotopes in Earth's crust and upper mantle induced by alpha particles from the decay of U and Th. *Journal of Geophysical Research: Solid Earth* **104**, 15439–15450.

Lide, D.R. (2009) *CRC Handbook of Chemistry and Physics, 90th Edition*. CRC Press, Taylor & Francis. 2804pp.

Love, S.G. and Brownlee, D.E. (1991) Heating and thermal transformation of micrometeoroids entering the Earth's atmosphere. *Icarus* **89**, 26–43.

Love, S.G. and Brownlee, D.E. (1993) A Direct Measurement of the Terrestrial Mass Accretion Rate of Cosmic Dust. *Science* **262**, 550–553.

Macpherson, C.G., Hilton, D.R., Sinton, J.M., Poreda, R.J. and Craig, H. (1998) High $^{3}He/^{4}He$ ratios in the Manus backarc basin: Implications for mantle mixing and the origin of plumes in the western Pacific Ocean. *Geology* **26**, 1007–1010.

Malvin, D.J., Wang, D. and Wasson, J.T. (1984) Chemical classification of iron meteorites—X. Multielement studies of 43 irons, resolution of group IIIE from IIIAB, and evaluation of Cu as a taxonomic parameter. *Geochimica et Cosmochimica Acta* **48**, 785–804.

Mann, I., Pellinen-Wannberg, A., Murad, E., Popova, O., Meyer-Vernet, N., Rosenberg, M., Mukai, T., Czechowski, A., Mukai, S., Safrankova, J. and Nemecek, Z. (2011) Dusty Plasma Effects in Near Earth Space and Interplanetary Medium. *Space Science Reviews* **161**, 1–47.

Marty, B. (2012) The origins and concentrations of water, carbon, nitrogen and noble gases on Earth. *Earth and Planetary Science Letters* **313-314**, 56–66.

Marty, B. and Dauphas, N. (2002) Formation and early evolution of the atmosphere, in: Fleet, A.J., Doyle, P., Gregory, F.J., Giffiths, J.S., Hartley, A.J., Holdsworth, R.E., Morton, A.C., Robins, N.S., Stoker, M.S., Turner, J.P. (Eds.), *The Early Earth: Physical, Chemical and Biological Development*. The Geological Society, London, pp. 213–229.

Marty, B. and Lussiez, P. (1993) Constraints on rare gas partition coefficients from analysis of olivine-glass from a picritic mid-ocean ridge basalt. *Chemical Geology* **106**, 1–7.

Marty, B., Robert, P. and Zimmermann, L. (2005) Nitrogen and noble gases in micrometeorites. *Meteoritics & Planetary Science* **40**, 881–894.

Matrajt, G., Taylor, S., Flynn, G., Brownlee, D. and Joswiak, D. (2003) A nuclear microprobe study of the distribution and concentration of carbon and nitrogen in Murchison and Tagish Lake meteorites, Antarctic micrometeorites, and IDPs: Implications for astrobiology. *Meteoritics & Planetary Science* **38**, 1585–1600.

Matsuda, J., Sudo, M., Ozima, M., Ito, K., Ohtaka, O. and Ito, E. (1993) Noble Gas Partitioning Between Metal and Silicate Under High Pressures. *Science* **259**, 788–790.

Matsui, T. and Abe, Y. (1986) Evolution of an impact-induced atmosphere and magma ocean on the accreting Earth. *Nature* **319**, 303–305.

Maurette, M. (2006) *Micrometeorites and the Mysteries of Our Origins*. Springer Berlin Heidelberg. 330pp.

Maurette, M., Duprat, J., Engrand, C., Gounelle, M., Kurat, G., Matrajt, G. and Toppani, A. (2000) Accretion of neon, organics, CO2, nitrogen and water from large interplanetary dust particles on the early Earth. *Planetary and Space Science* **48**, 1117–1137.

Mazor, E., Heymann, D. and Anders, E. (1970) Noble gases in carbonaceous chondrites. *Geochimica et Cosmochimica Acta* **34**, 781–824.

Merrihue, C. (1964) Rare gas evidence for cosmic dust in modern pacific red clay. *Annals of the New York Academy of Sciences* **119**, 351–367.

Meshik, A., Hohenberg, C., Pravdivtseva, O. and Burnett, D. (2014) Heavy noble gases in solar wind delivered by Genesis mission. *Geochimica et Cosmochimica Acta* **127**, 326-347.

Meshik, A., Pravdivtseva, O., Hohenberg, C. and Burnett, D. (2015) Refined Composition of Solar Wind Xenon Delivered by Genesis: Implication for rimitive Terrestrial Xenon. *Lunar and Planetary Science Conference XXXXVI*, Abstract #2640.

Mizuno, H., Nakazawa, K. and Hayashi, C. (1980) Dissolution of the primordial rare gases into the molten Earth's material. *Earth and Planetary Science Letters* **50**, 202–210.

Mojzsis, S.J., Krishnamurthy, R. and Arrhenius, G. (1999) Before RNA and After: Geophysical and Geochemical Constraints on Molecular Evolution, in: Gesteland, R., Cech, T., J., A. (Eds.), *RNA world 2nd edition*. Cold Spring Harbor Press, New York, pp. 1–47.

Morbidelli, A. and Wood, B.J. (2015) Late Accretion and the Late Veneer, in: Badro, J., Walter, M.J. (Eds.), *The Early Earth*. John Wiley & Sons, Inc, pp. 71–82.

Morbidelli, A., Lunine, J.I., O'Brien, D.P., Raymond, S.N. and Walsh, K.J. (2012) Building Terrestrial Planets. *Annual Review of Earth and Planetary Sciences* **40**, 251–275.

Moreira, M. (2013) Noble Gas Constraints on the Origin and Evolution of Earth's Volatiles. *Geochemical Perspectives* **2**, 229–403.

Moreira, M. and Charnoz, S. (2016) The origin of the neon isotopes in chondrites and on Earth. *Earth and Planetary Science Letters* **433**, 249–256.

Moreira, M., Kunz, J. and Allègre, C. (1998) Rare Gas Systematics in Popping Rock: Isotopic and Elemental Compositions in the Upper Mantle. *Science* **279**, 1178–1181.

Mukhopadhyay, S. (2012) Early differentiation and volatile accretion recorded in deep-mantle neon and xenon. *Nature* **486**, 101–104.

Munk, M.N. (1967a) Neon, argon, krypton, and xenon compositions of the Misteca and Carbo iron meteorites. *Earth and Planetary Science Letters* **3**, 133–138.

Munk, M.N. (1967b) Spallation neon, argon, krypton, and xenon in an iron meteorite. *Earth and Planetary Science Letters* **2**, 301-309.

Murer, C.A., Baur, H., Signer, P. and Wieler, R. (1997) Helium, neon, and argon abundances in the solar wind: In vacuo etching of meteoritic iron-nickel. *Geochimica et Cosmochimica Acta* **61**, 1303–1314.

Murty, S.V.S. and Ranjith Kumar, P.M. (2014) Volume correlated solar noble gases in Washingtonm County Iron Meteorite. *Lunar and Planetary Science Conference* **45**, abstract #1110.

Murty, S.V.S., Mahajan, R.R., Goel, S., Dutt, K. and Dhote, P.S. (2008) Solar gases in Kavarpura Iron Meteorite. *71st Annual Meteoritical society meeting*, #abstract 5033.

Nier, A.O. and Schlutter, D.J. (1990) Helium and neon isotopes in stratospheric particles. *Meteoritics* **25**, 263–267.

Nier, A.O. and Schlutter, D.J. (1992) Extraction of helium from individual interplanetary dust particles by step-heating. *Meteoritics* **27**, 166–173.

Nier, A.O. and Schlutter, D.J. (1993) The thermal history of interplanetary dust particles collected in the Earth's stratosphere. *Meteoritics* **28**, 675–681.

Okazaki, R., Noguchi, T., Tsujimoto, S.-i., Tobimatsu, Y., Nakamura, T., Ebihara, M., Itoh, S., Nagahara, H., Tachibana, S., Terada, K. and Yabuta, H. (2015) Mineralogy and noble gas isotopes of micrometeorites collected from Antarctic snow. *Earth, Planets and Space* **67**, 1–17.

Osawa, T. (2012) Solar Wind Noble Gases in Micrometeorites, in: Lazar, M. (Ed.), *Exploring the Solar Wind*. InTech, pp. 121–140.

Osawa, T. and Nagao, K. (2002a) Noble gas compositions of Antarctic micrometeorites collected at the Dome Fuji Station in 1996 and 1997. *Meteoritics & Planetary Science* **37**, 911–936.

Osawa, T. and Nagao, K. (2002b) On low noble gas concentrations in Antarctic micrometeorites collected from Kuwagata Nunatak in the Yamato Meteorite Ice Field. *Antarctic Meteorite Research* **15**, 165–177.

Osawa, T., Nagaoi, K., Nakamura, T. and Takaoka, N. (2000) Noble gas measurement in individual micrometeorites using laser gas-extraction system. *Antarctic Meteorite Research* **13**, 322–341.

Osawa, T., Nagao, K., Noguchi, T., Nakazawa, A. and Mikada, J.-i. (2003a) Remnant extraterrestrial noble gases in Antarctic cosmic spherules. *Antarctic Meteorite Research* **16**, 196–219.

Osawa, T., Nakamura, T. and Nagao, K. (2003b) Noble gas isotopes and mineral assemblages of Antarctic micrometeorites collected at the meteorite ice field around the Yamato Mountains. *Meteoritics & Planetary Science* **38**, 1627–1640.

Osawa, T., Yamamoto, Y., Noguchi, T., Iose, A. and Nagao, K. (2010) Interior textures, chemical compositions, and noble gas signatures of Antarctic cosmic spherules: Possible sources of spherules with long exposure ages. *Meteoritics & Planetary Science* **45**, 1320–1339.

Ott, U. (1988) Noble gases in SNC meteorites: Shergotty, Nakhla, Chassigny. *Geochimica et Cosmochimica Acta* **52**, 1937-1948.

Ott, U. (2014) Planetary and pre-solar noble gases in meteorites. *Chemie der Erde - Geochemistry* **74**, 519–544.

Owen, T. (2008) The Contributions of Comets to Planets, Atmospheres, and Life: Insights from Cassini-Huygens, Galileo, Giotto, and Inner Planet Missions. *Space Sci. Rev.* **138**, 301–316.

Ozima, M. and Podosek, F.A. (2002) *Noble Gas Geochemistry*. Cambridge University Press., Cambridge, New York, Oakleigh, Madrid, Cape Town. 286 pp.

Palache, C. and von Shannon, E. (1928) A new meteorite from Washington County, Colorado. *American Mineralogist* **13**, 406–409.

Paonita, A. (2005) Noble gas solubility in silicate melts:a review of experimentation and theory, and implications regarding magma degassing processes. *Annals of Geophysics* **48**, 647–669.

Pepin, R.O. (1991) On the Origin and Early Evolution of Terrestrial Planet Atmospheres and Meteoritic Volatiles. *Icarus* **92**, 2–79.

Pepin, R.O. (1997) Evolution of Earth's Noble Gases: Consequences of Assuming Hydrodynamic Loss Driven by Giant Impact. *Icarus* **126**, 148–156.

Pepin, R.O. (1998) Isotopic evidence for a solar argon component in the Earth's mantle. *Nature* **394**, 664–667.

Pepin, R.O. (2006) Atmospheres on the terrestrial planets: Clues to origin and evolution. *Earth and Planetary Science Letters* **252**, 1–14.

Pepin, R.O. and Signer, P. (1965) Primordial Rare Gases in Meteorites. *Science* **149**, 253–265.

Pepin, R.O. and Porcelli, D. (2002) Origin of Noble Gases in the Terrestrial Planets. *Reviews in Mineralogy and Geochemistry* **47**, 191–246.

Pepin, R.O., Palma, R.L. and Schlutter, D.J. (2000) Noble gases in interplanetary dust particles, I: The excess helium-3 problem and estimates of the relative fluxes of solar wind and solar energetic particles in interplanetary space. *Meteoritics & Planetary Science* **35**, 495–504.

Pepin, R.O., Palma, R.L. and Schlutter, D.J. (2001) Noble gases in interplanetary dust particles, II: Excess helium-3 in cluster particles and modeling constraints on interplanetary dust particle exposures to cosmic-ray irradiation. *Meteoritics & Planetary Science* **36**, 1515–1534.

Pepin, R.O., Schlutter, D.J., Becker, R.H. and Reisenfeld, D.B. (2012) Helium, neon, and argon composition of the solar wind as recorded in gold and other Genesis collector materials. *Geochimica et Cosmochimica Acta* **89**, 62–80.

Péron, S., Moreira, M., Colin, A., Arbaret, L., Putlitz, B. and Kurz, M.D. (2016) Neon isotopic composition of the mantle constrained by single vesicle analyses. *Earth and Planetary Science Letters* **449**, 145–154.

Péron, S., Moreira, M., Putlitz, B. and Kurz, M.D. (2017) Solar wind implantation supplied light volatiles during the first stage of Earth accretion. *Geochemical Perspectives Letters* **3**, 151–159.

Péron, S., Moreira, M. and Agranier, A. (2018) Origin of Light Noble Gases (He, Ne, and Ar) on Earth: A Review. *Geochemistry, Geophysics, Geosystems* **19**, https://doi.org/10.1002/2017GC007388.

Peucker-Ehrenbrink, B. (1996) Accretion of extraterrestrial matter during the last 80 million years and its effect on the marine osmium isotope record. *Geochimica et Cosmochimica Acta* **60**, 3187–3196.

Peucker-Ehrenbrink, B. and Ravizza, G. (2000) The effects of sampling artifacts on cosmic dust flux estimates: a reevaluation of nonvolatile tracers (Os, Ir). *Geochimica et Cosmochimica Acta* **64**, 1965–1970.

Pfalzner, S., M., S. and Menten, K. (2014) Short Dissipation Times of Proto-planetary Disks: An Artifact of Selection Effects? *The Astrophysical Journal Letters* **793**, L34.

Podosek, F.A., Woolum, D.S., Cassen, P. and Nichols Jr., R.H. (2000) Solar Gases in the Earth by Solar Wind Irradiation? *Journal of Conference Abstracts* **5**, 804 (Goldschmidt Conference abstract).

Porcelli, D. and Ballentine, C.J. (2002) Models for Distribution of Terrestrial Noble Gases and Evolution of the Atmosphere. *Reviews in Mineralogy and Geochemistry* **47**, 411–480.

Porcelli, D. and Halliday, A.N. (2001) The core as a possible source of mantle helium. *Earth and Planetary Science Letters* **192**, 45–56.

Porcelli, D. and Pepin, R.O. (2011) The origin of noble gases and major volatiles in the terrestrial planets, in: Holland, H.D., Turekian, K.K. (Eds.), *Isotope Geochemistry - From the treatise on geochemistry*. Elsevier Academic Press, London, Amsterdam, Burlington, San Diego, pp. 493–520.

Porcelli, D., Woolum, D. and Cassen, P. (2001) Deep Earth rare gases: initial inventories, capture from the solar nebula, and losses during Moon formation. *Earth and Planetary Science Letters* **193**, 237–251.

Porcelli, D., Ballentine, C.J. and Wieler, R. (2002a) *Noble Gases in Geochemistry and Cosmochemistry - Reviews in Mineralogy & Geochemistry* **47**. Mineralogical Society of America. 844pp.

Porcelli, D., Ballentine, C.J. and Wieler, R. (2002b) An Overview of Noble Gas Geochemistry and Cosmochemistry. *Reviews in Mineralogy and Geochemistry* **47**, 1–19.

Raquin, A. and Moreira, M. (2009) Atmospheric 38Ar/36Ar in the mantle: Implications for the nature of the terrestrial parent bodies. *Earth and Planetary Science Letters* **287**, 551–558.

Ray, D. and Ghosh, S. (2014) Washington County iron meteorite reclassified as IIIAB. *Meteoritics & Planetary Science* **49**, abstract #5007.

Raymond, S.N., O'Brien, D.P., Morbidelli, A. and Kaib, N.A. (2009) Building the terrestrial planets: Constrained accretion in the inner Solar System. *Icarus* **203**, 644–662.

Raymond, S.N., Schlichting, H.E., Hersant, F. and Selsis, F. (2013) Dynamical and collisional constraints on a stochastic late veneer on the terrestrial planets. *Icarus* **226**, 671–681.

Reynolds, J.H., Merrihue, C.M. and Pepin, R.O. (1962) Extinct radioactivity and primordial rare gases in iron meteorites (abstract). *Bull. Am. Phys. Soc.* **7**, 35.

Rubie, D.C., Frost, D.J., Mann, U., Asahara, Y., Nimmo, F., Tsuno, K., Kegler, P., Holzheid, A. and Palme, H. (2011) Heterogeneous accretion, composition and core–mantle differentiation of the Earth. *Earth and Planetary Science Letters* **301**, 31–42.

Rubie, D.C., Jacobson, S.A., Morbidelli, A., O'Brien, D.P., Young, E.D., de Vries, J., Nimmo, F., Palme, H. and Frost, D.J. (2015) Accretion and differentiation of the terrestrial planets with implications for the compositions of early-formed Solar System bodies and accretion of water. *Icarus* **248**, 89–108.

Ryder, G. (2001) Mass flux during the ancient lunar bombardment: The cataclysm. *Lunar and Planetary Science Conference* **32**, abstract#1326.

Ryder, G. (2002) Mass flux in the ancient Earth-Moon system and benign implications for the origin of life on Earth. *Journal of Geophysical Research: Planets* **107**, 6-1–6-13.

Ryder, G., Koeberl, C. and Mojzsis, S.J. (2000) Heavy Bombardment on the Earth at ~3.85 Ga: The Search for Petrographic and Geochemical Evidence, in: Canup, R.M., Righter, K. (Eds.), *Origin of the Earth and Moon*. University of Arizona Press, Tuscon, pp. 475–492.

Sarda, P., Staudacher, T. and Allègre, C.J. (1988) Neon isotopes in submarine basalts. *Earth and Planetary Science Letters* **91**, 73–88.

Sasaki, S. (1991) Off-disk penetration of ancient solar wind. *Icarus* **91**, 29–38.

Sasaki, S. (1999) Presence of a primary solar-type atmosphere around the earth: evidence of dissolved noble gas. *Planetary and Space Science* **47**, 1423–1431.

Sasaki, S. and Nakazawa, K. (1990) Did a primary solar-type atmosphere exist around the proto-earth? *Icarus* **85**, 21–42.

Schaefer, L. and Fegley Jr, B. (2010) Chemistry of atmospheres formed during accretion of the Earth and other terrestrial planets. *Icarus* **208**, 438–448.

Schaeffer, O.A. and Fisher, D.E. (1959) Cosmogenic Noble Gases in the Washington County Meteorite. *Nature* **183**, 660–661.

Schelhaas N., Ott U., and Begemann F. (1990) Trapped noble gases in unequilibrated ordinary chondrites. *Geochimica et Cosmochimica Acta* **54**(10), 2869–2882.

Schultz, L. and Franke, L. (2004) Helium, neon, and argon in meteorites: A data collection. *Meteoritics & Planetary Science* **39**, 1889–1890.

Schwarz, W.H., Trieloff, M. and Altherr, R. (2005) Subduction of solar-type noble gases from extraterrestrial dust: constraints from high-pressure low-temperature metamorphic deep-sea sediments. *Contributions to Mineralogy and Petrology* **149**, 675–684.

Signer, P. and Nier, A.O.C. (1962) The measurement and interpretation of rare gas concentrations in iron meteorites, in: Moore, C.B. (Ed.), *Research on meteorites*. John Wiley and Sons, New York, pp. 7–35.

Signer, P. and Suess, H.E. (1963) Rare gases in the sun, in the atmosphere, and in meteorites, in: Geiss, J., Goldberg, E.D. (Eds.), *Earth Science and Meteorites*, NorthHolland, Amsterdam, pp. 241–272.

Staudacher, T. and Allègre, C.J. (1982) Terrestrial xenology. *Earth and Planetary Science Letters* **60**, 389–206.

Staudacher, T. and Allègre, C.J. (1988) Recycling of oceanic crust and sediments: the noble gas subduction barrier. *Earth and Planetary Science Letters* **89**, 173–183.

Stuart, F.M., Harrop, P.J., Knott, S. and Turner, G. (1999) Laser extraction of helium isotopes from Antarctic micrometeorites: source of He and implications for the flux of extraterrestrial 3He to earth. *Geochimica et Cosmochimica Acta* **63**, 2653–2665.

Swartzendruber, L.J., Itkin, V.P. and Alcock, C.B. (1991) The Fe-Ni (iron-nickel) system. *Journal of Phase Equilibria* **12**, 288–312.

Taylor, S., Lever, J.H. and Harvey, R.P. (1998) Accretion rate of cosmic spherules measured at the South Pole. *Nature* **392**, 899–903.

Taylor, S., Lever, J.H. and Harvey, R.P. (2000) Numbers, types, and compositions of an unbiased collection of cosmic spherules. *Meteoritics & Planetary Science* **35**, 651–666.

Taylor, S., Matrajt, G., Lever, J.H., Jowiak, S.J. and Brownlee, D. (2007) Size distribution of antarctic micrometeorites. *Proc. 'Dust in Planetary Systems'*, 145–148.

Taylor, S., Matrajt, G. and Guan, Y. (2012) Fine-grained precursors dominate the micrometeorite flux. *Meteoritics & Planetary Science* **47**, 550–564.

Tera, F., Papanastassiou, D.A. and Wasserburg, G.J. (1974) Isotopic evidence for a terminal lunar cataclysm. *Earth and Planetary Science Letters* **22**, 1–21.

Toppani, A., Libourel, G., Engrand, C. and Maurette, M. (2001) Experimental simulation of atmospheric entry of micrometeorites. *Meteoritics & Planetary Science* **36**, 1377–1396.

Toppani, A., Marty, B., Zimmermann, L. and Libourel, G. (2003) Simulation of Nitrogen and Noble Gases release during Atmospheric Entry of Micrometeorites. *Lunar and Planetary Science Conference* **34**, abstract #2028.

Trieloff, M. (2002) Primordial noble gases in the Earth: remnants of accreted planetesimals or a solar protoatmosphere ? *Goldschmidt Conference Abstracts*, A784.

Trieloff, M. (2007) The formation of planetesimals and dissipation of the early solar nebula. *Meteoritics & Planetary Science* **42**, abstract #5057.

Trieloff, M. and Kunz, J. (2005) Isotope systematics of noble gases in the Earth's mantle: possible sources of primordial isotopes and implications for mantle structure. *Physics of the Earth and Planetary Interiors* **148**, 13–38.

Trieloff, M., Kunz, J., Clague, D.A., Harrison, D. and Allègre, C.J. (2000) The Nature of Pristine Noble Gases in Mantle Plumes. *Science* **288**, 1036–1038.

Trieloff, M., Kunz, J. and Allègre, C.J. (2002) Noble gas systematics of the Réunion mantle plume source and the origin of primordial noble gases in Earth's mantle. *Earth and Planetary Science Letters* **200**, 297–313.

Tucker, J.M. and Mukhopadhyay, S. (2014) Evidence for multiple magma ocean outgassing and atmospheric loss episodes from mantle noble gases. *Earth and Planetary Science Letters* **393**, 254–265.

Valbracht, P.J., Staudacher, T., Malahoff, A. and Allègre, C.J. (1997) Noble gas systematics of deep rift zone glasses from Loihi Seamount, Hawaii. *Earth and Planetary Science Letters* **150**, 399–411.

Voshage, H. (1967) Bestrahlungsalter und Herkunft der Eisenmeteorite, *Zeitschrift für Naturforschung A* **22**(4), 477–506.

Wade, J. and Wood, B.J. (2016) The oxidation state and mass of the Moon-forming impactor. *Earth and Planetary Science Letters* **442**, 186–193.

Walsh, K.J., Morbidelli, A., Raymond, S.N., O'Brien, D.P. and Mandell, A.M. (2011) A low mass for Mars from Jupiter's early gas-driven migration. *Nature* **475**, 206–209.

Wasson, J.T. and Schaudy, R. (1971) The chemical classification of iron meteorites—V groups IIIC and IIID and other irons with germanium concentrations between 1 and 25 ppm. *Icarus* **14**, 59–70.

Wetherill, G.W. (1975) Late heavy bombardment of the moon and terrestrial planets. *Proceedings of the 6th Lunar Science Conference* Vol. **2**, 1539–1561.

Wieler, R. (2002a) Cosmic-Ray-Produced Noble Gases in Meteorites. *Reviews in Mineralogy and Geochemistry* **47**, 125–170.

Wieler, R. (2002b) Noble Gases in the Solar System. *Reviews in Mineralogy and Geochemistry* **47**, 21–70.

Woolum, D., Cassen, P., Porcelli, D. and Wasserburg, D.J. (1999) Incorporation of solar noble gases from a nebula-derived atmosphere during magma ocean cooling . *Lunar and Planetary Science Conference* XXX, abstract# 1518.

Yada, T., Nakamura, T., Takaoka, N., Noguchi, T., Terada, K., Yano, H., Nakazawa, T. and Kojima, H. (2004) The global accretion rate of extraterrestrial materials in the last glacial period estimated from the abundance of micrometeorites in Antarctic glacier ice. *Earth Planet Sp* **56**, 67–79.

Yatsevich, I. and Honda, M. (1997) Production of nucleogenic neon in the Earth from natural radioactive decay. *Journal of Geophysical Research: Solid Earth* **102**, 10291–10298.

Yokochi, R. and Marty, B. (2004) A determination of the neon isotopic composition of the deep mantle. *Earth and Planetary Science Letters* **225**, 77–88.

Yokochi, R. and Marty, B. (2005) Geochemical constraints on mantle dynamics in the Hadean. *Earth and Planetary Science Letters* **238**, 17–30.

Zahnle, K. (1998) Origins of Atmospheres, in: Woodward, C.E., Shull, J.M., Thronson, J.H.A. (Eds.), *Origins, ASP Conference Series*, pp. 364–391.

Zahnle, K.J., Kasting, J.F. and Pollack, J.B. (1988) Evolution of a steam atmosphere during earth's accretion. *Icarus* **74**, 62–97.

Zahnle, K., Arndt, N., Cockell, C., Halliday, A.N., Nisbet, E., Selsis, F. and Sleep, N.H. (2007) Emergence of a Habitable Planet, in: Fishbaugh, E.K., Lognonné, P., Raulin, F., Marais, J.D., Korablev, O. (Eds.), *Geology and Habitability of Terrestrial Planets*. Springer New York, New York, pp. 35–78.

Zahnle, K., Schaefer, L. and Fegley, B. (2010) Earth's Earliest Atmospheres. *Perspectives in Biology* **2**, 1–17.

Zähringer, J. (1968) Rare gases in stony meteorites. *Geochimica et Cosmochimica Acta* **32**, 209–237.

Zhang, Y. (2014) Degassing History of Earth, in: Turekian, K.K. (Ed.), *Treatise on Geochemistry (Second Edition)*. Elsevier, Oxford, pp. 37–69.

APPENDIX A

Tab. A1: Furnace blank contributions (He, Ne, Ar) for Washington County measurements.

Blank	Temp. [°C]	^{4}He [10^{-9} cm³STP]	±	^{20}Ne [10^{-11} cm³STP]	±	^{36}Ar [10^{-12} cm³STP]	±
WC_2 blank series							
	800	1.86	0.15	1.39	0.04	2.18	0.16
	1100	1.66	0.14	1.35	0.04	2.40	0.11
	1400	1.59	0.21	1.44	0.05	3.19	0.23
	1600	1.96	0.17	2.07	0.06	3.53	0.43
	1800	3.38	0.15	8.38	0.25	6.39	0.27
WC_5 blank series[1)]							
	800	1.94	0.20	3.12	0.06	6.39	0.33
	1400	2.07	0.13	3.49	0.07	6.74	0.14
	1600	2.31	0.13	4.78	0.09	7.80	0.25
	1800	3.34	0.14	14.66	0.28	12.86	0.25
WC_11 blank series							
	800	1.84	0.14	1.40	0.03	2.15	0.16
	1100	1.64	0.13	1.36	0.03	2.37	0.11
	1400	1.74	0.21	1.27	0.03	2.98	0.26
	1600	1.94	0.16	2.08	0.04	3.49	0.43
	1800	3.35	0.13	8.40	0.16	6.31	0.27
WC_14 blank series							
	800	2.09	0.11	2.02	0.11	2.33	0.11
	1150	2.90	0.12	2.05	0.11	2.58	0.24
	1480	2.18	0.08	2.17	0.12	3.22	0.09
	1600	2.26	0.09	2.49	0.13	3.47	0.15
	1800	2.93	0.09	10.08	0.53	5.81	0.14

All uncertainties 1σ.

[1)]blank series of first analyzed sample (WC_5) is affected by a minor leakage in the SAES getter that was removed for subsequent measurements

Tab. A2: Furnace blank contributions (Xe) for WC_5 measurements

WC_5 Xe blank series		
Temp.	^{129}Xe [10^{-14} cm³STP/g]	±
800	9.94	1.50
1400	12.19	1.64
1600	8.56	1.29
1800	6.09	0.99

All uncertainties 1σ

Tab. A3: Blank corrections [%] from measured gas amounts for temperature steps of WC_2, WC_5, WC_11 and WC_14

WC-2	Blank corrections from total released gas amounts [%]							
Temp. [°C]	^{4}He	^{3}He	^{20}Ne	^{21}Ne	^{22}Ne	^{36}Ar	^{38}Ar	^{40}Ar
800	-	-	354.8	8.0	155.7	62.2	22.62	57.4
1050	8.2	0.0003	27.2	0.2	4.7	4.0	0.51	84.9
1140	2.6	0.0001	8.2	0.04	1.3	1.0	0.12	66.6
1350	1.4	0.0002	4.6	0.02	0.8	0.7	0.08	77.1
1380	3.8	0.0005	10.9	0.06	1.9	1.8	0.22	101.9
1390	26.1	0.0047	58.8	0.56	15.1	13.6	1.87	85.7
1400	54.9	0.0151	105.3	1.54	38.0	32.7	4.86	122.7
1410	61.2	0.0287	118.9	2.8	55.8	44.7	7.26	126.9
1450	44.0	0.0207	7.7	1.6	6.9	24.6	5.27	45.2
1800	88.0	-	79.1	13.7	69.9	58.1	14.17	90.0

WC-5[1)]	Blank corrections from total released gas amounts [%]							
Temp. [°C]	^{4}He	^{3}He	^{20}Ne	^{21}Ne	^{22}Ne	^{36}Ar	^{38}Ar	^{40}Ar
600	-	-	338.0	149.6	304.4	57.0	57.18	60.2
700	888.5	0.1049	314.9	86.6	265.9	22.0	21.13	21.7
800	123.5	0.0032	147.1	14.3	122.1	56.4	39.20	60.2
850	69.6	0.0017	129.0	8.4	95.6	63.3	38.38	68.5
900	41.4	0.0059	86.0	2.5	44.7	37.8	12.95	52.8
950	34.6	0.0046	74.5	1.7	33.9	33.0	7.85	59.3
1000	38.5	0.0058	68.1	1.4	30.3	30.4	6.53	65.5
1050	29.6	0.0006	69.8	1.3	29.3	27.0	4.65	69.1
1100	4.0	0.0001	21.3	0.1	4.4	3.9	0.49	63.1
1120	36.3	0.0009	62.4	1.5	30.2	25.9	4.95	57.2
1150	51.0	0.0021	77.2	3.8	51.8	36.3	8.87	60.0
1200	32.2	0.0008	56.3	1.3	26.3	17.9	3.01	51.6
1250	47.8	0.0017	61.3	2.0	33.7	24.7	4.34	63.4
1300	56.9	0.0025	61.1	3.7	43.3	39.0	8.51	71.0
1350	55.8	0.0023	57.4	3.6	41.0	40.4	9.46	72.8
1400	9.3	0.0001	34.5	0.4	9.7	7.8	1.03	61.0
1425	1.4	0.0000	9.1	0.1	1.7	1.3	0.16	76.3
1450	54.1	0.0020	74.2	3.5	47.9	41.4	9.76	80.7
1475	61.6	0.0030	77.5	5.1	55.6	50.2	12.85	78.4
1500	71.6	0.0033	88.5	5.1	61.6	49.2	11.38	87.2
1525	69.1	0.0047	89.0	7.9	69.9	50.2	11.60	88.8
1550	88.8	5.7798	96.0	74.6	94.0	61.3	39.03	63.8
1650	80.0	8.6147	91.5	79.1	92.0	86.6	57.93	92.1
1750	85.6	13.8227	63.7	62.1	64.2	65.9	60.31	77.7
1800	74.9	15.2777	49.9	49.4	50.0	75.9	75.19	74.1

WC-11	Blank corrections from total released gas amounts [%]							
Temp. [°C]	^{4}He	^{3}He	^{20}Ne	^{21}Ne	^{22}Ne	^{36}Ar	^{38}Ar	^{40}Ar
1050	7.1	0.0002	23.0	0.1	3.4	2.8	0.35	70.7
1100	4.1	0.0001	12.4	0.1	1.8	1.2	0.15	80.8
1150	16.3	0.0005	44.5	0.2	7.6	5.8	0.76	101.1
1250	14.2	0.0005	32.7	0.2	5.4	3.5	0.44	89.9
1300	50.2	0.0186	76.3	0.6	18.0	15.8	2.10	130.4
1320	78.6	0.0638	107.5	2.3	47.7	43.3	6.97	127.1
1340	74.7	0.0730	110.9	3.4	61.5	52.0	9.41	120.6
1360	75.6	0.0982	107.8	4.3	65.4	62.0	11.21	124.0
1380	66.3	0.0458	101.0	2.2	44.8	44.2	7.12	135.5
1390	55.6	0.0337	66.4	1.7	33.0	32.6	5.25	93.7
1400	34.7	0.0113	66.7	0.6	16.7	15.8	2.04	139.1
1410	24.5	0.0068	50.3	0.4	10.9	9.9	1.23	128.2
1420	16.8	0.0043	37.2	0.2	7.1	6.6	0.82	128.2
1430	13.0	0.0030	29.3	0.2	5.1	4.7	0.59	125.0
1440	3.4	0.0006	9.1	0.04	1.3	0.8	0.09	76.3
1450	35.9	0.0126	70.0	0.75	19.9	14.5	1.95	100.2
1800	62.5	-	32.3	0.67	13.8	10.6	1.60	47.6

WC-14	Blank corrections from total released gas amounts [%]							
Temp. [°C]	^{4}He	^{3}He	^{20}Ne	^{21}Ne	^{22}Ne	^{36}Ar	^{38}Ar	^{40}Ar
800	478.1	-	289.9	5.49	118.1	48.9	14.41	39.6
1050	35.8	0.0014	42.5	0.22	6.6	3.6	0.45	76.7
1140	12.8	0.0005	28.2	0.13	3.9	1.4	0.17	59.3
1350	8.8	0.0001	16.8	0.08	2.3	1.5	0.18	71.0
1480	3.2	0.0001	2.7	0.02	0.5	0.3	0.03	23.8
1600	79.4	0.0814	22.6	10.97	22.0	52.8	21.91	56.2
1800	114.1	1.1800	114.0	82.92	113.3	92.2	52.89	88.5

[1)]measurements of first analyzed sample (WC_5) are affected by a minor leakage in the SAES getter that was removed for subsequent samples

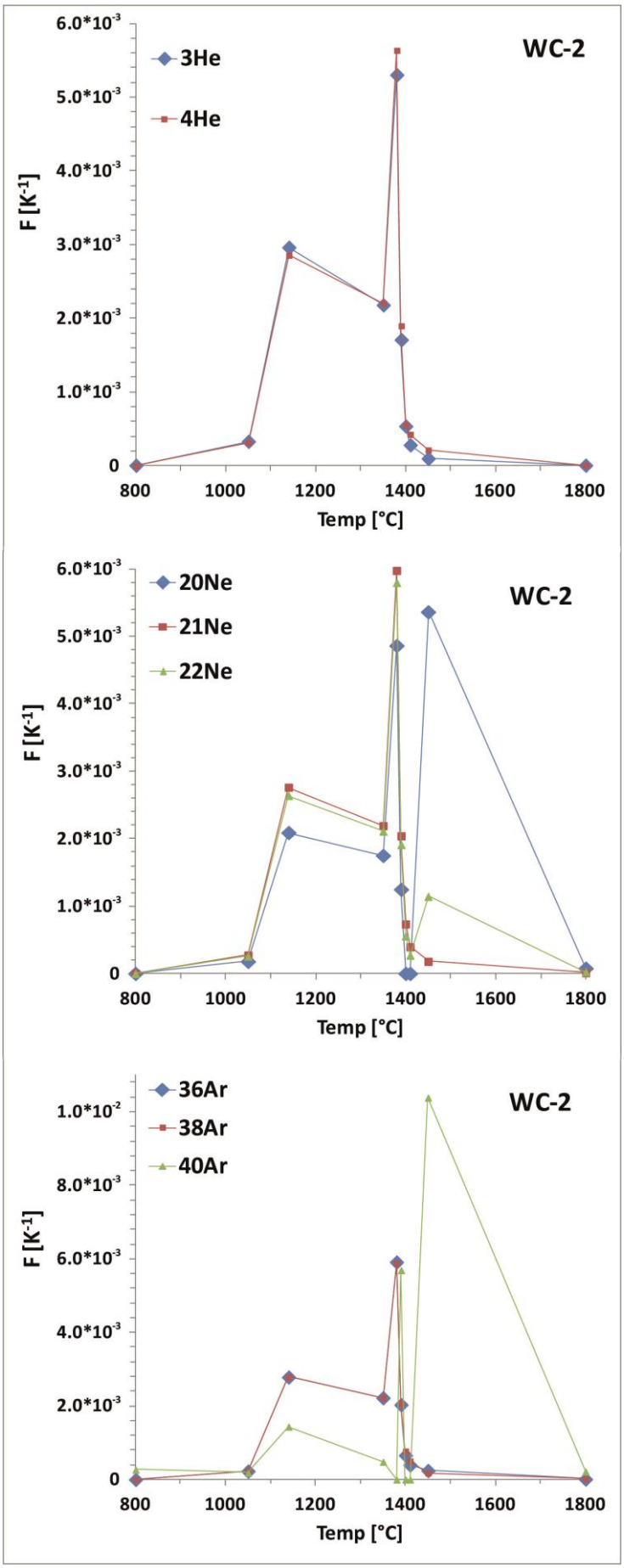

Fig. A1: Fractional release pattern for WC_2 (He, Ne and Ar). Major degassing peaks occur at 1140 °C and 1380 °C. For ^{20}Ne ,^{22}Ne and ^{40}Ar an additional gas release peak with air-like composition is observed at 1450 °C (Tab. 2.1).

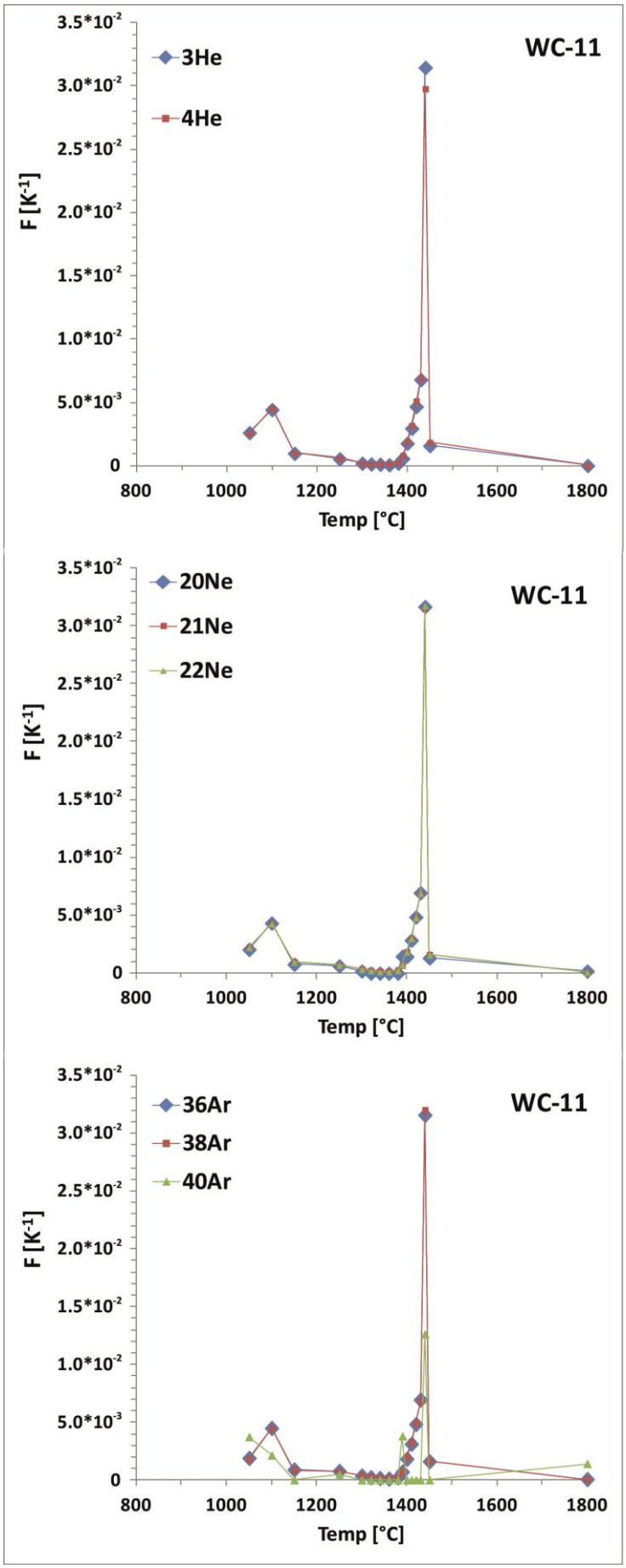

Fig. A2: Fractional release pattern for WC_11 (He, Ne and Ar). Major degassing peaks occur at 1100 °C and 1440 °C (Tab. 2.1).

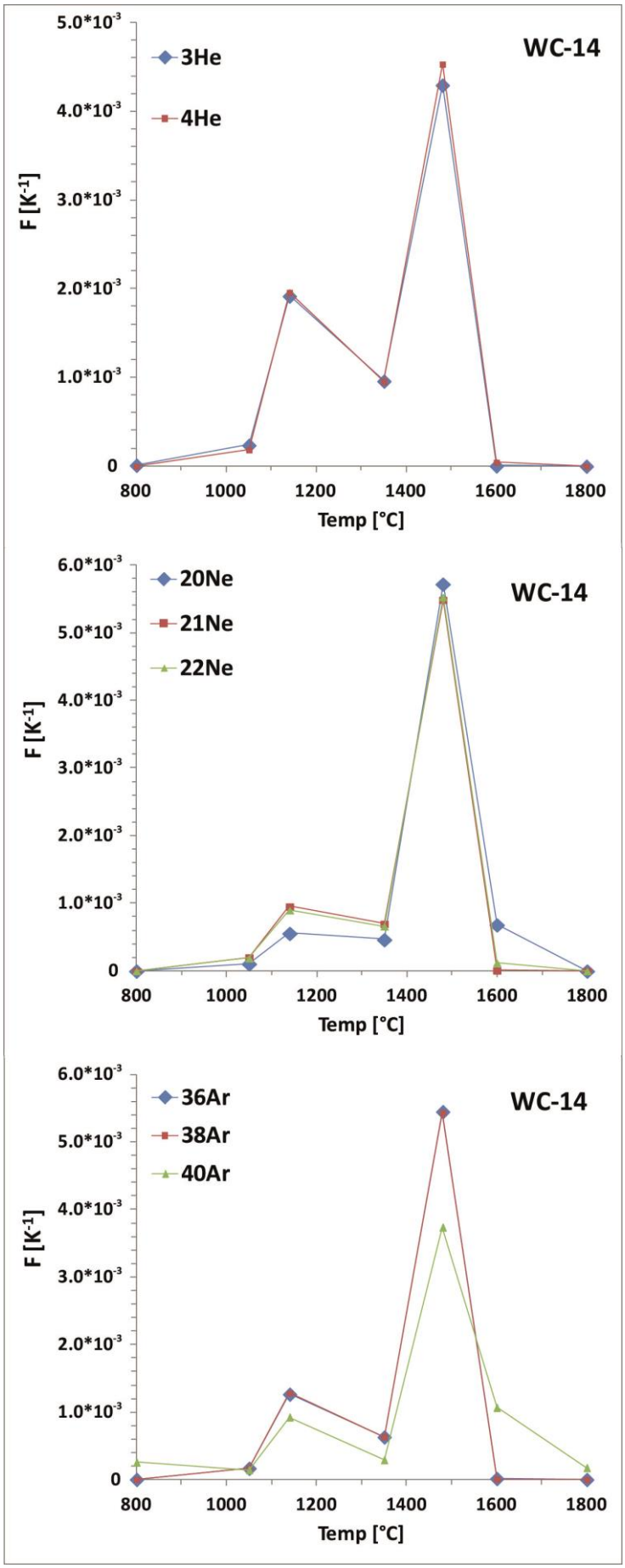

Fig. A3: Fractional release pattern for WC_14 (He, Ne and Ar). Major degassing peaks occur at 1140 °C and 1480 °C (Tab. 2.1).

APPENDIX B

Tab. B1: Comparison of current average annual particle mass flux (g/year) to Earth's upper atmosphere and to Earth's surface for impactor masses ranging from 10^{-16}–10^{25}g (β-meteorites, IDP, MM, large particles, large bodies, very large bodies) divided in decadal mass bins. The fractions that are evaporated during atmospheric entry and/or on impact are given in % in the last column.

Particle type	Mass Bin [g]	Density [g/cm³][a)]	Diameter [m][a)]	Upper Atmosphere Particle-flux [g/yr]	Surface Particle-flux [g/yr]	Evaporated in ATM [%]
β-meteorite	10^{-16} - 10^{-15}	1.5	7.4E-08	4.88E+04[b)]	4.88E+04[b)]	0
	10^{-15} - 10^{-14}	1.5	1.6E-07	8.65E+04[b)]	8.65E+04[b)]	0
	10^{-14} - 10^{-13}	1.5	3.4E-07	1.70E+05[b)]	1.70E+05[b)]	0
	10^{-13} - 10^{-12}	1.5	7.4E-07	4.98E+05[b)]	4.98E+05[b)]	0
	10^{-12} - 10^{-11}	1.5	1.6E-06	1.93E+06[b)]	1.93E+06[b)]	0
	10^{-11} - 10^{-10}	1.5	3.4E-06	8.75E+06[b)]	8.75E+06[b)]	0
IDP	10^{-10} - 10^{-9}	1.5	7.4E-06	3.46E+07[b)]	3.46E+07[b)]	0
	10^{-9} - 10^{-8}	1.5	1.6E-05	1.83E+08[b)]	1.83E+08[b)]	0
	10^{-8} - 10^{-7}	1.5	3.4E-05	9.16E+08[b)]	9.16E+08[b)]	0
MM	10^{-7} - 10^{-6}	2.5	6.2E-05	2.57E+09[b)]	1.03E+09–2.57E+08[h)]	60–90[f)]
	10^{-6} - 10^{-5}	2.5	1.3E-04	4.31E+09[b)]	1.73E+09–4.31E+08[h)]	60–90[f)]
	10^{-5} - 10^{-4}	2.5	2.9E-04	4.34E+09[b)]	1.74E+09–4.34E+08[h)]	60–90[f)]
	10^{-4} - 10^{-3}	2.5	6.2E-04	3.16E+09[b)]	1.27E+09–3.16E+08[h)]	60–90[f)]
large particle	10^{-3} - 10^{-2}	2.5	1.3E-03	1.41E+09[c)]	5.65E+08–1.41E+08[h)]	60–90[g)]
	10^{-2} - 10^{-1}	2.5	2.9E-03	4.68E+08[c)]	1.87E+08–4.68E+07[h)]	60–90[g)]
	10^{-1} - 10^{0}	2.5	6.2E-03	1.41E+08[c)]	5.65E+07–1.41E+07[h)]	60–90[g)]
	10^{0} - 10^{1}	2.5	1.3E-02	2.24E+07[c)]	8.96E+06–2.24E+06[h)]	60–90[g)]
	10^{1} - 10^{2}	2.5	2.9E-02	3.55E+06[c)]	1.42E+06–3.55E+05[h)]	60–90[g)]
large body	10^{2} - 10^{3}	2.5	6.2E-02	2.36E+07[d)]	2.94E+06[d)]	88
	10^{3} - 10^{4}	2.5	1.3E-01	9.65E+07[d)]	1.19E+07[d)]	88
	10^{4} - 10^{5}	2.5	2.9E-01	1.81E+08[d)]	2.00E+07[d)]	89
	10^{5} - 10^{6}	2.5	6.2E-01	2.15E+08[d)]	1.20E+07[d)]	94
	10^{6} - 10^{7}	2.5	1.3E+00	2.53E+08[d)]	6.64E+06[d)]	97
	10^{7} - 10^{8}	2.5	2.9E+00	3.07E+08[d)]	2.84E+06[d)]	99
	10^{8} - 10^{9}	2.5	6.2E+00	3.63E+08[d)]	2.87E+06[d)]	99
	10^{9} - 10^{10}	2.5	1.3E+01	4.24E+08[d)]	2.64E+06[d)]	99
	10^{10} - 10^{11}	2.5	2.9E+01	5.02E+08[d)]	2.00E+06	99.6
	10^{11} - 10^{12}	2.5	6.2E+01	5.97E+08[d)]	5.00E+05	99.9
	10^{12} - 10^{13}	2.5	1.3E+02	7.05E+08[d)]	1.00E+04	≈100
	10^{13} - 10^{14}	2.5	2.9E+02	6.51E+08[d)]	0	100
	10^{14} - 10^{15}	2.5	6.2E+02	1.72E+09[d)]	0	100
very large bodies	10^{15} - 10^{16}	2.5	1.3E+03	7.72E+09[d)]	0	100
	10^{16} - 10^{17}	2.5	2.9E+03	3.15E+10[d)]	0	100
	10^{17} - 10^{18}	2.5	6.2E+03	1.14E+11[d)]	0	100
	10^{18} - 10^{19}	2.5	1.3E+04	4.58E+11[d)]	0	100
	10^{19} - 10^{20}	2.5	2.9E+04	9.73E+11[d)]	0	100
	10^{20} - 10^{21}	2.5	6.1E+04	1.61E+12[e)]	0	100
	10^{21} - 10^{22}	2.5	1.3E+05	4.87E+12[e)]	0	100
	10^{22} - 10^{23}	2.5	2.8E+05	5.53E+12[e)]	0	100
	10^{24} - 10^{25}	2.5	1.3E+06	1.32E+13[e)]	0	100
Sum				**2.68E+13**	**2.85E+09 - 7.79E+09**	

a) the particle size was calculated assuming spherical shape and a mass density of 2.5 g/cm³ for MMs, large particles, large bodies and very large bodies (see Grotheer and Livi, 2014) and 1.5 g/cm³ for β-meteorites and IDPs (cf. Pepin et al., 2000, 2001; Kehm et al., 2002) **b)** data from Grün et al. (1985); gravitational focusing for near Earth fluxes by a factor of 2 was superimposed onto the reported model interplanetary flux **c)** data from Anders (1989) **d)** data from Bland and Artemieva (2006) **e)** the total available main belt mass for the 10^{15} to 10^{20}g mass bins from Bottke et al. (2005) and the mass flux for the respective bin given by Bland and Artemieva (2006) are compared to calculate the mass fluxes for the 10^{20} to 10^{25}g mass bins assuming equal mass to flux proportions for these bins as found by the comparison of the lighter mass bins. The main belt size distribution given in diameter is converted into masses assuming a spherical body shape and a mass density of 2.7 g/cm³ (Bottke et al., 2005) **f)** from Cordier and Folco (2014) **g)** tentatively assumed equal losses for "large particles" as for micrometeorites h) range of particle mass flux to Earth's surface after applying atmospheric entry losses of 60 to 90% (Cordier and Folco, 2014).

B1: ^{20}Ne concentration within the 50 nm thick outer particle shell

Assuming that the entire measured Ne-inventory in the smallest IDPs (mass bin of 10^{-10}–10^{-9} g) of $6.92*10^{-2}$ cm³STP/g represents saturation of SW-implanted Ne in the outermost particle shell of 50 nm thickness, the ^{20}Ne conentration within this outer particle layer can be calculated. First, the respective volume dependent mass of this layer has to be calculated using a spherical shaped grain geometry with $V=\frac{4}{3}\pi r^3$ and $V=\frac{m}{\rho}$. In the calculations the mean mass (geometric) of $3.16*10^{-10}$ g for the smallest IDP mass bin is used. Following Pepin et al. (2000, 2001) and Kehm et al. (2002) the density of the smallest IDPs is 1.5 g/cm³.
Then, the radius of the IDP particle is:

$$r = \sqrt[3]{\frac{3m}{4\pi\rho}} \qquad (1).$$

Where m is the mass and ρ the density of the IDP. The volume V of the 50 nm tick shell can be calculated by subsitution of eq. (1) in:

$$V = \left(\tfrac{4}{3}\pi r^3\right) - \left(\tfrac{4}{3}\pi(r - 50\ nm)^3\right) \qquad (2)$$

With eq. (2) and the desnsity of 1.5 g/cm³ the mass of the 50 nm shell can be calculated according to:

$$m = \rho * V \qquad (3)$$

The amount of ^{20}Ne that is sited within the 50 nm thick shell can be determined with the mean concentration of the measured particles ($6.92*10^{-2}$ cm³STP/g) and their mean mass ($3.16*10^{-10}$ g):

$$V\ [\mathrm{cm^3STP}] = m * {}^{20}\mathrm{Ne\ concentration\ [cm^3STP/g]} \qquad (4)$$

Dividing (4) trough (3) gives the wanted ^{20}Ne concentration within the outermost 50 nm thick particle layer. This concentration amounts to 1.73 cm³STP/g.
Calculating the mass of the outer particle shell for smaller sizes (β-meteorites) according to eq. (3) and using the ^{20}Ne concentration of 1.73 cm³STP/g from eq. (4) the ^{20}Ne inventory in cm³STP in the respective shell of β-meteorites can be calculated (Tab. B2). Dividing this inventory through the mean mass of the mass bin yields the ^{20}Ne concentration for the complete particle:

$$^{20}Ne\ \text{concentration}\ [\mathrm{cm^3STP/g}] = \frac{V\ [\mathrm{cm^3STP}]}{m} \qquad (5)$$

For m the mean geometric mass of the respective mass bin is used (Tab. B2).

Tab. B2: Geometric downscaling of the ^{20}Ne concentration measured in IDPs for samller particle sizes. According to the ^{20}Ne concentration of 1.73 cm³STP/g calculated in B1 for the 50 nm thick outermost particle shell the ^{20}Ne inventory in this layer for smaller β-meteorites and the ^{20}Ne concentration can be calculated.

Particle type	Mass Bin [g]	Density [g/cm³]a)	radius [m]	vol. (shell) [cm³]	mass (shell) [g]	^{20}Ne (shell) [cm³STP]	^{20}Ne (part.) [cm³STP/g]
β-meteorite	10^{-16} - 10^{-15}	1.5	3.69E-08	2.20E-16	3.30E-16	5.70E-16	1.73E+00
	10^{-15} - 10^{-14}	1.5	7.95E-08	2.00E-15	3.00E-15	5.18E-15	1.64E+00
	10^{-14} - 10^{-13}	1.5	1.71E-07	1.36E-14	2.04E-14	3.52E-14	1.11E+00
	10^{-13} - 10^{-12}	1.5	3.69E-07	7.46E-14	1.12E-13	1.93E-13	6.10E-01
	10^{-12} - 10^{-11}	1.5	7.95E-07	3.73E-13	5.60E-13	9.66E-13	3.05E-01
	10^{-11} - 10^{-10}	1.5	1.71E-06	1.79E-12	2.69E-12	4.64E-12	1.47E-01

a) assumed density for β-meteorites following Pepin et al. (2000, 2001) and Kehm et al. (2002).

B2: Ne-B concentration in the 50 nm shell of "inner Solar System bodies" during accretion

The ^{20}Ne concentration of solar wind irradiated materials of all sizes that accreted in the inner Solar System during early terrestrial formation can be calculated by geometric upcaling of the surface correlated Ne-B component (^{20}Ne/^{22}Ne: 12.61). For this purpose, the ^{20}Ne concentration of the SW-saturated 50 nm thick outer particle shell determined to 1.73 cm³STP/g (see B1) has to be multiplied with the respective volume fraction of the 50 nm shell from the total volume of the particle or body (Tab. B3). The density of the inner Solar System bodies is assumed 2.5 g/cm³ (Grotheer and Livi, 2014). Then the volume of the total particle can be calculated with:

$$V = \frac{m}{\rho} \qquad (6)$$

Where m is the mean geometric mass of each mass interval. The volume of the 50 nm thick particle shell can be calculated by using equations (1) and (2). The volume fraction of the particle shell from the particle volume multiplied with the maximum ^{20}Ne concentration of 1.73 cm³STP/g in the outer layer gives the respective ^{20}Ne concentration for larger particles and bodies for each mass interval.

$$^{20}\text{Ne concentration [cm}^3\text{STP/g]} = \frac{\text{V(i,50 nm)}}{\text{V(i,particle)}} * 1.73\ \text{cm}^3\text{STP/g} \qquad (7)$$

Where *i* is the index for a particular mass bin (Tab. B3). All particle sizes contain a ^{20}Ne/^{22}Ne ratio of 12.61.

Tab. B3: Geometric upscaling of the ^{20}Ne concentration for the surface correlated Ne-B component.

Particle type	Mass Bin [g]	Density [g/cm³]a)	vol. (part.) [cm³]	vol. (shell) [cm³]	fract. of shell from particle	^{20}Ne (part.) [cm³STP/g]
β-meteorite	10^{-16} - 10^{-15}	2.5	1.26E-16	1.26E-16	1.00E+00	1.73E+00
	10^{-15} - 10^{-14}	2.5	1.26E-15	1.24E-15	9.83E-01	1.70E+00
	10^{-14} - 10^{-13}	2.5	1.26E-14	9.11E-15	7.20E-01	1.24E+00
	10^{-13} - 10^{-12}	2.5	1.26E-13	5.17E-14	4.08E-01	7.05E-01
	10^{-12} - 10^{-11}	2.5	1.26E-12	2.62E-13	2.07E-01	3.58E-01
	10^{-11} - 10^{-10}	2.5	1.26E-11	1.27E-12	1.00E-01	1.73E-01
IDP	10^{-10} - 10^{-9}	2.5	1.26E-10	6.00E-12	4.74E-02	8.18E-02
	10^{-9} - 10^{-8}	2.5	1.26E-09	2.81E-11	2.22E-02	3.83E-02
	10^{-8} - 10^{-7}	2.5	1.26E-08	1.31E-10	1.03E-02	1.78E-02
MM	10^{-7} - 10^{-6}	2.5	1.26E-07	6.08E-10	4.81E-03	8.30E-03
	10^{-6} - 10^{-5}	2.5	1.26E-06	2.83E-09	2.23E-03	3.86E-03
	10^{-5} - 10^{-4}	2.5	1.26E-05	1.31E-08	1.04E-03	1.79E-03
	10^{-4} - 10^{-3}	2.5	1.26E-04	6.09E-08	4.82E-04	8.31E-04
large particle	10^{-3} - 10^{-2}	2.5	1.26E-03	2.83E-07	2.24E-04	3.86E-04
	10^{-2} - 10^{-1}	2.5	1.26E-02	1.31E-06	1.04E-04	1.79E-04
	10^{-1} - 10^{0}	2.5	1.26E-01	6.09E-06	4.82E-05	8.31E-05
	10^{0} - 10^{1}	2.5	1.26E+00	2.83E-05	2.24E-05	3.86E-05
	10^{1} - 10^{2}	2.5	1.26E+01	1.31E-04	1.04E-05	1.79E-05
large body	10^{2} - 10^{3}	2.5	1.26E+02	6.09E-04	4.82E-06	8.31E-06
	10^{3} - 10^{4}	2.5	1.26E+03	2.83E-03	2.24E-06	3.86E-06
	10^{4} - 10^{5}	2.5	1.26E+04	1.31E-02	1.04E-06	1.79E-06
	10^{5} - 10^{6}	2.5	1.26E+05	6.09E-02	4.82E-07	8.31E-07
	10^{6} - 10^{7}	2.5	1.26E+06	2.83E-01	2.24E-07	3.86E-07
	10^{7} - 10^{8}	2.5	1.26E+07	1.31E+00	1.04E-07	1.79E-07
	10^{8} - 10^{9}	2.5	1.26E+08	6.09E+00	4.82E-08	8.31E-08
	10^{9} - 10^{10}	2.5	1.26E+09	2.83E+01	2.24E-08	3.86E-08
	10^{10} - 10^{11}	2.5	1.26E+10	1.31E+02	1.04E-08	1.79E-08
	10^{11} - 10^{12}	2.5	1.26E+11	6.09E+02	4.82E-09	8.31E-09
	10^{12} - 10^{13}	2.5	1.26E+12	2.83E+03	2.24E-09	3.86E-09
	10^{13} - 10^{14}	2.5	1.26E+13	1.31E+04	1.04E-09	1.79E-09
	10^{14} - 10^{15}	2.5	1.26E+14	6.09E+04	4.82E-10	8.31E-10
very large bodies	10^{15} - 10^{16}	2.5	1.26E+15	2.83E+05	2.24E-10	3.86E-10
	10^{16} - 10^{17}	2.5	1.26E+16	1.31E+06	1.04E-10	1.79E-10
	10^{17} - 10^{18}	2.5	1.26E+17	6.09E+06	4.82E-11	8.31E-11
	10^{18} - 10^{19}	2.5	1.26E+18	2.83E+07	2.24E-11	3.86E-11
	10^{19} - 10^{20}	2.5	1.26E+19	1.31E+08	1.04E-11	1.79E-11
	10^{20} - 10^{21}	2.5	1.26E+20	6.10E+08	4.82E-12	8.32E-12
	10^{21} - 10^{22}	2.5	1.26E+21	2.83E+09	2.24E-12	3.86E-12
	10^{22} - 10^{23}	2.5	1.26E+22	1.32E+10	1.04E-12	1.80E-12
	10^{24} - 10^{25}	2.5	1.26E+24	2.79E+11	2.20E-13	3.80E-13

a) the density of the "inner Solar System bodies" is assumed to be 2.5g/cm³ following Grotheer and Livi (2014).

Tab. B4: $^{20}Ne/^{22}Ne$ ratios and ^{20}Ne inventories (cm^3STP/g) of terrestrial building blocks ranging from 10^{-16} to 10^{25} g (β-meteorites, IDPs, MMs, large particles, large bodies, very large bodies) divided in decadal mass bins. The annual Ne fluxes (cm^3 STP/year) are calculated reaching Earth's upper atmosphere for A) Ne-B carriers (inner Solar System bodies), B) Ne-A carriers (e.g., carbonaceous chondrites) and to Earth's surface for C) Ne-B, D) Ne-A. For this purpose, the Ne concentration of each mass bin was multiplied by the respective particle mass flux shown in Tab. B1.

Particle type	Mass Bin [g]	A)	20Ne/22Ne	20Ne Concentr. (cm^3STP/g)	Upper Atm. 20Ne-Flux ($cm^3STP/year$)	Upper Atm. 22Ne-Flux ($cm^3STP/year$)	B)	20Ne/22Ne	20Ne Concentr. (cm^3STP/g)	Upper Atm. 20Ne-Flux ($cm^3STP/year$)	Upper Atm. 22Ne-Flux ($cm^3STP/year$)	C)	20Ne/22Ne	20Ne Concentr. (cm^3STP/g)	Surface 20Ne-Flux ($cm^3STP/year$)	Surface 22Ne-Flux ($cm^3STP/year$)	D)	20Ne/22Ne	20Ne Concentr. (cm^3STP/g)	Surface 20Ne-Flux ($cm^3STP/year$)	Surface 22Ne-Flux ($cm^3STP/year$)
β-meteorite	10^{-16} - 10^{-15}	Ne-B upper atmosphere flux (inner Solar System bodies)	12.61	1.73E+00	8.43E+04	6.68E+03	Ne-A upper atmosphere flux (e.g. CI)	8.20	2.57E-07[d]	1.25E-02	1.53E-03	Ne-B surface flux	12.61[a]	1.73E+00[a]	8.43E+04	6.68E+03	Ne-A surface flux				
	10^{-15} - 10^{-14}		12.61	1.70E+00	1.47E+05	1.16E+04		8.20	2.57E-07[d]	2.22E-02	2.71E-03		12.61[a]	1.70E+00[a]	1.47E+05	1.16E+04					
	10^{-14} - 10^{-13}		12.61	1.24E+00	2.11E+05	1.67E+04		8.20	2.57E-07[d]	4.37E-02	5.32E-03		12.61[a]	1.24E+00[a]	2.11E+05	1.67E+04					
	10^{-13} - 10^{-12}		12.61	7.05E-01	3.51E+05	2.79E+04		8.20	2.57E-07[d]	1.28E-01	1.56E-02		12.61[a]	7.05E-01[a]	3.51E+05	2.79E+04					
	10^{-12} - 10^{-11}		12.61	3.58E-01	6.92E+05	5.48E+04		8.20	2.57E-07[d]	4.97E-01	6.06E-02		12.61[a]	3.58E-01[a]	6.92E+05	5.48E+04					
	10^{-11} - 10^{-10}		12.61	1.73E-01	1.51E+06	1.20E+05		8.20	2.57E-07[d]	2.25E+00	2.74E-01		12.61[a]	1.73E-01[a]	1.51E+06	1.20E+05					
IDP	10^{-10} - 10^{-9}		12.61	8.18E-02	2.83E+06	2.24E+05		8.20	2.57E-07[d]	8.89E+00	1.08E+00		12.61[b]	6.92E-02[b]	2.39E+06	1.90E+05					
	10^{-9} - 10^{-8}		12.61	3.83E-02	7.01E+06	5.56E+05		8.20	2.57E-07[d]	4.71E+01	5.74E+00		11.84[b]	9.69E-04[b]	1.78E+05	1.50E+04					
	10^{-8} - 10^{-7}		12.61	1.78E-02	1.63E+07	1.30E+06		8.20	2.57E-07[d]	2.35E+02	2.87E+01		12.10[b]	2.05E-04[b]	1.88E+05	1.55E+04					
MM	10^{-7} - 10^{-6}		12.61	8.30E-03	2.14E+07	1.69E+06		8.20	2.57E-07[d]	6.61E+02	8.07E+01		11.14[d]	1.15E-05[d]	2.96E+04	2.66E+03					
	10^{-6} - 10^{-5}		12.61	3.86E-03	1.66E+07	1.32E+06		8.20	2.57E-07[d]	1.11E+03	1.35E+02		11.10[d]	4.14E-06[d]	1.79E+04	1.61E+03					
	10^{-5} - 10^{-4}		12.61	1.79E-03	7.78E+06	6.17E+05		8.20	2.57E-07[d]	1.12E+03	1.36E+02		11.39[d]	9.06E-07[d]	3.94E+03	3.46E+02					
	10^{-4} - 10^{-3}		12.61	8.31E-04	2.63E+06	2.09E+05		8.20	2.57E-07[d]	8.13E+02	9.92E+01		9.55[c]	1.89E-07[d]	5.99E+02	6.27E+01					
large particle	10^{-3} - 10^{-2}		12.61	3.86E-04	5.45E+05	4.32E+04		8.20	2.57E-07[d]	3.63E+02	4.43E+01							8.20	2.57E-07[d]	3.63E+02	4.43E+01
	10^{-2} - 10^{-1}		12.61	1.79E-04	8.38E+04	6.64E+03		8.20	2.57E-07[d]	1.20E+02	1.47E+01							8.20	2.57E-07[d]	1.20E+02	1.47E+01
	10^{-1} - 10^{0}		12.61	8.31E-05	1.17E+04	9.31E+02		8.20	2.57E-07[d]	3.63E+01	4.43E+00							8.20	2.57E-07[d]	3.63E+01	4.43E+00
	10^{0} - 10^{1}		12.61	3.86E-05	8.64E+02	6.85E+01		8.20	2.57E-07[d]	5.75E+00	7.02E-01							8.20	2.57E-07[d]	5.75E+00	7.02E-01
	10^{1} - 10^{2}		12.61	1.79E-05	6.35E+01	5.04E+00		8.20	2.57E-07[d]	9.12E-01	1.11E-01							8.20	2.57E-07[d]	9.12E-01	1.11E-01
large body	10^{2} - 10^{3}		12.61	8.31E-06	1.97E+02	1.56E+01		8.20	2.57E-07[d]	6.08E+00	7.41E-01							8.20	2.57E-07[d]	7.55E-01	9.21E-02
	10^{3} - 10^{4}		12.61	3.86E-06	3.72E+02	2.95E+01		8.20	2.57E-07[d]	2.48E+01	3.03E+00							8.20	2.57E-07[d]	3.05E+00	3.71E-01
	10^{4} - 10^{5}		12.61	1.79E-06	3.24E+02	2.57E+01		8.20	2.57E-07[d]	4.65E+01	5.68E+00							8.20	2.57E-07[d]	5.15E+00	6.28E-01
	10^{5} - 10^{6}		12.61	8.31E-07	1.78E+02	1.42E+01		8.20	2.57E-07[d]	5.52E+01	6.73E+00							8.20	2.57E-07[d]	3.07E+00	3.75E-01
	10^{6} - 10^{7}		12.61	3.86E-07	9.76E+01	7.74E+00		8.20	2.57E-07[d]	6.50E+01	7.93E+00							8.20	2.57E-07[d]	1.71E+00	2.08E-01
	10^{7} - 10^{8}		12.61	1.79E-07	5.49E+01	4.36E+00		8.20	2.57E-07[d]	7.88E+01	9.61E+00							8.20	2.57E-07[d]	7.31E-01	8.91E-02
	10^{8} - 10^{9}		12.61	8.31E-08	3.02E+01	2.39E+00		8.20	2.57E-07[d]	9.33E+01	1.14E+01							8.20	2.57E-07[d]	7.38E-01	9.00E-02
	10^{9} - 10^{10}		12.61	3.86E-08	1.63E+01	1.30E+00		8.20	2.57E-07[d]	1.09E+02	1.33E+01							8.20	2.57E-07[d]	6.78E-01	8.27E-02
	10^{10} - 10^{11}		12.61	1.79E-08	8.98E+00	7.12E-01		8.20	2.57E-07[d]	1.29E+02	1.57E+01							8.20	2.57E-07[d]	5.14E-01	6.27E-02
	10^{11} - 10^{12}		12.61	8.31E-09	4.96E+00	3.93E-01		8.20	2.57E-07[d]	1.53E+02	1.87E+01							8.20	2.57E-07[d]	1.29E-01	1.57E-02
	10^{12} - 10^{13}		12.61	3.86E-09	2.72E+00	2.16E-01		8.20	2.57E-07[d]	1.81E+02	2.21E+01							8.20	2.57E-07[d]	2.57E-03	3.13E-04
	10^{13} - 10^{14}		12.61	1.79E-09	1.17E+00	9.25E-02		8.20	2.57E-07[d]	1.67E+02	2.04E+01										
	10^{14} - 10^{15}		12.61	8.31E-10	1.43E+00	1.13E-01		8.20	2.57E-07[d]	4.41E+02	5.38E+01										
very large bodies	10^{15} - 10^{16}		12.61	3.86E-10	2.98E+00	2.36E-01		8.20	2.57E-07[d]	1.98E+03	2.42E+02										
	10^{16} - 10^{17}		12.61	1.79E-10	5.65E+00	4.48E-01		8.20	2.57E-07[d]	8.10E+03	9.88E+02										
	10^{17} - 10^{18}		12.61	8.31E-11	9.44E+00	7.48E-01		8.20	2.57E-07[d]	2.92E+04	3.56E+03										
	10^{18} - 10^{19}		12.61	3.86E-11	1.77E+01	1.40E+00		8.20	2.57E-07[d]	1.18E+05	1.44E+04										
	10^{19} - 10^{20}		12.61	1.79E-11	1.74E+01	1.38E+00		8.20	2.57E-07[d]	2.50E+05	3.05E+04										
	10^{20} - 10^{21}		12.61	8.32E-12	1.34E+01	1.07E+00		8.20	2.57E-07[d]	4.15E+05	5.06E+04										
	10^{21} - 10^{22}		12.61	3.86E-12	1.88E+01	1.49E+00		8.20	2.57E-07[d]	1.25E+06	1.53E+05										
	10^{22} - 10^{23}		12.61	1.80E-12	9.93E+00	7.87E-01		8.20	2.57E-07[d]	1.42E+06	1.73E+05										
	10^{24} - 10^{25}		12.61	3.80E-13	5.00E+00	3.97E-01		8.20	2.57E-07[d]	3.38E+06	4.13E+05										
Sum					**7.82E+07**	**6.20E+06**				**6.88E+06**	**8.39E+05**				**5.81E+06**	**4.63E+05**				**5.43E+02**	**6.62E+01**
Resulting 20/22			**12.61**					**8.20**					**12.55**					**8.20**			

a) values are calculated by geometric downscaling from IDP data **b)** geometric mean of data from Nier and Schlutter (1990), Pepin et al. (2000, 2001) and Kehm et al. (2002); only values with errors <15% were used **c)** geometric mean of data from Osawa et al. (2000, 2003a, 2003b, 2010), Osawa and Nagao (2002a, 2002b), Bajo et al. (2011), Baecker (2014) and Okazaki et al. (2015); only values with errors <15% were used **d)** mean ^{20}Ne concentration for the primordial Ne-A component of CI chondrites (Mazor et al., 1970).

Tab. B5: For exemplification a late venner $^{20}Ne/^{22}Ne$ end-member of 8.2 (Ne-A) is assumed and a Ne-B mantle end-member of 12.61 is considered. To generate an atmospheric $^{20}Ne/^{22}Ne$ ratio of 9.8 by mixing a late veneer component and mantle degassing the fraction of mantle contribution is given by $\frac{\frac{1}{9.8}-\frac{1}{8.2}}{\frac{1}{12.61}-\frac{1}{8.2}} = 0.467$ (=46.7%) and the fraction of late veneer contribution is $1 - 0.467 = 0.553$ (= 53.3%). The ^{20}Ne atmospheric inventory is known ($6.52*10^{19}$ cm³STP; Zhang, 2014) as well as the mantle inventory ($6.55*10^{18}$ cm³STP for a moderately degassed mantle and $1.31*10^{18}$ cm³STP for a strongly degassed mantle; Marty, 2012). An absolute amount of $0.467 * 6.52 * 10^{19} cm^3 STP = 3.04 * 10^{19} cm^3 STP$ is therefore added to the asmosphere by mantle degassing. This amount accounts for a $\frac{3.04*10^{19} cm^3 STP}{(3.04*10^{19} + 6.55*10^{18}) cm^3 STP} = 0.823$ (= 82.3%) degassed mantle. This value is used in eq. (12) and adjusted according to the associated parameters. The respective fraction of Earth's mass (M_E) that is contributed by the late veneer (eq. (14)) is evaluated by applying an enhancement to the average annual mass flux (Tab. B1) to explain today's atmosperic and mantle Ne inventories according to the calculations shown in Table B7. The results of the calculations for different late veneer end-members in case of a moderately degassed and a strongly degassed mantle are shown in Table B5 and Figure 3.9.

Magma ocean model				
moderately degassed mantle				
atmospheric ^{20}Ne [cm³]			**6.52E+19**	
mantle ^{20}Ne [cm³]			**6.55E+18**	
Late veneer endmember	**mantle ^{20}Ne in atmosphere**	**mantle degassing**	**fraction of Late veneer**	**M_E**
5.2	79.9%	88.82%	20.1%	0.85%
6.2	72.3%	87.79%	27.7%	1.18%
7.2	61.8%	86.02%	38.2%	1.62%
8.2	46.7%	82.28%	53.3%	2.26%
8.4	42.8%	80.97%	57.2%	2.43%
8.6	38.5%	79.30%	61.5%	2.61%
8.8	33.8%	77.06%	66.2%	2.81%
9.0	28.5%	73.93%	71.5%	3.03%
9.2	22.6%	69.25%	77.4%	3.28%
9.4	16.0%	61.46%	84.0%	3.56%
9.6	8.5%	45.96%	91.5%	3.88%
9.8	0.0%	0.00%	100.0%	4.24%

Magma ocean model				
strongly degassed mantle				
atmospheric ^{20}Ne [cm³]			**6.52E+19**	
mantle ^{20}Ne [cm³]			**1.31E+18**	
Late veneer endmember	**mantle ^{20}Ne in atmosphere**	**mantle degassing**	**fraction of Late veneer**	**M_E**
5.2	79.9%	97.54%	20.1%	0.85%
6.2	72.3%	97.29%	27.7%	1.18%
7.2	61.8%	96.85%	38.2%	1.62%
8.2	46.7%	95.87%	53.3%	2.26%
8.4	42.8%	95.51%	57.2%	2.43%
8.6	38.5%	95.04%	61.5%	2.61%
8.8	33.8%	94.38%	66.2%	2.81%
9.0	28.5%	93.41%	71.5%	3.03%
9.2	22.6%	91.84%	77.4%	3.28%
9.4	16.0%	88.86%	84.0%	3.56%
9.6	8.5%	80.96%	91.5%	3.88%
9.8	0.0%	0.00%	100.0%	4.24%

Tab. B6: According to the calculations performed in Table B7 a certain fixed amount of ^{20}Ne has to be present in the mantle in function of the magma ocean depth, total accreted ^{20}Ne and the partial pressure in the atmosphere. This amount is available for mantle degassing in "phase II" after the giant Moon-forming impact (eq. (11) and eq. (12)). The amount of degassed Ne with a $^{20}Ne/^{22}Ne$ ratio of 12.61 (Ne-B) mixes with a late veneer contributed $^{20}Ne/^{22}Ne$ component (Ne-A: 5.2, 8.2 and 9.2, see Tab. B6) to generate today's atmospheric ^{20}Ne inventory (eq. (12)) and $^{20}Ne/^{22}Ne$ ratio of 9.8. Furthermore, sufficient ^{20}Ne has to be spared to achieve today's mantle inventory (eq. (13)). In any case the fraction of ^{20}Ne from the total accreted Ne (before the Moon-forming giant impact) that is dissolved (assuming a fixed Ne solubility of $2.5*10^{-4}$ cm³/g/bar) into the magma ocean (eq.(11)) of a certain depth is independent of the $^{20}Ne/^{22}Ne$ component of the late veneer and the related degree of mantle degassing. The results of the calculations are shown in Table B6 and Figure 3.10.

moderately degassed mantle

Late veneer $^{20}Ne/^{22}Ne$					**8.2**
degree of mantle degassing [%]					**82**
magma ocean depth [km]	**dissolved ^{20}Ne [cm³]**	**diss. ^{20}Ne [cm³/g]**	**total accreted ^{20}Ne [cm³]**	**part. pres. ^{20}Ne [bar]**	**fract. diss. ^{20}Ne [%]**
60	3.7E+19	5.36E-07	8.5E+21	2.1E-03	0.43
94	3.7E+19	3.46E-07	5.5E+21	1.4E-03	0.67
159	3.7E+19	2.07E-07	3.3E+21	8.3E-04	1.13
214	3.7E+19	1.56E-07	2.5E+21	6.2E-04	1.50
242	3.7E+19	1.38E-07	2.2E+21	5.5E-04	1.69
278	3.7E+19	1.21E-07	1.9E+21	4.8E-04	1.93
305	3.7E+19	1.11E-07	1.8E+21	4.4E-04	2.11
316	3.7E+19	1.07E-07	1.7E+21	4.3E-04	2.18
327	3.7E+19	1.04E-07	1.6E+21	4.1E-04	2.25
398	3.7E+19	8.64E-08	1.4E+21	3.5E-04	2.71
507	3.7E+19	6.91E-08	1.1E+21	2.8E-04	3.38
700	3.7E+19	5.18E-08	8.2E+20	2.1E-04	4.51
900	3.7E+19	4.18E-08	6.6E+20	1.7E-04	5.59
1138	3.7E+19	3.46E-08	5.5E+20	1.4E-04	6.77
1500	3.7E+19	2.81E-08	4.4E+20	1.1E-04	8.33
2000	3.7E+19	2.32E-08	3.7E+20	9.3E-05	10.10
2430	3.7E+19	2.07E-08	3.3E+20	8.3E-05	11.28
Late veneer $^{20}Ne/^{22}Ne$					**9.2**
degree of mantle degassing [%]					**69**
61	2.1E+19	3.08E-07	4.87E+21	1.2E-03	0.44
90	2.1E+19	2.07E-07	3.29E+21	8.3E-04	0.65
136	2.1E+19	1.38E-07	2.19E+21	5.5E-04	0.97
183	2.1E+19	1.04E-07	1.64E+21	4.1E-04	1.29
280	2.1E+19	6.91E-08	1.10E+21	2.8E-04	1.95
592	2.1E+19	3.46E-08	5.48E+20	1.4E-04	3.89
1079	2.1E+19	2.07E-08	3.29E+20	8.3E-05	6.49
Late veneer $^{20}Ne/^{22}Ne$					**5.2**
degree of mantle degassing [%]					**89**
61	5.9E+19	8.47E-07	1.34E+22	3.4E-03	0.44
151	5.9E+19	3.46E-07	5.48E+21	1.4E-03	1.07
256	5.9E+19	2.07E-07	3.29E+21	8.3E-04	1.79
346	5.9E+19	1.56E-07	2.46E+21	6.2E-04	2.38
454	5.9E+19	1.21E-07	1.92E+21	4.8E-04	3.06
854	5.9E+19	6.91E-08	1.10E+21	2.8E-04	5.35
1218	5.9E+19	5.18E-08	8.21E+20	2.1E-04	7.14
2206	5.9E+19	3.46E-08	5.48E+20	1.4E-04	10.70

strongly degassed mantle

Late veneer $^{20}Ne/^{22}Ne$					**8.2**
degree of mantle degassing [%]					**96**
magma ocean depth [km]	**dissolved ^{20}Ne [cm³]**	**diss. ^{20}Ne [cm³/g]**	**total accreted ^{20}Ne [cm³]**	**part. pres. ^{20}Ne [bar]**	**fract. diss. ^{20}Ne [%]**
52	3.2E+19	5.36E-07	8.49E+21	2.1E-03	0.38
73	3.2E+19	3.8E-07	6.02E+21	1.5E-03	0.53
90	3.2E+19	3.11E-07	4.93E+21	1.2E-03	0.65
101	3.2E+19	2.76E-07	4.38E+21	1.1E-03	0.72
136	3.2E+19	2.07E-07	3.29E+21	8.3E-04	0.97
182	3.2E+19	1.56E-07	2.46E+21	6.2E-04	1.29
279	3.2E+19	1.04E-07	1.64E+21	4.1E-04	1.94
429	3.2E+19	6.91E-08	1.10E+21	2.8E-04	2.90
589	3.2E+19	5.18E-08	8.21E+20	2.1E-04	3.87
942	3.2E+19	3.46E-08	5.48E+20	1.4E-04	5.81
1870	3.2E+19	2.07E-08	3.29E+20	8.3E-05	9.68
Late veneer $^{20}Ne/^{22}Ne$					**9.2**
degree of mantle degassing [%]					**92**
46	1.6E+19	3.08E-07	4.87E+21	1.2E-03	0.33
58	1.6E+19	2.4E-07	3.81E+21	9.6E-04	0.42
102	1.6E+19	1.38E-07	2.19E+21	5.5E-04	0.73
137	1.6E+19	1.04E-07	1.64E+21	4.1E-04	0.98
208	1.6E+19	6.91E-08	1.10E+21	2.8E-04	1.46
433	1.6E+19	3.46E-08	5.48E+20	1.4E-04	2.93
767	1.6E+19	2.07E-08	3.29E+20	8.3E-05	4.88
1878	1.6E+19	1.04E-08	1.65E+20	4.2E-05	9.71
Late veneer $^{20}Ne/^{22}Ne$					**5.2**
degree of mantle degassing [%]					**98**
55	5.3E+19	8.47E-07	1.34E+22	3.4E-03	0.40
137	5.3E+19	3.46E-07	5.48E+21	1.4E-03	0.98
232	5.3E+19	2.07E-07	3.29E+21	8.3E-04	1.63
313	5.3E+19	1.56E-07	2.46E+21	6.2E-04	2.16
410	5.3E+19	1.21E-07	1.92E+21	4.8E-04	2.78
765	5.3E+19	6.91E-08	1.10E+21	2.8E-04	4.87
1081	5.3E+19	5.18E-08	8.21E+20	2.1E-04	6.50
1889	5.3E+19	3.46E-08	5.48E+20	1.4E-04	9.74
2207	5.3E+19	3.14E-08	4.98E+20	1.3E-04	10.70

Tab. B7: The model calculation are performed by adjusting the critical parameters for the late veneer isotopic composition and degree of mantle degassing (Tab. B5) to the related amount of pre-lunar impact dissolved ^{20}Ne in the mantle that is available for degassing after the giant impact and the depth of the magma ocean in which the ^{20}Ne is dissolved (Tab. B6). The adjustments of the interdependent parameters are intended to result in a Ne composition that fits today's terrestrial Ne characteristics by a deviation of less then 1%. The Ne values that are aimed to be reconciled are the atmospheric ^{20}Ne inventory ($6.52*10^{19}$ cm³STP; Zhang, 2014) and ^{20}Ne/^{22}Ne ratio of 9.80 (eq. (12)) as well as the ^{20}Ne inventory of the mantle (eq. (13), $6.55*10^{18}$ cm³STP for a moderately degassed mantle and $1.31*10^{18}$ cm³STP for a strongly degassed mantle; Marty, 2012).
First, two separate periods of enhanced mass and Ne flux during accretion have to be considered: an early "phase I" before the Moon-forming impact and a "pahse II" of late accretion. For exemplified calculations a late veneer contribution in "phase II" with an isotopic ratio of ^{20}Ne/^{22}Ne: 8.2 (Ne-A) shall be assumed which already constrains all previously established Ne components: In "phase I", earlierst accretion happens within a gas shielded disk environment (e.g., for 5 Ma) with enhanced mass and Ne fluxes of $4.03*10^7$ times the present flux (exemplified case). SW-implantation is possible in a subsequent stage after the dissipation of the solar nebula (e.g., for 7 Ma) with prevailing mass and Ne fluxes of $1.50*10^6$ times the present flux (exemplified case). The fraction of SW irradiated material from the total terrestrial precursor material is then given by the time dependent flux rates:

$$\frac{(1.50 * 10^6) * 7\text{Ma}}{(1.50 * 10^6) * 7\text{Ma} + (4.03 * 10^7) * 5\text{Ma}} = 0.05\ (= 5.00\%) \quad (8)$$

This is justified if ~95% of Eath's mass is accreted before the Moon-forming impact by using the mass flux in Table B1:

$$(4.03 * 10^7) * \left(\sum_{10^{-16}g}^{10^{25}g} massbin\ flux\ \left[{}^{g}/_{yr}\right] \right) * 5Ma + (1.50 * 10^6) * \left(\sum_{10^{-16}g}^{10^{25}g} massbin\ flux\ \left[{}^{g}/_{yr}\right] \right) * 7Ma = 0.95\ M_E \quad (9)$$

The amount of accreted ^{20}Ne during SW-implantation in the inner Solar System is then given using the upper atmosphere Ne-B flux (Tab. B4):

$$(1.50 * 10^6) * \left(\sum_{10^{-16}g}^{10^{25}g} {}^{20}Ne\ bin\ flux\ (Ne-B)\ \left[{}^{cm^3STP}/_{yr}\right] \right) * 7Ma = 8.21 * 10^{20} cm^3STP\ {}^{20}Ne \quad (10)$$

The total amount of accreted ^{20}Ne in "phase I" (eq. (10)) is dissolved in a magma ocean of 700 km depth (exemplified case, Tab. B6). Here, the Ne solubility of $2.5*10^{-4}$ cm³STP/g/bar is used (Jambon et al., 1986; Paonita, 2005). The weight of the melt is calculated with 2.8 g/cm³ and the volume of a 700 km deep magma ocean on a growing Earth that has reached ≳90% of its present size. The partial pressure of the dissolving Ne is calculated by dividing the total accreted amount of ^{20}Ne (eq. (10)) through today's atmospheric inventory ($3.961*10^{24}$ cm³STP; Ozima and Podosek, 2002). The amount of dissolved ^{20}Ne then is:

$$\left(2.5 * 10^{-4} \frac{\text{cm}^3\text{STP}}{\text{g} * \text{bar}}\right) * \left(\frac{8.21 * 10^{20}}{3.961 * 10^{24}}\right) bar * (7.2 * 10^{26}\text{g}) \ = \ 3.7 * 10^{19}\text{cm}^3\text{STP} \quad (11)$$

This represents 4.51% of the total accreted ^{20}Ne (see Tab. B6 and Fig. 3.10).
In "phase II", after the giant Moon-forming impact that caused total atmospheric blow-off and the generation of a magma ocean, mantle degassing leads to reinjection of the previously dissolved ^{20}Ne (eq. (11)) into the atmosphere. The degassed Ne-B component mixes with the late veneer Ne-A component to generate the present atmospheric Ne inventory (Tab. B5). Here, the isotopic composition of the late veneer comes into play (exemplified case for ^{20}Ne/^{22}Ne: 8.2 (Ne-A)).
To mix with a Ne-B component (^{20}Ne/^{22}Ne: 12.61), resulting from 82.16% mantle degassing (Tab. B5), a late veneer flux of $1*10^5$ times the present flux with an isotopic composition of ^{20}Ne/^{22}Ne: 8.2 (upper atmosphere Ne-A flux in Tab. B4, exemplified case) prevailing for a 50 Ma period, is neede to result in the present atmospheric ^{20}Ne/^{22}Ne ratio of 9.80:

$$\frac{(3.7 * 10^{19}\text{cm}^3\text{STP} * 0.8216) + (1 * 10^5) * \left(\sum_{10^{-16}g}^{10^{25}g} {}^{20}Ne\ bin\ flux\ (Ne-A)\left[{}^{cm^3STP}/_{yr}\right]\right) * 50\ Ma}{\left(\frac{3.7 * 10^{19}\text{cm}^3\text{STP} * 0.8216}{12.61}\right) + (1 * 10^5) * \left(\sum_{10^{-16}g}^{10^{25}g} {}^{22}Ne\ bin\ flux\ (Ne-A)\left[{}^{cm^3STP}/_{yr}\right]\right) * 50\ Ma} = 9.80 \quad (12)$$

The atmospheric ^{20}Ne inventory is given by the numerator of eq. (12) and amounts to $6.52 * 10^{19}\text{cm}^3\text{STP}$. The remaining ^{20}Ne after mantle degassing determines the present mantle inventory observed today for a moderately degassed mantle and is calculatd with:

$$3.7 * 10^{19}\text{cm}^3\text{STP} * (1 - 0.8216) \approx 6.6 * 10^{18}\text{cm}^3\text{STP} \quad (13)$$

With an enhaced flux of $1*10^5$ times the present flux for 50 Ma the total accreted late veneer mass is calculated by applying Tab. B1:

$$(1 * 10^5) * \left(\sum_{10^{-16}g}^{10^{25}g} massbin\ flux\ \left[{}^{g}/_{yr}\right] \right) * 50\ Ma = 1.35 * 10^{26} g \quad (14)$$

This value amounts to 2.26% of the total mass of Earth of $5.97*10^{27}$ g (Tab. B5).

The results of the calculations for a range of parameter sets, exemplified above for a single case, that lead to satisfactory Ne inventories for Earth are shown in Table B7 and Figure 3.11.

moderately degassed mantle			
Late veneer $^{20}Ne/^{22}Ne$			**8.2**
M_E [%] accreted by Late veneer			**2.26**
degree of mantle degassing [%]			**82.16**
shielded accretion (e.g. 5 Ma)	**duration of SW-irrad. (e.g. 7 Ma)**	**fraction of SW-irrad**	**depth of magma ocean**
flux times present		**[%]**	**[km]**
atmospheric loss by giant impact [%]			**100**
2.1E+07	1.6E+07	51.2%	60
2.8E+07	1.0E+07	33.0%	94
3.4E+07	6.0E+06	19.8%	159
3.6E+07	4.5E+06	14.9%	214
3.7E+07	4.0E+06	13.2%	242
3.8E+07	3.5E+06	11.6%	278
3.8E+07	3.2E+06	10.6%	305
3.8E+07	3.1E+06	10.2%	316
3.8E+07	3.0E+06	9.9%	327
3.9E+07	2.5E+06	8.3%	398
4.0E+07	2.0E+06	6.6%	507
4.0E+07	1.5E+06	5.0%	700
4.1E+07	1.2E+06	4.0%	900
4.1E+07	1.0E+06	3.3%	1138
4.1E+07	8.1E+05	2.7%	1500
4.1E+07	6.7E+05	2.2%	2000
4.2E+07	6.0E+05	2.0%	2430
4.2E+07	3.0E+05	1.0%	10590
Late veneer $^{20}Ne/^{22}Ne$			**9.2**
M_E [%] accreted by Late veneer			**3.28**
degree of mantle degassing [%]			**69**
shielded accretion (e.g. 5 Ma)	**duration of SW-irrad. (e.g. 7 Ma)**	**fraction of SW-irrad**	**depth of magma ocean**
flux times present		**[%]**	**[km]**
atmospheric loss by giant impact [%]			**100**
3.0E+07	8.9E+06	29.4%	61
3.4E+07	6.0E+06	19.8%	90
3.7E+07	4.0E+06	13.2%	136
3.8E+07	3.0E+06	9.9%	183
4.0E+07	2.0E+06	6.6%	280
4.1E+07	1.0E+06	3.3%	592
4.2E+07	6.0E+05	2.0%	1079
4.2E+07	3.0E+05	1.0%	3300
Late veneer $^{20}Ne/^{22}Ne$			**5.2**
M_E [%] accreted by Late veneer			**0.85**
degree of mantle degassing [%]			**88.72**
shielded accretion (e.g. 5 Ma)	**duration of SW-irrad. (e.g. 7 Ma)**	**fraction of SW-irrad**	**depth of magma ocean**
flux times present		**[%]**	**[km]**
atmospheric loss by giant impact [%]			**100**
8.1E+06	2.5E+07	80.9%	61
2.8E+07	1.0E+07	33.0%	151
3.4E+07	6.0E+06	19.8%	256
3.6E+07	4.5E+06	14.9%	346
3.8E+07	3.5E+06	11.6%	454
3.8E+07	3.1E+06	10.2%	518
4.0E+07	2.0E+06	6.6%	854
4.0E+07	1.5E+06	5.0%	1218
4.1E+07	1.0E+06	3.3%	2206
4.1E+07	9.1E+05	3.0%	2640
4.2E+07	6.0E+05	2.0%	9480

strongly degassed mantle			
Late veneer $^{20}Ne/^{22}Ne$			**8.2**
M_E [%] accreted by Late veneer			**2.26**
degree of mantle degassing [%]			**95.7**
shielded accretion (e.g. 5 Ma)	**duration of SW-irrad. (e.g. 7 Ma)**	**fraction of SW-irrad**	**depth of magma ocean**
flux times present		**[%]**	**[km]**
atmospheric loss by giant impact [%]			**100**
2.1E+07	1.6E+07	51.2%	52
2.7E+07	1.1E+07	36.3%	73
3.0E+07	9.0E+06	29.7%	90
3.1E+07	8.0E+06	26.4%	101
3.4E+07	6.0E+06	19.8%	136
3.6E+07	4.5E+06	14.9%	182
3.8E+07	3.0E+06	9.9%	279
4.0E+07	2.0E+06	6.6%	429
4.0E+07	1.5E+06	5.0%	589
4.1E+07	1.0E+06	3.3%	942
4.2E+07	6.0E+05	2.0%	1870
4.2E+07	3.0E+05	1.0%	9882
Late veneer $^{20}Ne/^{22}Ne$			**9.2**
M_E [%] accreted by Late veneer			**3.28**
degree of mantle degassing [%]			**91.47**
shielded accretion (e.g. 5 Ma)	**duration of SW-irrad. (e.g. 7 Ma)**	**fraction of SW-irrad**	**depth of magma ocean**
flux times present		**[%]**	**[km]**
atmospheric loss by giant impact [%]			**100**
3.0E+07	8.9E+06	29.4%	46
3.3E+07	7.0E+06	23.0%	58
3.7E+07	4.0E+06	13.2%	102
3.8E+07	3.0E+06	9.9%	137
4.0E+07	2.0E+06	6.6%	208
4.1E+07	1.0E+06	3.3%	433
4.2E+07	6.0E+05	2.0%	767
4.2E+07	3.0E+05	1.0%	1878
4.2E+07	2.0E+05	0.7%	7840
Late veneer $^{20}Ne/^{22}Ne$			**5.2**
M_E [%] accreted by Late veneer			**0.85**
degree of mantle degassing [%]			**97.43**
shielded accretion (e.g. 5 Ma)	**duration of SW-irrad. (e.g. 7 Ma)**	**fraction of SW-irrad**	**depth of magma ocean**
flux times present		**[%]**	**[km]**
atmospheric loss by giant impact [%]			**100**
8.1E+06	2.5E+07	80.9%	55
2.8E+07	1.0E+07	33.0%	137
3.4E+07	6.0E+06	19.8%	232
3.6E+07	4.5E+06	14.9%	313
3.8E+07	3.5E+06	11.6%	410
3.8E+07	3.1E+06	10.2%	468
4.0E+07	2.0E+06	6.6%	765
4.0E+07	1.5E+06	5.0%	1081
4.1E+07	1.0E+06	3.3%	1889
4.1E+07	9.1E+05	3.0%	2207
4.2E+07	6.0E+05	2.0%	8870

Tab. B8: The calculations that are performed to produce the results in Table B7 have now to be reconciled with a certain amount of retained ^{20}Ne in the atmosphere in "phase II" after the giant Moon-forming impact (results for 2–8 % retained ^{20}Ne shown in Tab. B8). The amount of retained ^{20}Ne adds to the atmospheric inventory and applies to eq. (12). To generate today's atmospheric and mantle Ne inventories, in particular, the depth of the magma ocean (eq. (11)) and the degree of mantle degassing (eq. (12)) have to be adjusted to obtain the respective needed fraction of SW irradiated material (eq. (8) and eq. (10)) which delivers ^{20}Ne that is available for dissolution into the magma ocean. Decreasing amounts of SW irradiated material are needed if the fraction of surviving Ne after the giant impact increases. For simplicity, only the case of a late veneer contribution with a ^{20}Ne/^{22}Ne ratio of 8.2 (Ne-A) is considered. The results of the calculations are shown in Table B8 and Figure 3.12.

Giant impact eroded atmosphere

moderately degassed mantle

Late veneer ^{20}Ne/^{22}Ne			**8.2**	
M_E [%] accreted by Late veneer			**2.26**	
shielded accretion (e.g. 5 Ma)	**duration of SW-irrad. (e.g. 7 Ma)**	**fraction of SW-irrad**	**depth of magma ocean**	**mantle degassing**
flux times present		**[%]**	**[km]**	**[%]**
atmospheric loss by giant impact [%]			**98**	
3.9E+07	2.8E+06	9.2%	61	1.5
3.9E+07	2.8E+06	9.1%	64	5.2
3.9E+07	2.8E+06	9.1%	65	6.5
3.9E+07	2.5E+06	8.3%	101	33.3
4.0E+07	2.0E+06	6.6%	200	57.2
4.0E+07	1.9E+06	6.3%	226	60.0
4.0E+07	1.5E+06	5.0%	375	68.6
4.1E+07	1.3E+06	4.3%	489	71.6
4.1E+07	1.0E+06	3.3%	764	75.2
4.1E+07	9.0E+05	3.0%	908	76.2
4.2E+07	6.0E+05	2.0%	1805	78.7
4.2E+07	5.6E+05	1.9%	2037	79.0
4.2E+07	5.1E+05	1.7%	2500	79.4
atmospheric loss by giant impact [%]			**96**	
4.0E+07	1.4E+06	4.6%	126	3.5
4.0E+07	1.4E+06	4.6%	128	4.8
4.1E+07	1.3E+06	4.3%	177	25.9
4.1E+07	1.0E+06	3.3%	426	58.2
4.1E+07	9.0E+05	3.0%	554	63.4
4.1E+07	7.3E+05	2.4%	891	70.0
4.2E+07	6.0E+05	2.0%	1320	73.5
4.2E+07	4.5E+05	1.5%	2500	76.6
atmospheric loss by giant impact [%]			**94**	
4.1E+07	9.3E+05	3.1%	193	4.6
4.1E+07	9.0E+05	3.0%	230	16.8
4.1E+07	6.6E+05	2.2%	717	60.0
4.2E+07	6.0E+05	2.0%	905	64.2
4.2E+07	4.9E+05	1.6%	1486	70.3
4.2E+07	4.0E+05	1.3%	2500	73.9
atmospheric loss by giant impact [%]			**92**	
4.1E+07	7.0E+05	2.3%	261	5.1
4.1E+07	6.8E+05	2.2%	306	16.1
4.2E+07	6.0E+05	2.0%	537	43.6
4.2E+07	5.0E+05	1.6%	989	60.0
4.2E+07	3.8E+05	1.3%	2138	70.0
4.2E+07	3.7E+05	1.2%	2500	71.1

Giant impact eroded atmosphere

strongly degassed mantle

Late veneer ^{20}Ne/^{22}Ne			**8.2**	
M_E [%] accreted by Late veneer			**2.26**	
shielded accretion (e.g. 5 Ma)	**duration of SW-irrad. (e.g. 7 Ma)**	**fraction of SW-irrad**	**depth of magma ocean**	**mantle degassing**
flux times present		**[%]**	**[km]**	**[%]**
atmospheric loss by giant impact [%]			**98**	
3.9E+07	2.8E+06	9.2%	13	5.0
3.9E+07	2.8E+06	9.1%	16	21.9
3.9E+07	2.5E+06	8.3%	46	69.7
3.9E+07	2.3E+06	7.6%	76	80.0
4.0E+07	2.0E+06	6.6%	129	86.4
4.0E+07	1.7E+06	5.6%	211	90.0
4.0E+07	1.5E+06	5.0%	275	91.3
4.1E+07	1.3E+06	4.3%	368	92.4
4.1E+07	1.0E+06	3.3%	592	93.6
4.1E+07	9.0E+05	3.0%	706	93.9
4.1E+07	8.7E+05	2.9%	754	94.0
4.2E+07	6.0E+05	2.0%	1380	94.7
4.2E+07	4.9E+05	1.6%	2000	94.9
4.2E+07	4.4E+05	1.5%	2500	95.0
atmospheric loss by giant impact [%]			**96**	
4.0E+07	1.4E+06	4.6%	25	1.1
4.0E+07	1.4E+06	4.6%	26	5.0
4.1E+07	1.3E+06	4.3%	68	60.8
4.1E+07	1.2E+06	3.8%	152	80.0
4.1E+07	1.0E+06	3.3%	271	86.8
4.1E+07	9.0E+05	3.0%	374	89.1
4.1E+07	8.5E+05	2.8%	433	90.0
4.2E+07	6.0E+05	2.0%	965	93.0
4.2E+07	4.2E+05	1.4%	2000	94.2
4.2E+07	3.9E+05	1.3%	2500	94.4
atmospheric loss by giant impact [%]			**94**	
4.0E+07	9.3E+05	3.1%	39	4.7
4.1E+07	9.0E+05	3.0%	67	42.6
4.1E+07	7.7E+05	2.5%	231	80.0
4.2E+07	6.0E+05	2.0%	597	89.4
4.2E+07	5.8E+05	1.9%	668	90.0
4.2E+07	3.8E+05	1.2%	2000	93.4
4.2E+07	3.5E+05	1.1%	2500	93.7
atmospheric loss by giant impact [%]			**92**	
4.1E+07	7.0E+05	2.3%	52	4.5
4.1E+07	6.8E+05	2.2%	83	38.5
4.2E+07	6.0E+05	2.0%	262	77.2
4.2E+07	5.8E+05	1.9%	310	80.0
4.2E+07	4.4E+05	1.5%	916	90.0
4.2E+07	3.4E+05	1.1%	2000	92.6
4.2E+07	3.1E+05	1.0%	2500	93.0

Tab. B9: Without an early magma ocean in "phase I" before the Moon-forming impact, all particles reaching Earth's surface after ablation losses during descent through the protoatmosphere can directly incorporate their Ne inventory into Earth's interior. As for the calculations in Tab. B7, the Ne values that are aimed to be reconciled with a deviation of less than 1% are the atmospheric ^{20}Ne inventory ($6.52*10^{19}$ cm³STP; Zhang, 2014) and ^{20}Ne/^{22}Ne ratio of 9.80 (eq. (18)) as well as the ^{20}Ne inventory of the mantle (eq. (19), $6.55*10^{18}$ cm³STP for a moderately degassed mantle and $1.31*10^{18}$ cm³STP for a strongly degassed mantle; Marty, 2012).
During earliest accretion in "phase I", the Ne-B flux from the inner Solar System to the surface is characterized by an ^{20}Ne/^{22}Ne ratio of 12.55 (surface Ne-B flux in Tab. B4) which directly determines the isotopic ratio of Earth's interior. Only if a coeval Ne-A flux to the surface (surface Ne-A flux in Tab. B4) would be enhanced by a factor of $8*10^2$ over the Ne-B surface flux, the ^{20}Ne/^{22}Ne ratio would decrease below 12.50.
Comparable with Tab. B7 and eq. (8) the fraction of SW irradiated material from the total terrestrial precursor material is given by the time dependent flux rates that are needed to result in the Ne compositions observed today. For examplification, the Mooon-forming impcat is considered to erode any pre-existing atmosphere and the Ne-A component has an isotopic ratio of ^{20}Ne/^{22}Ne: 8.2. In this case the irradiated fraction is given by:

$$\frac{(9.17*10^5)*7\text{Ma}}{(9.17*10^5)*7\text{Ma}+(4.11*10^7)*5\text{Ma}} = 0.0303\ (=3.03\%) \quad (15)$$

As in Tab. B7 and eq. (9), this is justified if ~95% M_E is accreted before the Moon-forming impact by using Tab. B1:

$$(4.11*10^7)*\left(\sum_{10^{-16}g}^{10^{25}g} massbin\ flux\ \left[{}^{g}/_{yr}\right]\right)*5Ma+(9.17*10^5)*\left(\sum_{10^{-16}g}^{10^{25}g} massbin\ flux\ \left[{}^{g}/_{yr}\right]\right)*7Ma = 0.95\ M_E \quad (16)$$

The amount of incorporated ^{20}Ne into Earth during "phase I" is then given using the surface Ne-B flux (Tab. B4):

$$(9.17*10^5)*\left(\sum_{10^{-16}g}^{10^{-3}g} {}^{20}Ne\ bin\ surface\ flux\ (Ne-B)\ \left[cm^3STP/_{yr}\right]\right)*7Ma = 3.73*10^{19} cm^3STP\ {}^{20}Ne \quad (17)$$

In "phase II", after the giant Moon-forming impact that caused total atmospheric blow-off and the generation of a magma ocean, mantle degassing leads to reinjection of the previously incorporated ^{20}Ne into the atmosphere. Comparable with Tab. B7 and eq. (12), the degassed Ne-B component (^{20}Ne/^{22}Ne: 12.55), resulting from 82.27% mantle degassing, mixes with a late veneer flux of $1*10^5$ times the present flux with an isotopic composition of ^{20}Ne/^{22}Ne: 8.2 (upper atmosphere Ne-A flux in Tab. B4, exemplified case) prevailing for a 50 Ma period, to result in the present atmospheric ^{20}Ne/^{22}Ne ratio of 9.80:

$$\frac{(3.73*10^{19}\text{cm}^3\text{STP}*0.8227)+(1*10^5)*\left(\sum_{10^{-16}g}^{10^{25}g} {}^{20}Ne\ bin\ flux\ (Ne-A)\left[cm^3STP/_{yr}\right]\right)*50\ Ma}{\left(\frac{3.73*10^{19}\text{cm}^3\text{STP}*0.8227}{12.55}\right)+(1*10^5)*\left(\sum_{10^{-16}g}^{10^{25}g} {}^{22}Ne\ bin\ flux\ (Ne-A)\left[cm^3STP/_{yr}\right]\right)*50\ Ma} = 9.80 \quad (18)$$

The atmospheric ^{20}Ne inventory is given by the numerator of eq. (18) and amounts to $6.52*10^{19}\text{cm}^3\text{STP}$. The remaining ^{20}Ne after mantle degassing determines the present mantle inventory observed today for a moderately degassed mantle and is calculatd with:

$$3.73*10^{19}\text{cm}^3\text{STP}*(1-0.8227) \approx 6.6*10^{18}\text{cm}^3\text{STP} \quad (19)$$

If incomplete atmospheric erosion by the Moon-forming impact is taken into consideration a given fraction of the pre-existing atmosphere is retained. The amount of surviving atmospheric ^{20}Ne is given by the percentage (retained after the giant impact) of the amount delivered to the upper atmosphere (cf. eq. (10), upper atmosphere Ne-B flux in Tab. B4) that is substracted by the amount of incorporated ^{20}Ne within Earth (eq. (17)). For example, if the late veneer has an isotopic ratio of ^{20}Ne/^{22}Ne: 8.2 (Ne-A) and 94% of the atmophere is erorded by the impactor then the amount of surviving ^{20}Ne is:

$$0.06*\left[\left((5.22*10^5)*\left(\sum_{10^{-16}g}^{10^{25}g} {}^{20}Ne\ bin\ flux\ (Ne-B)\ \left[cm^3STP/_{yr}\right]\right)*7Ma\right)-\left((5.22*10^5)*\left(\sum_{10^{-16}g}^{10^{-3}g} {}^{20}Ne\ bin\ surface\ flux\ (Ne-B)\ \left[cm^3STP/_{yr}\right]\right)*7Ma\right)\right] = 1.59*10^{19} cm^3STP\ {}^{20}Ne \quad (20)$$

This amount adds to the atmospheric ^{20}Ne inventory used for the caluclations in eq. (18) requiring adjustment of the assocaited degree of mantle degassing (i.e., 68.88%) and the amount of incorporated ^{20}Ne before the Moon-forming impact (eq. (17)). Consequently, surviving atmospheric ^{20}Ne after the Moon-forming impact decreases the needed fraction of SW irradiated material from the total terrestrial precursor material that is directly incorporated within Earth. For 6% surviving atmospheric ^{20}Ne the fraction is determined with:

$$\frac{(5.22*10^5)*7\text{Ma}}{(5.22*10^5)*7\text{Ma}+(4.17*10^7)*5\text{Ma}} = 1.72\% \quad (21)$$

These results and the results for a variety of parameters are shown in Tab. B9 and Figure 3.16.

non-Magma ocean model moderately degassed mantle		
atmospheric ^{20}Ne [cm³]		**6.52E+19**
mantle ^{20}Ne [cm³]		**6.55E+18**
Late veneer endmember	**fraction of SW-irrad. [%]**	**mantle degassing [%]**
atmospheric loss by giant impact [%]		**100**
5.2	4.78%	88.72
6.2	4.38%	87.75
7.2	3.83%	85.99
8.2	3.03%	82.27
8.6	2.59%	79.28
9.2	1.74%	69.20
9.8	0	0
atmospheric loss by giant impact [%]		**98**
5.2	3.82%	85.96
6.2	3.50%	84.68
7.2	3.07%	82.49
8.2	2.42%	77.83
8.6	2.07%	74.11
9.2	1.39%	61.40
9.8	0	0
atmospheric loss by giant impact [%]		**96**
5.2	3.18%	83.14
6.2	2.92%	81.60
7.2	2.55%	78.97
8.2	2.02%	73.40
8.6	1.73%	68.95
9.2	1.16%	53.73
9.8	0	0
atmospheric loss by giant impact [%]		**94**
5.2	2.73%	80.33
6.2	2.50%	78.52
7.2	2.19%	75.44
8.2	1.72%	68.88
8.6	1.48%	63.73
9.2	0.99%	46.00
9.8	0	0
atmospheric loss by giant impact [%]		**92**
5.2	2.39%	77.53
6.2	2.19%	75.46
7.2	1.91%	71.91
8.2	1.51%	64.45
8.6	1.29%	58.55
9.2	0.87%	38.30
9.8	0	0
atmospheric loss by giant impact [%]		**83**
5.2	1.53%	64.85
6.2	1.40%	61.63
7.2	1.22%	56.05
8.2	0.96%	44.30
8.6	0.82%	34.85
9.2	0.56%	3.65
9.8	0	0
atmospheric loss by giant impact [%]		**70**
5.2	1.00%	46.55
6.2	0.92%	41.65
7.2	0.80%	33.10
8.2	0.63%	15.40
8.6	0.54%	1.20
9.2	-	-
9.8	-	-

non-Magma ocean model strongly degassed mantle		
atmospheric ^{20}Ne [cm³]		**6.52E+19**
mantle ^{20}Ne [cm³]		**1.31E+18**
Late veneer endmember	**fraction of SW-irrad. [%]**	**mantle degassing [%]**
atmospheric loss by giant impact [%]		**100**
5.2	4.36%	97.45
6.2	3.95%	97.19
7.2	3.41%	96.74
8.2	2.60%	95.73
8.6	2.17%	94.87
9.2	1.32%	91.56
9.8	0	0
atmospheric loss by giant impact [%]		**98**
5.2	3.48%	96.81
6.2	3.16%	96.49
7.2	2.72%	95.92
8.2	2.08%	94.66
8.6	1.73%	93.59
9.2	1.05%	89.43
9.8	0	0
atmospheric loss by giant impact [%]		**96**
5.2	2.90%	96.17
6.2	2.64%	95.79
7.2	2.27%	95.10
8.2	1.74%	93.61
8.6	1.45%	92.32
9.2	0.88%	87.31
9.8	0	0
atmospheric loss by giant impact [%]		**94**
5.2	2.49%	95.53
6.2	2.26%	95.08
7.2	1.94%	94.28
8.2	1.49%	92.53
8.6	1.24%	91.03
9.2	0.75%	85.22
9.8	0	0
atmospheric loss by giant impact [%]		**92**
5.2	2.17%	94.89
6.2	1.98%	94.38
7.2	1.70%	93.46
8.2	1.30%	91.45
8.6	1.08%	89.74
9.2	0.66%	83.10
9.8	0	0
atmospheric loss by giant impact [%]		**70**
5.2	0.92%	87.87
6.2	0.83%	86.63
7.2	0.71%	84.45
8.2	0.55%	79.63
8.6	0.45%	75.56
9.2	0.28%	59.89
9.8	0	0

Acknowledgments

I am deeply thankful to my supervisor Prof. Dr. Mario Trieloff for his work that enabled me to conduct my research in the exceptional field of noble gas geo- and cosmochemistry and giving me the opportunity to work in the 'Klaus-Tschira-Labor für Kosmochemie' at the 'Institut für Geowissenschaften' in Heidelberg. I am explicitly grateful for his support, long-lasting discussions and many helpful suggestions to complete my work, for his understanding and patience.

I am furthermore remarkably thankful to my co-supervisor Prof. Dr. Ulrich Ott from the University of West Hungary, Sopron, for his support, numerous constructive discussions and comments and especially for his substantial and detailed scientific advices.

The Klaus Tschira Stiftung gGmbH is acknowledged for financial support.

My sincere thanks go to the members of the research group for geo- and cosmochemistry at the 'Institut für Geowissenschaften' in Heidelberg, PD Dr. Jens Hopp and Dr. Winfried Schwarz, for their support, helpful discussions, comments and corrections as well as for introducing me into the mysteries of noble gas mass spectrometry.

Many thanks to Dr. Alexander Varychev from the 'Institut für Geowissenschaften' in Heidelberg for his support during my work at the SEM.

I want to thank Dr. Jutta Zipfel from the 'Senckenberg Forschungsinstitut und Naturmuseum' in Frankfurt for providing a valuable sample of the iron meteorite Washington County. For suggestions and preparation of the sample, Oliver Wienand and Ilona Fin from the 'Institut für Geowissenschaften' in Heidelberg are highly appreciated.

For helpful suggestions and advices during the beginning of my work, I want to thank Dr. Bastian Baecker who carried out his PhD thesis about noble gases in micrometeorites on which my initial studies were based on.

Furthermore, I want to thank apl. Prof. Dr. Hans-Peter Gail from the 'Institut für theoretische Astrophysik' in Heidelberg for discussions concerning an intended publication.

Finally, I am pleased to thank many friends and colleagues, too many to name them all, for encouragements and helpful discussions. Natascha Geißert is embraced for her encouraging and motivating support, her sympathy and love as long as I know her. Thanks to Franziska Geißert for comments and correction reading.

I dedicate this work to my parents, Wolfgang and Erika Vogt, who always stood behind me and supported me in all my decisions. You always gave me strength and encouragement!

Thank you!

Eidesstattliche Versicherung gemäß § 8 der Promotionsordnung der Naturwissenschaftlich-Mathematischen Gesamtfakultät der Universität Heidelberg

1. Bei der eingereichten Dissertation zu dem Thema

Acquisition of solar wind implanted neon by terrestrial precursor material resembled by iron meteorites and interplanetary dust: implications for the early evolution of the Earth´s mantle-atmosphere system

handelt es sich um meine eigenständig erbrachte Leistung.

2. Ich habe nur die angegebenen Quellen und Hilfsmittel benutzt und mich keiner unzulässigen Hilfe Dritter bedient. Insbesondere habe ich wörtlich oder sinngemäß aus anderen Werken übernommene Inhalte als solche kenntlich gemacht.

3. Die Arbeit oder Teile davon habe ich wie folgt/bislang nicht[1)] an einer Hochschule des In- oder Auslands als Bestandteil einer Prüfungs- oder Qualifikationsleistung vorgelegt.

Titel der Arbeit:_____

Hochschule und Jahr:_____

Art der Prüfungs- oder Qualifikationsleistung:_____

4. Die Richtigkeit der vorstehenden Erklärungen bestätige ich.

5. Die Bedeutung der eidesstattlichen Versicherung und die strafrechtlichen Folgen einer unrichtigen oder unvollständigen eidesstattlichen Versicherung sind mir bekannt.

Ich versichere an Eides statt, dass ich nach bestem Wissen die reine Wahrheit erklärt und nichts verschwiegen habe.

_____ _____

Ort und Datum Unterschrift

[1)]Nicht Zutreffendes streichen. Bei Bejahung sind anzugeben: der Titel der andernorts vorgelegten Arbeit, die Hochschule, das Jahr der Vorlage und die Art der Prüfungs- oder Qualifikationsleistung.